Development of a Pyrolysis Model for Numerical Simulations of Flame Spread over Surfaces

Ontwikkeling van een pyrolysemodel
voor numerieke simulaties van vlamuitbreiding over oppervlakken

Shivanand R. Wasan

Promotoren: prof. dr. ir. B. Merci, prof. dr. ir. J. Vierendeels
Proefschrift ingediend tot het behalen van de graad van
Doctor in de Ingenieurswetenschappen: Werktuigkunde-Elektrotechniek

Vakgroep Mechanica van Stroming, Warmte en Verbranding
Voorzitter: prof. dr. ir. R. Sierens
Faculteit Ingenieurswetenschappen
Academiejaar 2009 - 2010

UNIVERSITEIT
GENT

ISBN 978-90-8578-339-8
NUR 978, 928
Wettelijk depot: D/2010/10.500/15

Supervisors:

Prof. Bart Merci
Prof. Jan Vierendeels

Research facility:

Department of Flow, Heat and Combustion Mechanics
Sint-Pietersnieuwstraat 41
B-9000 Ghent
Belgium

Members of the examination committee:

Prof. Geraldine Heynderickx	Ghent University	secretary
Prof. Bart Merci	Ghent University	supervisor
Dr. ir. Pieter Rauwoens	Ghent University	
Dr. Guillermo Rein	University of Edinburgh	
Prof. Luc Taerwe	Ghent University	chairman
Dr. ir. Erwin Theuns	VK Group, Belgium	
Prof. Patrick van Hees	University of Lund	
Prof. Jan Vierendeels	Ghent University	supervisor

The research presented in this dissertation was supported by a Ph.D. fellowship of the Research Foundation - Flanders (FWO).

TO
MY PARENTS
&
TEACHERS

Acknowledgement

I would like to extend my sincere gratitude towards my supervisors for guiding me during my research at Ghent University, Belgium. I appreciate my supervisor Prof. Bart Merci for his trust in me and introducing me to the field of fire. I am indebted to Prof. Jan Vierendeels for the effort in the model development and solving numerical issues.

I thank FWO-Fund for Scientific research-Flanders (Belgium)(FWO-Vlaanderen) and Ghent University for the financial help as scholarship during my stay in Belgium.

I appreciate Pieter Rauwoens for his help to handle some model development tasks to complete this work. I thank him for his patience in correcting this thesis.

I wish to extend my gratitude to all my colleagues and friends for their cooperation during my stay in the department. I thank Yves for his quick solutions for the computer/server problems. I specially thank Patricia for her parental affection towards my family.

I thank Prof. Partick van Hees from University of Lund to allow me to conduct experiments and Dr. Ulf Goransson for his wonderful help to conduct some interesting experiments during my stay in University of Lund, Sweden.

Last but not least, speaking on my family, I would like to heartly thank my wife for her wonderful support during my stay in Belgium. My wife and son always kept me cheerful during my final year in Belgium. They were the source for my motivation. I express my regards to my brother for his wonderful conversations. Never to forget, I thank with my soul to my parents for their advise kept me focussed all time.

Gent, Jan 2010
Shivanand R. Wasan

Summary

In many cultures, fire is believed to originate from the cosmos, ever since the creation of this universe. Mankind started to use fire as a heat source. Up until today, heat from combustion is useful to satisfy energy needs, burning solids, liquids and gases. Fire has pros and cons, depending on the view point of an individual and the purpose of application.

The present work is situated in the field of Fire Safety Engineering (FSE). From a fire prevention point of view, exploring the nature of fire helps to understand the phenomena that take place during the process of fire development, from ignition to a fully developed fire. A study is made to understand some major aspects of fire development through numerical simulations by developing a simplified model to resemble the pyrolysis process, occurring in the solid. The pyrolysis model is kept simple so that, in a later stage, coupling to simulations of phenomena in the gas phase is possible to fully study fire development and flame spread phenomena in numerical simulations. The present work, focusing on pyrolysis modeling, only briefly touches this aspect.

When a solid is exposed to a radiant heat flux, be it from flames or from an external heat source, the temperature in the solid rises. Heat is transferred into the solid by conduction. When the temperature is high enough, the solid undergoes degradation, 'pyrolysis', and combustible volatiles, 'pyrolysis gases', are released. These gases flow out of the solid, mix with air and, if the circumstances allow so, burn to generate flames. These flames can further develop as the pyrolysis process proceeds in the solid, with the pyrolysis gases as fuel to feed to the flames. The flames provide radiant heat to the un-burnt solid, thus feeding heat to sustain the ongoing endothermic pyrolysis process. Char oxidation can also provide heat to this purpose, but this is not taken into consideration in the present work.

Materials are classified into two categories: solids which leave a considerable amount of char after pyrolysis process as residue ('charring materials') and solids that do not ('non-charring materials'). The material can contain moisture in the form of free and bound water. Only free moisture is considered in the present work. The developed pyrolysis model is successfully applied to charring and non-charring materials, possibly containing moisture.

The pyrolysis model uses enthalpy as basic quantity. The pyrolysis process is modelled as an infinitely fast, endothermic process, taking in an infinitely thin front, at a given pyrolysis temperature. Chemical kinetics during pyrolysis and char oxidation are not included in the model. The convective heat flux with the flow of pyrolysis gases is taken into account. The pyrolysis gases are assumed to leave the solid as soon as they are generated. More complex transport models, including the effects of pressure pile-up, cracks or inward flow

with condensation, are possible, but this is beyond the scope of the present work. The evaporation process of the free moisture and the corresponding mass flow rate of water vapour are treated in a similar manner, i.e. the evaporation of the moisture occurs in an infinitely thin front at temperature equal to 373 K.

Firstly, the basic thermodynamic description of the model is revisited for charring and non-charring materials, possibly containing moisture. The notion 'heat of pyrolysis' is carefully defined and its relation to the formation enthalpies of individual constituents is explained. Solving only one equation, for enthalpy, on a fixed computational mesh, provides a useful model for the pyrolysis process inside the solid material. The adoption of a piecewise linear representation of the temperature field is important to obtain continuous pyrolysis gases mass flow rates in time.

The first applications concern one-dimensional reference test cases, with imposed external heat flux on dry and wet charring and non-charring materials. The present model formulation is robust with respect to numerical aspects (cell size and time step) and the developed model performs well for variable external heat fluxes. Numerical reference results, obtained with the more complex moving mesh model, are reproduced and the model performs better than the integral model. This was confirmed for variable material thickness and boundary conditions, revealing that the model provides good results for thermally thin and thermally thick materials. It is also shown that possible interruption of the pyrolysis process, due to excessive heat losses, is automatically predicted with the present approach.

For charring and non-charring materials, the model results are also compared to experimental data, again confirming the potential of the model. Part of the experimental data was generated in an experimental campaign, executed during a visit to the University of Lund (Sweden). Cone calorimeter experiments were performed on square, horizontally mounted, MDF samples (9.8cm by 9.8cm, 1.65cm thick). The evolution in time was reported of the mass loss rate and the temperature distribution inside the material, i.e. at the surface and at different depths. Different externally imposed heat fluxes are investigated (20 kW/m^2, 30 kW/m^2 and 50 kW/m^2) on dry and wet material.

Next, two-dimensional cases are considered, in order to examine the potential of the model for flame spread simulations. First, we use a numerical reference case, using correlations from the literature to impose an external heat flux. The results reveal a running pyrolysis front, as in real vertically upward flame spread. The findings are also put into perspective with corresponding one-dimensional results. Coupling to CFD (Computational Fluid Dynamics) simulations in the gas phase is briefly touched, to show the potential to fully simulate fire development and flame spread.

Finally, results are reported from large scale flame spread tests, also executed during a visit to the University of Lund (Sweden). Temperature was measured. Vertical upward flame spread was studied for two parallel particle board plates (0.025 m thick, 0.4 m wide and 2.5 m high), vertically mounted face-to-face. Two types of burners were used, corresponding to different horizontal spacing between the two plates: a sand burner (distance: 30.5 cm) and a honeycomb burner (distance: 10.5 cm). The temporal surface temperature evolution is measured over the height of one of the plates. Re-radiation, natural convection due to

buoyancy, and forced convection, due to mechanical ventilation, affect the flame spread. Good agreement to the experimental observations is obtained in the numerical simulation results, provided that a heat flux is imposed, based on the temperature measurements.

The major future developments are the inclusion of different additional effects, occurring in reality during the pyrolysis process, such as char oxidation, the formation of cracks, complex shrinkage and the possible condensation of gases inside the solid. Also, the current pseudo-2D formulation can be extended to a truly 3D reconstruction method with front tracking.

Samenvatting

In vele culturen wordt geloofd dat vuur afstamt uit de kosmos, van bij het begin van de creatie van het universum. De mens begon vuur te gebruiken als warmtebron. Tot op vandaag is warmte uit verbranding nuttig om energienoden te vervullen. Hierbij worden vaste, vloeibare en gasvormige brandstoffen verbrand. Vuur heeft dus voor- en nadelen, afhankelijk van het individuele standpunt en het doel van de toepassing.

Het onderhavige werk situeert zich in het domein van Fire Safety Engineering (FSE). Vanuit het standpunt van brandpreventie helpt het bestuderen van de aard van vuur om de fenomenen te begrijpen die optreden tijdens de ontwikkeling van een brand, van ontsteking tot volontwikkelde brand. Er wordt een studie uitgevoerd om enkele belangrijke aspecten van brandontwikkeling te begrijpen door middel van numerieke simulaties, door een vereenvoudigd model te ontwikkelen dat het pyrolyseproces, dat plaatsvindt in het vaste materiaal, nabootst. Het pyrolysemodel wordt eenvoudig gehouden opdat, in een later stadium, een koppeling met simulaties van fenomenen die optreden in de gasfase, mogelijk wordt om de ontwikkeling van brand en fenomenen van vlamuitbreiding volledig te bestuderen in numerieke simulaties. Het onderhavige werk, dat zich richt op pyrolysemodellering, raakt die laatste aspect slechts summier aan.

Wanneer een vast materiaal wordt blootgesteld aan een warmteflux door straling, hetzij vanwege vlammen, hetzij vanwege een externe warmtebron, stijgt de temperatuur in het vaste materiaal. De warmte wordt overgedragen in het vaste materiaal door conductie. Wanneer de temperatuur voldoende hoog is, degradeert het vaste materiaal ('pyrolyse') en worden brandbare vluchtige gassen ('pyrolysegassen') vrijgesteld. Deze gassen stromen uit het vaste materiaal, mengen met lucht en, wanneer de omstandigheden dit toelaten, verbranden en vormen vlammen. Deze vlammen kunnen verder ontwikkelen naarmate het pyrolyseproces verder doorgaat in het vaste materiaal, met de pyrolysegassen als brandstof om de vlammen te voeden. De vlammen zorgen voor stralingswarmte naar het onverbrande vaste materiaal en levert aldus warmte om het aan de gang zijnde endotherme pyrolyseproces in stand te houden. Oxidatie van 'char' kan hier ook warmte voor leveren, maar dit wordt niet in rekening gebracht in het onderhavige werk.

Materialen worden gecatalogeerd in twee categorieën: vaste materialen die een aanzienlijke hoeveelheid 'char' als residu achterlaten na het pyrolyseproces ('verkolende materialen') en materialen die dat niet doen ('niet-verkolende materialen'). Het materiaal kan vocht bevatten, in de vorm van vrij en gebonden water. Enkel vrij vocht wordt beschouwd in het onderhavige werk. Het ontwikkelde Pyrolysemodel wordt met succes toegepast op verkolende en niet-verkolende materialen, die al dan niet vocht bevatten.

Het pyrolysemodel gebruikt enthalpie als basisgrootheid. Het pyrolyseproces wordt gemodelleerd als een oneindig snel, endotherm proces dat doorgaat in een oneindig dun front, dat zich op pyrolysetemperatuur bevindt. Chemische reactiekinetiek en char oxidatie worden niet in het model gebracht. De convectieve warmteflux met de stroom van pyrolysegassen wordt wel in rekening gebracht. Er wordt verondersteld dat de pyrolysegassen het vaste materiaal verlaten zodra ze gegenereerd worden. Complexere transportmodellen, die het effect van drukopbouw, scheuren of condensatie van inwaartse stromen, in rekening brengen, zijn mogelijk maar vallen buiten het bereik van het onderhavige werk. Het verdampingsproces van het vrije vocht en het overeenkomstige massadebiet waterdamp worden op dezelfde manier behandeld, i.e. de verdamping van het vocht gebeurt in een oneindig dun front op een temperatuur gelijk aan 373 K.

Vooreerst wordt de thermodynamische basisbeschrijving van het model hernomen voor verkolende en niet-verkolende materialen, mogelijks met vocht. De notie 'pyrolysewarmte' wordt zorgvuldig gedefinieerd en het verband met de vormingsenthalpieën van individuele constituenten wordt uitgelegd. Het oplossen van één vergelijking, voor enthalpie, op een vast rekenrooster, levert een bruikbaar model voor het pyrolyseproces in het vaste materiaal. De aanname van een stuksgewijs lineaire voorstelling van het temperatuursveld is belangrijk om een continue evolutie van het massadebiet pyrolysegassen in functie van de tijd te bekomen.

Vervolgens betreffen de eerste toepassingen eendimensionale referentie testgevallen, met opgelegde externe warmteflux op droge en natte verkolende en niet-verkolende materialen. De huidige modelformulering is robuust met betrekking tot numerieke aspecten (celafmeting en tijdstap) en het model presteert goed voor variabele warmtefluxen. Numerieke referentieresultaten, bekomen met het complexere model met een bewegend rooster, worden gereproduceerd en het hier ontwikkelde model presteert beter dan het integraalmodel. Dit werd bevestigd voor variabele materiaaldiktes en randvoorwaarden, wat aantoont dat het model goede resultaten oplevert voor thermisch dikke en dunne materialen. Er wordt ook getoond dat een mogelijke onderbreking van het pyrolyseproces, als gevolg van overmatige warmteverliezen, automatisch voorspeld wordt met de onderhavige aanpak.

Voor verkolende en niet-verkolende materialen worden de simulatieresultaten met het model ook vergeleken met experimentele gegevens. Deze experimentele gegevens werden gedeeltelijk gegenereerd gedurende een verblijf aan de Universiteit van Lund (Zweden). Cone calorimeter experimenten werden uitgevoerd op vierkante MDF monsters (9.8 cm op 9.8 cm, 1.65 cm dik), horizontaal geplaatst. De evolutie in de tijd werd gerapporteerd van het massaverlies per tijdseenheid en van de temperatuursverdeling in het materiaal, i.e. aan het oppervlak en op verschillende dieptes. Verschillende extern opgelegde warmtefluxen werden onderzocht (20 kW/m^2, 30 kW/m^2 en 50 kW/m^2), op droog en nat materiaal.

Vervolgens worden tweedimensionale testgevallen beschouwd om het potentieel van het model voor simulaties van vlamuitbreiding te onderzoeken. Eerst gebruiken we een numeriek referentiegeval met correlaties uit de literatuur om een externe warmteflux op te leggen. De resultaten tonen een lopend pyrolysefront, zoals in werkelijke verticaal opwaartse vlamuitbreiding. De bevindingen worden ook in perspectief geplaatst met overeenkomstige eendimensionale resultaten. Koppeling met CFD (Computational Fluid Dynamics) simulaties in de gasfase wordt kort aangehaald, om het potentieel te tone nom brandontwikkeling

en vlamuitbreiding volledig te simuleren.

Tot slot worden resultaten gerapporteerd van grootschalige testen op vlamuitbreiding, ook uitgevoerd tijdens een verblijf aan de Universiteit van Lund (Zweden). De temperatuur werd opgemeten. Verticale opwaartse vlamuitbreiding werd bestudeerd voor twee parallelle vezelplaten (0.025 m dik, 0.4 m breed en 2.5 m hoog), verticaal recht tegenover elkaar geplaatst. Er werden twee types brander gebruikt en ieder type komt overeen met een bepaalde horizontale afstand tussen de platen: een zandbrander (afstand: 30.5 cm) en een honingraat brander (afstand: 10.5 cm). De tijdsevolutie van de oppervlaktetemperatuur wordt gemeten over de hoogte van één van de platen. Wederzijdse bestraling, natuurlijke convectie als gevolg van thermiek en gedwongen convectie door mechanische ventilatie, beïnvloeden de vlamuitbreiding. Er is een goede overeenkomst tussen de resultaten van de numerieke simulaties en de experimentele waarnemingen, op voorwaarde dat een warmteflux wordt opgelegd die gebaseerd is op de opgemeten temperaturen.

De voornaamste toekomstige ontwikkelingen zijn het inbrengen van bijkomende effecten die in werkelijkheid voorkomen tijdens het pyrolyseproces, zoals char oxidatie, de vorming van scheuren, complex krimpen en de mogelijke condensatie van gassen in het vaste materiaal. Ook kan de huidige pseudo-tweedimensionale formulering uitgebreid worden naar een werkelijk driedimensionale reconstructie methode met front tracking.

Table of Contents

List of Figures

List of Tables

Nomenclature

Acronyms

1D	one dimensional
2D	two dimensional
ABS	Acroylonitrile butadiene styrene
BML	Bray Moss Libby
CFD	Computational fluid dynamics
CO	carbon monoxide
CO_2	Carbon dioxide
DNS	Direct numerical simulation
EBU	Eddy breakup
FDS	Fire Dynamics Simulator
HIPS	High impact polystyrene
pdf	Probability density function
PMMA	Polymethylmethacrylate
POM	Polyoxymethylene
PS	Polystyrene
LES	Large eddy simulation
RNG	Re-normalised group
RTE	Radiation transfer equation
WSGG	Weighted sum of grey gases

Latin symbols

A	Arrhenius constant	-
B	body force (per unit volume)	N/m^3
C	decay constant	-
C_μ	proportionality constant	-
C_{EBU}	constant for eddy break up model	-
$C_{\epsilon 1}$, $C_{\epsilon 1}$	constants	-
D	burner length	m
D	diffusivity	m^2/s
E	empirical constant	-
E_a	Arrhenius activation energy	kJ/mol
F	function	-
F	fuel	-
G_k	kinetic energy production	m^2/s^3
I_λ	Intensity of radiation	W/m^3
K	constant	-

L	length	m
N	number of gas species	-
N_0	Avagadro number	-
O	oxygen	-
P	products	-
P_k	source term	m^2/s^3
Pr	molecular Prandtl number	-
Pr_t	turbulent Prandtl number	-
Q	heat release rate	W
R	universal gas constant	J/(mol K)
R_{soot}	soot generation rate	kg/m^3s
Re	Reynolds number	-
S	surface	m^2
S_λ	source function	-
$\tilde{S}$	stress mean tensor	1/s
S	source term for species conservation	-
T_w	temperature at the wall	K
T_0	temperature in the first cell	K
V	volume	m^3
V	spread rate	m/s
Y	mixture fraction	-
$\langle U \rangle$	mean velocity	m/s
a	variable	-
a	speed of sound	m/s
a_k	function	-
b	variable	-
c	specific heat	kJ/(kg K)
e	exponential	-
f	surface force	N
g	acceleration due to gravity	m/s^2
h	height	m
h	enthalpy	J/kg
h	heat transfer coefficient	$W/(m^2K)$
i	integer	-
k	conductivity	W/m K
k	reaction rate constant	m/s^2
k	turbulent kinetic energy	m^2/s^2
k_a	absorption coefficient	1/m
k_k	grey gas absorption coefficient	1/m
k_s	scattering coefficient	1/m
m	mass	kg
$\dot{m}''$	mass flow rate	$kg/(m^2\ s)$
l_0	integral length scale	m
l_{pk}	Prandtl-Kolmogorov length scale	m
p	pressure	Pa
q	heat flux	W/m^2
$\vec{r}$	position vector	m

$\vec{s}$	direction vector	-
t	time	s
u	convective velocity	m/s
u	instantaneous velocity in x-direction	m/s
$u^{'}$	fluctuating velocity component in x-direction	m/s
v	velocity	m/s
x	x-direction	-
y	height	m
y	y-direction	-
y^{+}	y-coordinate	-

Greek symbols

α	mass fraction	-
α	species	-
α	absorption coefficient	-
β	Schvab-Zeldovich coupling parameter	-
γ	constant	-
δ	perturbations	-
δ	thermal penetration depth	m
δ_f	flame length	m
ϵ	emissivity	-
ϵ	eddy dissipation rate	m^2/s^3
$\phi(\tau)$	impulse function	-
Φ	scattering phase function	-
Γ	blending factor	-
κ	von Karman constant	-
λ	constant	1/s
μ	dynamic viscosity	Pa s
μ_T	turbulent viscosity	Pa s
ν	characteristic kinematic viscosity	m^2/s
ρ	density	kg/m^3
$\Omega^{'}$	solid angle	-
σ	Stephan-Boltzmann constant	$W/(m^2\ K^4)$
σ	stress tensor	Pa
σ	Prandtl number	-
τ	time	s
τ	time constant	s
$\dot{\omega}$	reaction rate	$kg/(m^3\ s)$
ξ	char fraction	-
∞	reference	-

Subscripts

0	first cell
0	reference value
1	second cell

amb	ambient
b	buoyancy
b	burner
bs	back surface
c	char
$cond$	conduction
$conv$	convection
$enth$	enthalpy
eq	equilibrium
$evap$	evaporation
ext	external
f	front
f	flame
f, pyr	pyrolysis front
g	pyrolysis gases
i	cell number
ig	ignition
k	kinetic energy
k	species
l	left
lam	laminar
max	maximum
n	last cell
net	net value
P	first near-wall node P
pyr	pyrolysis
pyr, max	maximum pyrolysis gases value
r	right
ref	reference
res	residual
s	surface
t	turbulent
$turb$	turbulent
v	virgin
v, dry	virgin dry
v, wet	virgin wet
w	water
w	wall
w, l	liquid water
w, v	water vapour

Superscripts

0	reference value
k	present iteration level
$k+1$	next iteration level
n	present time step value

$n+1$	next time step value
$+$	increment
$'$	fluctuation quantity in Reynolds averaging
$''$	fluctuation quantity in Favre averaging

Diacriticals

$-$	time-averaged quantity
$\sim$	Mass-weighted average quantity

1

Introduction

Fire is a major source of energy that continues to fulfil energy requirements to mankind. It is believed that fire was one of the five elements responsible for the formation of this universe. Fire is obtained after burning wood, coal and other materials. In developing countries, people still rely on the fire, from firewood and bagasse, for carrying out their daily routines such as cooking, heating, etc. Despite its benefits, fire can be destructive. With the advance in the field of science and technology, man has come to realize the potential risks associated with fire. Fire begins with a spark in most cases, but eventually becomes all-consuming. The goal of this work is to understand the process occurring in the solid and its effect on flame spread phenomena. More specifically, the behaviour of fire on building materials such as wood, wood derivatives (furnitures, clothes, etc.), biofuels, and plastics are studied. Flame spread plays an important role in the development of fire. When a solid is exposed to an external heat flux (i.e. in the form of radiation coming from flames and other sources), it undergoes degradation, with release in flammable volatile gases. Release of these gases from the solid leads to a change in the density of the solid; in general, the pyrolysis process is responsible for a change in the thermophysical properties of the solid material. These volatiles reach the surface and ignite when they mix with the oxygen in the air. When a sufficient amount of volatiles is available for the ignition, a sustained flame is created on the surface leading to the fire. Depending on the orientation of the solid undergoing pyrolysis, fire spreads on the surface, which is called flame spread. Different factors influence this process, the most important being the intensity of heat flux falling on the solid, the amount of volatiles released from the material in the form of volatile flammable pyrolysis gases, and the orientation of the solid.

The solids are classified into two different groups, when it comes to fire safety engineering. Solids that leave behind a considerable amount of residue after pyrolysis, called char, are classified as charring materials (e.g. wood, building materials, char forming plastics, etc). On the other hand, solids which do not leave any residue are known as non-charring materials

(e.g. PMMA, PVC, plastics, etc). The flame spread as a whole is divided into three separate sections:

- Pyrolysis process: This concerns the solid phase in which solid thermal degradation takes place, leading to the evolution of volatiles.
- Ignition: The released volatiles mix with the ambient air to form a flammable mixture that in turn forms flash, before a sustained flame is established on the solid surface.
- Flame spread: The flames formed grow in size by heating the unburnt solid. A heat and mass transfer takes place between the unburnt solid and the turbulent flames.

It is important to understand these individual processes, not only to further our understanding of the flame spread phenomenon, but also to prevent this phenomenon from happening because of its harmful effects on mankind. Knowledge of the pyrolysis process helps in controlling the fire in the early stage. In the case of the charring materials, developing char provides heat transfer resistance to the pyrolysis front. This resistance reduces the supply of volatiles to form flames. It is thus important to develop a perfect emitter or a poor conductor of heat to reduce the occurrence of fire/flame spread. Ignition studies reveal the temperature at which the material begins to degrade for a particular heat flux intensity. By combining the findings from ignition and flame spread studies, it is possible to determine a safe distance between two structures.

Performing numerical simulations by using a good model can serve this purpose. This model must predict the characteristics of fire discussed above, namely the ignition time, the mass flow rate of pyrolysis gases to the stoichiometric level, the flame propagation index and other features of fire. These characteristics must be predicted not only on lab scale but also on pilot scale and mega scale. To perform such a task, it is essential to keep the pyrolysis model as simple as possible; therefore, an enthalpy-based model is developed.

1.1 Problem description

The physical problem considered in this work is schematically represented in Figure 1.1. The figure (left) shows the pyrolysis process taking place in the solid. When solids are exposed to a radiant external heat flux, coming from a fire, burner, etc, the temperature in the solid rises due to conduction. When the surface temperature reaches the critical temperature, the pyrolysis temperature T_{pyr}, the solid degrades with the evolution of volatile flammable pyrolysis gases. This is an endothermic chemical process which consumes energy. The evolved gases move towards the surface and ignite, after mixing with the ambient air. The combustion of these volatiles is an exothermic process. Upon combustion, flames form on the surface, providing some amount of additional heat to the solid. This accelerates the pyrolysis process. If the solid contains moisture (not necessary), then a mass flux of water vapour is released from the solid. This flux does not contribute to the generation of flames. Yet another process that is responsible for the total deformation of the solid, is the char oxidation. This part is not considered in the present work. In numerical simulations, this physical problem is simplified to a one-dimensional problem using an enthalpy-based model. When a constant external heat flux is applied explicitly on the front surface, there is a temperature rise in the solid. The solid heats up due to conduction, according to

Fourier's law. After the pyrolysis process, gases are released from the solid, reaching the surface immediately to form flames. The pyrolysis process is modelled as an infinitely fast, endothermic process, occurring in an infinitely thin front, which is maintained at pyrolysis temperature. Details on the modelling technique and applicability are discussed in chapters 2, appendix A and appendix B. The model also considers the surface losses in the form of convection and radiation.

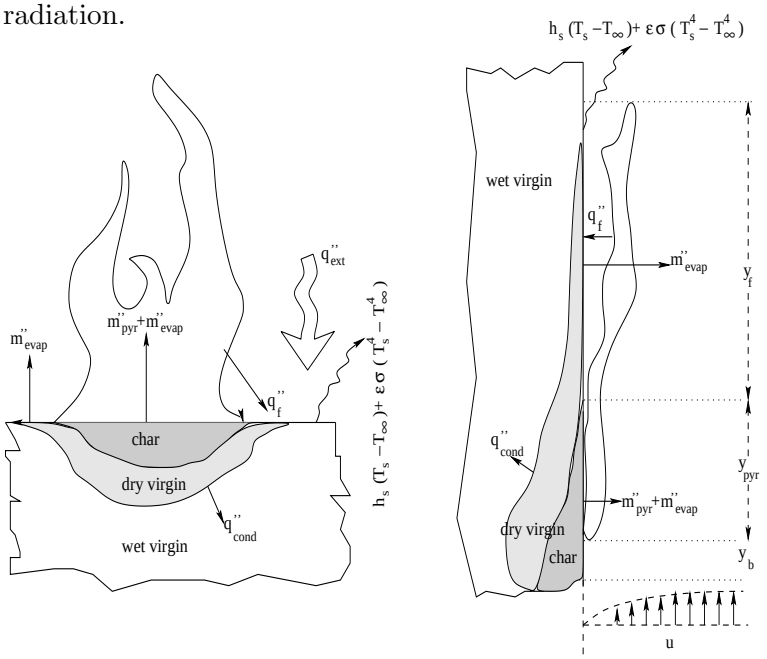

Figure 1.1: Physical problem under study in this work. Left: Pyrolysis process; right: Flame spread over solid

Figure 1.1 (right) shows the schematic upward flame spread. Flame spread is a complicated process which occurs in the gas phase, unlike the pyrolysis process which occurs in the solid phase. Flame spread starts with the ignition of the volatiles released from the pyrolyzing solid. A minimum gas-fuel stoichiometric proportion has to be achieved in order to establish a sustained flame over the solid. With continuous heating of the solid, volatiles are continuously released. These volatiles burn and rise to provide heat towards the unburnt solid by radiation. Mathematical models have been developed to determine this flame height, based on the pyrolysis gases mass flow rate and heat of combustion. In the present work, an enthalpy-based model for the pyrolysis of solid materials is coupled to the gas phase to study the flame spread phenomenon. The gas phase is modelled using a standard $k - \epsilon$ model with eddy dissipation model in Fluent (known as Eddy Breakup model) for the combustion process. The radiation effects are considered using a DOM radiation model and soot modelling is inducted using the Moss-Brookes model.

1.2 Literature review

The pioneers working in the field of pyrolysis modelling were Bamford, Cranck and Malan [11], who started as early as 1945. They modelled the pyrolysis process as a unimolecular rate of decomposition of virgin wood to char. Their model predicted the temperature distribution

along the depth of the solid. Roberts et al. [93] stressed that an overall first-order reaction with a definite heat of reaction [11] is too simple to model the entire pyrolysis process. They state that the results are the outcome of experimental conditions and therefore need to be compared with the model they developed, using a first-order Arrhenius rate model as in [11] but with a finite difference method.

Weatherford and Sheppard [123] performed an experimental and numerical study on the thermal processes involved in the ignition of wood slabs. A first-order Arrhenius model developed by Bamford et al. [11] is used in their study. The paper also discusses the ignition temperature and presents a generalised correlation of ignition threshold data. Simms and Law [100] conducted experiments to study the effect of moisture content on both the pilot and spontaneous ignition times of specimens of different wood products over a wide range of intensity of radiation. They found that moisture increases the values of thermal properties, i.e. the thermal conductivity, and the volumetric specific heat. They also showed that heat is transferred directly by molecular diffusion of the water during evaporation. They combined the heat of wetting and latent heat of evaporation within the terms of specific heat. Wesson et al. [127] point out the spectral absorption of the wood samples in order to calculate an average absorption over the range of spectral quality of the incident radiation. In doing so, they were able to predict the time for ignition.

In 1974 Kashiwagi [56] proposed a radiative model for the pyrolysis process that describes the ignition of solid fuel. This model includes the gas phase reactions and a finite absorption coefficient of the solid. He also demonstrated the in-depth absorption of the incident radiation by a solid fuel, which significantly affects the ignition delay time. He described the effects caused in ignition delay by chemical parameters such as pyrolysis activation energy, and gas phase reaction activation energy. Other important parameters affecting the ignition delay in the radiative ignition are the value of absorption coefficient of the solid phase and the endothermicity/exothermicity of the pyrolysis of a solid fuel. Furthermore, in [57,59], he described the effect of sample orientation on auto-ignition delay times and the maximum external radiative flux for auto-ignition. He came to the conclusion that ignition delay times were shorter with the horizontal sample than with the vertical orientation at the same external radiant flux. He also found that surface temperature was higher for vertical sample orientation than for the horizontal at all intensities.

In [29], Kung presented a theoretical model to study the pyrolysis process of a wood slab. A first-order Arrhenius decomposition is considered for the mass loss rate of pyrolysis volatiles. The model includes variable density, specific heat and thermal conductivity, obtained by interpolation between the virgin wood and char. Later in [30], he analysed a cylindrical wood in the experimental study, to deduce the heat value of the reaction of wood. He defined the value of ΔQ_{pyr} as the heat of reaction, exothermic if positive, as the enthalpy per unit mass of generated vapours referenced at the ambient temperature T_∞, relative to the enthalpy per unit mass of virgin wood at T_∞.

Yoshizawa and Kubota [135] tried to gain a better understanding of the mechanism of gas phase ignition of a solid. They calculated the temperature and composition distributions from the fringe shift[1] in the gas phase on application of radiation. An analysis of gas phase products shows that CO and CO_2 were the dominant species in the gas phase pyrolysis

[1] It is the behaviour of a pattern of "fringes" when the phase relationship between the component sources changes. This is most often referred to in interferometry experiments such as the Michelson-Morley.

products and that they appeared shortly after the start of irradiation.

Wichmann and Atreya [128] developed a first-order Arrhenius rate of a decomposition model for the pyrolysis of charring materials. They formulated the model considering the pyrolysis process to occur in four stages: (i) inert heating, (ii) initial pyrolysis, (iii) thin char, and (iv) thick char. Their solution indicates that the surface temperature controls the volatile production rate in the initial stages. The maximum value of mass flow rate is attained when the surface turns to char and not immediately after the pyrolysis begins. They performed a numerical study of the mass flow rate derived in the kinetically controlled stage as well as in the diffusion controlled stage. Moreover, they estimated the char formation time for the ongoing pyrolysis process.

Chen et al. [27] developed an integral thermal pyrolysis model for the transient pyrolysis of charring and non-charring materials. Despite neglecting the chemical kinetics, they were still close to exact solutions. The results obtained from the integral model were in excellent agreement with the experimental findings. In [28], they applied to the charring materials by deriving their properties. The effect of various parameters on pyrolysis temperature (T_{pyr}) was investigated by applying to the integral model [27]. They also performed the similarity relationships and sensitivity analysis. During this study, they found that the ratio of thermal capacities does not significantly affect the other important variables (k_v, c, ρ), but is found to have little influence on the heat of the pyrolysis ratio ($\lambda = \frac{L}{c(T_{pyr}-T_o)}$) and char conductivity.

Moghtaderi et al. [75] also developed an integral model for both charring and non-charring materials. They used a constant pyrolysis temperature because for most solid fuels the activation energy is so high that the solid may be assumed to pyrolyse abruptly when it reaches a so-called pyrolysis temperature (T_{pyr}). Note that the same holds true in the current work. The authors developed their model in such a way that it has three distinct phases during the pyrolysis process, namely the initial preheat phase, the infinite pyrolysis phase and finally the finite pyrolysis phase. They tested the accuracy of the integral model for both charring and non-charring materials with exact analytical solutions. The model was coupled to the gas phase to study the real scenario. The radiant heat flux was found to be much stronger than the flame heat flux, which is in agreement with our experimental results and numerical model results in chapter 6. Moghtaderi's [74] review on the modelling of a charring solid offers an elaborate classification of pyrolysis models into thermal and comprehensive models. Thermal models predict the conversion of the virgin fuel into products, based on a critical pyrolysis criterion and the energy balance. On the other hand, comprehensive models describe the degradation of the fuel by a chemical kinetic scheme coupled with the conservation equation for the transport of heat and/or mass. The review compares the integral model with the comprehensive models (models with kinetic schemes). Numerical studies were performed on the reference model (integral model), the constant pressure model (thermo-physical properties vary with temperature), the constant property model (no pressure gradient) and the quasi-steady model (i.e. negligible accumulation of mass and energy of volatiles within the solid/system). The results show that the quasi-steady model over-predicts the yield of gaseous species.

Jia et al. [54] assumed the pyrolysis process to be a stefan problem, and therefore compared it to the analytical solution results for some ideal cases. The model is very similar to the model developed by Chen et al. [27]. These authors approached the pyrolysis problem by decoupling the solution process, by calculating the new front position from the previous time

step temperatures of char and virgin materials. In the next stage, the new temperature field is computed from the new front position. A limitation of this technique is the implicit assumption that the temperature profiles at different depths are monotonic. The model was extended to higher dimensions but they found that the mass flux peak value dropped. This is also the case for our enthalpy-based model results, which are presented in chapter 6.

Spearpoint and Quintiere [102] again revised and developed the integral model to study the effect of the grain orientation either parallel or perpendicular to the heat flux. The numerical solution results of this integral model were compared to short-time solutions (a short time after ignition) and long-time solutions (a long time after ignition). They also compared the simulation results for burning rate, thermal penetration depth, char depth, char oxidation and surface temperature. The short-time solution gave a reasonable match with the initial mass loss rate, after ignition. The long-time solution, however, followed the decay behaviour of the experimental burning rate. The authors noticed a back effect, when the pyrolysis front approaches the insulated back surface.

Weng and Fan [125] developed an integral model for the pyrolysis of charring materials under controlled oxygen atmosphere. The special feature of this model is that it includes char oxidation. In order to model the oxidative pyrolysis process, they assumed that char oxidation is oxygen controlled and the oxygen is diffused through the porous char material. Good agreement was found between the model and the results from [60] for different ambient oxygen concentrations. Moreover, the model was tested for the effect of heat of pyrolysis, pyrolysis temperature, emissivity, diffusion coefficient of ambient atmosphere in air and the thickness of the char zone.

In [77], Ohlemiller et al. conducted experiments in varying oxygen concentrations. Their results show that the mass flux is always higher when oxygen is present, compared to the nitrogen environment. According to them, char oxidation is exothermic and is responsible for higher surface temperature. They also found that an increase in oxygen level increases the gas concentration (CO, CO_2, H_2O). The paper mainly focussed on the chemical composition in the mass flow rate of pyrolysis gases.

On the other hand, Kashiwagi et al. [60] showed that with the increase in the oxygen concentration, the mass loss rate increases. Tests were performed for different intensities of heat fluxes. It was found that with the increase in the external heat flux intensity, the mass loss rate increases. They discovered a clear separation between the char and the original wood, which is a rare case. Moreover, they reported that CO_2 yield was 6 to 8 times higher in air than in N_2 atmosphere, while it was twice as high in the case of CO.

Recently, Lautenberger [65] has developed a generalized pyrolysis model for combustible solids. In this model, a genetic algorithm is developed to estimate the material properties that are used in the model. The thermo-physical properties k, ρ and c are temperature dependent. Permeability of gases through the pores, their diffusivity and other features are considered, together with the solid phase reactions. The gas phase homogeneous reactions occurring in the pores are also taken into consideration. The complete model is governed by Arrhenius reaction rates. The model is tested on charring and non-charring materials and results are obtained for smoldering of polyurethane foam. The numerical results are in good agreement with the experiments for non-charring, charring and smoldering pyrolysis processes. Lautenberger et al. [66] proposed a model for the oxidative pyrolysis of wood.

Here oxidation is considered as an additional chemical reaction with an Arrhenius reaction rate. The model again shows good agreement with the experimental results of [60]. From simulation results, they conclude that with good thermal properties the results should be close to experimental results.

After offering a brief overview of the studies on the pyrolysis process and focusing only on models developed for dry solids, it is important to consider the wet charring materials. The initial moisture content plays an essential role in the development of small-scale fires. This greatly hinders the start of the pyrolysis process. A brief survey of the wet charring material modelling is presented below:

Alves and Figueiredo [4] presented a model for the pyrolysis of wet charring materials. The moisture evaporation in the model implies a complex reaction scheme. Maybe, the model developed was the first of its kind to be applied on wet charring materials. In the model, the drying rate was controlled only by heat supply and vapour-liquid equilibrium. The model defines the boiling point of water as the temperature at which moisture is in equilibrium with water vapour at the atmospheric pressure. The model used interpolates thermophysical properties. Numerical simulation results were in good agreement with the experimental results. However, the model neglected water vapour diffusion, bound water diffusion and pressure gradients inside the solid.

Fredlund [45] developed a two-dimensional model for the pyrolysis of wet charring materials. The mass loss rate as well as the evaporation of moisture are assumed to follow a first-order Arrhenius reaction rate law. The model uses Darcy's law for mass transfer of volatile pyrolysis products and water vapour. Fredlund charted all the thermal properties as a function of temperature. These values were used in the model, which produced results in good agreement with the experiments. His model was capable of predicting a plateau around 100^0C, the boiling point of water. He mentioned that the amount of moisture present had a decisive influence on the charring rate.

The model developed by Bilbao et al. [13] is again based on a first-order Arrhenius reaction rate. They calculated the temperature profiles by thermal transmission mechanisms inside the solid together with the heat generated or consumed owing to the decomposition of the material. They saw that with the increase in the moisture content, the duration of the pyrolysis process increased. They obtained the drying/evaporation plateau when the solid reached the boiling point of water. This model was later studied by [97], with the same boundary conditions; however, the model gave no drying plateau, as observed in [13].

Melaaen [71] considered source terms for drying and pyrolysis processes. The mass loss rate implies an Arrhenius reaction rate scheme. He developed separate sub-models to determine the thermophysical properties used in the model. The model predicts a drying plateau as seen in [13, 45]. Their results show that an increase in moisture content delays the pyrolysis process, which is supported by other researchers' findings. Their simulations show that the vapour pressure is equal to the local pressure of water at the temperature plateau, which is the boiling point of water. They were, however, not able to compare their numerical simulation results with the experimental results.

A transport model for the drying of wooden particles exposed to convection and radiation was studied in an inert atmosphere by Di Blasi [41]. Moisture evaporation is described

according to the Clausius-Clapeyron expression with a one-step, global chemical reaction or as a heat-controlled process. The model assumes that there is no degradation during drying, so that the solid density remains constant. The model is solved by an operator splitting method, the first stage accounting for the evaporation process and the second stage for the transport process. The process of water evaporation has two fronts i.e. one for evaporation of capillary water, and the other for the evaporation of bound water. The temperature gradients determine the position of the front position. The author also focuses on the effect of permeability of the gas flow. A decrease in the permeability of the gas flow generates gas over-pressures, which in turn induces the boiling point elevation of water.

Bryden et al. [25, 26] applied a two-step, five-reaction model for solid pyrolysis. Drying is modelled using an Arrhenius expression. They added a third regime, called thermal wave regime, which was different from the two regimes (thermally thick and thermally thin). In the case of thermally thin ($\text{Bi} \leq 0.2$) materials, the heat transfer is rapid and the effect of moisture content and particle shrinkage has little effect on the pyrolysis process. The drying and pyrolysis occur in sequence. In thermally thick materials ($0.2 \leq \text{Bi} \leq 10$), there are significant spatial temperature variations. Due to this, there is a small overlap between the drying and pyrolysis fronts. Shrinkage of the char layer creates steeper temperature gradients, which reduces the pyrolysis time. Finally, in the thermal wave regime ($\text{Bi} \geq 10$), the effect of moisture greatly affects the pyrolysis process. In [25], the authors include the char shrinkage after the pyrolysis process. The shrinkage is defined as the ratio between the reduced dimension and the original dimension. They found that shrinkage has a negligible effect on the pyrolysis process in thermally thin materials, but reduces the pyrolysis to 15% to 30% in the case of a thermally thick pyrolysis process.

Drying, pyrolysis and char oxidation were modelled by Benkoussas et al. [12]. Based on the value of the Biot number, i.e. the ratio of the external heat transfer to the internal heat transfer, they classified different regimes and assumed $Bi = 0.1$ for the transition regime between a thermally thin and a thermally thick regime. Bryden et al. [25, 26], however, considered $\text{Bi} = 0.2$ for this transition regime. As observed by Bryden [25], Benkoussas et al. also reported the overlap of the drying and pyrolysis process for thermally thick solids. Their results show that the pyrolysis process is kinetically-controlled for fine particles. As particle size increases, the heat diffusion becomes smaller and the pyrolysis process is controlled by heat diffusion. Peters and Bruch [79] developed a flexible and stable numerical method to predict the thermal decomposition of large wood particles due to drying and pyrolysis. A one-step Arrhenius rate model is adopted for the modelling of pyrolysis. They applied two methods for pyrolysis modelling, the first one being the heterogeneous reaction approach, which includes the reaction and the transport time scale for heat transfer. The second method is the constant evaporation temperature approach, which is limited to heat transport. The heterogeneous reaction model under-predicts the drying rate significantly, leading to extended drying times. Hence they reported that this approach is not suitable for studies of the pyrolysis process.

Sand et al. [95] developed a model that includes the transport phenomena, phase changes and species transport. Generalized porous media transport equations are used inside and Navier-Stokes equations outside. The pyrolysis process is modelled in a more sophisticated way, by using a two-step mechanism, i.e. a primary and a secondary pyrolysis step. The numerical simulation results were in good agreement with the experimental results. A three-dimensional model for enclosure fire growth was developed by Yuen et al. [136]. Empirical

correlations derived from experiments were used to develop zone models of flame spread. The authors also developed a fire field model which includes the moisture evaporation using an Arrhenius expression. The heat of pyrolysis used in this work is $'0'$. They reported that the flame spread rate is slow with the increase in the moisture content of the solid under study.

Non-charring materials (mostly polymers such as Polymethylmethacrylate (PMMA), Polystyrene (PS), Polyvinyl chloride (PVC), etc.) are used in daily applications, household appliances, etc. It is necessary to understand the behaviour of these kind of materials when exposed to fire or heat. Di Blasi [14] described the physics of the non-charring materials. She pointed out that the process between the flames and the solid (non-charring) is a phenomenon that is in a quasi-stationary state. However, this cannot be attributed to char forming polymers. Fernandez-Pello in chapter 2 ([33]) focused on non-charring material (PMMA) to introduce the solid phase in the fire. He thoroughly discusses the different parameters involved during the flame spread. Kashiwagi [58] described the flame spread phenomena using non-charring materials. He carried out experiments in a controlled oxygen atmosphere to determine the mass flow rate of pyrolysis gases.

Vovelle et al. [117] conducted experiments on PMMA and particle board to examine the transient thermal degradation process. They studied the effects of oxygen content on the mass flow rate of pyrolysis gases released after the pyrolysis process. Also a brief investigation was performed to study the effect of temperature on the mass flow rate. In [118], the radiant heat flux was varied to study the evolution of the mass flow rate of pyrolysis gases. They obtained the heat of gasification for PMMA equal to 1666 J/kg, which agrees with the value measured by Tewarson [1]. Tewarson and Ogden [108] studied the fire behaviour of PMMA. A complete description on the PMMA behaviour when exposed to fire is described by giving details on flame spread modelling both in the solid and the gas phase.

Staggs [104–106] worked on both non-charring and charring polymers. He developed a finite-rate model for polymer degradation. In addition, the heat of gasification was investigated based on Tewarson's and Pion's effective heat of gasification [106] for PMMA and Polyethylene. Results show that there is a difference of 20 to 40 % in the value of heat of gasification, between Tewarson's and Pion's method and Staggs' work.

Sohn et al. [101] demonstrated three different models in non-charring materials (opaque solids, semi-transparent solids): a. fixed temperature, infinitely thin front; b. a one-step reaction mechanism approximated by an Arrhenius equation; c. pyrolysis occurring in the zone (following the Arrhenius form). They considered the in-depth radiation absorption effect on the mass flow rate and temperature distribution. Inclusion of the in-depth radiation adsorption model c showed higher mass loss rate compared to the models a and b.

1.3 Models in the fire community - a brief survey

When examining the works mentioned above, we need to know the characteristics of the models that were developed. The following section therefore describes the important models that are used in the study of pyrolysis.

1.3.1 Arrhenius model

The Arrhenius model was the first model developed to study the decomposition of solid materials. When a solid is exposed to an external heat flux, the temperature of the solid increases. Due to the rise in temperature, the material undergoes degradation, which begins at the surface and then proceeds into the solid, causing the release of volatiles. The pyrolysis process transforms the solid from virgin material to char when the solid surface temperature reaches a critical value. This is seen with the change in density from ρ_v to ρ_c [29, 30]. A single-step decomposition of solid is:

$$\text{virgin} \xrightarrow{\Delta} \text{char} + \text{pyrolysis gases} \tag{1.1}$$

The reactions intensify when the solid exceeds the critical temperature. During pyrolysis, the pyrolysis zone temperature is kept low, making the process endothermic. After the solid has completely transformed into char, the solid temperatures rise again. Park et al. [78] refer to the Arrhenius model as a finite-rate kinetics model, considering a global one-step finite rate reaction. There are others who consider more than a one-step reaction [25, 26, 71, 97]

$$k = Ae^{-E/RT} \tag{1.2}$$

where k is the rate constant, A is the Arrhenius constant, E is the pre-exponential factor, R is the universal gas constant and T is the temperature in K. The pyrolysis process occurs in a zone of finite thickness. In this zone, the pyrolysis reactions occur with the release of volatiles which escape to the surface of the solid. The model assumes there is no accumulation of pyrolysis gases in the solid; they reach the surface as soon as they are produced. These volatiles reach the temperature of the char as they pass through, i.e. a thermal equilibrium is reached. The amount of volatiles flowing out in the form of mass flow rate is caused by the density change in the solid.

Di Blasi [14] used the Arrhenius model to discuss in detail the combustion processes of charring and non-charring solid fuels. She even showed the Arrhenius model for multiple reactions e.g. one-stage global models, one-stage, multi-reaction models and two-stage, semi-global models. Benkoussas et al. [12] applied this model to thermal degradation of woody fuel particles. Benkoussas not only applied this model to the pyrolysis process, but also to the endothermic drying and exothermic char oxidation process, considering each process as a separate reaction. Nathasak Boonmee [21] applied this model in the study of auto-ignition of wood and compared the results with the experiments. Lautenberger et al. [65,66] developed a model that gives good results for the non-charring polymers, charring solids, intumescent solids, and smoldering combustion in porous media. They developed a genetic algorithm that can be used to estimate the model input parameters from bench-scale fire tests of thermogravimetric (TG) analysis. Yang et al. [131–133] modified the work of Kung [29] to incorporate the surface losses. They predicted the ignition time of a material by using the heating time and the surface exposed to the external radiation. However, Lin et al. [42,68] proposed a partial differential equation for the moving boundaries both virgin solid and char; they mentioned that the pyrolysis front speed follows the Arrhenius law.

1.3.2 Integral model

An integral model was applied on the pyrolysis of charring materials by Quintiere [85], Chen [27,28], Moghtaderi [75], Spearpoint [102], Weng [125] and many others. The sequence of events that are prominent in the integral model are clearly discussed by Moghtaderi [75]. Heat supplied to the material from the external source is conducted into the solid and some heat is lost to the surroundings in the form of radiation. Three distinct phases are seen during the integral model development namely: a) the preheat phase, b) the infinite-body pyrolysis phase, and c) the finite-body pyrolysis phase. The first is the initial heating of the solid virgin material in which the density of the solid is uniform throughout. The second stage begins with further heating of the solid to the pyrolysis temperature, in which the pyrolysis process begins. During this pyrolysis process, the solid is divided into two zones, the char and virgin zone, separated by the pyrolysis front. Heat is utilized for the transformation of virgin to char, which causes the evolution of volatiles. Some heat is conducted into the solid to heat the virgin material, which acts as a heat sink. During this phase, the thermal front is still within the solid. The third phase begins when the thermal front reaches the back surface; at this moment the pyrolysis front is approaching the back surface. Depending on the boundary condition at the back surface, the behaviour of the pyrolysis process varies. When the pyrolysis front reaches the back surface, the end of this finite-body pyrolysis phase is marked. Moghtaderi [75] implemented the integral model on non-charring materials and found that the model performs well for both charring and non-charring materials, showing good agreement with experimental results.

1.3.3 Extended Integral model

Theuns et al. [111] extended the integral model for pyrolysis of charring materials by including a finite and semi-infinite cooling state. When the solid is exposed to an external radiation heat flux, the temperature in the solid increases. Heat is then conducted into the solid to heat the virgin material. Some heat is lost in the form of reradiation from the surface. When the surface temperature reaches the pyrolysis temperature, the pyrolysis process begins. This process continues as long as the external heat flux is high enough to maintain the pyrolysis front temperature equal to the pyrolysis temperature. The external heat flux may momentarily drop, for example when the heat provided by the external heat source is switched off, or when the fire providing the heat is extinguished. This leads to insufficient heat supply to the pyrolysis process, which can no longer proceed. Consequently, the pyrolysis process stops, leading to a drop in the mass flow rate of gases from the solid. Theuns et al. [111] discussed semi-infinite heating state and finite heating state. The authors also described the rise in the heat flux, i.e. when the pyrolysis gases catch fire when reaching the surface; or due to flash over or a sudden rise in the external heat flux and vice versa. They found that the integral model performed satisfactorily when the boundary condition is constant or varying sufficiently slowly. When sudden changes were applied to the model, the mass flow rate of the gases showed unusual behaviour. They added that the extended integral model shows good results compared to the integral model itself.

1.3.4 Moving grid model

The moving grid model, which is similar to the integral model, was developed by Theuns et al. [109,112]. Like the integral model, the moving grid model has an infinitely thin pyrolysis front. This front separates the virgin solid from the char. The griding is constant during the heat up of the virgin material. The pyrolysis process begins when the front temperature reaches the pyrolysis temperature T_{pyr}. The progress of the pyrolysis process generates the char, thereby causing the release of volatiles. There is a expanding char zone and a shrinking virgin layer, separated by a thin pyrolysis front. The model performs well for variable heat flux. In this model, the grid in the virgin zone is different from the char zone, to ease the difficulties during modelling. The model has four phases as is the case for the integral model developed by Mogtaderi [75]:

- virgin heat-up phase; i.e. the surface temperature is below the pyrolysis temperature
- pyrolysis phase; i.e. the front temperature is at the pyrolysis temperature T_{pyr}
- char heat-up phase; i.e. the pyrolysis front has reached the back surface
- heat/cooling of the solid; i.e. the external source is switched off or extinguished / the pyrolysis gases ignite, leading to increased external heat flux on the material.

The model is indeed good with the results shown in [109, 112] predict results for variable heat fluxes scenario. But, the model is limited to one-dimensional analysis, extension to higher dimensions is not easy.

1.3.5 Enthalpy based model

The enthalpy based model was first developed by Alexiades and Solomon [3] for melting and freezing processes. Later, Theuns [109] used this model for the pyrolysis of charring materials. The model uses enthalpy as a basic quantity. The pyrolysis process of charring materials is treated as a one-dimensional problem. The approach belongs to the volume-of-fluid (VOF) family. The char fraction denotes whether a computational cell is virgin material, char or 'mushy', i.e. a combination of virgin and char. The pyrolysis process is modelled as an endothermic, isothermal process at a front, when the temperature reaches the prescribed pyrolysis temperature. The treatment of temperature in the model is in relation to the enthalpy field, which is important for the accuracy and physical correctness of the model. The temperature is treated as a constant in a cell. Detailed modelling procedure and equations will be discussed in appendix A. Because this model is incomplete, it cannot be used to study flame spread. More specifically, the model has a limitation in the zero-th order temperature per cell, i.e. the mass flow rate drops to zero after each cell is pyrolysed. The model is therefore modified to a piecewise linear temperature representation. Chapter 2 presents details on this model, the modelling technique and the solution procedure to make it capable of performing flame spread simulations. Results obtained for charring materials are presented in chapter 3 and those for non-charring and wet charring materials in chapter 3 .

1.3.6 Dual mesh model

The dual mesh model has been developed by Yan and Holmstedt [130], by incorporating the Arrhenius model, the integral model and the enthalpy based model. The concept of dual mesh was also implemented on charring materials in the Ph.D thesis of Theuns [109]. The Arrhenius model yields good results in terms of mass flow rates, when applied on a fine mesh. Using a coarse mesh, however, oscillations occur leading to unrealistic mass flow rates. Fine mesh leads to higher computational costs. So, Yan and Holmstedt introduced the idea of applying fine mesh in the pyrolysing cell while leaving coarse mesh in the virgin and char layers. The reason is that the char volume fractions are constant in the char and virgin layers, respectively; in other words, the density is constant. Yan [130] developed the pyrolysis model that assumes pyrolysis to be an infinitely fast process, considering no kinetics. The pyrolysis process occurs in the local small individual mesh at an infinite rate. De Ris and Yan [35] modified the model incorporating the finite rate, using the Arrhenius model. This model was applied on both charring and non-charring materials. The model performs well when finer mesh is used near the pyrolysis front. Else it gives results which are similar to the enthalpy based model results (chapter 3.)

1.4 Flame spread phenomenon

So far, we have discussed the different models which are used in the field of solid pyrolysis modelling. The following section elaborates on the processes that occur in the gas phase, leading to the phenomenon of flame spread. When the mass flow rate in the form of volatiles reaches the surface, it mixes with oxygen and ignites. Di Blasi [14,15,17–19] gives a detailed explanation on the flame spread over charring and non-charring materials. In these papers, the author discusses the processes taking place both in the solid and gaseous phase, assuming that the Arrhenius law is the underlying mechanism.

Ignition can be auto-ignition or pilot, depending on the experiments and configurations required. Boonmee [21] studied the process of auto-ignition of wood. He conducted theoretical and experimental studies on the auto-ignition of wood. Spearpoint [102,103] worked on the ignition of solids taking into account the grain orientation and other parameters. Atreya [7] discovered that flames formed by igniting volatiles are initially seen as a flash. These flames continue for some fraction of time, but then attain a steady burning regime. Afterwards they continue spreading over the surface of the solid. This process is typical of the flame spread phenomenon. Before going into the details of flame spread, it is very important to understand the different parameters influencing this phenomenon. We can further our understanding by studying the flammability properties of materials. An excellent theoretical review is given by Quintiere [87] on the flammability concepts of materials. Moreover, the review of Delichatsios et al. [37] makes the study complete by including charring materials.

Hasemi et al. [51] studied wall flame behaviour and upward flame spread within vertical channels for different width/depth ratios. They found that radiation feedback from the flame to the unburnt solid is the major factor for rapid flame spread. Later, Yuji Hasemi [49] further investigated the significance of concurrent flame spread, using the information available from the King's Cross fire in 1987, which drew strong international attention in

the fire community towards the importance of flame spread on inclined surfaces. Hasemi discussed the thermal modelling of the concurrent turbulent flame spread concept. He studied the flame spreading velocity for two types of correlations, in the sense that any growing flame spread starting with a finite ignition source must fall in between the steady fire and exponential fire. The theoretical concepts on this part of flame spread modelling are dealt with in chapter 5.

Apart from these flaming processes, there exits a process called Smouldering, which is slow and operates at low temperature. It is the flameless form of combustion, which is sustained by the heat evolved on oxidation of volatiles released from the solid. Ohlemiller has discussed the process of smoldering combustion very precisely in [1]. An excellent example is the burning of a cigarette. Here, fine particles provide a large surface area per unit mass of fuel, which enables the surface to get in contact with the oxygen. These particles in turn provide thermal insulation that helps to reduce heat losses, permitting sustained combustion despite lower heat release rates. The other reason for sustained combustion is the char oxidation, which provides heat source in most self-sustained smoldering combustion. Rein et al. [91] differentiate smoldering from flaming combustion obtained during a wildfire. Smoldering is an oxidation reaction in which heat release occurs on the surface of the solid; in flaming combustion, these processes occur in the gas phase above the solid surface. The authors investigated the wildfire occurring due to peat undergoing smoldering combustion.

1.5 Present work

We have presented a brief overview of the existing research and models in the field of fire safety engineering, while also relating several concepts and results to our own investigation. From the literature review, we can see the models that are present in the field of fire safety engineering are limited to one dimension. To extend these models to higher dimensions is difficult. Also, the other limitation of the integral model is when simulating for variable heat flux. The sudden rise and fall in the heat flux at the boundary has direct influence on the entire temperature field. All these led to the development of an enthalpy based model that is computational fast and simple. The model developement in chapter 2 and later chapters are taken from the author's contribution [119, 120]. Chapter 2 discusses the enthalpy based model, which is developed by considering enthalpy as a basic variable. This model uses a piecewise linear temperature representation. The model equations and the approach to solve the unknown variables employed in the developed of the enthalpy based model are discussed. Chapter 3 focuses on the numerical simulation results of the enthalpy based model compared to the experiments. The effect of different model parameters on the mass flow rate is discussed. Here, the advantage of using the enthalpy based model for flame spread modelling is also emphasised. Chapter 3 also deals with the application of the enthalpy based model to non-charring and wet charring materials, making the model capable of being applied to a variety of materials in the building industry. Chapter 4 deals with the cone calorimeter experiments from a experimental campaign [121]. Here, the numerical simulation results of the enthalpy-based model are compared to the cone calorimeter results for the pyrolysis process. In chapter 5 flame spread modelling is briefly discussed, giving a concise overview of the theoretical modelling aspects in appendix D. The enthalpy based model is extended from a one-dimensional to a two-dimensional configuration. Chapter 5 shows the way in which

the enthalpy based model is developed, i.e. a pseudo-2D configuration to study the flame spread phenomena using correlations along with the flame spread results after coupling the enthalpy based model for the solid pyrolysis process to the gas phase to study the actual flame spread phenomena. In chapter 6 details on the flame spread experiments conducted at Lund University are presented [122]. The enthalpy based model is tested to compare flame spread experimental results by imposing heat flux depicting the real flame spread scenario. Finally, chapter 7 some conclusions are drawn and some specific remarks are offered for the future development in chapter 8 of this model to incorporate the other physical processes occurring during real fires.

2

Enthalpy Model

2.1 Introduction

Many models developed in the field of fire safety vary in their domain of application and complexity. To that point of view, the enthalpy based model is developed keeping in mind that the model remains as simple as possible. This model is applicable to dry or wet charring and non-charring materials. The model is extendable to multi-dimensional solid phase treatments, as required for general flame spread simulations. This is a difference to many existing simplified pyrolysis models, which might look very similar to the present model at first sight, but which are basically limited to one-dimensional configurations (or, at least, implementation for multi-dimensional solid-phase treatments becomes very cumbersome). Also, the present model can be combined with any model for the transport of gases or water vapour inside the solid material. In the same sense, e.g. a model for char oxidation can be added. This chapter is largely based on the work of Wasan et al. [120].

The inclusion of pyrolysis kinetics is deliberately avoided. Whereas this limits the field of application to high-temperature pyrolysis and to situations where pyrolysis kinetics is not prevalent, it is relevant for flame spread situations as in a developing fire.

There are two major parts in the model description:

- the local relation between enthalpy and temperature.
- the energy equation to be solved in the solid material.

First, these parts are described in detail and we define precisely what is meant by "heat of pyrolysis" ΔQ_{pyr} in this model, in order to avoid any confusion on this term. Afterwards, the model and terminology are put in perspective with respect to existing models in the literature.

Later, in chapter 3, numerical issues and implementation, including the solution procedure, are described in detail. An interesting feature is the use of fixed computational mesh.

2.2 Heat of Pyrolysis

The focus of the enthalpy based model is on thermodynamic description of the phenomena. This approach is largely based on [29], one of the first theoretical papers on this topic. This is elaborated here to obtain an easy-to-use enthalpy-based pyrolysis model for three-dimensional simulations on a fixed computational mesh. The approach is to consider five constituents: virgin solid material, char, volatiles, liquid water and water vapour. In [29], the endothermic pyrolysis process is assumed to take place at a constant (pyrolysis) temperature T_{pyr}. At this temperature, the required energy to produce a mass unit of volatiles out of solid virgin material, for the pyrolysis process is denoted as $L(T_{pyr})$. In our notation, this is related to ΔQ_{pyr}. It is important to note that this energy is defined at temperature T_{pyr}. This is further discussed below.

In [5,45], the same thermodynamic description for the enthalpy, in terms of temperature and local composition, is followed, in combination with Arrhenius type expressions to include pyrolysis process kinetics. The "heat of reaction" L_g of those references corresponds to ΔQ_{pyr} below.

For charring materials, Atreya and Sibulkin report confusion on the notion and terminology of 'pyrolysis heat' (or 'heat of gasification') in the literature. Wide range of values are found in the literature for certain materials. Atreya [5, 7] mentions confusion, but used heat of pyrolysis equal to '0'. Sibulkin [98] reports the heat of pyrolysis definition as the difference in total enthalpy between the products of pyrolysis at the surface temperature and the virgin material at ambient temperature. He points that heat of pyrolysis is 3 to 4 times the value of heat of reaction, and the value is half the heat of gasification. For wood [7, 40, 98] values from 2×10^5J/kg up to 7×10^6J/kg.

In [21], Boonmee has taken into consideration and describes on the heat of pyrolysis in terms of formation enthalpies. Below, we describe the relation between the different approaches and explain how the knowledge on formaiton enthalpies is effectively avoided by introduction of ΔQ_{pyr} into the model description.

In non-charring materials, it is very natural to define heat of pyrolysis at the surface temperature (equal to T_{pyr}), where the gasification process of the solid material is taking place. There is indeed a strong similarity to the vaporization process of liquids (although the latter is in principle a reversible process in closed systems). Staggs [106] reports that heat of gasification for PE is 1.826-2.981$\times10^5$ J/kg. Tewarson [1, 108] report a value of 2.32×10^5 J/kg.

Lautenberger [65] defines the heat of pyrolysis ΔQ_{pyr} as a user specified quantity of energy required to convert unit mass of condensed phase species to gases at the pyrolysis temperature, while the heat of gasification L includes a contribution for the sensible enthalpy required to heat the condensed phase from its initial temperature to its volatilization tem-

perature. To clear the doubt prevailing on the idea of heat of pyrolysis ΔQ_{pyr}, a review on the idea of different researchers was performed.

As seen in chapter 1, except for the Arrhenius model and dual mesh model, all the other models are based on the principle that the endothermic pyrolysis process is assumed to take place at a constant (pyrolysis) temperature T_{pyr}. At this temperature, the required energy to produce a mass unit of volatiles out of solid virgin material, for the pyrolysis process is denoted as $L(T_{pyr})$, this corresponds to ΔQ_{pyr} in the enthalpy based model.

2.3 Thermodynamics: Relation between enthalpy and temperature

The model approach is based on the fact that enthalpy is the basic variable, as mentioned above. It is crucial to define the local relation between enthalpy and temperature. The idea is to keep the solid phase model as simple as possible, because the gas phase is more complex i.e. having turbulence, combustion, radiation and soot effects. Starting with a most general manner, later simplification of different process can be made. The model constitutes of 5 constituents:

- (dry) virgin solid material (v)
- char (c)
- pyrolysis gases (g)
- water as liquid (w, l)
- water vapour (w, v)

In fact, if desired, the pyrolysis gases can be further decomposed into different species in a mixture of volatiles, where each species is created at a different temperature.

One must keep in mind that the above five constituents do not all co-exist. At atmospheric pressure, e.g. it is assumed that liquid water only exists if T<373 K, whereas water vapour only exists when T>373 K. It is also assumed, virgin solid material and char cannot co-exist. This keeps the model as simple as possible.

As in [29], the model assumes pyrolysis as an infinitely fast, irreversible, endothermic and isothermal process, taking place at the pyrolysis temperature T_{pyr}, which is a model parameter. As such, reaction kinetics are not considered and the pyrolysis zone becomes infinitely thin (pyrolysis front). This assumption makes the model particularly appealing due to its simplicity to couple to gas phase combustion CFD simulations (e.g. for flame spread simulations). Note that virgin solid material now only exists as long as $T < T_{pyr}$.

The specific enthalpy at position (x, y, z) at time t can be expressed as a mass weighted sum of the specific enthalpies of the consituents, present at (x, y, z) at that time. In general, the specific enthalpy at any time and any position can be written as:

$$h(x, y, z, t) = \sum_i \alpha_i(x, y, z, t) \cdot h_i(T_i(x, y, z, t)) \tag{2.1}$$

with $\alpha_i(x,y,z,t) = \widetilde{\rho}_i(x,y,z,t)/\widetilde{\rho}(x,y,z,t)$ and $\widetilde{\rho}(x,y,z,t) = \sum_i \widetilde{\rho}_i(x,y,z,t)$. Thus $\alpha_i(x,y,z,t)$ is the local mass fraction of constituent i and $\widetilde{\rho}_i(x,y,z)$ denotes the local mass concentration of this constituent. The model assumes that the specific enthalpy of each constituent is only dependent on the temperature.

If a constituent is not present at (x,y,z,t), the mass fraction of that constituent is zero in 2.1. If virgin solid material or char is present, i.e. $\widetilde{\rho}_v = \rho_v$ and $\widetilde{\rho}_c = \rho_c$: the local mass concentration equals the bulk density of that constituent. If transport of moisture is not considered and the initial moisture distribution is uniform, $\widetilde{\rho}_{w,l} = \rho_{w,l}$ at positions where moisture is present. This corresponds to the 'moisture bulk density'.

In principle, the local temperature of each constituent can be different, but a thermal equilibrium is assumed locally, so that, from now on, $T(x,y,z,t)$ will be used as the local temperature for all constituents ($T_i(x,y,z,t) = T(x,y,z,t)$ for all i). With this assumption, only one energy equation has to be solved to compute the temperature distribution. For ease of notion, (x,y,z,t) is omitted from now on.

The relation between the enthalpy and temperature for each constituent is as follows:

$$h_i(T) = h_i^0\,(T_{ref}) + \int_{T_{ref}}^{T} c_i(T)dT \tag{2.2}$$

The total specific enthalpy is indeed the sum of the formation enthalpy at a reference temperature T_{ref} (typically chosen as 298K) and the thermal enthalpy. For gases and water vapour, the thermal capacity at constant pressure is used.

In principle, equations (2.1) and (2.2) completely define the relation between the specific enthalpy and the temperature, when the local composition of the material is known. Some difficulties arise, though. First of all, the exact composition of the pyrolysis gases is typically not known, which makes it effectively impossible to evaluate relation (2.2) for the volatiles. Even though there is a possibility of exact knowledge from literature to obtain the relation for all the constituents but in order to keep the model as simple as possible this idea is avoided. There is also another difficulty, i.e. the formation enthalpies of the virgin solid material and char are not known. The concept of heat of pyrolysis can be introduced, which makes things easy to draw the relation between the individual enthalpies (2.2). By this concept, the relation between the formation enthalpy and the exact gas composition can be drawn. Most of the pyrolysis models (except the Arrhenius model) use the concept of constant pyrolysis temperature process, i.e. pyrolysis occuring at temperature equal to T_{pyr}. In the present model, modelling pyrolysis as an isothermal process at $T = T_{pyr}$, an amount of mass (m_v) of the solid virgin material is transformed into an amount of (m_c) char and an amount of mass $(m_v - m_c)$ pyrolysis gases, all happen to take place at $T = T_{pyr}$. This endothermic process requires an amount of energy equal to $(m_v - m_c)\Delta Q_{pyr}$. As in [29, 130], it is worth to note, the heat of pyrolysis is defined as the amount of energy required to produce a unit mass of volatiles out of solid dry virgin material, at $T = T_{pyr}$. The relation then reads:

$$m_v h_v(T_{pyr}) + (m_v - m_c)\Delta Q_{pyr} = m_c \cdot h_c(T_{pyr}) + (m_v - m_c) \cdot h_g(T_{pyr}) \tag{2.3}$$

The model assumes that pyrolysis process happen in a infinitely thin front maintained at the pyrolysis temperature. Taking the limit to an infinitesimally small volume at (x,y,z),

this can be rewritten in terms of bulk densities:

$$h_v(T_{pyr}) + \left(1 - \frac{\rho_c}{\rho_v}\right) \Delta Q_{pyr} = \frac{\rho_c}{\rho_v} h_c(T_{pyr}) + \left(1 - \frac{\rho_c}{\rho_v}\right) h_g(T_{pyr}) \tag{2.4}$$

In words, expression (2.3) reads: the sum of the enthalpies of char and pyrolysis gases at T_{pyr} is $(m_v - m_c)\Delta Q_{pyr}$ higher than the enthalpy of virgin solid material at that temperature. This equation determines ΔQ_{pyr}, but, as mentioned above, since the constitution of the virgin material, the char material and the pyrolysis gas is typically not exactly known, their formation enthalpies are unknown. On the other hand, only enthalpy differences are important. Thus, a shift Δh_i can be applied for each constituent:

$$\begin{aligned} h_i(T) &= h_i^0(T_{ref}) + \Delta h_i + \int_{T_{ref}}^{T} c_i(T) dT \\ &\text{or} \\ h_i(T) &= h_i^*(T_{ref}) + \int_{T_{ref}}^{T} c_i(T) dT \end{aligned} \tag{2.5}$$

with $h_i^*(T_{ref}) = h_i^0(T_{ref}) + \Delta h_i$. Prescribing the heat of pyrolysis ΔQ_{pyr}, fulfilment of equation (2.4) implies that the shifts Δh_i for the virgin, char and pyrolysis gases cannot all be chosen independently. Indeed, only two constants can be chosen freely, while the third one is determined by equation (2.4). The procedure on the formation enthalpies are discussed in the later section.

From now on, $h_v^*(T_{pyr})$ and $h_g^*(T_{pyr})$ are chosen equal to zero for charring materials. Because of equation (2.4) and equation (2.5), this results in:

$$\begin{aligned} h_v(T) &= \int_{T_{pyr}}^{T} c_v(T) dT \\ h_g(T) &= \int_{T_{pyr}}^{T} c_g(T) dT \\ h_c(T) &= \left(\frac{\rho_v}{\rho_c} - 1\right) \Delta Q_{pyr} + \int_{T_{pyr}}^{T} c_c(T) dT \end{aligned} \tag{2.6}$$

Another choice should be made for non-charring materials (i.e. $\rho_c = 0$). Then only 2 constituents exist and only one constant can be chosen. If, again, $h_v^*(T_{pyr})$ is chosen equal to zero, the enthalpy of virgin material and volatiles as a function of temperature is give by:

$$\begin{aligned} h_v(T) &= \int_{T_{pyr}}^{T} c_v(T) dT \\ h_g(T) &= \Delta Q_{pyr} + \int_{T_{pyr}}^{T} c_g(T) dT \end{aligned} \tag{2.7}$$

Possible presence of moisture does not affect the balance equation (2.4), as pyrolysis takes place at T_{pyr} >373 K and water vapour does not affect the thermodynamics of the pyrolysis process. Obviously, when there is moisture in the virgin material, evaporation must be accounted for. This process taken place at 373 K and the latent heat L_v is defined by

$$\left(h_{w,l}^0 + \int_{T_{ref}}^{373} c_{w,l}(T) dT\right) + L_v = \left(h_{w,v}^0 + \int_{T_{ref}}^{373} c_{w,v}(T) dT\right) \tag{2.8}$$

With expression (2.5) for the specific enthalpy, applied to the water liquid and water vapour, it is clear from equation (2.8) that, if the specific enthalpy of the liquid water is shifted, the same shift should be made in the specific enthalpy of the water vapour and visa versa. Here, we consider $h^*_{w,l}(T_{ref}) = 0$, with T_{ref}= 298 K results in:

$$\begin{aligned} h_{w,l}(T) &= \int_{T_{ref}}^{T} c_{w,l}(T)dT && \text{if } T < 373\ K \\ h_{w,v}(T) &= \int_{T_{ref}}^{373} c_{w,v}(T)dT + L_v + \int_{373}^{T} c_{w,v}(T)dT && \text{if } T > 373\ K \end{aligned} \tag{2.9}$$

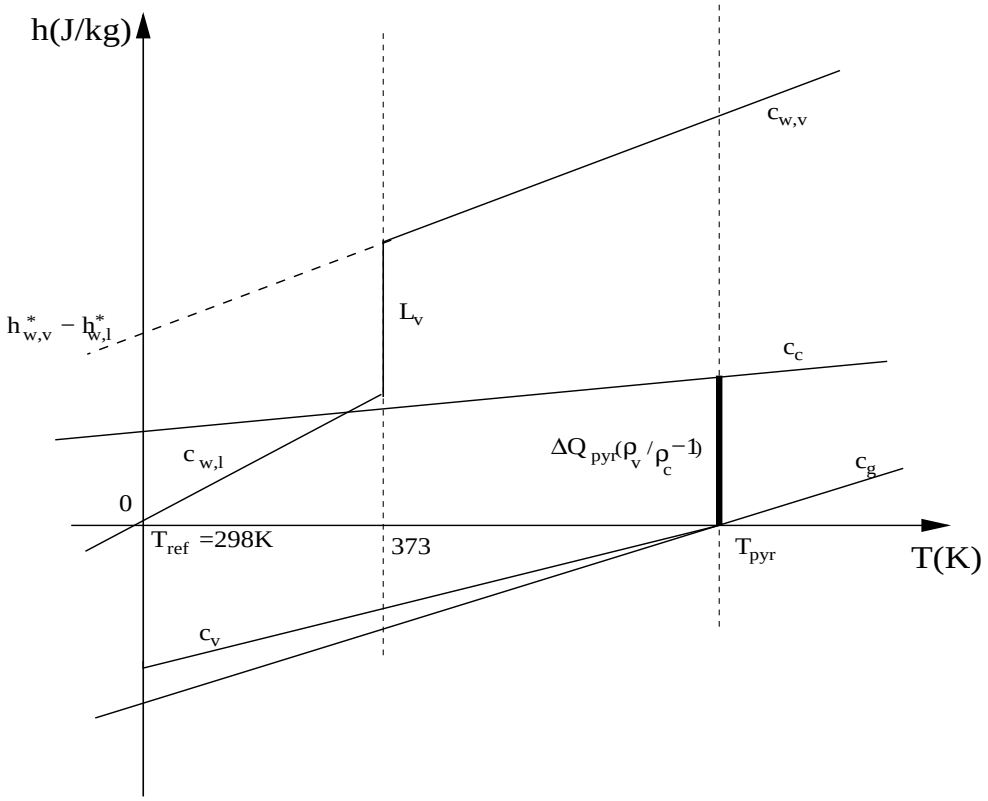

Figure 2.1: Enthalpy of different constituents as function of temperature for charring materials

Figures 2.1 and 2.2 summarise the above discussion for charring and non-charring materials. For ease of drawing, constant thermal capacities are assumed.

With expressions (2.1), (2.6) or (2.7) and (2.9), it is possible to define the local relations between the specific enthalpy and the temperature for the different temperature ranges:

2.3.1 T > T_{pyr}

This is only possible in case of charring material, i.e. when the solid char continues to heat up as a result of continuing exposure to external heat flux. Under this condition, only char,

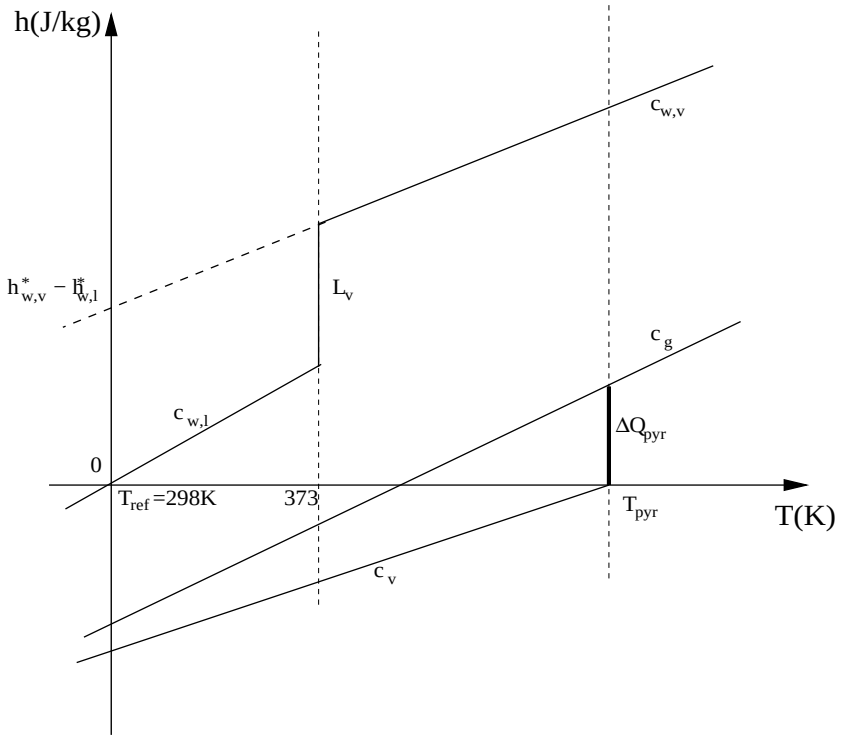

Figure 2.2: Enthalpy of different constituents as function of temperature for non-charring materials

pyrolysis gases and water vapour can be present. Expression (2.1), then reads:

$$h(T) = \alpha_c h_c(T) + \alpha_g h_g(T) + \alpha_{w,v} h_{w,v}(T) \tag{2.10}$$

2.3.2 373 K < T < T_{pyr}

For charring materials, there are two possibilities for the local composition:

- char + gases + water vapour (during a cooling phase after pyrolysis) - expression (2.10);
- virgin + water vapour - In this case, the expression becomes:

$$h(T) = \alpha_v h_v(T) + \alpha_{w,v} h_{w,v}(T) \tag{2.11}$$

  For non-charring materials, only expression (2.11) is possible.

2.3.3 T < 373 K

For charring materials, there are again two possibilities for the local composition:

- char + gases(during a cooling phase after pyrolysis) :

$$h(T) = \alpha_c h_c(T) + \alpha_g h_g(T) + \alpha_{w,l} h_{w,l}(T) \tag{2.12}$$

  If condensation is accounted for, a term with liquid water must be added. We do not consider condensation in the present study.
- virgin + liquid water - In this case, the expression becomes:

$$h(T) = \alpha_v h_v(T) + \alpha_{w,l} h_{w,l}(T) \tag{2.13}$$

  For non-charring materials, only expression (2.13) is possible.

If it is assumed that water vapour and pyrolysis gases leave the solid as soon as they are generated, $\alpha_g = \alpha_{w,v} = 0$ in the expression above.

2.4 Formation enthalpies: discussion

In the previous section, we illustrated a direct link between the formation enthalpies of the different constituents and the 'heat of gasification' or 'heat of pyrolysis'. The lack of precision in the definition seems to be an important source of confusion in the terminology in the literature. Indeed, starting from the basic expression (2.2), it becomes clear how ΔQ_{pyr} depends on the temperature where it is defined. In fact, this is seen in expression (2.4): if one knew the exact composition, thermal capacities at all temperatures and standard formation enthalpies of all constituents, ΔQ_{pyr} can be computed as function of T_{pyr}. This also shows that ΔQ_{pyr} is not a model parameter to be chosen freely. Rath et al. [90] performed experiments on beech and spruce wood (charring materials) to study the heat of pyrolysis process, while, Staggs [106] studied the heat of gasification on polymers. Rath reports that heat of pyrolysis is not a constant property of the material. But, it varies depending on the initial sample weight and on the conditions associated during measurement. This may be due to the final char yield which seems to be an exothermic primary char formation process competing with an endothermic volatile formation process.

Boonmee et al. [21], described how ΔQ_{pyr} can be computed from the formation enthalpies of virgin material, char and volatiles. However, as mentioned, one typically does not dispose of the knowledge, required to compute ΔQ_{pyr}. Rather, one uses the notion of ΔQ_{pyr} in order to avoid the necessity to have this complete knowledge. Prescription of ΔQ_{pyr} then leads to expressions like (2.6) or (2.7). Indeed, only enthalpy difference are of importance, so one has the liberty to choose e.g. $h_v^* = 0$, without loss of generality in the pyrolysis model. In fact, this is implicitly done in e.g. [5, 29, 45]. In [5, 21, 45] the discussion on formation enthalpy is avoided by discussion of time derivative of enthalpy. This is equivalent to stating that only enthalpy differences need to be considered and the formation enthalpy of virgin material can be chosen equal to zero.

The discussion is similar for the water vaporization process, which is considered independent of the pyrolysis process. We do not consider condensation here.

2.5 Model description - Enthalpy equation

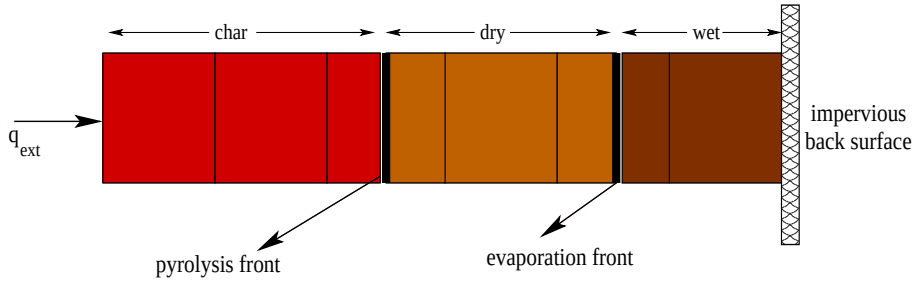

Figure 2.3: One-dimensional schematic representation of the solid under study

Figure 2.3 shows the schematic representation of the one-dimensional configuation under study. Pyrolysis process occurs in an infinitely thin front maintained at the pyrolysis temperature for the pyrolysis process. This process begins when the surface temperature attains the predefined pyrolysis temperature T_{pyr}. Pyrolysis process occurs with the conversion of virgin material to char at the pyrolysis temperature. The movement of these volatiles takes place in both direction from the moving front. The flux that moves away from the surface or in the direction of the moving front condenses due to lower interior temperatures. The back surface is perfectly insulated and impervious to passage of volatiles. This part is not considered in the model. The model assumes that the pyrolysis gases immediately leave the solid at the front surface. The flux that moves towards the surface, opposite direction to the moving front, ignites in the gas phase.

In the similar way, the evaporation process is modelled: the evaporation process occurs in an inifinitely thin front maintained at the evaporation temperature. When the surface of the solid reaches the boiling point of water 373K, the solid begins to loose moisture in the form of water vapour. During this process the moisture absorbs heat and evaporates into water vapour leaving behind a dry solid.

The solid material is divided into a number of control volumes, which are kept fixed during the simulations (fixed computational mesh). In fact, it is a particularly appealing feature of the present model that the equations are solved on a fixed computational mesh. Provided that a piecewise linear temperature field is used, this mesh need not be extremely fine and time steps in the solution procedure for the enthalpy equation need not be extremely small. This allows the model to be used for multi-dimensional solid phase treatments, which becomes far more cumbersome with intrinsically one-dimensional pyrolysis model, such as an integral type model, or with moving mesh, or dual mesh models discussed in chapter 1. Discretization issues and a sensitivity study will be discussed in the next chapter. The present section mainly focuses on the model equations to be solved to develop enthalpy based model using a piecewise linear temperature representation. A finite volume formulation is used to describe the model and this will be used in the solution procedure described in appendix B. The PDE formulation is provided in appendix C.

For a fixed control (sub-)volume 'V', the energy equation reads:

$$\frac{\partial}{\partial t}\int_V \tilde{\rho} h dV = -\int_S \vec{\dot{q}}'' \cdot \vec{n} dS \tag{2.14}$$

with $\vec{\dot{q}}'' \cdot \vec{n}$ the heat flux out of the volume $'V'$ through the boundary S, as $\vec{n}$ is the unit normal vector, pointing outward with respect to the volume. Note that, in principle, the specific internal energy should be used in the left hand side of equation (2.14). In the solid material, though, we ignore the (thermodynamic) effect from static pressure. Therefore, we use 'enthalpy' from now on. We also assume that there will be no accumulation of water vapour or pyrolysis gases inside the material, so that $\tilde{\rho}_g = \tilde{\rho}_{w,v} = 0$ inside the material. Note that $\tilde{\rho}_g = \tilde{\rho}_{w,v} = 0$ does not imply that there are no convective fluxes related to these constituents (discussed below). In a more general approach, one can work with specific internal energy and accumulation of pyrolysis gases, water vapour and water liquid. Then a mass balance equation for each constituent is required and if the velocity for some of these constituents has to be determined as well, also a momentum equation is needed for those constituents.

2.5.1 Heat fluxes through the volume boundaries

The right hand side of equation (2.14) consists of conduction and convection heat fluxes, i.e.:

$$\vec{\dot{q}}'' = \vec{\dot{q}}''_{cond} + \vec{\dot{q}}''_{conv} \tag{2.15}$$

Conduction is modelled by Fourier's law:

$$\vec{\dot{q}}''_{cond} = -k\nabla T \tag{2.16}$$

The local thermal conductivity 'k' is used. The value might depend on temperature and local composition at the cell face. In principle, the effect of the presence of pores in the char needs to be taken into account. In these pores, conduction in the gas phase can take place, possibly in combination with natural convection and, at sufficiently high temperatures, radiation. Such effects are not explicitly included in the model, but the model simply assumes $k = k_c$ in the char. This is exact in the limit of zero porosity and is an approximation in the case of non-zero porosity.

The convection fluxes due to transport of pyrolysis gases and water vapour (and possibly liquid water) given by:

$$\vec{\dot{q}}''_{conv} \cdot \vec{n} = \dot{m}''_g h_g(T) + \dot{m}''_{w,v} h_{w,v}(T) + \dot{m}''_{w,l} h_{w,l}(T) \tag{2.17}$$

Here, $\dot{m}''_i$ denotes the mass flux (kg/m^{2}s) of constituent 'i' leaving the volume, as determined below. The specific enthalpies are computed from (2.6) or (2.7) and (2.9).

2.5.2 Motion of pyrolysis and evaporation front

For charring materials, the motion of the pyrolysis front (at $T = T_{pyr}$) is determined from a local energy and mass balance at the front (shown for a one-dimensional configuration figure 2.4). This boils down to expressing that the net conductive heat flux to the front (i.e. the difference between incoming and outgoing conductive heat fluxes) is used to provide the heat of pyrolysis per unit of time for the pyrolysis process:

$$(\rho_v - \rho_c) v_{f,pyr} \cdot \Delta Q_{pyr} = -k_c \nabla T\big|_c + k_v \nabla T\big|_v \tag{2.18}$$

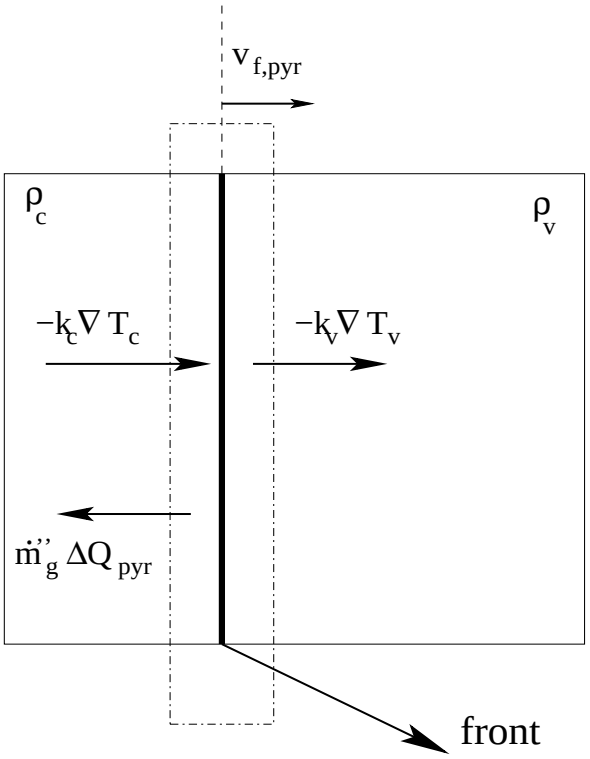

Figure 2.4: Energy balance around the pyrolysis front

with $v_{f,pyr}$ the pyrolysis front velocity in the direction normal to the front, from the char towards the virgin material. Note that no convection term from the pyrolysis gases appears explicitly in equation (2.18), as they leave the pyrolysis front at temperature $T = T_{pyr}$ and this phenomena is taken into account by the definition of ΔQ_{pyr} (refer eq. 2.3). The local balance at the front indeed reveals that virgin material becomes a combination of char and pyrolysis gases, all at $T = T_{pyr}$.

The mass of gases, produced per unit of time and per unit of pyrolysis front area, is also related to the motion of the pyrolysis front through the mass balance:

$$\dot{m}_g^{''} = (\rho_v - \rho_c) \cdot v_{f,pyr} \tag{2.19}$$

The heat balance equation (2.18) determines the pyrolysis front motion. It is important to note that a motion of the front requires an amount of energy. This is reflected in the relation between the enthalpy in the cell and the local composition and temperature field (refer to section 2.3). Note that, when there is no pyrolysis, e.g. in a cooling phase, expression 2.18 merely relates the temperature derivatives to the local thermal conductivities (change of material type over the pyrolysis front).

For non-charring materials, the conduction term in the char in expression 2.18 is replaced by the incident heat flux onto the solid material surface and ρ_c is equal to zero in 2.19 (conservation of mass).

At T=373 K, the following expression gives the motion of the evaporation front:

$$\dot{m}_w^{''} L_v = -k_{v,dry} \nabla T\big|_{v,dry} + k_{v,wet} \nabla T\big|_{v,wet} \tag{2.20}$$

The subscript v, dry stands for 'dry virgin'. This is the same as the solid virgin material

mentioned till now in the text. The subscript v, wet stands for 'wet virgin'. This is the section of the solid that possess moisture. This is merely important in the determination of the conductivity (conduction through water vapour and pyrolysis gases are ignored in this work). $\dot{m}_w''$ denotes the mass of water that evaporates per unit of time and unit area of the evaporation front, equal to $\dot{m}_w'' = \tilde{\rho}_{w,l} v_{f,evap}$, where $v_{f,evap}$ is the evaporation front velocity in the direction normal to the front, from the dry virgin towards the wet virgin material.

Expression (2.20) is valid for charring and non-charring materials. As mentioned above, the mass concentration of liquid water, $\tilde{\rho}_{w,l}$, can be computed from transport equations. As mentioned earlier, if no transport of the liquid water is taken into account and the initial moisture distribution is uniform, the mass concentration of liquid water in the virgin wet materials equals the initial 'moisture bulk density' $\tilde{\rho}_{w,l} = \tilde{\rho}^0_{v,wet} - \tilde{\rho}^0_{v,dry}$, which can be computed from the initial values of the bulk densities of the virgin wet $\tilde{\rho}^0_{v,wet}$ and the virgin dry material $\tilde{\rho}^0_{v,dry} = \rho_v$.

If no water vapour is accumulated in the solid material, $\tilde{\rho}_{w,v}$ is zero at all times and only evaporation can take place. When in such a case the evaporation front temperature drops below 373 K, the position of the front is kept fixed, $\dot{m}_w''$ becomes equal to zero and equation (2.20) gives a relation between the temperature gradients at each side of the front.

2.6 Discussion: Relation with existing pyrolysis models

The theoretical concepts, elaborated above from basic thermodynamic principles, have already been described in e.g. [21, 29, 45]. The derivation and the relation between heat of pyrolysis and formation enthalpies, considering 5 constituents is revisited. As such, this theoretical concept is not new. The novelty in the present work, though, is that a model has been developed that:

- is applicable to charring and non-charring materials;
- is applicable to materials with moisture content;
- is applicable in three dimensions;
- does not rely on any assumptions on temperature fields;
- is easy to implement, using a fixed computational mesh;
- is relatively cheap in terms of computing times;
- readily and correctly deals with transient phenomena (e.g. imposed heat flux);
- can be combined with any transport model for gases, liquid water and water vapour.

Application of the model is illustrated below. It is useful, though, to already put the present model into perspective with respect to existing pyrolysis models.

For non-charring materials, the model boils down to the use of a heat of gasification at the pyrolysing surface, at $T = T_{pyr}$. This notion is also used in e.g. [27,69,83,85]. The calculation then consists of solving a conduction problem, with an incoming heat flux and a moving boundary as the pyrolysis takes place. Note that no moving mesh is required: it suffices to compute the front motion as described above and temperatures need not be computed in regions where there is no material left. Also, the problem can be three-dimensional, in

contrast to integral type models [54, 75, 85, 102, 110, 125] or models where essentially one-dimensional configurations are assumed [14]. Thus, the modified enthalpy based model is applicable to flame spread over thermally thick and thermally thin materials.

This is also true for charring materials no moving mesh [109] or dual mesh [130] is required for the solution of the equations and the applicability in three dimensions is an interesting advantage over integral type models [54, 75, 102, 110, 125].

Admittedly, pyrolysis kinetics is deliberately not taken into account. This implies a limitation in applicability to situations where sharp fronts provide a good approximation for the pyrolysis and evaporation processes. Note however, that multiple fronts (at different temperatures) can easily be introduced, so that the pyrolysis process could be modeled by means of several fronts. At each front, a species of the pyrolysis gas mixture is then generated. Note that also a char oxidation front can be introduced this way. Obviously, transport of oxygen must be considered then, but this is no problem with the present model, which can be combined with any transport model for any species.

Finally, it is confirmed that the model readily deals with any transient imposed heat fluxes onto the solid material, as illustrated below. This means that coupling to CFD packages is relatively straightforward. The heat flux onto the solid material is then obtained from the gas phase CFD calculations, while the present model gives mass flow rates and temperatures as boundary conditions to the CFD package. In this context, we mention that in e.g. FDS, version 5 [70], Arrhenius expressions are used but, more importantly, the equation in the solid material is essentially one-dimensional. This is thus a limitation of that model.

2.7 Model development

We know that, the model is developed with enthalpy as the basic variable. The enthalpy update is computed for one-dimensional case as:

$$(\tilde{\rho}h)_i^{n+1,k+1} = (\tilde{\rho}h)_i^n + \frac{\Delta t}{\Delta x_i}\Big[\left(\dot{q}''^{n+1,k+1}_{cond,i-1/2} - \dot{q}''^{n+1,k+1}_{cond,i+1/2}\right) + \left(\dot{q}''^{n+1,k}_{conv,i-1/2} - \dot{q}''^{n+1,k}_{conv,i+1/2}\right)\Big] \tag{2.21}$$

To consolidate the chapter, the solution procedure is put in appendix B. In this section a detailed description on the model development is made. The statement made before is repeated, the model is based on enthalpy as the basic variable. From the (2.15) and (2.16) it is clear that one requires to compute conduction and convection fluxes.

2.7.1 Conductive Fluxes

The conductive fluxes of cell faces are calculated using Fourier's law:

$$\dot{q}''_{cond,i\pm1/2} = -k_{i\pm1/2}\left.\frac{dT}{dx}\right|_{r/l,i} \tag{2.22}$$

The value of thermal conductivity 'k' depends on the local composition of the (sub-) volume. If the cell is char, thermal conductivity of the cell $k_{i\pm1/2} = k_c$, i.e. the cell face $i + 1/2$ is in char material. If the cell is not pyrolysing or pyrolysed, the composition is different at every time step, depending on the evaporation front. In such a case, thermal conductivity is $k_{i\pm1/2} = \alpha_v k_v + \alpha_{w,l} k_{w,l}$. This determines the thermal conductivity of the control volume in case of drying. Thus, when the cell face is virgin dry, thermal conductivity is $k_{i\pm1/2} = k_v$. For the temperature derivatives, a piecewise linear representation of the temperature field is used.

Figure 2.5 illustrates the temperature function for temperatures stored in the cell centers. If there is no front in the cell, a straight line connects two neighbouring temperatures. If a front is present between two cell centers, the linearity is broken into two parts: linear from cell center $'i'$ to the front, and again linear from the front to cell center $'i + 1'$. Hence, it is clear that each cell has two gradients, one gradient over each face.

2.7.1a Spatial temperature derivatives

In each computational cell, the temperature T_i is stored in the cell centre (with coordinate x_i). Two temperature gradients are stored for each computational cell. The exact definitions, according to all possible configurations are:

- No pyrolysis front in between x_i and x_{i+1}:

$$\left.\frac{dT}{dx}\right|_{r,i} = \left.\frac{dT}{dx}\right|_{l,i+1} = \frac{T_{i+1} - T_i}{x_{i+1} - x_i} \tag{2.23}$$

- $x_{i+1/2} \leq x_{f,pyr} < x_{i+1}$

$$\left.\frac{dT}{dx}\right|_{r,i} = \left.\frac{dT}{dx}\right|_{l,i+1} = \frac{T_{f,pyr} - T_i}{x_{f,pyr} - x_i} \tag{2.24}$$

- $x_i \leq x_{f,pyr} < x_{i+1/2}$

$$\left.\frac{dT}{dx}\right|_{r,i} = \left.\frac{dT}{dx}\right|_{l,i+1} = \frac{T_{i+1} - T_{f,pyr}}{x_{i+1} - x_{f,pyr}} \tag{2.25}$$

Special care needs to be taken for the left side derivative of the first cell and the right side derivative of the last cell.

When the pyrolysis front is in the first cell, with $x_f^{n+1,k} < x_0$, the following relationship is taken between the spatial temperature derivatives at both sides of the front from equation (2.18).

$$(\rho_v - \rho_c)\, v_{f,pyr} \Delta Q_{pyr} = -k_c \left.\frac{dT}{dx}\right|_{l,0} + k_v \left.\frac{dT}{dx}\right|_{r,0} \tag{2.26}$$

This expression stems from a local mass and energy balance around the pyrolysis front, as explained in section 2.5.2.

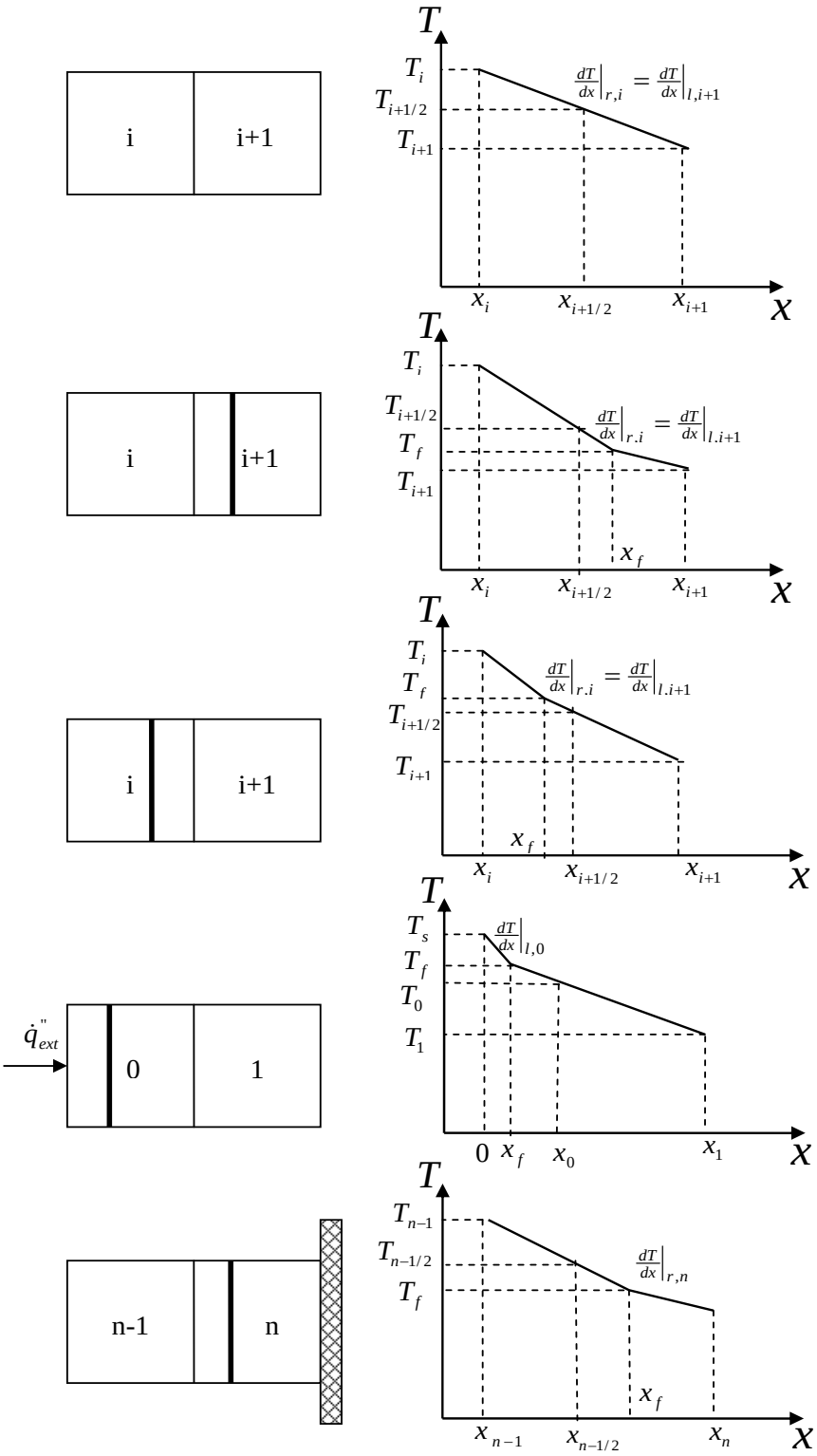

Figure 2.5: Piecewise linear temperature distribution

If there is no pyrolysis front, an extrapolation of the temperature field from inside the solid material is made:

$$\left.\frac{dT}{dx}\right|_{l,0} = \left.\frac{dT}{dx}\right|_{r,0} \tag{2.27}$$

In a similar way, the spatial temperature gradient in the last cell is computed as:

$$(\rho_v - \rho_c)\, v_{f,pyr} \Delta Q_{pyr} = -k_c \left.\frac{dT}{dx}\right|_{l,n-1} + k_v \left.\frac{dT}{dx}\right|_{r,n} \tag{2.28}$$

Else, the model uses:

$$\left.\frac{dT}{dx}\right|_{r,n} = \left.\frac{dT}{dx}\right|_{l,n} \tag{2.29}$$

The cell phase temperatures can be computed as:

- No front between x_i and x_{i+1}:

$$T_{i+1/2} = T_i + \left.\frac{dT}{dx}\right|_{r,i} (x_{i+1/2} - x_i) \tag{2.30}$$

- $x_{i+1/2} \leq x_{f,pyr} < x_{i+1}$:

$$T_{i+1/2} = T_i + \left.\frac{dT}{dx}\right|_{r,i} (x_{i+1/2} - x_i) \tag{2.31}$$

- $x_i \leq x_{f,pyr} < x_{i+1/2}$:

$$T_{i+1/2} = T_{i+1} - \left.\frac{dT}{dx}\right|_{l,i+1} (x_{i+1} - x_{i+1/2}) \tag{2.32}$$

- $x_{f,pyr} < x_{1/2}$:

$$\begin{aligned} T_s = T_{f,pyr} - \left.\frac{dT}{dx}\right|_{l,0} x_{f,pyr} \\ \text{with} \left.\frac{dT}{dx}\right|_{l,0} \text{taken from eqn. 2.26} \end{aligned} \tag{2.33}$$

- $x_{f,pyr} \geq x_{n-1/2}$:

$$\begin{aligned} T_{n+1/2} = T_{f,pyr} + \left.\frac{dT}{dx}\right|_{r,n-1} \left(x_{n+1/2} - x_{f,pyr}\right) \\ \text{with} \left.\frac{dT}{dx}\right|_{r,n-1} \text{taken from eqn. 2.28} \end{aligned} \tag{2.34}$$

In case of evaporation process i.e. when the evaporation front is present in the cell, the above expressions are true, using $T_{f,evap}$ and $x_{f,evap}$ instead of $T_{f,pyr}$ and $x_{f,pyr}$.

But, when both the fronts are in the same cell or are within distance Δx_i, the following expressions are seen:

- $\left(x_i \leq x_{f,pyr} \leq x_{i+1/2}\right)$ & $\left(x_i \leq x_{f,evap} \leq x_{i+1/2}\right)$
  - $\left(x_{f,evap} \geq x_{f,pyr}\right)$:

$$\begin{aligned} \left.\frac{dT}{dx}\right|_{r,i} &= \frac{T_{i+1} - T_{f,evap}}{x_{i+1} - x_{f,evap}}; \\ T_{i+1/2} &= T_{i+1} - \left.\frac{dT}{dx}\right|_{r,i} \left(x_{i+1} - x_{i+1/2}\right) \end{aligned} \tag{2.35}$$

  - $\left(x_{f,pyr} \geq x_{f,evap}\right)$:

$$\begin{aligned} \left.\frac{dT}{dx}\right|_{r,i} &= \frac{T_{i+1} - T_{f,pyr}}{x_{i+1} - x_{f,pyr}}; \\ T_{i+1/2} &= T_{i+1} - \left.\frac{dT}{dx}\right|_{r,i} \left(x_{i+1} - x_{i+1/2}\right) \end{aligned} \tag{2.36}$$

- $\left(x_i \leq x_{f,pyr} \leq x_{i+1/2}\right)$ & $\left(x_{i+1/2} \leq x_{f,evap} \leq x_{i+1}\right)$

$$\begin{aligned} \left.\frac{dT}{dx}\right|_{r,i} &= \frac{T_{f,evap} - T_{f,pyr}}{x_{f,evap} - x_{f,pyr}}; \\ T_{i+1/2} &= T_{evap} - \left.\frac{dT}{dx}\right|_{r,i} \left(x_{evap} - x_{i+1/2}\right) \end{aligned} \tag{2.37}$$

- $x_i \leq x_{f,evap} \leq x_{i+1/2}$ & $x_{i+1/2} \leq x_{f,pyr} \leq x_{i+1}$:

$$\begin{aligned} \left.\frac{dT}{dx}\right|_{r,i} &= \frac{T_{f,pyr} - T_{f,evap}}{x_{f,pyr} - x_{f,evap}}; \\ T_{i+1/2} &= T_{f,pyr} - \left.\frac{dT}{dx}\right|_{r,i} \left(x_{f,pyr} - x_{i+1/2}\right) \end{aligned} \tag{2.38}$$

- $\left(x_{i+1/2} \leq x_{f,pyr} \leq x_{i+1}\right)$ & $\left(x_{i+1/2} \leq x_{evap} \leq x_{i+1}\right)$
  - $\left(x_{f,evap} \geq x_{f,pyr}\right)$:

$$\begin{aligned} \left.\frac{dT}{dx}\right|_{r,i} &= \frac{T_{f,pyr} - T_i}{x_{f,pyr} - x_i}; \\ T_{i+1/2} &= T_i + \left.\frac{dT}{dx}\right|_{r,i} \left(x_{i+1/2} - x_i\right) \end{aligned} \tag{2.39}$$

  - $\left(x_{f,pyr} \geq x_{f,evap}\right)$:

$$\begin{aligned} \left.\frac{dT}{dx}\right|_{r,i} &= \frac{T_{f,evap} - T_i}{x_{f,evap} - x_i}; \\ T_{i+1/2} &= T_i + \left.\frac{dT}{dx}\right|_{r,i} \left(x_{i+1/2} - x_i\right) \end{aligned} \tag{2.40}$$

2.7.2 Convective fluxes

Equation (2.21) shows that the fluxes through the cell faces determine the update in enthalpy of the cell. Besides heat transfer by means of conduction, energy is also transported with the movement of water vapour and volatiles out of the solid material. The water vapour and volatiles are assumed to be everywhere in local thermal equilibrium with the solid material through which they flow, as they absorb heat. The assumption is made that there is no accumulation of volatiles or water vapour in the solid material. Also, there is no diffusion of volatiles towards the virgin solid. The convective flux through cell face $(i-1/2)$ reads:

$$\dot{q}''^{,n+1,k}_{conv,i-1/2} = -\dot{m}''^{n+1,k}_{w,v,i-1/2} \cdot h_{w,v}(T^{n+1,k}_{i-1/2}) - \dot{m}''^{n+1,k}_{g,i-1/2} \cdot h_g(T^{n+1,k}_{i-1/2}) \tag{2.41}$$

We recall that, $h_{w,v}(T) = c_{w,v}(T - 373)$ for evaporation and $h_g(T) = c_g(T - T_{pyr})$ for pyrolysis process.

During the pyrolysis process, the motion of the front determines the amount of mass lost in the form of volatiles. This mass flow rate can be determined as:

$$\begin{aligned}
\dot{m}''^{n+1,k}_{g,i-1/2} &= \sum_{j=i}^{N} (\rho_v - \rho_c) \frac{\xi_j^{n+1,k} - \xi_j^n}{\Delta t} \Delta x_j; \\
\xi_i^{n+1,k+1} &= min\left[max\left[0, \frac{x_{f,pyr}^{n+1,k+1} - x_{i-1/2}}{\Delta x_i} \right], 1 \right] \\
\dot{m}''^{n+1,k}_{w,v,i-1/2} &= \sum_{j=i}^{N} \tilde{\rho_{w,l}} \frac{\xi_{w,j}^{n+1,k} - \xi_{w,j}^n}{\Delta t} \Delta x_j; \\
\xi_{w,i}^{n+1,k+1} &= min\left[max\left[0, \frac{x_{f,evap}^{n+1,k+1} - x_{i-1/2}}{\Delta x_i} \right], 1 \right]
\end{aligned} \tag{2.42}$$

The cell face temperatures are computed, using the piecewise linear representation of the temperature. Also note that the model only considers uni-directional flow of pyrolysis gases towards the side where the external heat flux is imposed. The model could be extended to account for other mass fluxes, but this is not relevant for the present study.

2.8 Reconstruction of temperature field and fronts' position

From equation (2.21), the enthalpy update can be calculated. For the constuction of the fluxes, the knowledge of temperature and front position is needed, though. Therefore, from the updated enthalpy values, the temperature field and front position must be reconstructed. Two constraints determine the relation between these variables i.e. the enthalpy is a function of temperature and the local composition and the motion of the front correlates the temperature gradient on both sides of the fronts.

2.8.1 Constraint 1: enthalpy as a function of temperature and composition

A function $F_{enth,i}$ is introduced for each computational cell, to express the relationship between the enthalpy value and the temperature. This relates to expressions (2.10) to (2.13). As we assume here that water vapour and volatiles leave the solid immediately as soon as they are formed, the mass fraction $\alpha_{w,v}$ and α_g are zero.

The model considers that the value of enthalpy is averaged over the computational cell. For a one dimensional configuration, this reads:

$$(\tilde{\rho}h)_i \Delta x_i = \int_{x_{i-1/2}}^{x_{i+1/2}} \sum_k \tilde{\rho}_k(x)\, h_k(T(x))\, dx \tag{2.43}$$

where $T(x)$ is the piecewise linear temperature distribution. The local mass concentration of the components is a piecewise constant function, whose value depends on the front position. As such, a few possible configurations can be distinguished, for which different expressions can be formulated, all derived from the general form:

$$\begin{aligned} F_{enth,i}\left(T_i, (\tilde{\rho}h)_i, x_{f,pyr}, T_{f,pyr}, x_{f,evap}, T_{f,evap}\right) &\triangleq \\ \int_{x_{i-1/2}}^{x_{i+1/2}} \sum_k \tilde{\rho}_k(x) h_k(T(x))\, dx - (\tilde{\rho}h)_i \Delta x_i &= 0 \end{aligned} \tag{2.44}$$

The different possible cell configurations for both charring and non-charring materials are presented. The following expressions are valid for charring and non-charring materials. In the latter, ρ_c must be simply set to zero.

- Cell i is char (only relevant in charring materials):

$$\begin{aligned} &F_{enth,i}\left(T_i, (\tilde{\rho}h)_i\right) = \\ &\left(\frac{x_i - x_{i-1/2}}{2}\right)\left[\rho_c c_c\left(T_i - \frac{1}{4}\Delta x_i \left.\frac{dT}{dx}\right|_{l,i} - T_{pyr}\right) + (\rho_v - \rho_c)\,\Delta Q_{pyr}\right] \\ &+\left(\frac{x_{i+1/2} - x_i}{2}\right)\left[\rho_c c_c\left(T_i + \frac{1}{4}\Delta x_i \left.\frac{dT}{dx}\right|_{r,i} - T_{pyr}\right) + (\rho_v - \rho_c)\,\Delta Q_{pyr}\right] \\ &-(\tilde{\rho}h)_i \Delta x_i \end{aligned} \tag{2.45}$$

- Cell i contains the pyrolysis front:

$$\begin{aligned} (\mathbf{x_{f,pyr}} \le \mathbf{x_i}):\ &F_{enth,i}\left(T_i, (\tilde{\rho}h)_i, x_{f,pyr}, T_{f,pyr}\right) = (x_{f,pyr} - x_{i-1/2})\cdot \\ &\left[\rho_c c_c\left(T_{f,pyr} - \left(\frac{x_{f,pyr} - x_{i-1/2}}{2}\right)\left.\frac{dT}{dx}\right|_{l,i} - T_{pyr}\right) + (\rho_v - \rho_c)\,\Delta Q_{pyr}\right] \\ &+(x_i - x_{f,pyr})\left[\rho_v c_v\left(\frac{T_{f,pyr} + T_i}{2} - T_{pyr}\right)\right] \\ &+(x_{i+1/2} - x_i)\left[\rho_v c_v\left(T_i + \frac{\Delta x_i}{4}\left.\frac{dT}{dx}\right|_{r,i} - T_{pyr}\right)\right] \\ &+\left(x_{f,pyr}^{n+1,k+1} - x_{f,pyr}^{n+1,k}\right)(\rho_v - \rho_c)\, c_{pyr}\left(T_{f,pyr} - T_{pyr}\right) \\ &-(\tilde{\rho}h)_i \Delta x_i \end{aligned} \tag{2.46}$$

$$
\begin{aligned}
(\mathbf{x_{f,pyr}} > \mathbf{x_i}):\ & F_{enth,i}\left(T_i, (\tilde{\rho}h)_i, x_{f,pyr}, T_{f,pyr}\right) = \\
& \left(x_i - x_{i-1/2}\right)\left[\rho_c c_c\left(T_i - \frac{\Delta x_i}{2}\left.\frac{dT}{dx}\right|_{l,i} - T_{pyr}\right) + \left(\rho_v - \rho_c\right)\Delta Q_{pyr}\right] \\
& + \left(x_{f,pyr} - x_i\right)\left[\rho_c c_c\left(\frac{T_{f,pyr} + T_i}{2} - T_{pyr}\right) + \left(\rho_v - \rho_c\right)\Delta Q_{pyr}\right] \\
& + \left(x_{i+1/2} - x_f\right)\left[\rho_v c_v\left(T_{f,pyr} + \left(\frac{x_{i+1/2} - x_{f,pyr}}{2}\right)\left.\frac{dT}{dx}\right|_{r,i} - T_{pyr}\right)\right] \\
& \quad + \left(x_{f,pyr}^{n+1,k+1} - x_{f,pyr}^{n+1,k}\right)\left(\rho_v - \rho_c\right) c_{pyr}\left(T_{f,pyr} - T_{pyr}\right) \\
& - \left(\tilde{\rho}h\right)_i \Delta x_i
\end{aligned}
\tag{2.47}
$$

- Cell i is virgin dry material and does not contain a front:

$$
\begin{aligned}
& F_{enth,i}\left(T_i, (\tilde{\rho}h)_i\right) = \\
& \left(\frac{x_i - x_{i-1/2}}{2}\right)\left[\rho_v c_v\left(T_i - \frac{1}{4}\Delta x_i \left.\frac{dT}{dx}\right|_{l,i} - T_{pyr}\right)\right] \\
& + \left(\frac{x_{i+1/2} - x_i}{2}\right)\left[\rho_v c_v\left(T_i + \frac{1}{4}\Delta x_i \left.\frac{dT}{dx}\right|_{r,i} - T_{pyr}\right)\right] \\
& - \left(\tilde{\rho}h\right)_i \Delta x_i
\end{aligned}
\tag{2.48}
$$

- Cell i contains the evaporation front:

$$
\begin{aligned}
(\mathbf{x_{f,evap}} \leq \mathbf{x_i}):\ & F_{enth,i}\left(T_i, (\tilde{\rho}h)_i, x_{f,evap}, T_{f,evap}\right) = \left(x_{f,evap} - x_{i-1/2}\right)\cdot \\
& \left[\rho_v c_v\left(T_{f,evap} - \left(\frac{x_{f,evap} - x_{i-1/2}}{2}\right)\left.\frac{dT}{dx}\right|_{l,i} - T_{pyr}\right)\right] \\
& + \left(x_i - x_{f,evap}\right)\left[\rho_v c_v\left(\frac{T_{f,evap} + T_i}{2} - T_{pyr}\right)\right] \\
& + \left(x_{i+1/2} - x_i\right)\left[\rho_v c_v\left(T_i + \frac{\Delta x_i}{4}\left.\frac{dT}{dx}\right|_{r,i} - T_{pyr}\right)\right] \\
& + \left(x_i - x_{f,evap}\right)\left[\rho_{w,l} c_{w,l}\left(\frac{T_{f,evap} + T_i}{2} - T_{ref}\right)\right] \\
& + \left(x_{i+1/2} - x_i\right)\left[\rho_{w,l} c_{w,l}\left(T_i + \frac{\Delta x_i}{4}\left.\frac{dT}{dx}\right|_{r,i} - T_{ref}\right)\right] \\
& + \left(x_{f,evap}^{n+1,k+1} - x_{f,evap}^{n+1,k}\right)\cdot \\
& \rho_{w,l}\left[c_{w,v}\left(T_{f,evap} - \left(x_{f,evap} - x_{i-1/2}\right)\left.\frac{dT}{dx}\right|_{l,i} - T_{evap}\right) - L_v\right] \\
& - \left(\tilde{\rho}h\right)_i \Delta x_i
\end{aligned}
\tag{2.49}
$$

$$
\begin{aligned}
(\mathbf{x_{f,evap}} > \mathbf{x_i}):\ & F_{enth,i}\left(T_i, (\tilde{\rho}h)_i, x_{f,evap}, T_{f,evap}\right) = \\
& (x_i - x_{i-1/2})\left[\rho_v c_v\left(T_i - \frac{\Delta x_i}{2}\frac{dT}{dx}\Big|_{l,i} - T_{pyr}\right)\right] \\
& + (x_{f,evap} - x_i)\left[\rho_v c_v\left(\frac{T_{f,evap}+T_i}{2} - T_{pyr}\right)\right] \\
& + (x_{i+1/2} - x_{f,evap})\cdot \\
& \left[\rho_v c_v\left(T_{f,evap} + \left(\frac{x_{i+1/2}-x_{f,evap}}{2}\right)\frac{dT}{dx}\Big|_{r,i} - T_{pyr}\right)\right] \\
& + (x_{i+1/2} - x_{f,evap})\cdot \\
& \left[\rho_{w,l} c_{w,l}\left(T_{f,evap} + \left(\frac{x_{i+1/2}-x_{f,evap}}{2}\right)\frac{dT}{dx}\Big|_{r,i} - T_{ref}\right)\right] \\
& + \left(x_{f,evap}^{n+1,k+1} - x_{f,evap}^{n+1,k}\right)\rho_{w,l}\left[c_{w,v}\left(T_i - \frac{\Delta x_i}{2}\frac{dT}{dx}\Big|_{l,i} - T_{evap}\right) - L_v\right] \\
& - (\tilde{\rho}h)_i\,\Delta x_i
\end{aligned}
\tag{2.50}
$$

- Cell i is virgin wet material and does not contain a front:

$$
\begin{aligned}
& F_{enth,i}\left(T_i, (\tilde{\rho}h)_i\right) \\
& = \left(\frac{x_i - x_{i-1/2}}{2}\right)\left[\rho_v c_v\left(T_i - \frac{1}{4}\Delta x_i\frac{dT}{dx}\Big|_{l,i} - T_{pyr}\right)\right] \\
& + \left(\frac{x_i - x_{i-1/2}}{2}\right)\left[\rho_{w,l} c_{w,l}\left(T_i - \frac{1}{4}\Delta x_i\frac{dT}{dx}\Big|_{l,i} - T_{ref}\right)\right] \\
& + \left(\frac{x_{i+1/2} - x_i}{2}\right)\left[\rho_v c_v\left(T_i + \frac{1}{4}\Delta x_i\frac{dT}{dx}\Big|_{r,i} - T_{pyr}\right)\right] \\
& + \left(\frac{x_{i+1/2} - x_i}{2}\right)\left[\rho_{w,l} c_{w,l}\left(T_i + \frac{1}{4}\Delta x_i\frac{dT}{dx}\Big|_{r,i} - T_{ref}\right)\right] \\
& - (\tilde{\rho}h)_i\,\Delta x_i
\end{aligned}
\tag{2.51}
$$

In equation 2.46 and 2.47 for pyrolysis process and equation 2.49 and 2.50 for evaporation process, the last but one term is added just to improve stability. They vanish any way when the fronts are at the respective temperature e.g. T_{pyr} for pyrolysis process and T_{evap} for evaporation.

2.8.2 Constraint 2: motion of the front

For the cells containing a front, the model requires an extra constraint. This closure is done by introducing an additional function $F_{f,pyr}(x_{f,pyr}, T_{f,pyr}, T_i)$ for the cell i, containing the pyrolysis front, so that the discretization of $(\rho_v - \rho_c)\cdot v_{f,pyr}\cdot\Delta Q_{pyr} = -k_c\nabla T\big|_c + k_v\nabla T\big|_v$, expression 2.18, leads to $F_{f,pyr}(x_{f,pyr}, T_{f,pyr}, T_i) = 0$, with the following expression for $F_{f,pyr}$:

- Pyrolysis front is before the cell center:

$$\begin{aligned}(\mathbf{x_{f,pyr}} \leq \mathbf{x_i}):\ & F_{f,pyr}(x_{f,pyr}, T_{f,pyr}, T_i) \\ & = \frac{x_{f,pyr} - x^n_{f,pyr}}{\Delta t}(\rho_v - \rho_c)\Delta Q_{pyr}(x_i - x_f) \\ & + k_c \left(\frac{T_{f,pyr} - T_{i-1}}{x_{f,pyr} - x_{i-1}}\right)(x_i - x_{f,pyr}) \\ & - k_v(T_i - T_{f,pyr})\end{aligned} \tag{2.52}$$

- Pyrolysis front is after the cell center:

$$\begin{aligned}(\mathbf{x_{f,pyr}} > \mathbf{x_i}):\ & F_{f,pyr}(x_{f,pyr}, T_{f,pyr}, T_i) \\ & = \frac{x_{f,pyr} - x^n_{f,pyr}}{\Delta t}(\rho_v - \rho_c)\Delta Q_{pyr}(x_{f,pyr} - x_i) \\ & + k_v \left(\frac{T_{i+1} - T_{f,pyr}}{x_{i+1} - x_{f,pyr}}\right)(x_{f,pyr} - x_i) \\ & - k_c(T_{f,pyr} - T_i)\end{aligned} \tag{2.53}$$

For non-charring materials, as dicussed earlier ρ_c equals zero and the conduction terms in the char is replaced by the external heat flux. When the solid is wet containing the evaporation front, the above discussed constraint for pyrolysis process is modified for evaporation process in the following manner:

- Evaporation front is before the cell center:

$$\begin{aligned}(\mathbf{x_{f,evap}} \leq \mathbf{x_i}):\ & F_{f,evap}(x_{f,evap}, T_{f,evap}, T_i) \\ & = \frac{x_{f,evap} - x^n_{f,evap}}{\Delta t}\rho_{w,l}L_v(x_i - x_{f,evap}) \\ & + k_{v,wet}\left(\frac{T_{f,evap} - T_{i-1}}{x_{f,evap} - x_{i-1}}\right)(x_i - x_{f,evap}) \\ & + k_{v,dry}(T_i - T_{f,evap})\end{aligned} \tag{2.54}$$

- Evaporation front is after the cell center:

$$\begin{aligned}(\mathbf{x_{f,evap}} > \mathbf{x_i}):\ & F_{f,evap}(x_{f,evap}, T_{f,evap}, T_i) \\ & = \frac{x_{f,evap} - x^n_{f,evap}}{\Delta t}\rho_{w,l}L_v(x_{f,evap} - x_i) \\ & + k_{v,dry}\left(\frac{T_{i+1} - T_{f,evap}}{x_{i+1} - x_{f,evap}}\right)(x_{f,evap} - x_i) \\ & + k_{v,wet}(T_{f,evap} - T_i)\end{aligned} \tag{2.55}$$

$k_{v,dry}$ is used for clarity, to understand the concept. In general, $k = \sum_i \alpha_i k_i$, so that effectively $k_{v,dry} = k_v$ and $k_{v,wet} = \alpha_v k_v + \alpha_{w,l} k_{w,l}$ in the above equation.

2.8.3 Inversion of the constraint to determine temperature and fronts' position

Using expressions (2.45) to (2.55), for a given enthalpy field, the corresponding temperature field and front positions can be found. However, direct inversion of equations (2.45) to (2.55) is a tedious task, since all equations are coupled. Indeed, an expression for a cell i does not only involve the local temperature T_i, but also the temperature values of the neighbouring nodes. Since an iterative procedure is adopted anyway, this coupling is not taken into account for the inversion of the system and only the temperature of cell i is considered as an unknown in the functions. The neighbouring temperatures are then taken from the previous iteration level (as known quantities). This allows a much cheaper inversion, since every cell can be treated independently.

For cells that do not contain a pyrolysis or evaporation front, the determination of $T_i^{n+1,k+1}$ from $(\tilde{\rho}h)_i^{n+1,k+1}$ is straightforward, setting $F_{enth,i}\left(T_i^{n+1,k+1},(\tilde{\rho}h)_i^{n+1,k+1}\right)=0$, using expressions (2.45) to (2.48). E.g. if the cell is completely char (does not contain a front), expression (2.45) yields:

$$\begin{aligned} &F_{enth,i}\left(T_i^{n+1,k+1},(\tilde{\rho}h)_i^{n+1,k+1}\right)=\left(\frac{x_i-x_{i-1/2}}{2}\right)\cdot \\ &\left[\rho_c c_c\left(T_i^{n+1,k+1}-\frac{1}{4}\Delta x_i\left.\frac{dT}{dx}\right|_{l,i}^{n+1,k}-T_{pyr}\right)+(\rho_v-\rho_c)\,\Delta Q_{pyr}\right] \\ &+\left(\frac{x_{i+1/2}-x_i}{2}\right)\cdot \\ &\left[\rho_c c_c\left(T_i^{n+1,k+1}+\frac{1}{4}\Delta x_i\left.\frac{dT}{dx}\right|_{r,i}^{n+1,k}-T_{pyr}\right)+(\rho_v-\rho_c)\,\Delta Q_{pyr}\right] \\ &-(\tilde{\rho}h)_i^{n+1,k+1}\,\Delta x_i \end{aligned} \tag{2.56}$$

from which $T_i^{n+1,k+1}$ immediately follows. This indicates that the solid char just heats up by the heat provided from the external heat source. When the cell contains the pyrolysis front the solution procedure as described in appendix B is used. As a first possibility that the update in the enthalpy $(\tilde{\rho}h)_i$ leads to a variation in the pyrolysis front position, keeping the front temperature constant, equal to pyrolysis temperature T_{pyr}. This is expressed as:

$$\begin{aligned} &F_{f,pyr}\left(T_i^{n+1,k+1},x_{f,pyr}^{n+1,k+1};T_{pyr}\right)=0 \\ &F_{enth,i}\left(T_i^{n+1,k+1},x_{f,pyr}^{n+1,k+1};\tilde{\rho}h_i^{n+1,k+1},T_{pyr}\right)=0 \end{aligned} \tag{2.57}$$

The notation means that the quantities behind the semi-colon (';') are 'known', whereas the variables ahead of the semi-colon are to be computed. Linearization around $(T_i^{n+1,k+1},x_{f,pyr}^{n,k})$ yields a Taylor expansion, with $\Delta T_i=T_i^{n+1,k+1}-T_i^{n+1,k}$ and $\Delta x_{f,pyr}=x_{f,pyr}^{n+1,k+1}-x_{f,pyr}^{n+1,k}$,

is:

$$\begin{aligned}
&F_{f,pyr}(T_i^{n+1,k}, x_{f,pyr}^{n+1,k}; T_{pyr}) \\
&+\frac{F_{f,pyr}(T_i^{n+1,k}+\delta T_i, x_{f,pyr}^{n+1,k}; T_{pyr}) - F_{f,pyr}(T_i^{n+1,k}, x_{f,pyr}^{n+1,k}; T_{pyr})}{\delta T_i}\Delta T_i \\
&+\frac{F_{f,pyr}(T_i^{n+1,k}, x_{f,pyr}^{n+1,k}+\delta x_{f,pyr}; T_{pyr}) - F_{f,pyr}(T_i^{n+1,k}, x_{f,pyr}^{n+1,k}; T_{pyr})}{\delta x_{f,pyr}}\Delta x_{f,pyr} = 0
\end{aligned} \tag{2.58}$$

$$\begin{aligned}
&F_{enth,i}(T_i^{n+1,k}, x_{f,pyr}^{n+1,k}; (\tilde{\rho}h)_i^{n+1,k+1}, T_{pyr}) \\
&+\frac{F_{enth,i}(T_i^{n+1,k}+\delta T_i, x_{f,pyr}^{n+1,k}; (\tilde{\rho}h)_i^{n+1,k+1}, T_{pyr})}{\delta T_i}\Delta T_i \\
&-\frac{F_{enth,i}(T_i^{n+1,k}, x_{f,pyr}^{n+1,k}; (\tilde{\rho}h)_i^{n+1,k+1}, T_{pyr})}{\delta T_i}\Delta T_i \\
&+\frac{F_{enth,i}(T_i^{n+1,k}, x_{f,pyr}^{n+1,k}+\delta x_{f,pyr}; (\tilde{\rho}h)_i^{n+1,k+1}, T_{pyr})}{\delta x_{f,pyr}}\Delta x_{f,pyr} \\
&-\frac{F_{enth,i}(T_i^{n+1,k}, x_{f,pyr}^{n+1,k}; (\tilde{\rho}h)_i^{n+1,k+1}, T_{pyr})}{\delta x_{f,pyr}}\Delta x_{f,pyr} = 0
\end{aligned} \tag{2.59}$$

For the numerical calculations of the partial derivatives, the perturbation δx_f and δT_i use $0.001\Delta x_f$ and $0.1K$ respectively. The equations can be written in the form:

$$\begin{aligned}
a_{11}\Delta T_i + a_{12}\Delta x_f &= b_1 \\
a_{21}\Delta T_i + a_{22}\Delta x_f &= b_2
\end{aligned} \tag{2.60}$$

with

$$\begin{aligned}
a_{11} &= \frac{\delta F_{f,pyr}}{\delta T_i}; a_{12} = \frac{\delta F_{f,pyr}}{\delta x_{f,pyr}}; \\
b_1 &= -F_{f,pyr}\left(T_i^{n+1,k}, x_{f,pyr}^{n+1,k+1}; T_{pyr}\right) \\
a_{21} &= \frac{\delta F_{enth,i}}{\delta T_i}; a_{22} = \frac{\delta F_{enth,i}}{\delta x_{f,pyr}}; \\
b_2 &= -F_{enth,i}\left(T_i^{n+1,k}, x_{f,pyr}^{n+1,k+1}; (\tilde{\rho}h)_i^{n+1,k+1}, T_{pyr}\right)
\end{aligned}$$

This system is solved using Cramer's method, yielding ΔT_i and $\Delta x_{f,pyr}$, and thus $T_i^{n+1,k+1}$ and $x_{f,pyr}^{n+1,k+1}$ are computed. The convergence check has been reported in appendix B.

Exactly the same strategy is adopted to calculate $T_i^{n+1,k+1}$, when the cell is not pyrolysing i.e. $T_{f,pyr} < T_{pyr}$ as:

$$\begin{aligned}
&F_{f,pyr}(T_i^{n+1,k+1}, T_{f,pyr}^{n+1,k+1}; x_{f,pyr}^n) = 0 \\
&F_{enth,i}(T_i^{n+1,k+1}, T_{f,pyr}^{n+1,k+1}; \tilde{\rho}h)_i^{n+1,k+1}, x_{f,pyr}^n = 0
\end{aligned} \tag{2.61}$$

Then the perturbations are for T_i and $T_{f,pyr}$ (instead of T_i and $x_{f,pyr}$) and $x_{f,pyr}$ is assumed to be constant equal to $x_{f,pyr}^n$, value of pyrolysis front at the previous time level. This

is because the model assume that pyrolysis is irreversible process, mentioned in the first assumption.

A similar strategy holds true when calculating the variables $T_{f,evap}$ and $x_{f,evap}$ for the evaporation front temperature and front position in case of the evaporation process.

2.8.4 Treatment of boundaries

It is very important to formulate the first and last cell of the solid one-dimensional configuration under study. In the first cell, i.e. the front is before the cell center ($x_{f,pyr} < x_0$) and the last cell, i.e. when the front is after the cell center ($x_{f,pyr} > x_n$), a piecewise linear extrapolation is adopted: $T_{f,pyr}$ is related to $x_{f,pyr}$ such that it is on the straight line through (x_0, T_0) and (x_1, T_1) for the first cell as:

$$F_{f,pyr}(x_{f,pyr}, T_{f,pyr}, T_0) = T_0 - \frac{T_1^{n+1,k} - T_0}{x_1 - x_0}(x_0 - x_{f,pyr}) - T_{f,pyr} \tag{2.62}$$

and for the last cell, a similar approach is adopted:

$$F_{f,pyr}(x_{f,pyr}, T_{f,pyr}, T_n) = T_n + \frac{T_n - T_{n-1}^{n+1,k}}{x_n - x_{n-1}}(x_{f,pyr} - x_{n-1}) - T_{f,pyr} \tag{2.63}$$

The reason for this change is because, if equation (2.52)-(2.53) are used, these functions return zero by construction of the temperature profile. Hence, the alternative constraints at the boundaries. The same extrapolation is performed if the evaporation front is in the first or the last cell, yielding constraints

$$F_{f,evap}(x_{f,evap}, T_{f,evap}, T_0) = T_0 - \frac{T_1^{n+1,k} - T_0}{x_1 - x_0}(x_0 - x_{f,evap}) - T_{f,evap} \tag{2.64}$$

and for the last cell:

$$F_{f,evap}(x_{f,evap}, T_{f,evap}, T_n) = T_n + \frac{T_n - T_{n-1}^{n+1,k}}{x_n - x_{n-1}}(x_{f,evap} - x_{n-1}) - T_{f,evap} \tag{2.65}$$

2.9 Discussion: zero-th order temperature field representation

In [109], a zero-th order representation is adopted for the temperature field, i.e. the temperature is uniform in each of the computational cells. The essential difference to the model formulation as presented above is that, when the mushy cell (cell containing the pyrolysis front) is pyrolysing, its temperature is kept fixed, equal to the pyrolysis temperature. In combination herewith, a computational cell only starts pyrolysing when its temperature becomes equal to the pyrolysis temperature. This has serious consequences on the evolution of the pyrolysis gases mass flow rates and pyrolysis front motion: when the pyrolysing cell has just become pure char, the next cell to pyrolyse must first still heat up to T_{pyr} and during this period, $\dot{m}_g''$ drops to zero, which is unacceptable. Indeed, as the only heat transfer

mechanism towards the virgin material is by conduction, it is inevitable that, at the moment when the formerly pyrolysing cell becomes pure char, the temperature of the neighbouring virgin cell is still below the pyrolysis temperature. This was already recognised in [130], but the problem was not really solved there. A dual mesh technique was introduced, effectively reducing the mentioned undesired phenomenon, but not solving the problem. More on this zero-th temperature field representation, solution procedure, model development equations and test cases is discussed in appendix A.

2.10 Conclusion

In this chapter, the basic model equations have been described. The assumptions and simplifications have been pointed out. In the following chapters, this model will be applied.

3

One-dimensional case studies

3.1 Dry Charring materials

3.1.1 Introduction

The enthalpy based model developed in chapter 2 is applied on one-dimensional test case, as a starting point. Numerical issues and implementation, including the solution procedure, are described in detail, pertaining to charring materials. An interesting feature of the model is the use of a fixed computational mesh. The chapter illustrates the accuracy of the results by means of a series of basic one-dimensional test cases. The configuration already discussed earlier is used (see figure 2.3), where the externally imposed heat flux is not computed from flame radiation, in order to aviod related uncertainty. The following will be taken into discussion:

- comparison to numerical reference results [125] and experimental data [60];
- the importance of the use of a piecewise linear approximation of the temperature field in the solid material in charring materials;
- sensitivity of the results with respect to the grid size and the time step size.

The complete set of results aims at illustrating the robustness and accuracy of the simple model.

3.1.2 Verification studies

3.1.2a Configuration

Consider a one-dimensional configuration, with an external radiative heat flux imposed at one side. Accounting for external heat loss from the exposed surface by convection and reradiation, the net heat flux, entering the solid by conduction, becomes:

$$\dot{q}''_{cond,0-1/2} = \epsilon \dot{q}''_{ext} - h(T_s - T_{amb}) - \epsilon \cdot \sigma \cdot (T_s^4 - T_{amb}^4) \tag{3.1}$$

The back surface is perfectly insulated and impervious: $\dot{q}''_{n-1/2} = 0$.

The present enthalpy based model results are compared to the experiments of [60], which were conducted on a 3.8 cm cubic sample of white pine, subjected to a radiant heat flux of 40 kW/m^2 on only one surface. The experiments were performed in an inert atmosphere. Preconditioning was done on the sample in order to remove the moisture content. The sample was placed on an electronic balance for continuous weight recording, from which the pyrolysis gases mass flow rate could be determined. The temperature was recorded by thermocouples, placed in the sample at three different depths (surface, 5 mm and 10 mm depth). The numerical simulation results are compared to the numerical simulations of [125], where an integral model is used. The model uses the same values for the thermo-physical properties of white pine as in [125]:

Properties	Value	Units
ρ_v	380.0	kg/m^3
ρ_c	76.0	kg/m^3
c_v	1196.0	J/(kgK)
c_c	986.8	J/(kgK)
k_v	0.36	W/(mK)
k_c	0.2	W/(mK)

Table 3.1: Thermo-physical properties of White Pine

The model parameters used in the simulations are: ΔQ_{pyr}=1.2 MJ/kg, T_{amb}=300 K, T_{pyr}=658 K. The value of convection heat transfer coefficient h = 15 W/(m^{2}K), σ = 6.67 $\times$ 10^{-8} W/(m^{2}K^4) and emissivity ϵ = 0.9. It is evident that the results strongly depend on these values, but a parameter study is not the topic of the present work. The basic configuration consists of 40 cells and a physical time step equal to 0.5 s. The dependence of the results on these choices are discussed below.

In Figure 3.1, the evolution of the pyrolysis gases mass flow rate as function of time is presented. A first important observation is that the model is able to reproduce the numerical results of [125]. Per se, this is not surprising as the model uses identical settings for the configuration and material properties, but the methodology is strongly different. Here, a simple technique is used with a fixed computational mesh that is extendable to multi-dimensional configurations (see below), whereas integral type models are intrinsically one-dimensional.

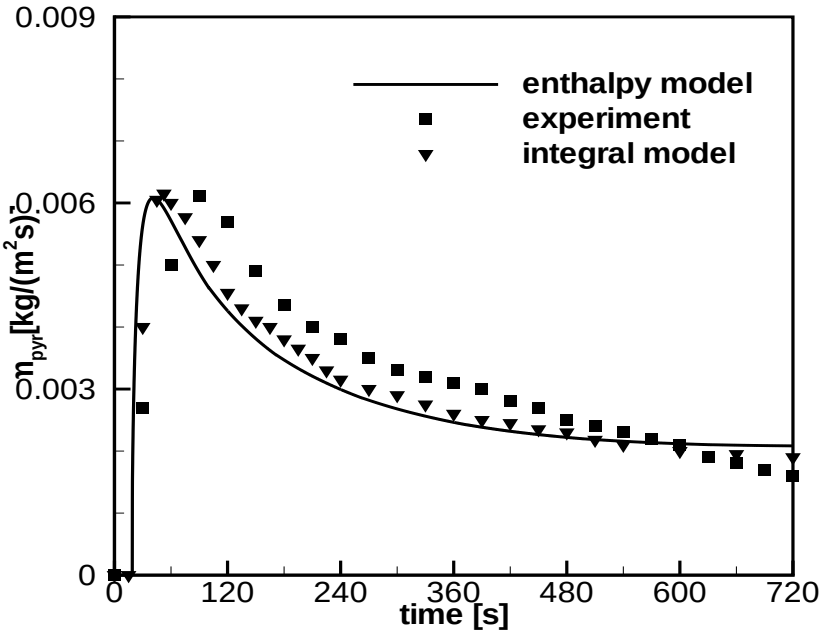

Figure 3.1: Pyrolysis gases mass flow rate evolution in time(40 cells)

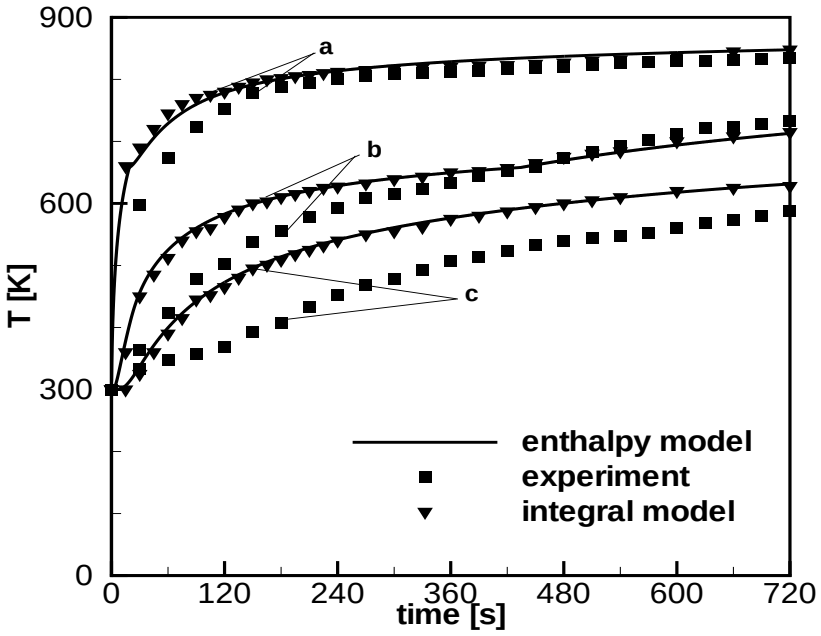

Figure 3.2: Temperature evolution in time(Depths: (a) surface; (b) 5 mm and (c) 10 mm)

Agreement with the experimental data is not perfect. In the experiments, pyrolysis starts immediately. In the numerical simulations, the material first needs to heat up (at the exposed surface) up to the pyrolysis temperature before the pyrolysis process can start and pyrolysis gases are generated. As mentioned in [125], the peak mass flow rate corresponds

very well to the experimentally reported value. Agreement with the experimental data can be improved by variation of the material properties or by inclusion of finite rate kinetics.

The observations for the temperature evolution inside the material in figure 3.2, as measured by thermocouples at the surface and at depths equal to 5mm and 10mm, are very similar. The author agrees with the statement in [125] that the relatively poor agreement at the deepest location is due to the simplicity of the pyrolysis model. The temperature rises more rapidly than in the experiments. Adjustment of material properties could lead to better agreement with experimental observations.

3.1.2b Sensitivity to numerical accuracy

The dependence of the results on the number of computational cells and the physical time step (Figure 3.3) are discussed. Clearly, differences are very small, even for a number as low as 20 cells. Table 3.2 quantifies this, reporting the maximum mass flow rate value and the relative error, compared to the results obtained for a 320 cells mesh. For 40 cells, the model simulation was complete within 5 mins. But, for 320 cells, the model took 10 mins time. The program is written in house code using C++ programming langauge. We did not make any effort to optimize the algorithm. The CPU used for the computations is a cluster Intel QuadCore Xeon X5355 2,66GHz (L2 cache=2x4MB, FSB=1333MHz). The value of $\dot{m}''_{g,max}$ is determined by constructing a parabola through the obtained discrete maximum value and the values obtained at the previous and subsequent time step. The relative error is computed as

$$\frac{\|\dot{m}''_{g,max} - \dot{m}''_{g,max,320}\|}{\|\dot{m}''_{g,max,320}\|} \tag{3.2}$$

Cells	$\dot{m}''_{g,max}[kg/m^2s]$	%error $\dot{m}''_{g,max}$
20	0.00619	2.60
40	0.00608	0.81
80	0.00605	0.29
160	0.00603	0.033
320	0.00603	0

Table 3.2: Effect of number of cells on maximum flow rate value. Time step equal to 0.1s

The errors remain well below 5%, even for the coarsest mesh. This is typically less than other uncertainties and implies that the model and method are robust with respect to the number of computational mesh cells.

The effect of the physical time step size on the results is presented, for the configuration with 40 cells. Except for the two largest time steps, deviations between the curves are again very small (see Table 3.3). Now the result with Δt = 0.1 s is used as reference value to compute the relative errors. Again, the error remains well below 5%, unless time steps as large as 10 s are taken. From table 3.3 it is thus clear that quite large time steps can be taken with the present model and method, without substantial loss in accuracy. The model is able to complete the simulation presented in less than 5 mins. In combination with the robustness

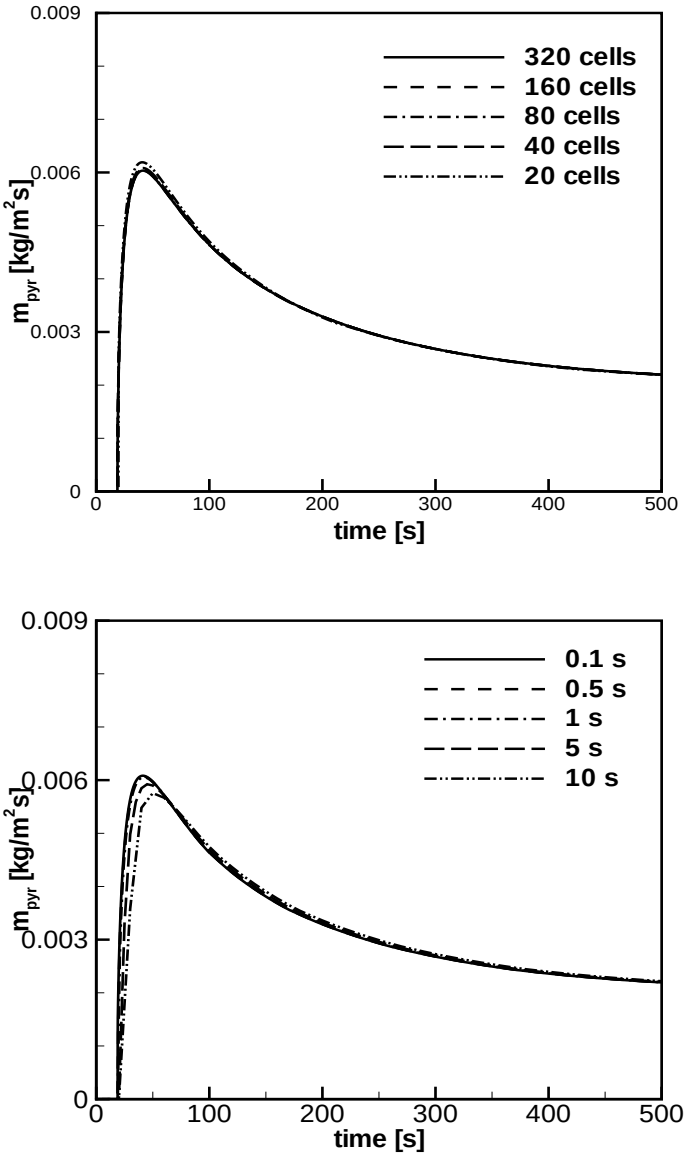

Figure 3.3: Top: Influence of the number of cells on the evolution of pyrolysis gases mass flow rate in time (physical time step equal to 0.5 s). Bottom: Influence of the physical time step size on the evolution of pyrolysis gases mass flow rate in time (number of cells equal to 40)

with respect to the number of computational cells, this property makes the present model and method appealing for coupling to CFD simulations, in particular in multi-dimensional configurations (as conduction in the solid material is readily taken into account).

3.1.3 Comparison to zero-th temperature field representation

So far, we focussed on results obtained with a piecewise linear representation. Figure 3.4 reveals that this is essential to obtain a continuous mass flow rate evolution in time. Indeed, a zero-th order temperature field representation, i.e. a uniform temperature per computational

time step size[s]	$\dot{m}''_{g,max}$[kg/m^{2}s]	%error $\dot{m}''_{g,max}$
0.1	0.00608	0
0.5	0.00606	0.22
1	0.00605	0.49
5	0.00592	2.63
10	0.00575	5.38

Table 3.3: Effect of time step size on maximum flow rate value. Number of cells equal to 40.

cell, as might be the first natural choice, is not sufficient: the pyrolysis gases mass flow rate evolution in time reveals discontinuities. As explained earlier, the mass flow rate (21) inevitably always drops to zero when the char fraction in the mushy cell (i.e. the cell containing the pyrolysis front) becomes equal to 1.

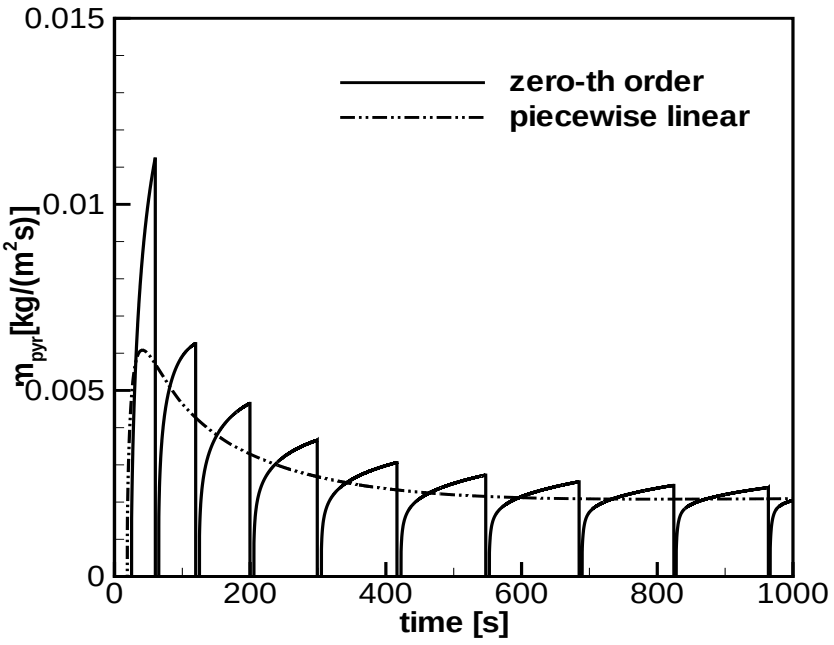

Figure 3.4: Pyrolysis gases mass flow rate seen for the zero-th order and piecewise linear enthalpy based model

Indeed, as long as the mushy cell is pyrolysing, its temperature is kept constant, equal to T_{pyr}. As the only heat transfer mechanism towards the virgin material is by conduction, it is inevitable that, at the moment when the mushy cell becomes pure char, the temperature of the neighbouring virgin cell is still below the pyrolysis temperature. Thus, this cell first needs to heat up to T_{pyr} , the criterion for the onset of pyrolysis. During this heat up phase, the char fraction remains equal to zero, so that the mass flow rate (refer, equation (2.42)) drops to zero when the char fraction in the mushy cell becomes equal to 1. Clearly, this behaviour is not physical. Moreover, it makes coupling to CFD gas phase combustion

simulations impossible: depending on the chemistry model applied, this may extinguish the flame (while this might not be the case in reality). Also, it is not easy to reconstruct (or 'guess') the actual pyrolysis gases mass flow rate evolution in time from the results, obtained with the zero-th order temperature field representation. This is revealed in figure 3.4 as well. The only constraint for reconstruction that can readily be imposed, is that the total mass consumed, after char fraction ξ evolution from 0 to 1, must be equal to in both cases, but this constraint does not learn anything about the rates of mass loss. It is thus impossible to reconstruct the dashed line from the solid line results in figure 3.4. This is particularly true during the simulations (when the future is un-known), but even the application of a filter afterwards will not result in the dashed line.

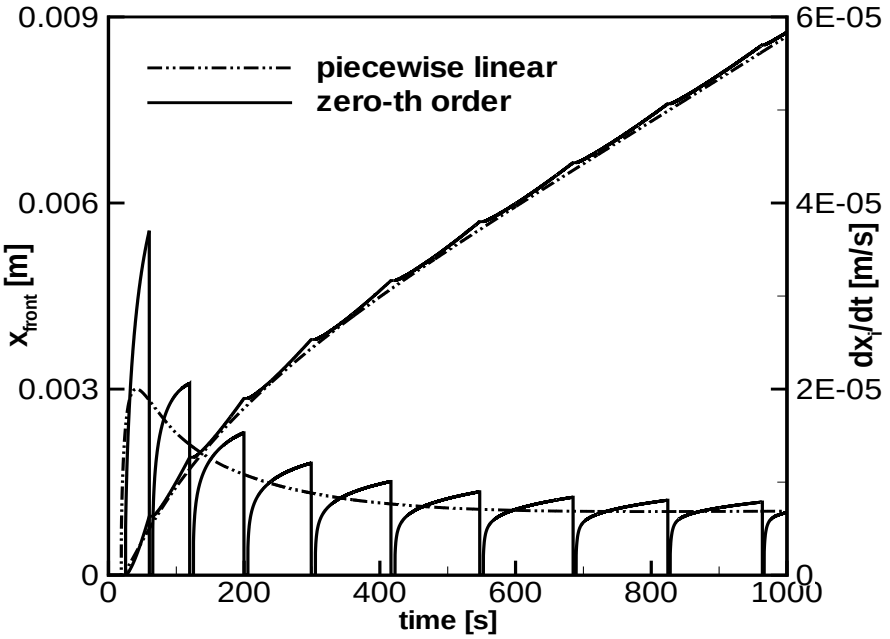

Figure 3.5: Temperature distribution at three positions seen for the zero-th order and piecewise linear enthalpy based model

Figure 3.5 shows the evolution of the position and the speed of the pyrolysis front as function of time. It is observed that during the intervals where the pyrolysis gases mass flow rate drops to zero, the pyrolysis front position does not change in the zero-th order temperature field representation results (horizontal lines). When the mushy cell starts to pyrolyse, the front accelerates, primarily due to a decrease of the conductive heat loss to the neighbouring virgin cell (this neighbouring cell heats up, while the mushy cell remains at pyrolysis temperature with the zero-th order temperature representation). The final velocities in each cell are higher than with the piecewise linear temperature field results (as was already reflected in the mass flow rates, figure 3.4). Clearly, the smooth and continuous behaviour of the latter results are much closer to physical reality.

Figure 3.6 shows the evolution of the surface temperature as function of time. As mentioned, this is in principle an easier quantity than the pyrolysis gases mass flow rates, as there is

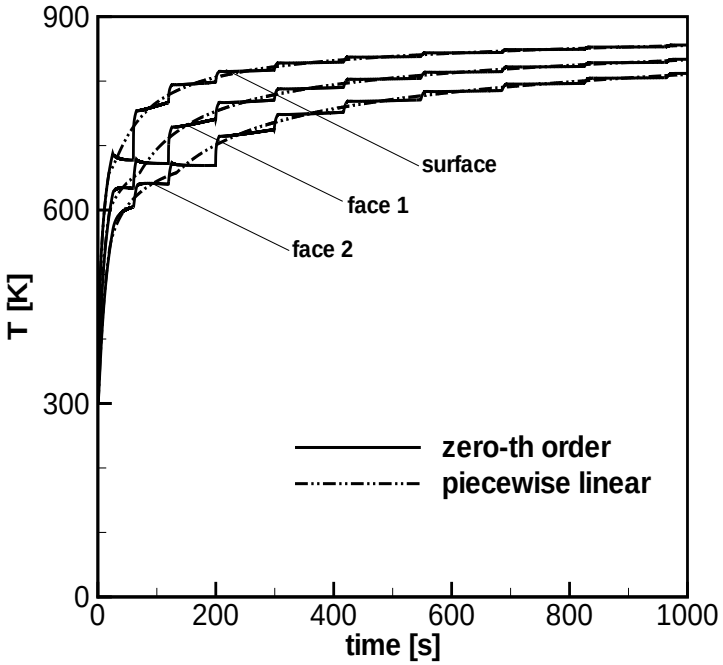

Figure 3.6: Temperature distribution at three positions seen for the zero-th order and piecewise linear enthalpy based model

no derivation with respect to time. Indeed, the curves are close together. A more or less stepwise evolution is observed with the zero-th order representation, though. Indeed, as the pyrolysis mass flow rate drops to zero, there are no convective heat losses with the pyrolysis gases and the material can heat up more rapidly than when there is a continuous flow of pyrolysis gases. Note that there is a decrease in surface temperature during pyrolysis of the first cell with the zero-th order temperature field, is merely due to extrapolation. This was also reported in [109]. Temperatures at different depths also show a similar trend.

3.1.4 Enthalpy-Temperature Distribution

Figure 3.7 shows the instantaneous enthalpy and temperature distribution along the length of the one-dimensional solid at t = 500 s, 1000 s, 1500 s and 2000 s, for simulations with 320 cells. At the pyrolysis front, with temperature T_{pyr}, the (practically) vertical line in enthalpy corresponds to $(\rho_v - \rho_c)\,\Delta Q_{pyr}$. The reference value E=0 J/m^3 corresponds to the situation $T = T_{pyr}$ for virgin material. Here E is the enthalpy equal to $\tilde{\rho}h$. The virgin cells have a negative enthalpy level. The temperature distribution clearly reveals two different gradients at both sides of the sharp front. At all times, the temperature profile at the left side of the front is almost linear. At the right side, in the virgin material, this is not true, but the profile becomes more and more linear as time proceeds.

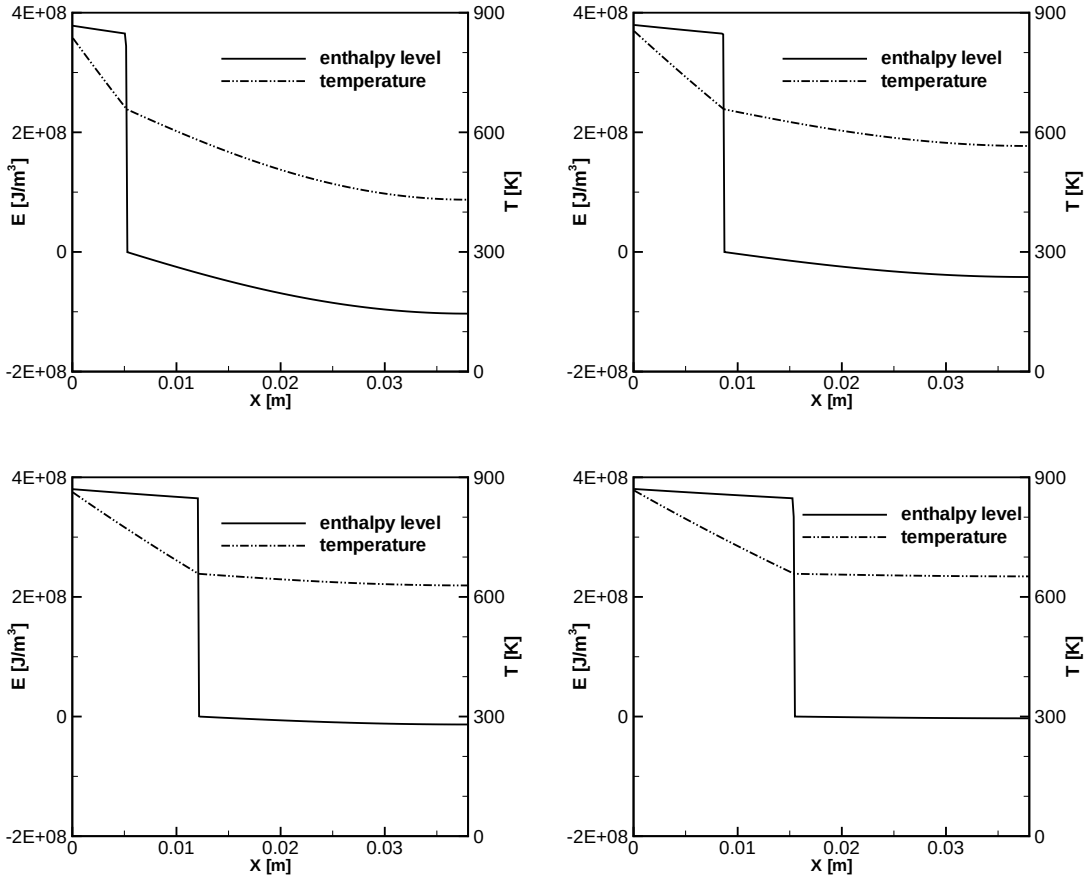

Figure 3.7: Enthalpy and temperature distribution along the length of the one-dimensional solid under study at t=500 s, 1000 s, 1500 s and 2000 s

3.1.5 Validation studies

The enthalpy model is validated to moving grid model. Validation is what we define as the exact principles and boundary condition used much match with the current model under study. Moving grid model uses the same modelling features as the enthalpy based model.

3.1.5a Time dependent behaviour

The following subsections are based on Wasan et al. [119]. The configuration under study is the same as in figure 2.3. An external heat flux is imposed at one side. In flame spread simulations, the incoming heat flux onto the solid material stems from flames and their hot products (radiation and convection). Constant heat fluxes are imposed, in order to avoid uncertainty with respect to heat flux coming from flames. Three challenging cases are considered as in [113].

The intention is to illustrate that the enthalpy based model, with a limited number of computational cells and relatively large time steps, reproduces the numerical reference results, obtained with the more complex moving grid model. Therefore, identical settings are

used for the boundary conditions, model parameters and material properties [55, 113], as discussed next. The properties correspond to filter paper.

Properties	*Value*	*Units*
ρ_v	650.0	kg/m^3
ρ_c	350.0	kg/m^3
c_v	1257.0	J/(kgK)
c_c	1257.0	J/(kgK)
c_{pyr}	1040.0	J/(kgK)
k_v	0.1257	$W/(mK)$
k_c	0.1257	$W/(mK)$

Table 3.4: Thermo-physical properties used in the simulations

External heat loss from the exposed surface, by convection and re-radiation, is taken into account: $\dot{q}''_{net} = \epsilon \dot{q}''_{ext} - h(T_s - T_\infty) - \epsilon\sigma\left(T_s^4 - T_\infty^4\right)$, while the back surface is perfectly insulated and impervious. The heat flux $\dot{q}''_{ext}$ varies in time, as described below.

The convection coefficient is set to h =15 W/m^{2}K , while the emissivity equals ϵ =1.0 and $\sigma = 5.67 \times 10^{-8}$ W/(m^{2}K^4). The pyrolysis temperature is set to $T_{pyr} = 573\ K$ and the heat of pyrolysis equals $\Delta Q_{pyr} = 7.54 \times 10^5$ J/kg. Obviously, the choice of parameters is very important and results can be sensitive to this choice (see below). However, in the present section, focus is on the representation of the mentioned reference results. Therefore, we stick to the exact same settings as in [113]. As initial condition, there is only virgin material at temperature $T = T_{amb}$=300 K. The solid has a thickness of 0.03 m and the material properties used in these simulations are taken from [55]. Numerical simulation were performed on a cartesian grid of 40 cells and with a physical time step equal to 0.5 s.

1. Case 1: Sudden increase of heat flux at start of pyrolysis
   The initially imposed external heat flux is 30 kW/m^2. Figure 3.8 (top) shows the mass flow rate of the pyrolysis gases in time, bottom figure shows the intensity of external heat flux applied on the front surface of the solid in time. After 12.0 s, reported as the onset of pyrolysis in [113], there is a sudden increase to 50 kW/m^2. This sudden rise represents the additional heat flux due to combustion of the volatiles in the gas phase as they leave the solid. Figure 3.8 reveals good agreement with the integral and moving grid simulation results.
2. Case 2: Sudden increase of heat flux at fixed time
   In this case, the initially imposed external heat flux of 30 kW/m^2 is suddenly increased to 50 kW/m^2 at t=60 s. This resembles e.g. additional heat flux due to a distant object catching fire or due to flashover. Figure 3.9 reveals that there is again good agreement of the present model with the moving grid results. In particular, the unphysical drop in the mass flow rate, as observed with the integral model of e.g. [111], is not seen here. Also, the second peak in the mass flow rate is predicted quite accurately. There is no overshoot as in the integral model.
3. Case 3: Sudden increase and fall of external heat flux
   The initially imposed external heat flux is 30 kW/m^2. At t=12.0 s, there is a sudden increase to 50 kW/m^2. At t=41 s, the external heat flux is suddenly decreased again to 30 kW/m^2. This models e.g. variable exposure to flames or a instance when the external heat flux is switched off. Figure 3.10 shows again good agreement of

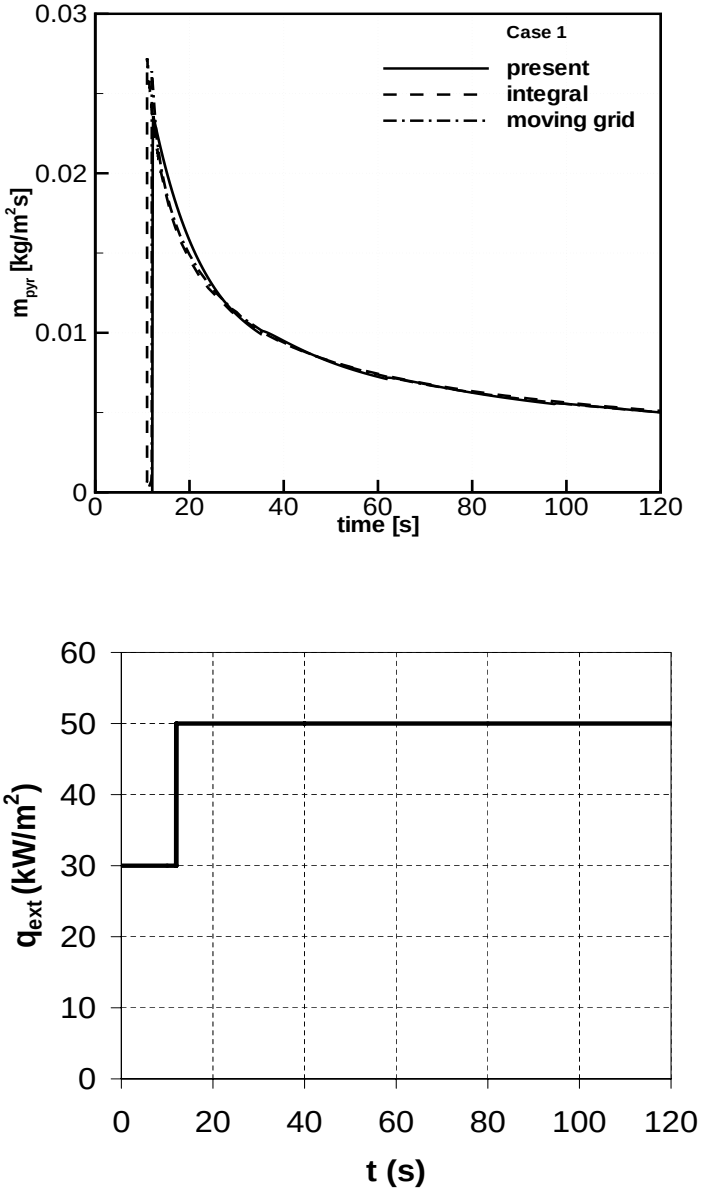

Figure 3.8: Case 1: Evolution of pyrolysis gases mass flow rate in time when sudden increase of heat flux is applied at start of pyrolysis

the present model with the moving grid reference results. The unphysical rise in mass flow rate with the integral model (at t=41 s) is again not encountered with the present enthalpy based model and the drop in the mass flow rate is well captured (no undershoot).

4. Case 4: Smooth increase and fall of external heat flux
   Finally, instead of applying a sudden rise and fall in the external heat flux, a sinusoidal increase to 50 kW/m^2 followed by a decrease again to 30 kW/m^2 is applied. The exact

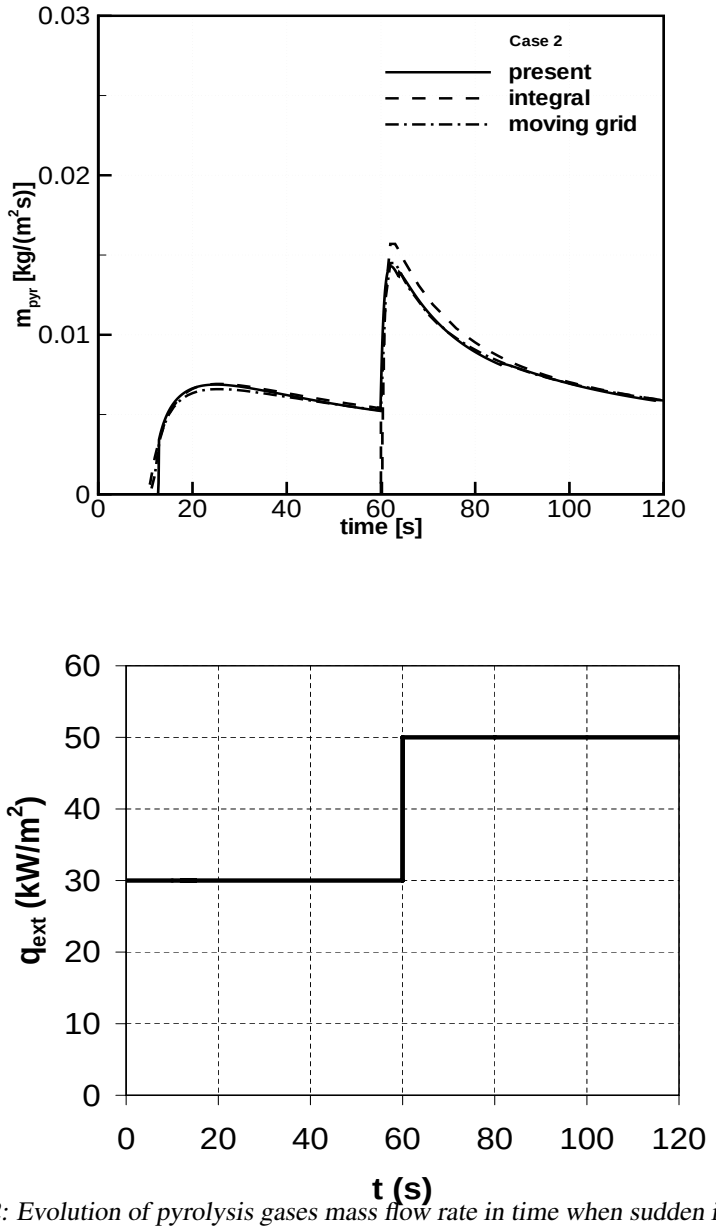

Figure 3.9: Case 2: Evolution of pyrolysis gases mass flow rate in time when sudden increase of heat flux is applied at fixed time

formula is given below:

$$\begin{aligned}
0 \le t \le 12\ s;\ t \ge 41\ s: &\qquad \dot{q}''_{ext} = 30\ \mathrm{kW/m^2} \\
12 \le t \le 21\ s: &\qquad \dot{q}''_{ext} = \left(40 + 10 \cdot \sin\frac{(t-16)}{10}\pi\right)\ \mathrm{kW/m^2} \\
21 \le t \le 31\ s: &\qquad \dot{q}''_{ext} = 50\ \mathrm{kW/m^2} \\
31 \le t \le 41\ s: &\qquad \dot{q}''_{ext} = \left(40 - 10 \cdot \sin\frac{(t-36)}{10}\pi\right)\ \mathrm{kW/m^2}
\end{aligned} \tag{3.3}$$

Figure 3.11 confirms once again that the moving grid model results are well reproduced. The error in the peak value of the mass flow rate is about 4.5%. The peak mass flow

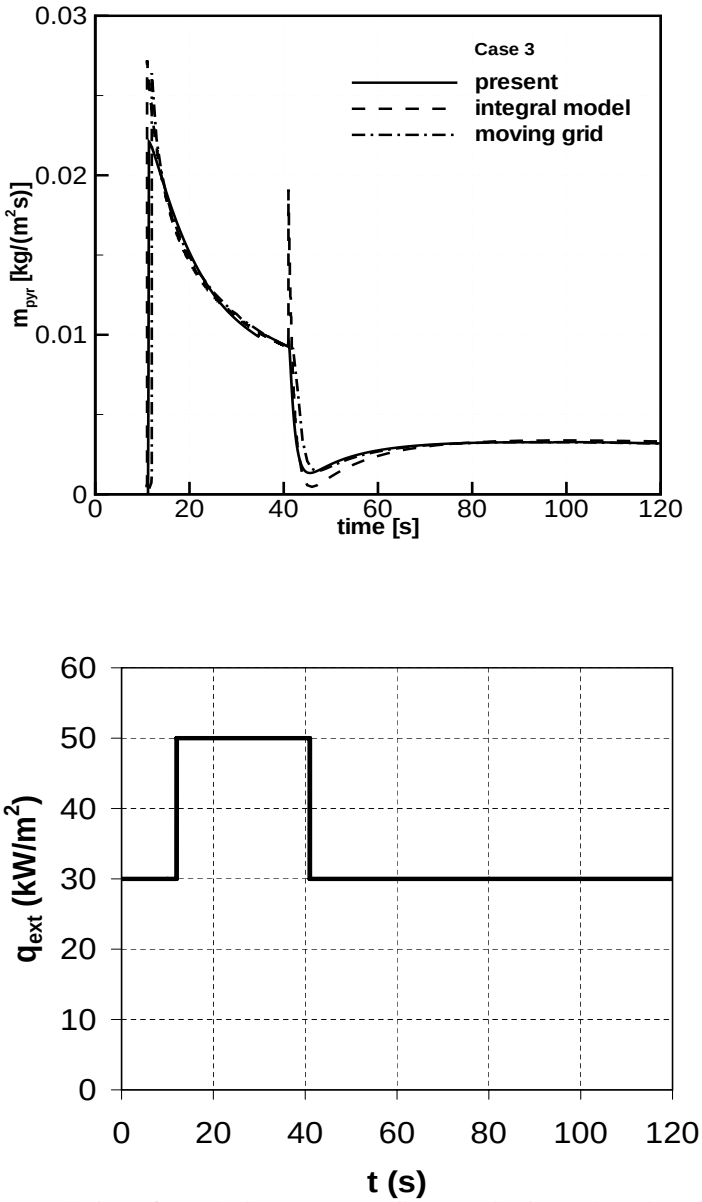

Figure 3.10: Case 3: Evolution of pyrolysis gases mass flow rate in time when there is a sudden increase and fall of heat flux

rate is obtained at t=19.15 s with the present enthalpy based model (in comparison to t=20.15 s in the moving grid model results of [113]). Also the drop is captured well again.

But, the integral model still suffers from the over and under-prediction during rise and fall in the external heat flux. In integral model, the variation in boundary conditions immediately affects the mass flow rate leading to unphysical results. The good agreement for Case 4 is not surprising, as there was already good agreement in Case 1 to 3, which is more extreme, thus more challenging, than the smooth evolutions of Case 4.

From the above tests one can see that integral model has some deficiencies. When external heat flux imposed on the solid is smooth and constant, the integral model shows good

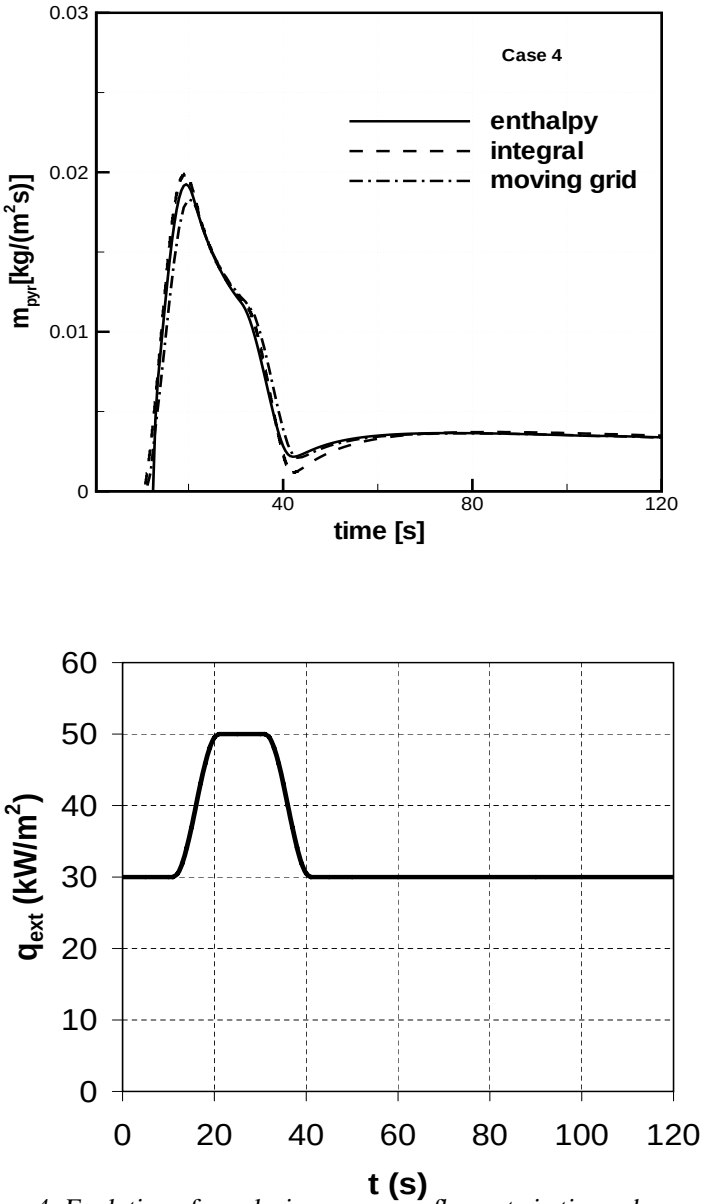

Figure 3.11: Case 4: Evolution of pyrolysis gases mass flow rate in time when applied with a smooth increase and fall of heat flux

results. But when there is a sudden rise or fall in the external heat flux, integral model suffers to give reliable results for mass flow rate of pyrolysis gases. This is due to integral model formulation: sudden changes at the boundary are immediately felt on the complete temperature profile of the solid, and influences the mass flow rate as well.

The Sensitivity of the results to numerical aspects is again discussed, for (Case 2), based on:

$$\frac{\|\dot{m}''_{\mathrm{g,max}} - \dot{m}''_{\mathrm{g,max,moving\ mesh}}\|}{\|\dot{m}''_{\mathrm{g,max,moving\ mesh}}\|} \tag{3.4}$$

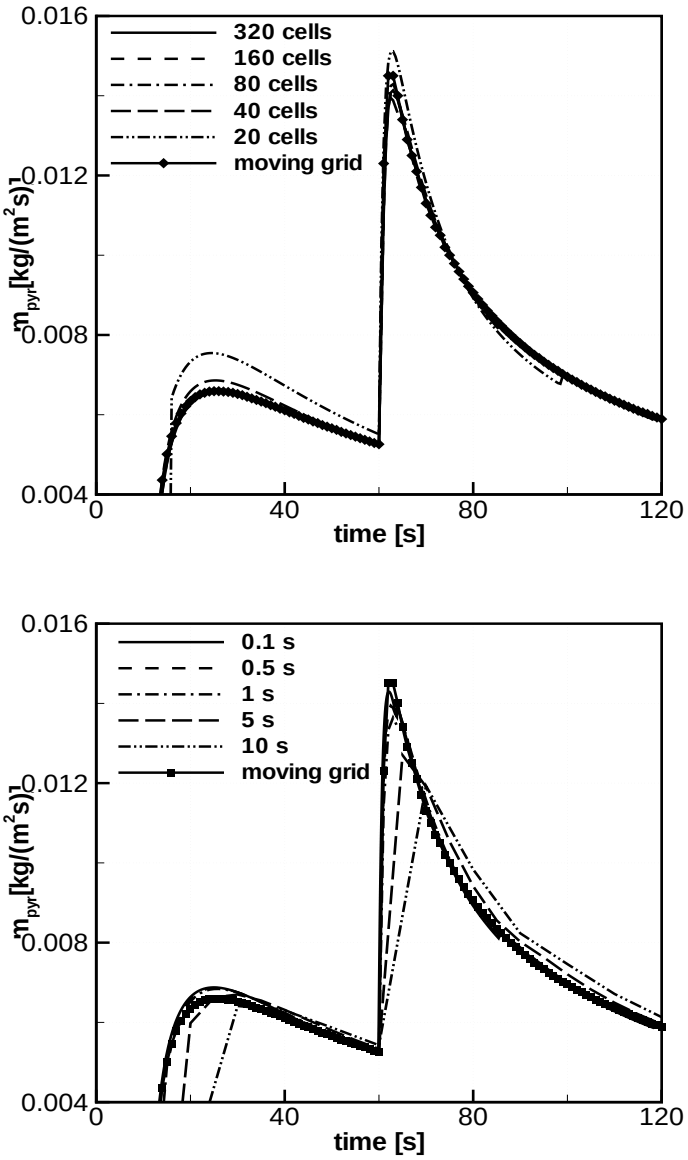

Figure 3.12: Evolution in time of pyrolysis gases mass flow rate for case 2: influence of computational cell size (top, with Δ t=0.5 s) and physical time step size (bottom, with 40 cells)

Figure 3.12 (top) reveals the effect of the number of cells on the mass flow rate evolution in time. Clearly, the differences are small, except for the low number of cells. This is true because it takes a long time to heat the solid from ambient temperature (T_∞) to pyrolysis temperature (T_{pyr}). The error analysis in table 3.5 quantifies on this observation, reporting the maximum mass flow rate and the relative error, compared to the results of the moving grid model of [113]. The maximum value for first peak $\dot{m}''_{\mathrm{g,max,1}}$ and second peak $\dot{m}''_{\mathrm{g,max,2}}$ are estimated by constructing a parabola through the obtained discrete maximum value and the value obtained at the previous and subsequent time step. The errors remain below 5%, except for the coarsest mesh. This implies that the model and method are very robust with respect to the number of computational mesh cells.

The bottom figure 3.12 reveals the effect of the physical time step size on the results for the

Cells	$\dot{m}''_{g,max,1}$	%error	$\dot{m}''_{g,max,2}$	%error
Moving mesh [113]	0.00659	0	0.0145	0
320	0.00657	0.28	0.0141	2.50
160	0.00656	0.43	0.0142	2.24
80	0.00664	0.77	0.0143	1.42
40	0.00686	4.10	0.0139	3.81
20	0.00754	14.51	0.0151	4.32

Table 3.5: Effect of number of cells on maximum flow rate value for case 2. Time step equal to 0.5 s.

time step size [s]	$\dot{m}''_{g,max,1}$	%error	$\dot{m}''_{g,max,2}$	%error
Moving mesh [113]	0.00659	0	0.0145	0
0.1	0.00687	4.35	0.0143	1.42
0.5	0.00686	4.10	0.0139	3.81
1.0	0.00683	3.77	0.0136	5.92
5.0	0.00670	1.70	0.0134	7.83
10.0	0.00687	4.36	0.0122	15.78

Table 3.6: Effect of time step size on maximum flow rate value. Number of cells equal to 40

configuration with 40 cells. Except for very large time steps, deviations between the curves are below 10% (Table 3.6).

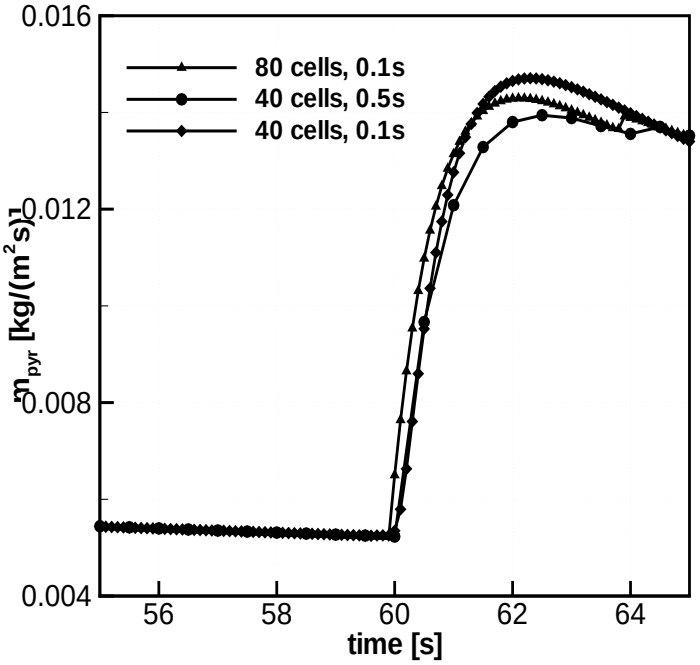

Figure 3.13: Zoom of evolution in time of pyrolysis gases mass flow rate for case 2 around the time where the external heat flux suddenly rises

From table 3.5 and table 3.6 it is clear that quite large time steps can be taken with the present model and method, without substantial loss in accuracy. In combination with the robustness with respect to the number of computational cells, this property make the enthalpy based model and method appealing for coupling to CFD simulations, in particular in more dimensional configurations.

Figure 3.13 is the zoom of 3.9, when the external heat flux suddenly rises. An interesting feature of the integral model: there is a drop in the mass flow rate [113]. This is not observed for the enthalpy based model, even for large cell size and small time step. The test is conducted for three different cases (a: $\Delta x = 3.75 \cdot 10^{-4}$ m and Δt=0.1 s; b: Δx=7.5 $\cdot 10^{-4}$ m and $\Delta t = 0.1$ s; c: $\Delta x = 7.5 \cdot 10^{-4}$ m and $\Delta t = 0.5$ s).

3.1.6 Influence of solid thickness

The effect of the solid thickness, as in [110] is discussed. The thickness of the solid is varied from 2mm (thermally thin material) to 50 mm (thermally thick). The boundary conditions are fixed: the front surface is exposed to a constant externally imposed heat flux of 50 kW/m^2 and the back surface is perfectly insulated.

Properties	Value	Units
ρ_v	600.0	kg/m^3
ρ_c	60.0	kg/m^3
c_v	2500.0	J/(kgK)
c_c	2500.0	J/(kgK)
k_v	0.36	W/(mK)
k_c	0.23	W/(mK)
c_{pyr}	0.0	J/(kgK)

Table 3.7: Thermo-physical properties of Particle Board

The thermo-physical properties are now chosen exactly the same as in [110] (corresponding to particle board) again in order to illustrate representation of the numerical reference results are in table 3.7. The model parameters, convection heat transfer coefficient h = 5.0 W/(m^{2}K), T$_{pyr}$ = 648 K, and $\Delta Q_{pyr} = 8.7 \cdot 10^5$ J/kg. The emissivity $\epsilon = 1.0$ and $\sigma = 5.67 \cdot 10^{-8}$ W/(m^{2}K^4).

Figure 3.14 confirms the good agreement with the moving grid results over the entire range of thicknesses. Clearly, onset of pyrolysis occurs earlier for the smaller thickness, due to more rapid heating of the material up to the pyrolysis temperature. For thickness larger than 10 mm, the start of pyrolysis remains practically unchanged. The heating process is then as if the solid were of infinite thickness.

For the thermally thin materials (L<10 mm), a single peak is observed in the mass flow rate. The peak is higher for the smaller thicknesses, due to the more rapid heating and thus faster pyrolysis front motion.

For the thermally thick materials, two peaks are observed. The second peak is due to the

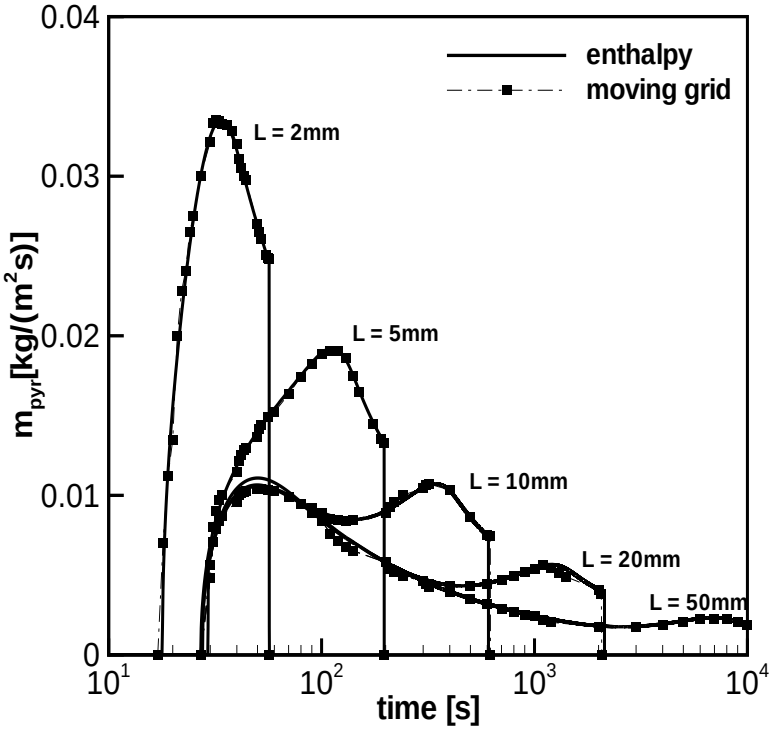

Figure 3.14: Mass flow rate of pyrolysis gases (different material thicknesses)

so called back effect [102]. Note that the first peak is quasi-identical for all thermally thick materials, as they behave as infinitely thick materials during that stage. The duration of the pyrolysis obviously depends on the total mass of the solid and thus directly on the solid thickness.

Figure 3.15 shows the temperature distribution in the solid at different time level before the start of pyrolysis process for three different thicknesses (L=10 mm, 5 mm and 2 mm). For thermally think materials (top and middle row), the back surface has no influence on the growing penetration depth, as seen in figure 3.29. But for thermally thin materials, the back surface boundary condition has a strong influence on the penetration depth, $\sqrt{\alpha t}$. This is seen in the figure 3.15, bottom row. Also, the solid attains an uniform temperature before pyrolysis begins, seen in the bottom left figure.

3.1.7 Effect of boundary condition on the back side

Another numerical test, the back side boundary condition is varied, describing the convective heat loss as follows:

$$\dot{q}''_{bs} = h_{bs} \left(T_{bs} - T_{amb} \right) \tag{3.5}$$

Unless mentioned otherwise, the same model parameters and material properties as in the previous section are used here. Emissivity ϵ at the back surface is set equal to zero, as

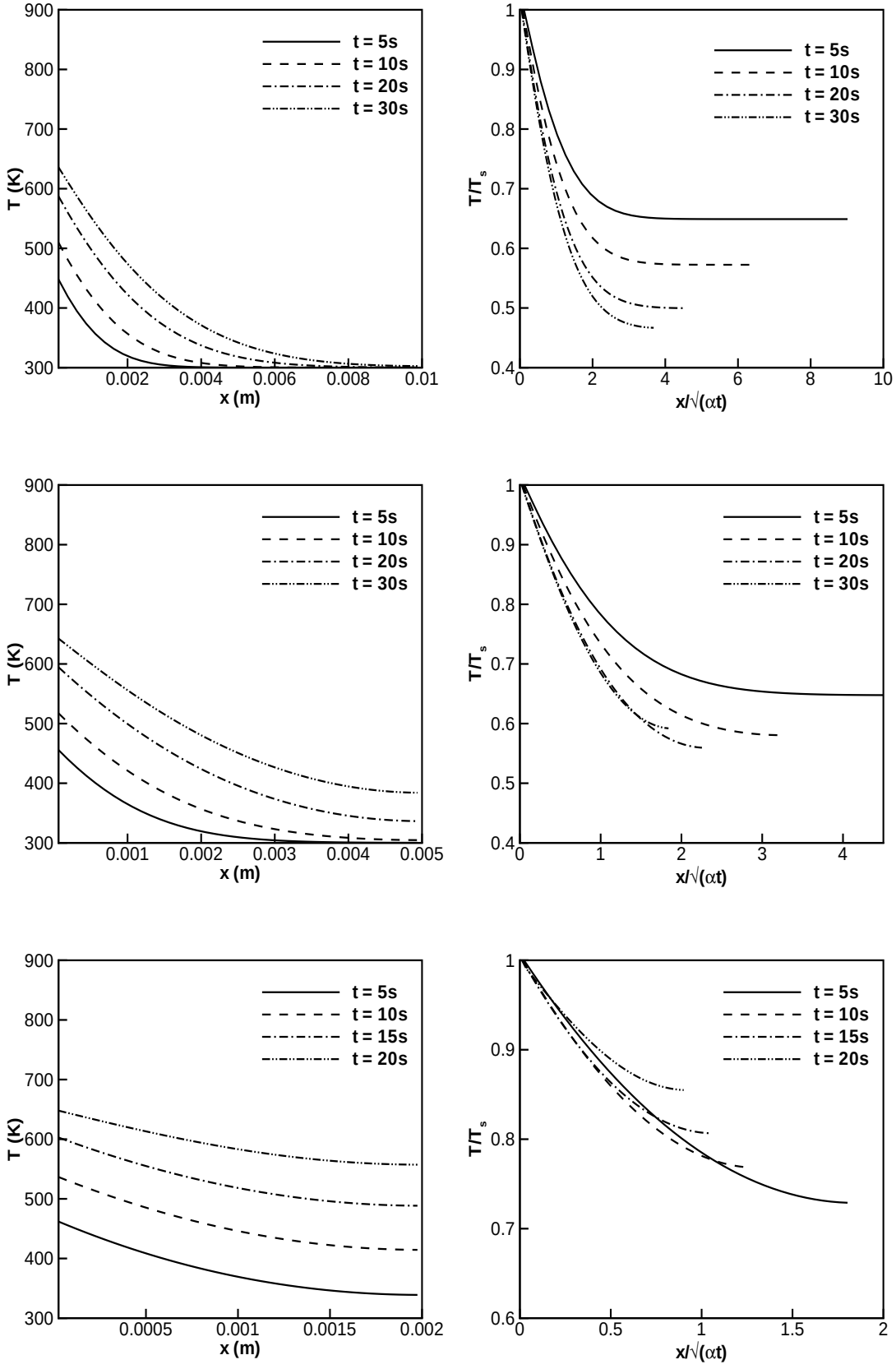

Figure 3.15: Left: Temperature distribution along the length of the solid; Right: Dimensionless temperature distribution along the dimensionless length at different time level; Top row: thickness=10 mm; Middle row: thickness=5 mm; Bottom row: thickness=2 mm

typically the temperature T_{bs} is not high.

Before discussing the results, a steady state analysis of the equilibrium situation is performed. In that case, the net incoming heat flux at the front surface equals conduction through the solid material, as well as (convective) heat losses at the back surface. In the assumption that the steady state situation is complete charring of the material, this reads:

$$\begin{aligned} &\dot{q}''_{ext} - \epsilon\sigma\left(T_{s,eq}^4 - T_{amb}^4\right) - h_s \cdot (T_{s,eq} - T_{amb}) \\ &\quad = k_c \cdot \frac{T_{s,eq} - T_{bs,eq}}{L} = h_{bs} \cdot (T_{bs,eq} - T_{amb}) \end{aligned} \tag{3.6}$$

These are two equations (3.5 and 3.6) for two unknown variables ($T_{s,eq}$ and $T_{bs,eq}$). The last identity shows that, in the relation between the two surface temperatures, the Biot number[1] appears, based on the back surface convection coefficient:

$$T_{s,eq} = T_{bs,eq} + \frac{h_{bs}L}{k_c} \cdot (T_{bs,eq} - T_{amb}) \tag{3.7}$$

Elimination of $T_{s,eq}$ in 3.6 yields a single equation for $T_{bs,eq}$. The solution of this equation depends on h_s, h_{bs} and ϵ. Figure 3.16 shows the result for $\epsilon = 1$ and fixed h_s (top) or fixed h_{bs} (bottom). Obviously, if $T_{bs,eq} < T_{pyr}$, the assumption of complete charring of the material is incorrect.

Figure 3.16 confirms that, when h_{bs}=0 W/m^{2}K, i.e. perfect insulation at the back surface, the steady state situation yields $T_{s,eq} = T_{bs,eq}$. The higher the convection coefficient h_s, the lower the equilibrium temperature due to the lower net incoming heat flux. The left picture further reveals that the difference between the back surface temperature and the front surface temperature increases as the heat losses at the back surface increase (higher h_{bs}). The dashed line at $T = T_{pyr} = 648$ K reveals that the assumption of complete charring is no longer fulfilled for large values of h_{bs} (e.g. $h_{bs} > 10.2$ W/(m^{2}K) for $h_s = 0$ W/(m^{2}K)). The right picture of fig. 3.16 shows that complete charring is only possible for sufficiently low values of hbs. For $h_{bs} = 10$ W/(m^{2}K), curve c, it is seen that complete charring only happens when $h_s < 1$ W/(m^{2}K).

The numerical simulation results as obtained with the present pyrolysis model are discussed. Note that no case dependent adjustments are made to the model whatsoever. This is a particularly appealing model feature. First, the convective heat transfer coefficient h_{bs} is varied from 0 (perfect insulation) to 20 W/m^{2}K, while at the front surface $h_s = 0$ W/m^{2}K and $\epsilon = 1$ [110]. The material properties are the same as in the previous section. The solid thickness equals 20 mm. A constant heat flux of 50 kW/m^2 is imposed.

Figure 3.17 (top) confirms the agreement with the moving grid model results. When the pyrolysis front approaches the back boundary, the second peak (back effect) is only seen for sufficiently low values of the back boundary convective heat transfer coefficient. Indeed, there is no piling up of heat when heat losses through the back surface are too high.

In [110], it is discussed that the integral model suffers the deficiency that mass flow rate curves cross each other when h_{bs} is varied. This unphysical feature is not observed with the present model, as illustrated in the zoom (figure 3.17, bottom).

[1] Biot number (named after french physicist Jean-Baptiste Biot) is the ratio of the conductive (internal) resistance to heat transfer to the convective (external) resistance to heat transfer [124].

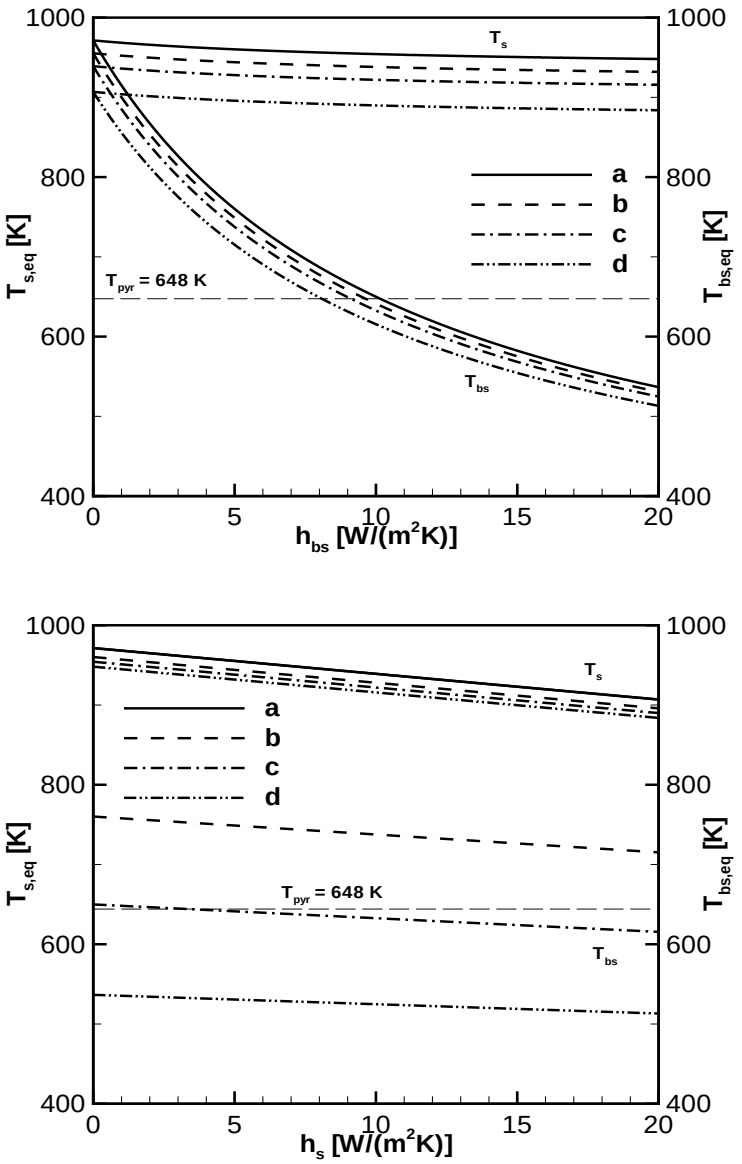

Figure 3.16: Steady state front and back surface temperature in case of complete charring of the material. Top: fixed h_s; Bottom: fixed h_{bs}. Values: a: 0 W/m^{2}K; b: 5 W/m^{2}K; c: 10 W/m^{2}K; d: 20 W/m^{2}K;

Figure 3.18 (top) shows the effect of h_{bs} on the front and back surface temperatures (T_s and T_{bs}). Obviously, there is little effect on T_s. Note the onset of pyrolysis at t=27 s, in agreement with the top picture of fig. 3.18. As h_{bs} increases, Tbs increases less and less rapidly, due to relatively higher heat losses through the back surface. Interestingly, differences become visible for t >250 s, which is also the period where differences become visible in the pyrolysis gases mass flow rates fig. 3.17(bottom). In other words, from t = 250 s onwards, the back surface boundary condition affects the pyrolysis process.

Note here, that for $h_{bs} < 10.2$ W/m^{2}K, where complete charring of the material should happen (see above), the steady state temperatures of fig. 3.16 is indeed predicted. For

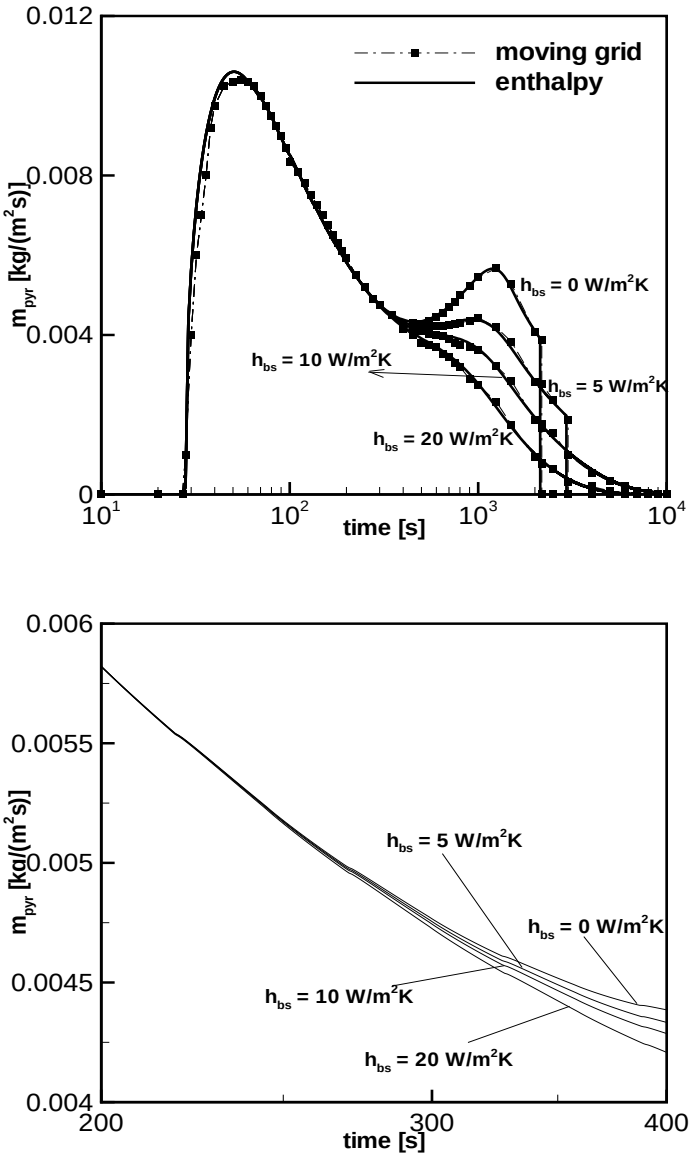

Figure 3.17: Influence of back surface boundary condition (h_{bs}) and fixed front surface boundary condition ($h_s = 10$ W/m^{2}K); Top: mass flow rate of pyrolysis gases; Bottom: t=200 s - 400 s

higher values of h_{bs}, the steady state analysis is no longer applicable and indeed other steady state temperatures are predicted as well as the ending of the pyrolysis process (see below).

The bottom picture of fig. 3.18 reveals the position of the pyrolysis front as function of time. Obviously, the higher h_{bs}, the lower the pyrolysis mass flow rate (see above) and, correspondingly, the slower $x_{f,pyr}$ increases in time. Interestingly, for $h_{bs} = 20$ W/m^{2}K, the pyrolysis process stops after a while: $x_{f,pyr}$ does not increase any more for $t > 10000$ s. In other words, an equilibrium situation is met. The situation is then as follows: $T_{s,eq} = 946$ K, $x_{f,eq} = 0.0134$ m and $T_{bs,eq} = 555$ K. Thus, the net heat flux into the solid material equals: $(50000 - 1 \times 5.67 \times 10^{-8}(946^4 - 300^4)) \approx 5100$ W/m^2). This indeed corresponds to the conduction through the char material (approx. equal to 0.23 $\times$ (946-648)/(0.0134-0)), the

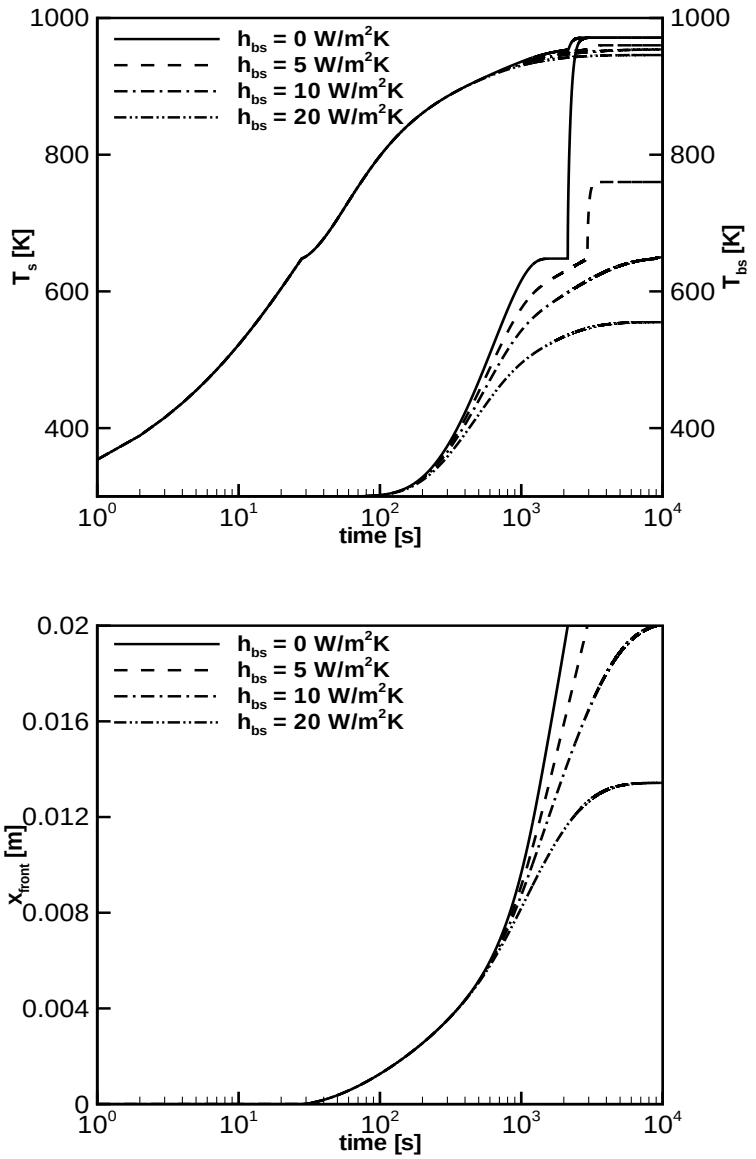

Figure 3.18: Influence of back surface boundary condition (h_{bs}) and fixed front surface boundary condition ($h_s = 10$ W/m^{2}K); Top: front and back surface temperature T_s and T_{bs}; Bottom: pyrolysis front position x_f

conduction through the virgin material (approx. equal to 0.36 × (648-555)/(0.02-0.0134) and the convective heat losses at the back surface 20 × (555-300)). It is a very appealing model feature that the stopping of the pyrolysis process is automatically predicted when there is insufficient net incoming heat flux.

3.1.8 Effect of boundary condition on the front side

Figure 3.19 and 3.20 shows the results when the front boundary condition is varied, while keeping the back boundary condition fixed ($h_{bs} = 10$ W/m^{2}K). Figure 3.20 (top) shows the effect of h_{bs} on the front and back surface temperatures (T_S and T_{bs}). Obviously, the effect

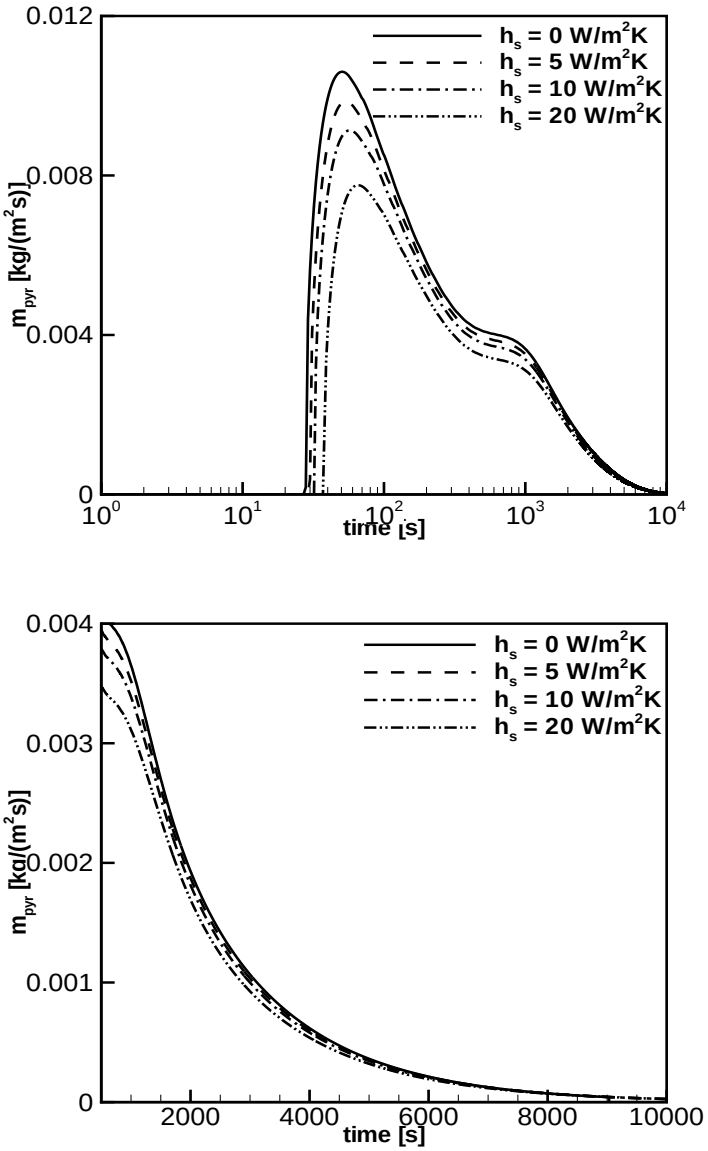

Figure 3.19: Influence of front surface boundary condition (h_s) and fixed back surface boundary condition (h_{bs}=10 W/m^{2}K); mass flow rate of pyrolysis gases (top); zoom (t=500 s-1000 s, bottom);

of the lower net incoming heat flux (due to relatively higher convective heat losses at the front surface for higher h_s values), is that T_s rises less rapidly. Consequently, the onset of pyrolysis occurs later for higher values of h_s. Also, the pyrolysis gases mass flow rate in general decreases, as the front moves less rapidly (figure 3.20, bottom). This effect becomes negligible after a relatively long time. The bottom right picture, showing the position of the pyrolysis front as function of time, confirms that, with h_{bs}=10 W/(m^{2}K), charring is only complete for the lowest h_s values. When pyrolysis is incomplete, a similar energy balance is confirmed as described above for figure 3.17 and 3.18.

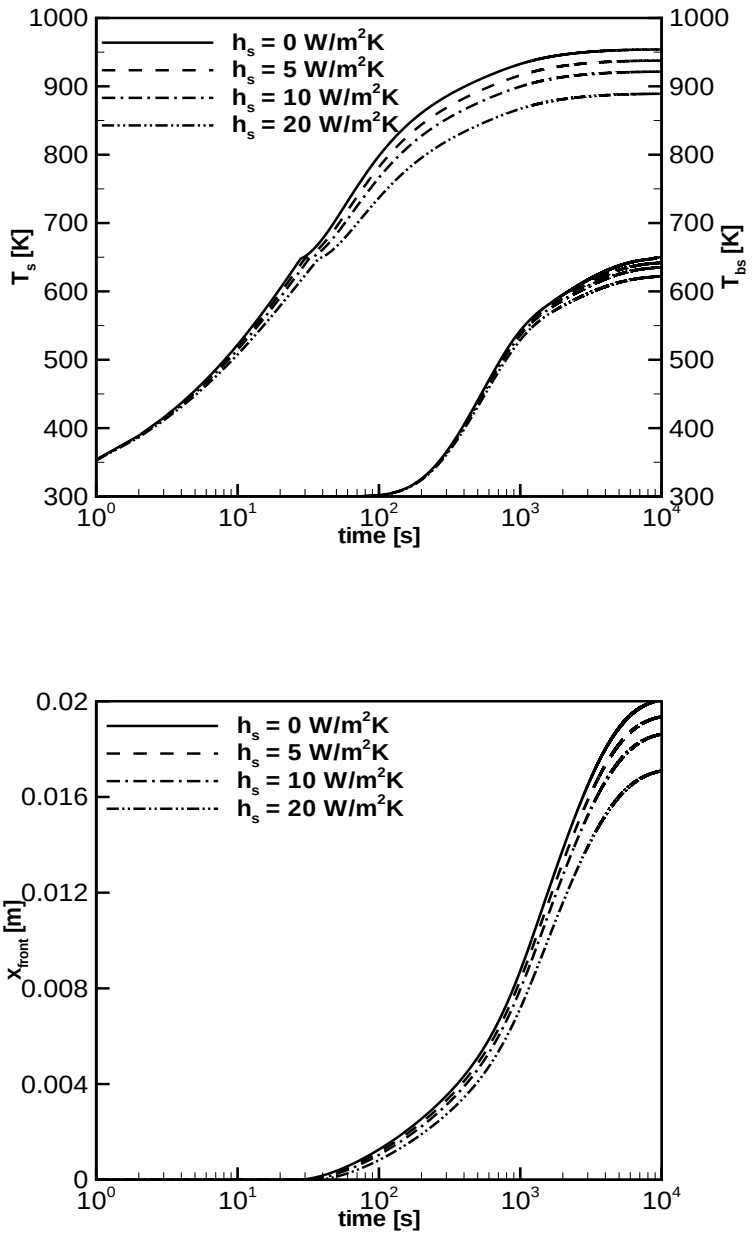

Figure 3.20: Influence of front surface boundary condition (h_s) and fixed back surface boundary condition (h_{bs}=10 W/m^{2}K); front and back surface temperature T_s and T_{bs}(top); pyrolysis front position x_f (bottom)

3.1.9 Experimental test case

Enthalpy based model for pyrolysis of charring materials is tested with experimental results carried using cone calorimeter apparatus reported in [38]. The experiments were conducted on a 2.54 cm thick plywood sample. The imposed extrernal heat flux equals 50 kW/m^2. The sample was placed in an inert atmosphere, which prevents the ignition of the pyrolysis gases in the gas phase, so that there is no additional heat flux. Numerical simulations were performed using 40 cells and a physical time step size equal to 1.0 s. The thermo-physical material properties (table 3.8) are taken from [109].

Properties	Value	Units
ρ_v	462.0	kg/m^3
ρ_c	60.0	kg/m^3
c_v	4000.0	J/(kgK)
c_c	2000.0	J/(kgK)
k_v	0.60	$W/(mK)$
k_c	0.45	$W/(mK)$
c_{pyr}	0.0	J/(kgK)

Table 3.8: Thermo-physical properties of Plywood

The model parameters used in the simulations are $\Delta Q_{pyr} = 4.0 \times 10^5$ J/kg, T_{pyr}=623 K, $\epsilon = 1.0$ at the front surface and ϵ =0.0 at the back surface. The value of Stefan-Boltzmann constant is $\sigma = 5.67 \cdot 10^{-8}$ W/(m^{2}K^4).

Figure 3.21 shows the result of the mass flow rate obtained with the enthalpy based model using the above properties, compared to the experiments. As mentioned by Yan et al. [35], the back side boundary condition in the experiments was not fully specified in [38], on the sample holder and rear boundary condition. For simplicity, a perfect insulation is assumed at the back surface (h_{bs}=0 W/m^{2}K). At the start, a simple settings are tested. Afterwards, the boundary conditions are varied, by applying a non-zero heat transfer coefficient at the back surface and front surface like before.

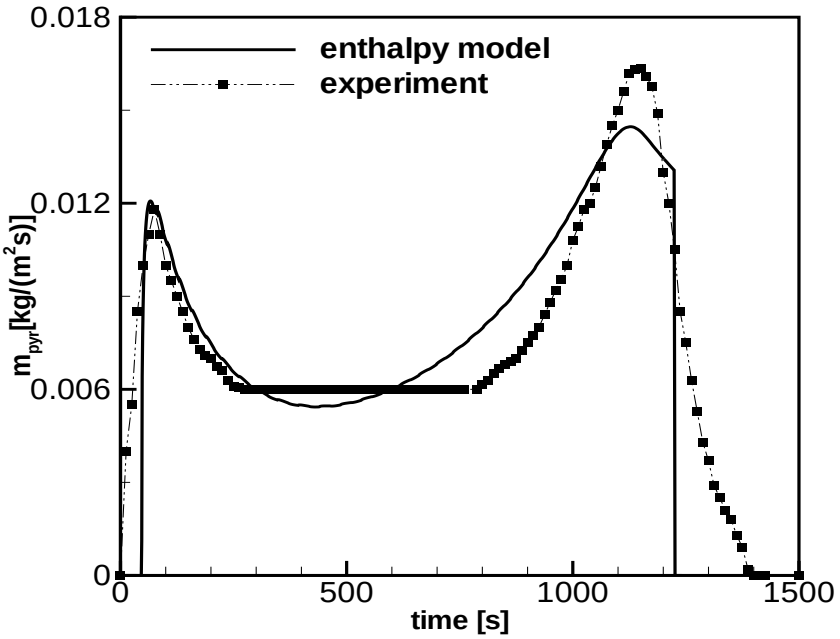

Figure 3.21: Evolution in time of pyrolysis gases mass flow rate (experimental case)

In figure 3.21, the model cannot capture the immediate onset of pyrolysis, as it needs to heat up to T_{pyr} at the front surface. Yet, the peak around 100 s is very well captured. The

subsequent decrease is also very well reproduced as the pyrolysis front moves inside the solid and the char layer develops. Also the second peak around 1200 s is well captured. The end of the pyrolysis process is seen with the drop in the mass flow rate of pyrolysis gases from the solid. This is also properly captured by the enthalpy based model, but the pyrolysis process suddenly ends.

3.1.10 Effect of model parameters

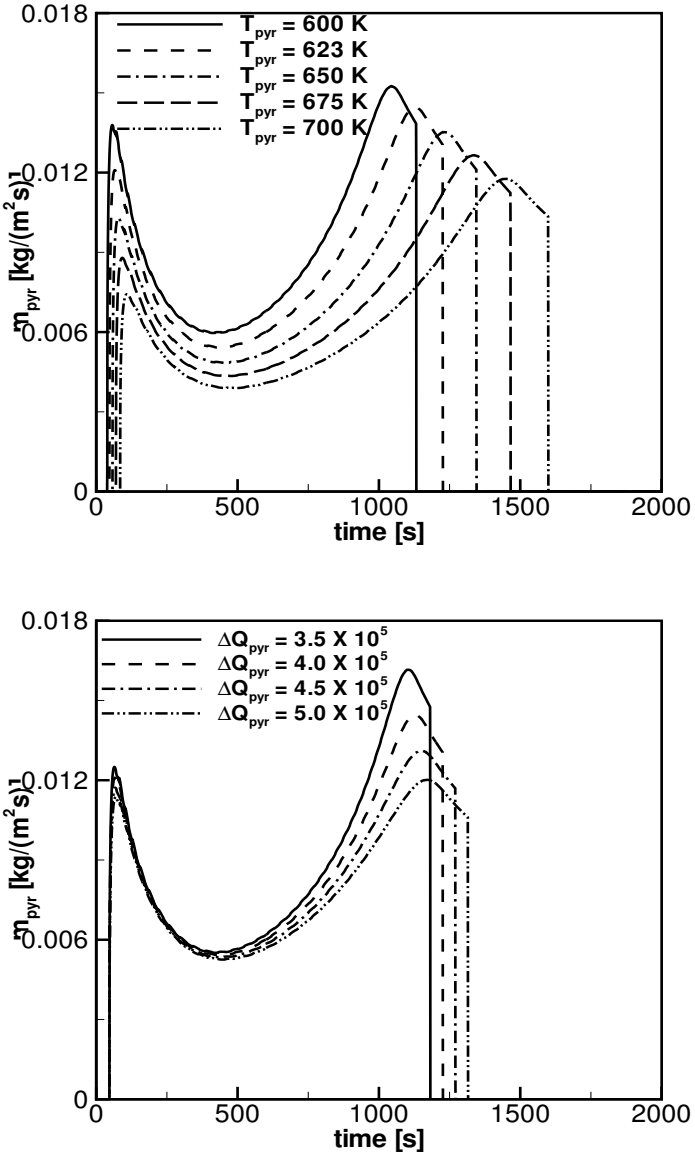

Figure 3.22: Effect of pyrolysis temperature (with $\Delta Q_{pyr} = 4 \times 10^5$ J/kg, top) and heat of pyrolysis (with $T_{pyr} = 623\ K$, bottom)

The effect of different model parameters e.g. pyrolysis temperature T_{pyr}, heat of pyrolysis

ΔQ_{pyr} and emissivity ϵ on the mass flow rate of pyrolysis gases is discussed. Influence of pyrolysis temperature T_{pyr} has a immediate effect on the mass flow rate of pyrolysis gases shown in figure 3.22, top . Obviously the higher the pyrolysis temperature, the longer it takes for pyrolysis to begin. Indeed, the solid takes time to reach the pyrolysis temperature T_{pyr}. Also, the peak becomes lower, due to slower pyrolysis front motion: more heat is conducted away from the front to the virgin material (equation (2.21)), due to steeper temperature gradients (as the pyrolysis temperature is higher). The duration for the entire pyrolysis process is increased with increase in the value of pyrolysis temperature (T_{pyr}) with a lower second peak value of mass flow rate of pyrolysis gases.

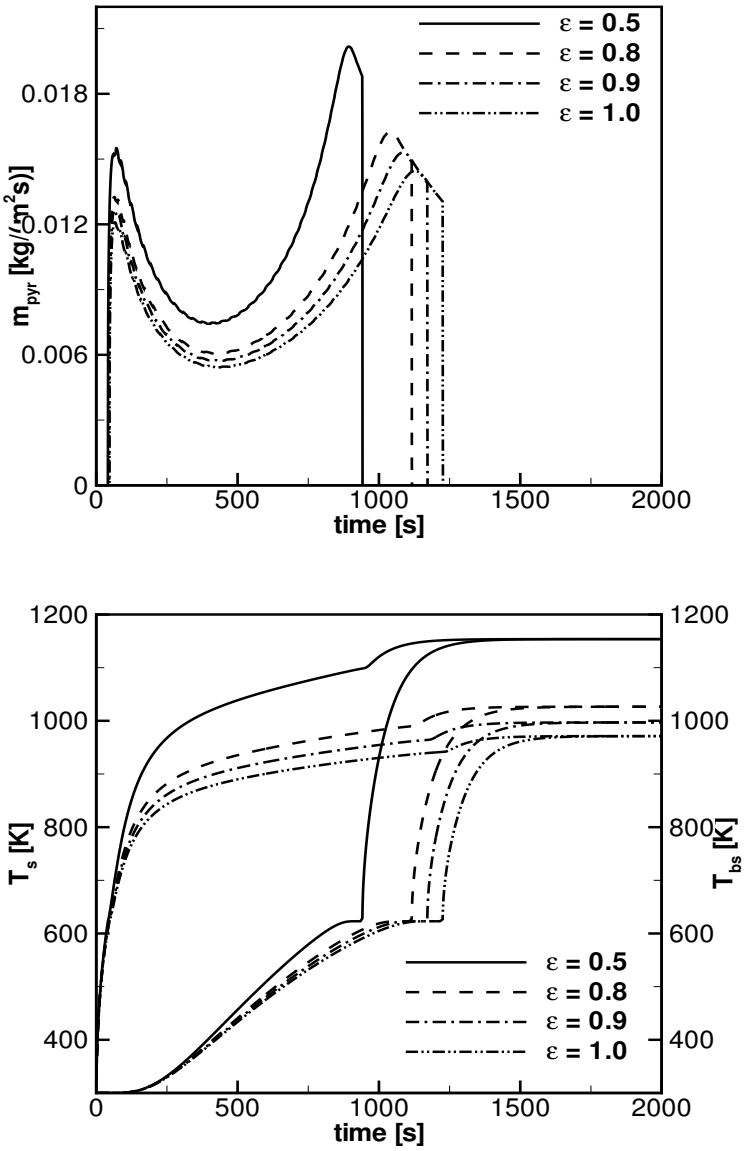

Figure 3.23: Effect of emissivity on pyrolysis gases mass flow rate (top) and front and back surface temperature (bottom)

The influence of the heat of pyrolysis ΔQ_{pyr} is less important (figure 3.22, bottom). Obvi-

ously, the mass flow rate increases as ΔQ_{pyr} is lower, as less heat is required for the pyrolysis process. The onset of pyrolysis is independent of ΔQ_{pyr} as this only depends on the heating up stage up to T_{pyr}. The role of ΔQ_{pyr} is more prominent only during the pyrolysis process phase, discussed in section 2.2. The second peak value for mass flow rate drops with increase in the value of heat of pyrolysis (ΔQ_{pyr}).

Figure 3.23 shows the influence of front surface emissivity ϵ and the back surface convective heat transfer coefficient h_{bs}. Top figure reveals that the mass flow rate is lower for higher ϵ, as the net heat flux into the material decreases. Heat losses are higher, than heat available for pyrolysis process. Due to higher loss at the front surface, the second peak value drops with the increase in the emissivity (ϵ). Obviously, this also reduces the front and back surface temperatures (figure, bottom). The front surface temperature is mostly affected by the emissivity, applied on the front surface, has negligible effect on the back surface temperature T_{bs}. After the solid has turned to char, the front and back surface temperatures attain a equilibrium temperature.

Figure 3.24 shows the influence of thermal capacity of virgin material and char on the pyrolysis gases mass flow rate. It is clear that the thermal heat capacity of virgin material has a higher influence (top figure) compared to thermal capacity of char (bottom figure). Obviously, higher thermal capacity lead to a higher consumption of heat by the virgin material and hence the peak value drops, also the duration of the pyrolysis process increases. The influence of thermal heat capacity of char on the pyrolysis gases evolution is not high.

Figure 3.25 shows the effect of thermal conductivity of virgin material (top) and char (bottom) on pyrolysis gases mass flow rate. The effect of thermal conductivity of char is significant (bottom figure) during the finite rate period. Increase in the thermal conductivity of char leads to higher heat transfer to the virgin material, higher mass flow rate of pyrolysis gases and duration of the pyrolysis process decreases. Increase in the thermal conductivity of virgin material has little effect as seen with the short time taken for pyrolysis process completion (top figure).

Figure 3.26 is similar to figure 3.16, with the material properties are taken from table 3.8. It is seen that, with the current settings for model parameters and material properties, for h_s=0 W/m^{2}K, complete charring is not seen for h_{bs} >17.5 W/m^{2}K. The other observations are similar as in figure 3.16, on the contrary, the temperatures drop quickly. The horizontal dashed line is the pyrolysis temperature i.e. T_{pyr}=623 K.

Figure 3.27 (top) shows the effect of non-zero back surface convective heat transfer coefficient h_{bs} on the mass flow rate of pyrolysis gases. Qualitatively, very similar observations are made as in figures (3.17 and 3.18). Obviously, the absolute values are different, due to the differences in configuration.

With the decrease in the value of back surface heat transfer coefficient h_{bs}, the second peak value increases and the pyrolysis process duration is reduced (middle figure). For low value of h_{bs}, the second peak is higher than the first peak. This was not observed in the earlier discussions. Of course, this is due to the different thermo-physical material properties.

Figure 3.27 (top right) show the front and back surface temperatures attain a equilibrium temperature when the solid is completely char, i.e. the solid has no pyrolysis front and the

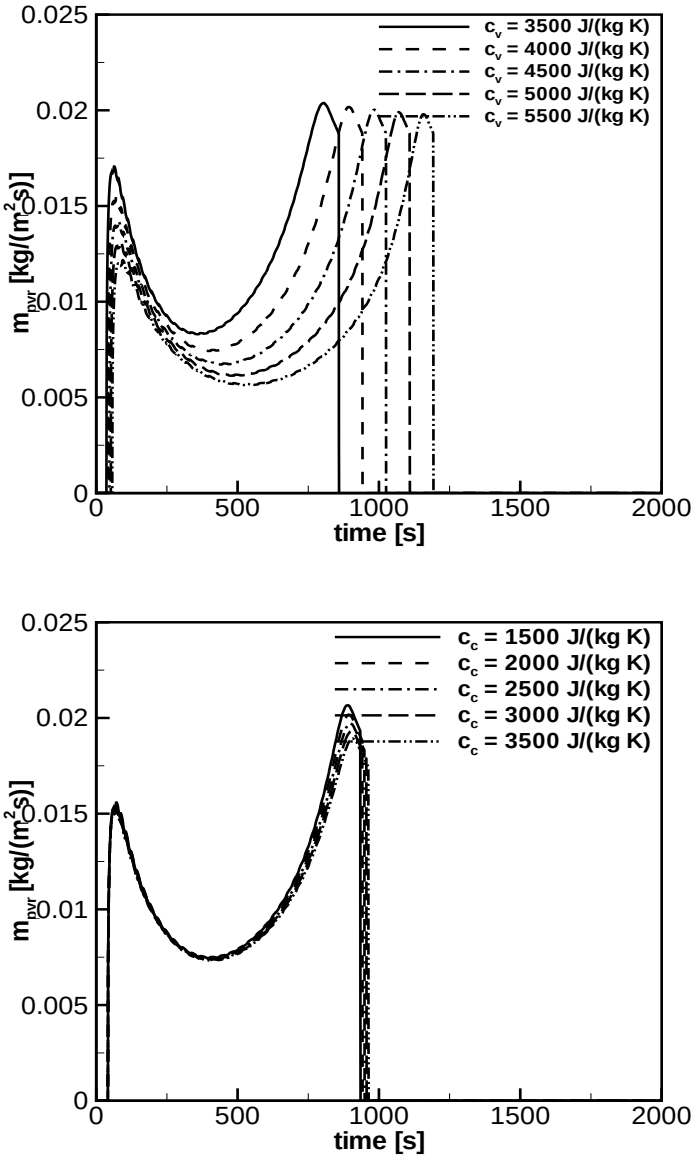

Figure 3.24: Effect of thermal capacity of virgin material c_v (top) and thermal capacity of char c_c (bottom) on pyrolysis gases mass flow rate

material has only the conductive term in equation (2.21). For h_{bs}=0 W/m^{2}K, the equilibrium temperatures for front and back surfaces are identical. Finally, the figure (bottom) shows the pyrolysis front position when the back surface heat transfer coefficient h_{bs} is varied. Except for high value of h_{bs}=20 W/m^{2}K, the pyrolysis front reaches the back surface, clearly indicating that the solid is totally consumed. Note that, for h_{bs}=20 W/m^{2}K, the interruption of the pyrolysis process is automatically predicted and an equilibrium situation appears as described before.

Figure 3.28 the front surface heat transfer coefficient (h_s) is varied. A similar observation as figures 3.19 and 3.20 can be made here. To summerise, increase in the heat transfer

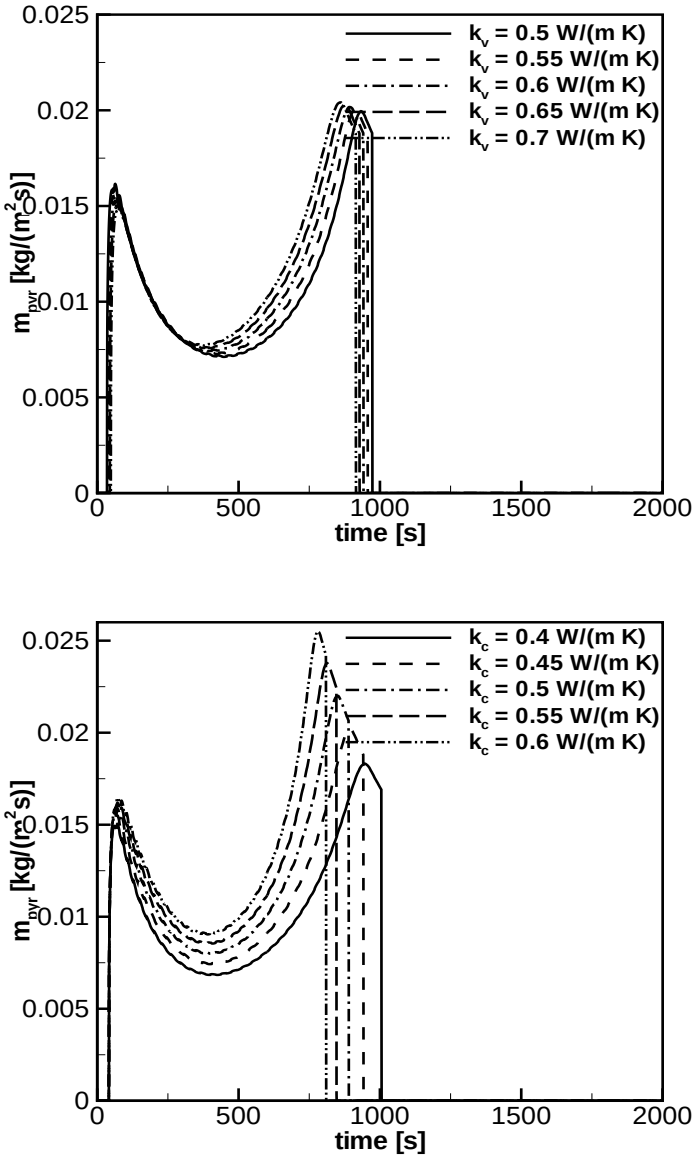

Figure 3.25: Effect of thermal conductivity of virgin material k_v (top) and thermal conductivity of char k_c (bottom) on pyrolysis gases mass flow rate

coefficient h_s on the front surface, keeping h_{bs} fixed at 15 W/m^2K, complete charring only occurs for sufficiently low values of h_s, as seen in figure 3.28. Recall that all these findings are automatically predicted with the enthalpy based pyrolysis model.

3.1.11 Temperature distribution

Figure 3.29 (top) shows the temperature distribution along the length of the solid under study at different time level before the pyrolysis process start. When the solid is exposed to

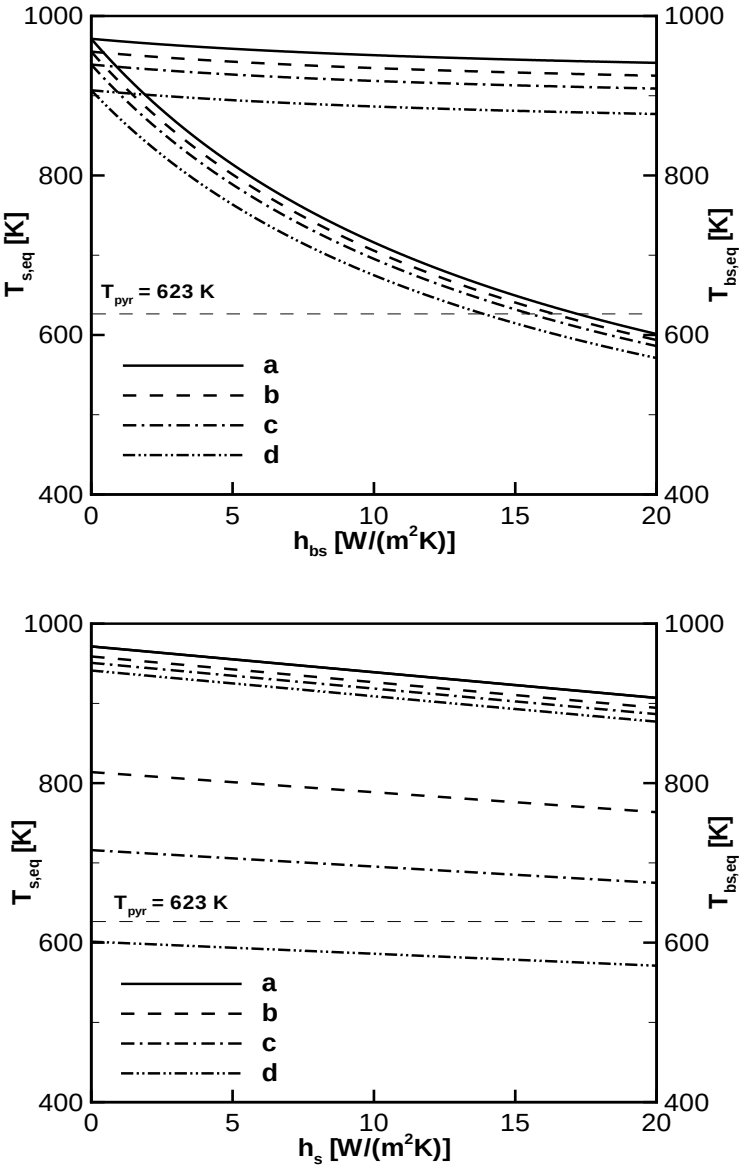

Figure 3.26: Steady state front and back surface temperature in case of complete charring of the material (experimental configuration). Top: fixed h_s; Bottom: fixed h_{bs}. Values: a: 0 W/m^{2}K; b: 5 W/m^{2}K; c: 10 W/m^{2}K; d: 20 W/m^{2}K. Emissivity (ϵ) =1

an external heat flux, temperature in the solid increases due to conduction. For a thermally thick material, the backface boundary condition has a negligible effect on the solution. The thermal penetration depth gives the length the thermal front has travelled before pyrolysis begins. In this case, the pyrolysis starts ($T_s = T_{pyr}$) just before t=20 s. The bottom figure shows the temperature ratio as function of the depth divided by the growing thermal penetration depth ($\delta = \sqrt{\alpha t}$). Clearly, the back surface has no influence.

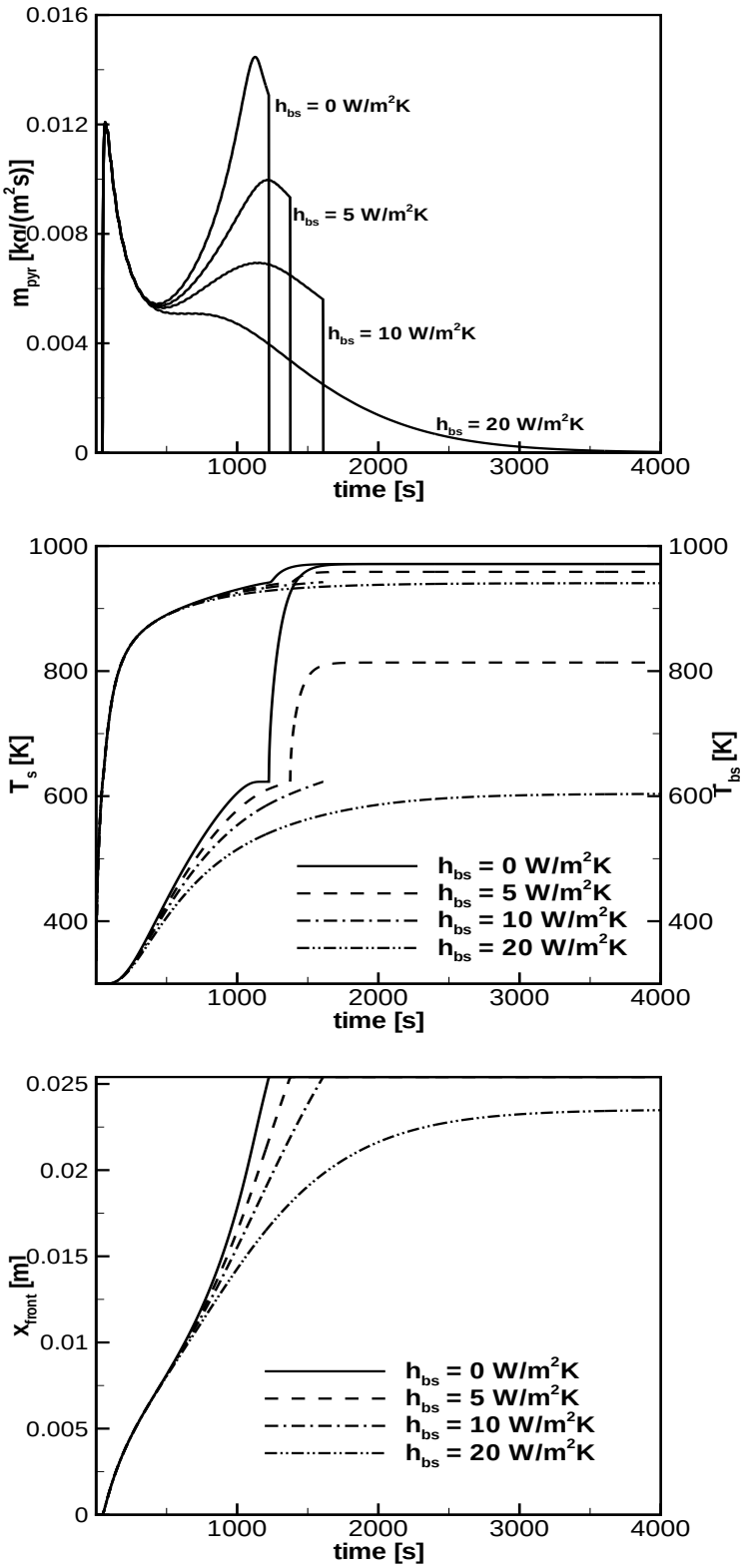

Figure 3.27: Effect of h_{bs} on mass flow rate (top), front and back surface temperatures (middle) and pyrolysis front position (bottom)

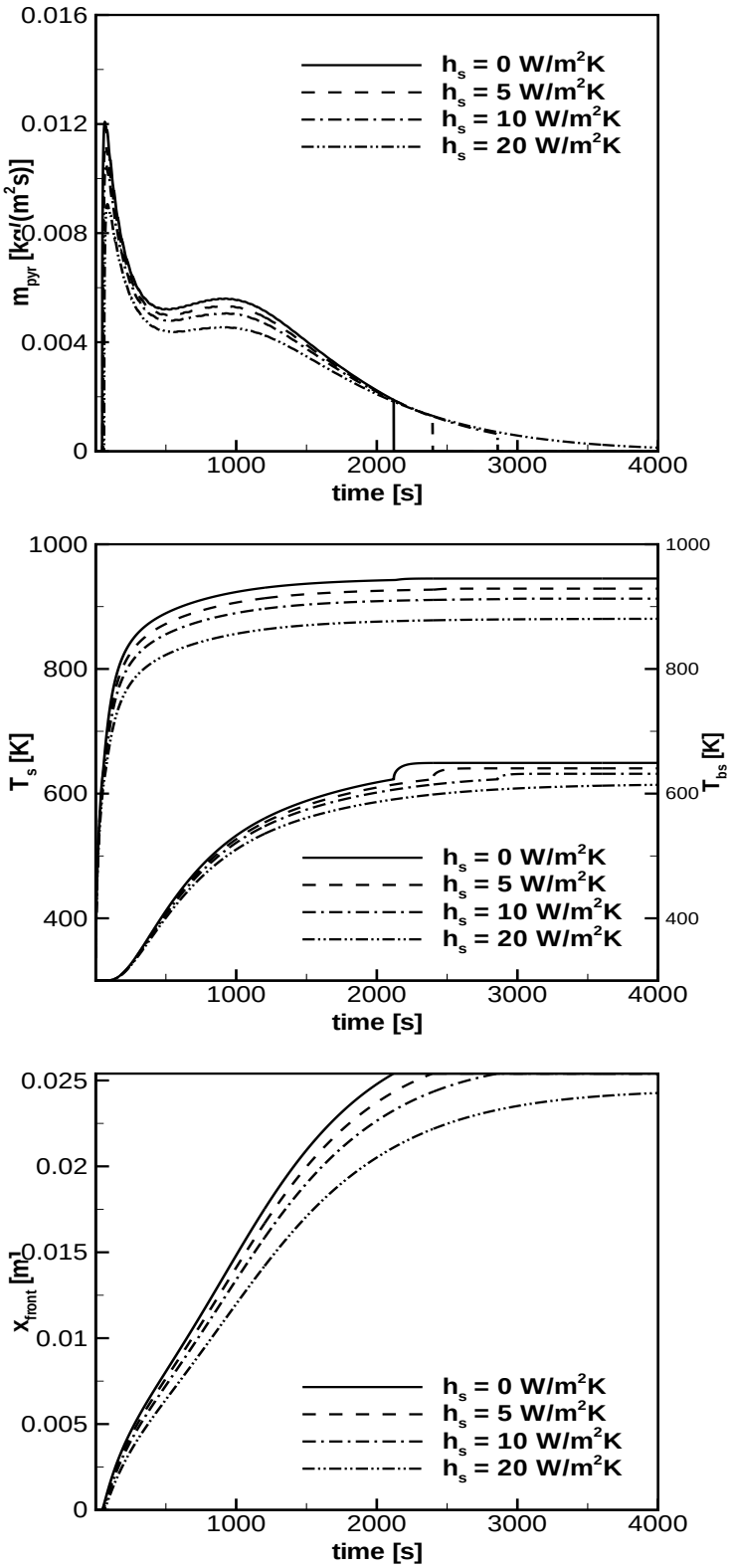

Figure 3.28: Effect of h_s on mass flow rate (top), front and back surface temperatures (middle) and pyrolysis front position (bottom)

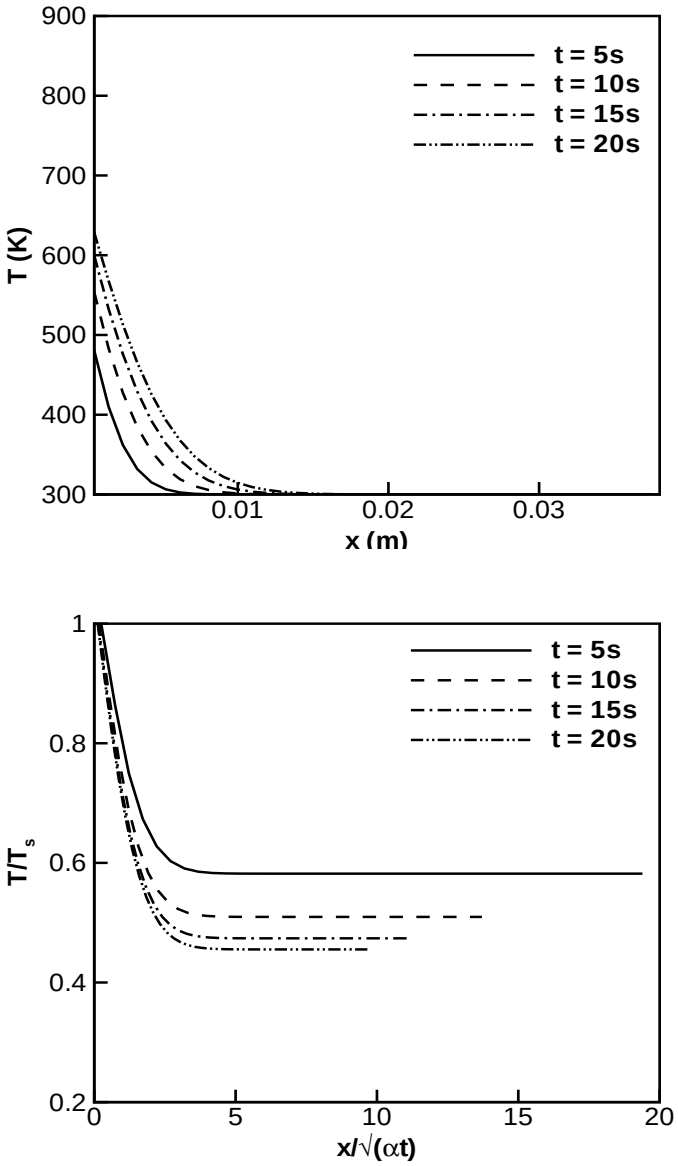

Figure 3.29: Top: Temperature distribution along the length of the solid; Bottom: Dimensionless temperature distribution along the dimensionless length at different time level. Thickness=3.8 cm

3.2 Wet charring materials

3.2.1 Introduction

The enthalpy based model is applied on wet charring materials (biomass, wet wood, etc), where moisture level in the solid is above 5% dry weight. Numerical simulation results are presented for both materials below. The influence of moisture in charring materials is dealt in this section. A review on the research in the field of wet charring materials was already made in the introduction.

Moisture in solids exists in three different forms: moisture in vapour in the porous media. moisture in liquid, which is the unbound water, and moisture as bound water in the solid. The fibre saturation point[2] is the critical point at which all cell walls have the maximum amount of bound water, but no liquid free water in solids (e.g. wood). The sum of all these gives the total moisture content in the solid.

A schematic representation of a one-dimensional solid was shown in figure 2.3. Note that for evaporation to take place, the surface temperature has to reach the evaporation temperature T_{evap} (373 K). This takes place much earlier than the pyrolysis process, as pyrolysis process starts only when surface temperature reaches $T_{pyr} \gg 373$ K. Similar to the pyrolysis process modelled earlier, evaporation of water takes place in a infinitely thin front maintained at T_{evap}=373 K. At this front, moisture present in liquid form transforms into vapor and moves out of the solid leaving behind a dry solid with no moisture. The evaporation front moves ahead of the pyrolysis front, also seen in figure 2.3. The effect of this front on the pyrolysis process is dicussed in this section.

During pyrolysis of wet charring materials (one-dimensional case), moisture evaporates and escapes in both directions (from the front). The flux that moves towards the exposed surface is assumed in thermal equilibrium with the virgin dry solid or the char material ($T > T_{evap}$). The flux moving towards the back surface condenses in the virgin wet solid, as this region has lower temperature ($T < T_{evap}$). Accumulation of this moisture eventually leads to a large plateau during evaporation process [4, 13, 26, 45, 71]. This behaviour is taken into account and is seen in the numerical simulation results.

3.2.2 Results and discussion

The thermo-physical properties are taken as table 3.1. The thickness of the solid equals 3.8 cm. The basic configuration consists of 40 cells and a physical time step equal to 0.1 s.

Figure 3.30 shows the effect of moisture in the solid exposed to an external radiation heat flux of 40 kW/m^2. The moisture content is varied from (0, 5, 10 and 15 %). The latent heat of vaporization is $L_v = 2.27 \times 10^6$ J/kg and the thermal capacities of liquid water and water vapour are $c_{w,l}$=4184 J/(kgK) and $c_{w,v}$=2000 J/(kgK), respectively. In figure 3.30, the total mass flow rate is the sum of the water vapour mass flow rate and the pyrolysis gases mass flow rate. Note that the mass flow rate is computed at the exposed surface of the solid. An increase in the moisture content in the solid clearly leads to a longer pyrolysis process. Indeed, part of the incoming heat flux is consumed in the evaporation process of the unbound moisture, to convert the liquid water to water vapour, thereby consuming heat in the form of latent heat of vaporization. Focusing on the first 500s (top) shows the onset of the evaporation and pyrolysis processes. Obviously, the evaporation process starts already when the surface temperature equals 373 K, while the pyrolysis process only starts when it equals T_{pyr}. The evaporation mass flow rate begins first with a higher peak value (depending on the moisture content) and then decreases, similar to pyrolysis process. Further heating brings the surface temperature to the pyrolysis temperature. When pyrolysis begins, flammable

[2]Fibre-saturation point is the moisture content of cellular material at which the cell walls are completely saturated while the cavities are liquid free. It maybe defined as the equilibrium moisture content as the humidity of the sourrounding atmosphere approaches saturation

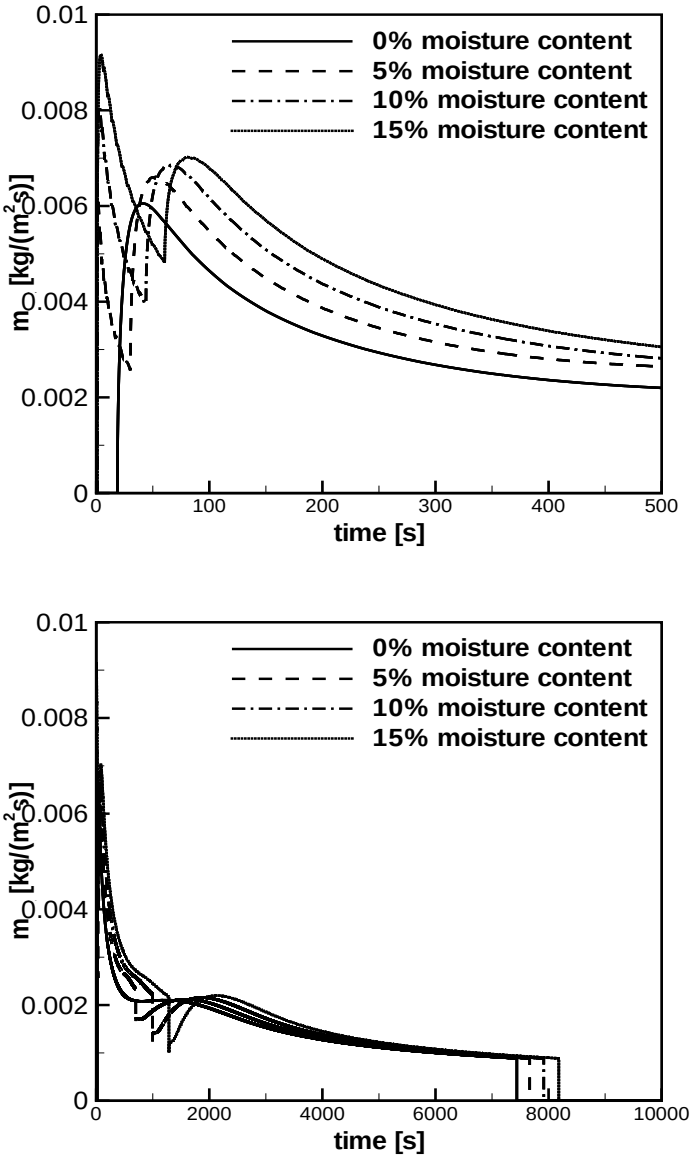

Figure 3.30: Total mass flow rate evolution in time. Top: Zoom up to 500 s; bottom: up to 10,000 s for different moisture contents

volatiles are released, in addition to the water vapour mass flow rate, thus resulting in a higher total mass flow rate. For dry solid heating (i.e. 0% moisture) the total mass flow rate only consists of the pyrolysis gases mass flow rate.

A sudden drop in the total mass flow rate is observed when the evaporation front reaches the back surface, because the evaporation front reaches this surface with a non-zero velocity (figure 3.30, bottom). The pyrolysis gases mass flow rate increases then, because no heat is consumed in the evaporation process any more. The remainder of the pyrolysis process takes place in dry virgin material, so that very similar mass flow rate profiles are observed. To a good approximation, the initial moisture bulk density determines the shift of the profiles.

The higher the moisture content, the more the curves are shifted to the right (longer global evaporation/pyrolysis process).

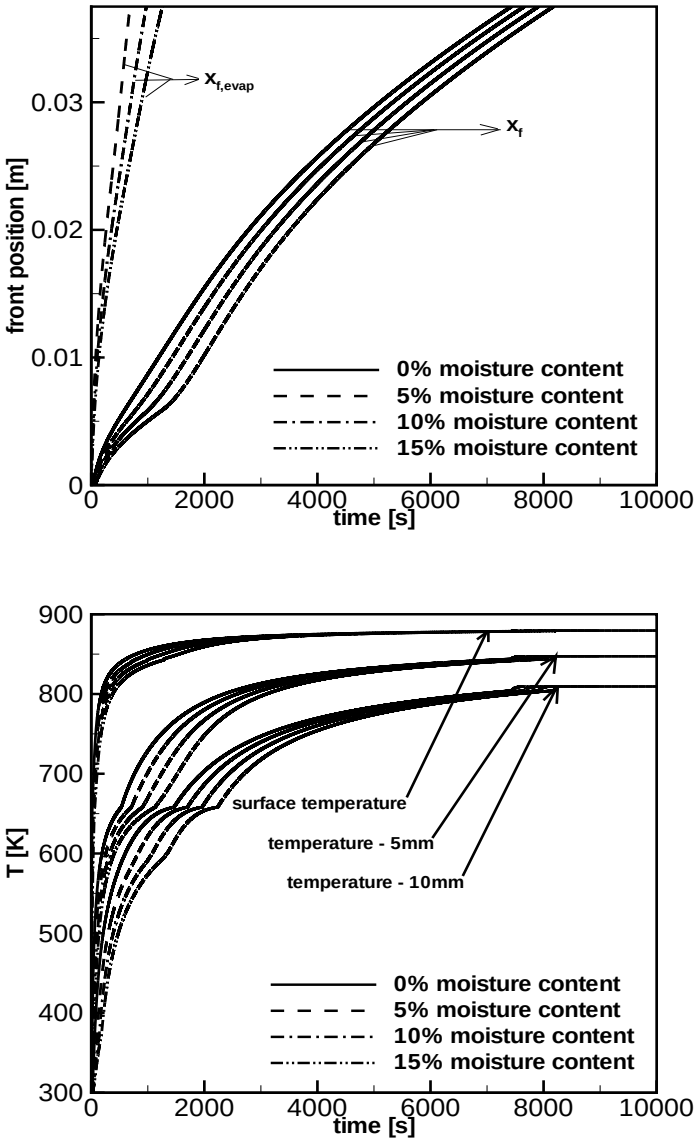

Figure 3.31: Top: Pyrolysis and evaporation front positions in time; Bottom: Temperature distribution at different depths for different moisture contents

Figure 3.31 (top) shows the front positions in time. It clarifies that evaporation front motion is quick compared to the pyrolysis front motion. Also, with increase in the moisture content, the speed of the evaporation front decreases, seen with the drop in the slope. Dry solid has only the pyrolysis front, so there is no $x_{f,evap}$ curve. The pyrolysis front $x_{f,pyr}$ motion for dry solid is quick compared to the wet solid, because in wet charring materials, heat is utilized for the evaporation process. Hence, less heat is available for the pyrolysis process to proceed. When the solid is dry (evaporation front has reached the back surface) the pyrolysis front motion accelerates and all curves become essentially parallel.

Figure 3.31 (bottom) shows the temperature distribution in the solid at different depths (surface, 5 mm and 10 mm). With the increase in moisture content in the solid, the inner solid temperature rises more slowly. Obviously, this is again due to the heat consumed during the evaporation process in the form of latent heat of vaporization (L_v). When evaporation process is complete in the solid, temperatures rise more quickly. Finally, equilibrium temperatures are reached upon completion of pyrolysis process, when only char is left. The model does not consider char oxidation. This is considered future work in the development of the enthalpy based model.

3.2.3 Comparison with experiment

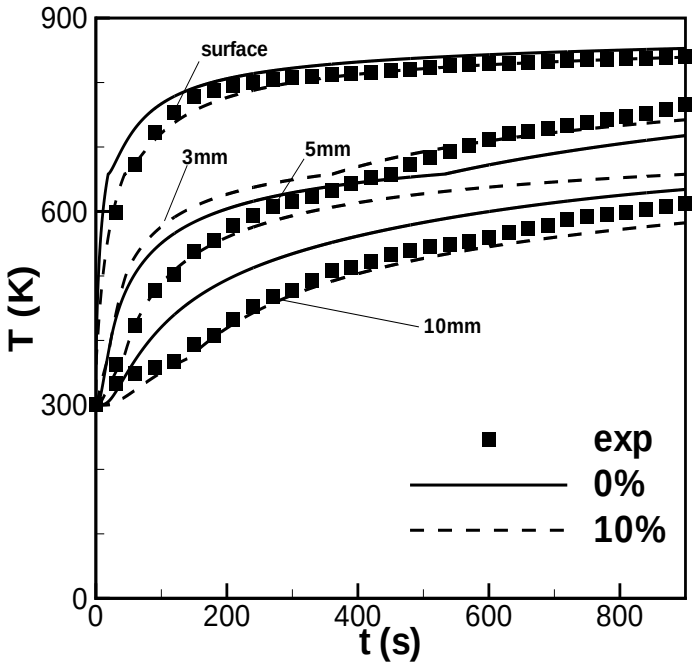

Figure 3.32: Temperature distribution with different moisture contents compared to experiment

Figure 3.32 shows the temperature distribution obtained from experiments, and numerical simulations performed on wet charring material with different moisture contents. Numerical simulation results are compared to the experimental results from Kashiwagi et al. [60] for temperatures distribution at three different depths i.e. surface, 5 mm and 10 mm. With the increase in the moisture content, the solid temperature rise is slow. Agreement with the experimental data is not perfect (in particular at 5 mm depth), but the global trends are well captured. When the solid is exposed to a heat flux, the solid first begins to dry, with the release of moisture. Later, the pyrolysis occurs with the release of flammable volatile pyrolysis gases. In reality, there is always some moisture in the solid (white pine). During the heating/pyrolysis process water escapes in the form of water vapor from the front surface. Temperature distribution in the solid shows that for 10% moisture content simulation results are in good agreement with the temperatures at 10 mm deep solid. This

shows that water has condensed inside the solid leading to a locally higher moisture level (approx. 10%).

During the pyrolysis process, the solid shrinks and other volume deformations occur, due to weight loss in the form of volatiles. The thermocouple that was placed at 5 mm depth in the solid. Thus eventually comes to a lower depth due to char shrinkage. This may explain why the temperatures at 3 mm deep are in good agreement for later times (t>500 s).

3.2.4 Effect of thickness

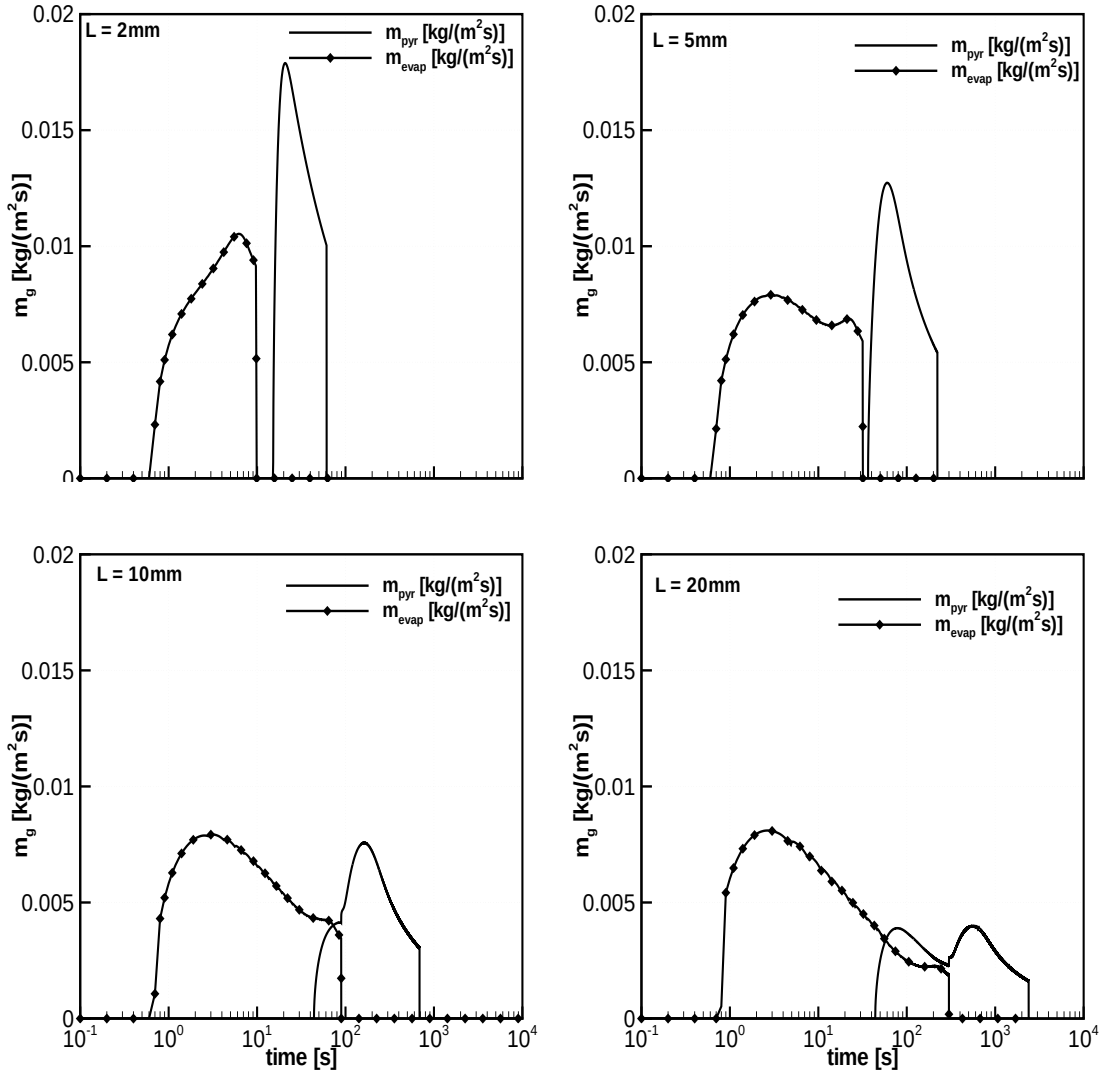

Figure 3.33: Mass flow rate of pyrolysis gases for different material thicknesses

Figure 3.33 shows the effect of solid thickness on evaporation and pyrolysis processes. The solid thickness is varied from 2 mm (thermally thin) to 40 mm (thermally thick). The

boundary conditions remain the same as discussed before. The solid has a moisture content equal to 10%. The lines with symbols represent the evaporation process, while solid lines are for the pyrolysis process. For 2 mm thick wet solid, evaporation is complete before the pyrolysis process begins. This is due to the rapid heating of the solid to the evaporation temperature $373K$. Biot number, Bi is $15 \times 0.002/0.36 = 0.083$, but for L=5 mm we still see this independence and then Bi≤ 0.208 i.e. $15 \times 0.005/0.36$.

Pyrolysis and evaporation occur simultaneously for L>5 mm i.e. Bi> 0.208 here. Obviously, this value is not general and depends on the materials properties.

3.3 Non-charring materials

3.3.1 Introduction

The enthalpy based model is now applied to non-charring and wet charring materials. In non-charring materials, regression occurs at the front surface due to pyrolysis, no char layer. This makes the virgin solid always exposed to external heat flux and pyrolysis takes place on the surface, when temperature reaches the pyrolysis temperature.

In non-charring materials, after pyrolysis, no residue (char) is left behind. While the solid is pyrolysing, the surface temperature is always at the pyrolysis temperature T_{pyr}. The external heat flux directly falls on the virgin unburnt solid. In the numerical model, this is done with the char properties set to zero. More information on the non-charring materials is already discussed by Fernandez-Pello [33], 2^{nd} chapter and by di Blasi [14].

Some works on noncharring materials have already been discussed in the introduction. Focussing on PMMA research, Vovelle et al. [117] report experimental values for heat of gasification equal to 1695 J/kg in nitrogen and 1654 J/kg in air. Tewarson [1] reported values for most of the solid PMMA used in building industry, for heat of gasification ranging from 1590-1885 J/kg. Kashiwagi [59] studied the effect of oxygen concentration on PMMA and PE burning. They found that the surface temperature did not change with increasing heat flux, but decreased with decrease in oxygen concentration. Also the mass flow rate increases with increase in oxygen concentration.

3.3.2 Results and discussion

Numerical simulations for pyrolysis of dry non-charring materials are performed, setting the conduction and convection fluxes in the char to zero. The thermo-physical properties are taken from Sohn et al. [101] are put in table 3.9.

The value of heat transfer coefficient heat transfer coefficient and emissivity is h = 0.02 W/(m^{2}K) and $\epsilon = 0.92$, respectively and $\sigma = 5.67 \cdot 10^{-8}$ W/(m^{2}K^4). The model parameters are: $\Delta Q_{pyr} = 10.07 \cdot 10^5$ J/kg, $T_{pyr} = 630$ K. The ambient and initial temperature are set to 300 K. The solid has thickness equal to 3cm. A physical time step of 0.5 s and total number

Properties	Value	Units
ρ_v	1150.0	kg/m^3
c_v	1420.0	J/(kgK)
k_v	0.185	W/(mK)

Table 3.9: Thermo-physical properties of PMMA solid

of cells is 80 cells are considered in the simulations. The solid is exposed to a radiant heat flux $\dot{q}''_{ext} = 50$ kW/m^2. The boundary conditions read as follows:

$$\begin{aligned} x = x_f; \quad & \dot{q}''_{net} = \epsilon \dot{q}''_{ext} - h_s \left(T_s - T_{amb}\right) - \epsilon\sigma \left(T_s^4 - T_{amb}^4\right) \\ x = l; \quad & k\frac{dT}{dx} = 0 \end{aligned} \tag{3.8}$$

The numerical results are compared to the theoretical results obtained from Sohn et al. [101]. Similar boundary conditions are used in the simulations in order to illustrate the representation of the numerical results. Two tests were conducted on non-charring materials:

- considering the surface losses with the value of heat transfer coefficient h_s and emissivity ϵ as mentioned above in table 3.9;
- without any surface heat losses, i.e. only the first term is kept from equation (3.8).

Figure 3.34 (top) shows the mass flow rate of pyrolysis gases for non-charring material (PMMA). The results from enthalpy based model are in good agreement with the results obtained from Sohn et al. [101], when heat losses are considered. Obviously, when the convection and radiation losses are not taken into account, the mass loss rate is higher and material is consumed in a short time period.

The mass loss rate of pyrolysis gases is seen when the surface temperature reaches the pyrolysis temperature T_{pyr}. After some time, the mass loss rate attains a quasi-steady state: the incoming heat flux provides energy for the pyrolysis process and for heat conduction into the virgin solid. The external heat flux falling on the solid is utilized for pyrolysis process, while some heat is conducted into the solid. This conducted heat in the form of conduction flux generates the thermal front, to heat the solid. After a while, the mass flow rate rises, due to the back effect: less heat is conducted into the remainder of the solid material and thus a larger part of the external heat flux is utilized for the pyrolysis process. Obviously, this is more pronounced when there is no heat loss at the external surface. This accelerates the pyrolysis process, with higher release of pyrolysis volatiles. The movement of pyrolysis front is seen in figure 3.34 (bottom). As expected, pyrolysis front moves faster when the surface losses are not taken into account. On close observation, the front become more steep when the front moves close to the back surface. This corresponds with the evolution of more gases. All these issues are well captured with the present model.

Figure 3.35 shows the temperature distribution in the solid with and without losses. In both figures, the surface temperature never exceeds the pyrolysis temperature (630 K). The internal temperatures rise slowly as heat travels in the solid by conduction. The temperature rise is more quick without losses (bottom figure). In this figure, the temperature in the solid rises quickly and the pyrolysis duration is greatly reduced as seen with the front almost

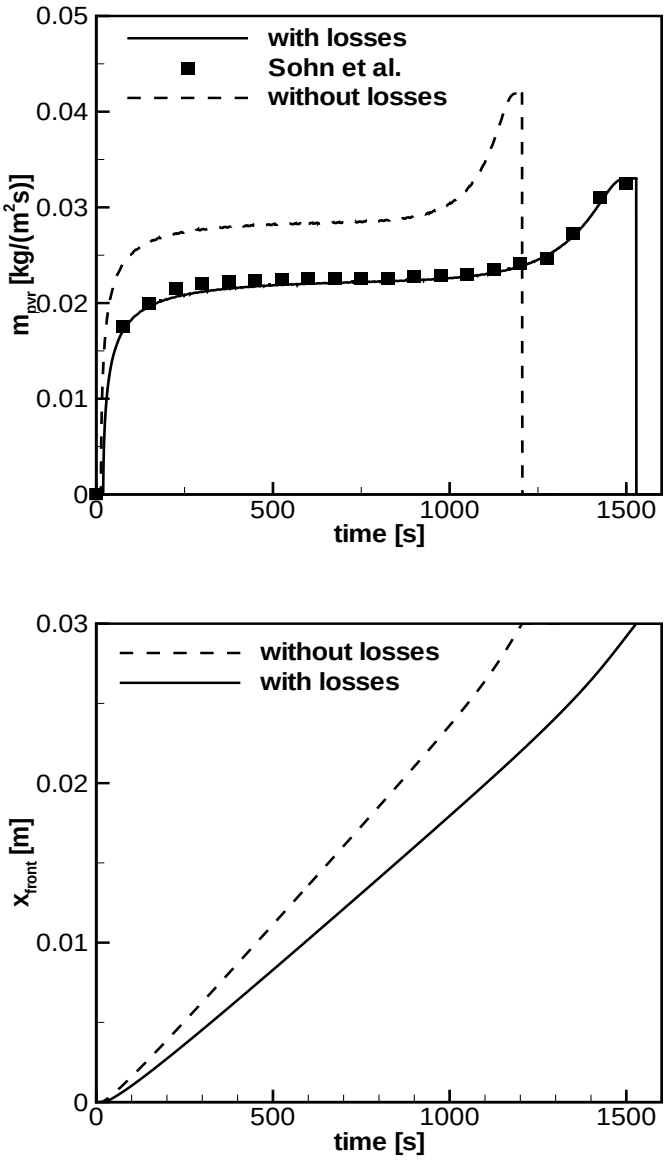

Figure 3.34: Mass loss rate (top) and pyrolysis front position (bottom) in time

reaching 0.028 m in 1200 s (bottom figure), while it takes 1200 s to complete just 0.023 m. The temperatures recorded in the figure are the cell center temperatures (post-processing), so that the peak temperatures are slightly lower than T_{pyr}. The back effect becomes clearly visible in latter stages. This illustrates the reduction in the conductive heat flux: the temperature gradient becomes less steep. The temperatures are plotted at every 200 s. After 1000 s the surface regressions is quicker, due to the back effect, leading to a higher mass loss rate.

Figure 3.36 shows the enthalpy distribution in the solid. The enthalpy in the solid is never positive, but remains in the sub-zero level in the virgin solid. At the pyrolysis front, the enthalpy equals 0.

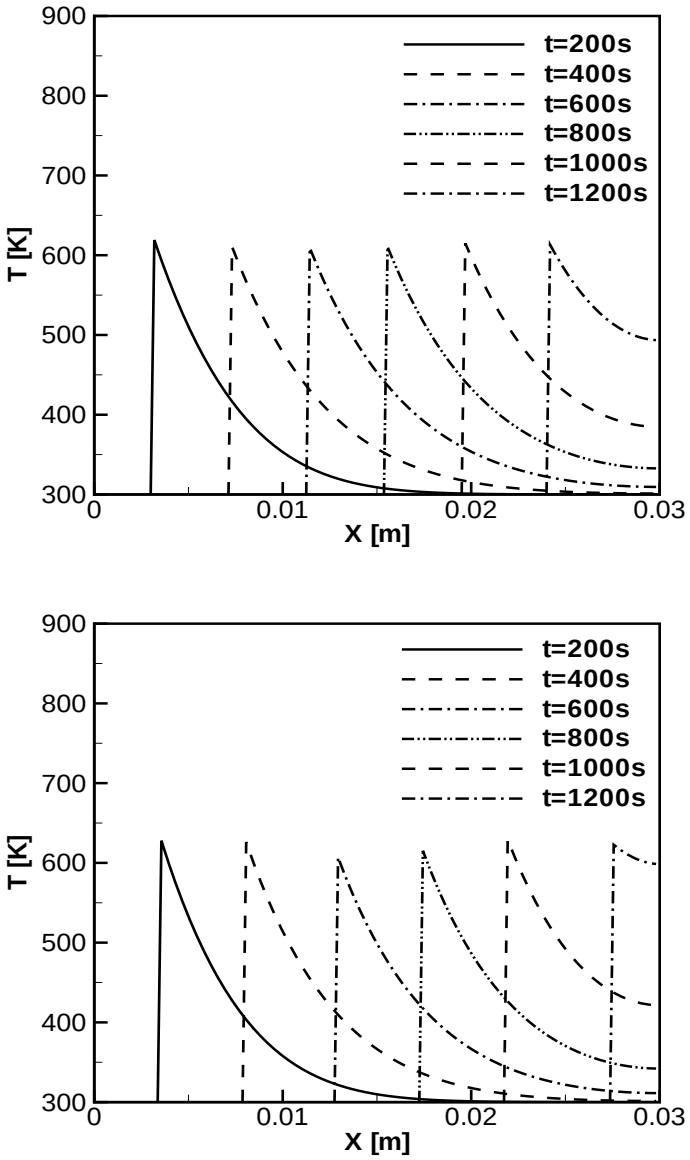

Figure 3.35: Temperature distribution in the solid at different time levels (200s, 400s, 600s, 800s, 1000s and 1200s) with losses (top) and without losses (bottom)

3.3.3 Effect of model parameters of non-charring materials

In this section, the effect of the different parameters on mass flow rate of pyrolysis gases is discussed.

Figure 3.37 (top) shows the influence of convective heat transfer coefficient h_s on the mass flow rate of pyrolysis gases. Decreasing the value of h_s increases the mass flow rate, and also decreases time takes for the pyrolysis to complete. Obviously, this is due to the lower heat loss occuring at the front surface due to lower convection heat loss. Also, with increase in h_s, the start of pyrolysis is delayed, due to the rise in convection loss. Figure 3.37 (bottom) shows the effect of heat of pyrolysis on the mass flow rate of pyrolysis gases. Unlike as

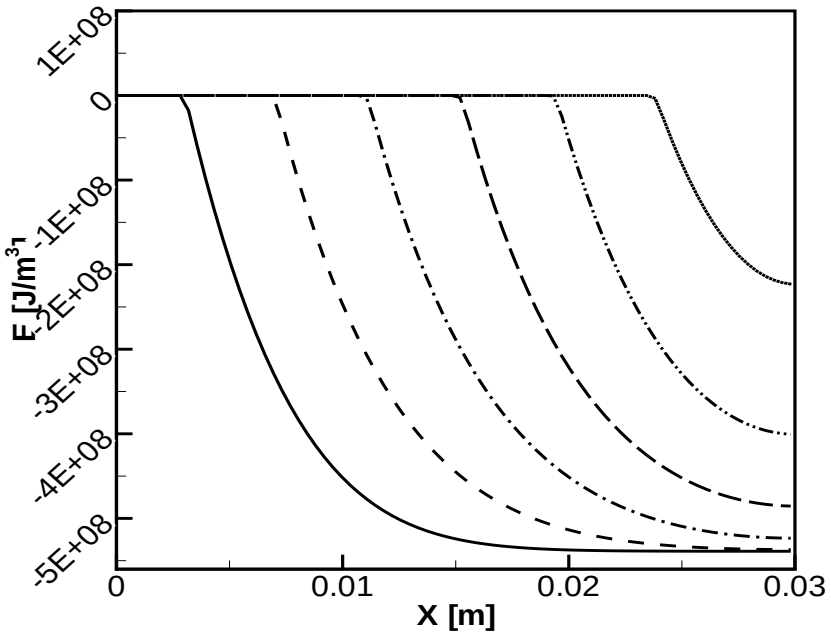

Figure 3.36: Enthalpy distribution in the solid at different time levels (—: 200 s; − − −: 400 s; –·–: 600 s; – –:800 s; –··–:1000 s; · · · :1200 s) with losses

in charring materials, the influence of heat of pyrolysis is large in non-charring materials. With increase ΔQ_{pyr}, the duration of pyrolysis increases, along with a decrease in mass flow rate. Lower heat of pyrolysis consumes less heat to pyrolyse the material and the pyrolysis temperature is reached more quickly.

Figure 3.38 (top) shows that the influence of emissivity is small compared to the other parameters. Obviously, this is true because the radiation heat loss is low, because, the surface temperature does not exceed the pyrolysis temperature in non-charring materials. For charring materials, the surface temperature increases more and, hence the radiation loss is high.

The bottom figure shows the effect of pyrolysis temperature on the mass flow rate of pyrolysis gases. With an increase in the pyrolysis temperature T_{pyr} value, the pyrolysis gases mass flow rate drops and the duration of pyrolysis process increases. There is a delay in the start of pyrolysis, due to the longer time taken to heat the solid to the pyrolysis temperature for a heat flux value. For higher pyrolysis temperature, T_{pyr}=700 K, pyrolysis process duration strongly increases.

Figure 3.39 (top) shows the temperature distribution along the length of the solid under study at different time before the onset of the pyrolysis process. The results are obtained for external heat flux $\dot{q}''_{\text{ext}} = 50$ kW/m^2. The surface temperature rise is slow in the beginning, due to the heat loss into the solid by conduction and surface losses.

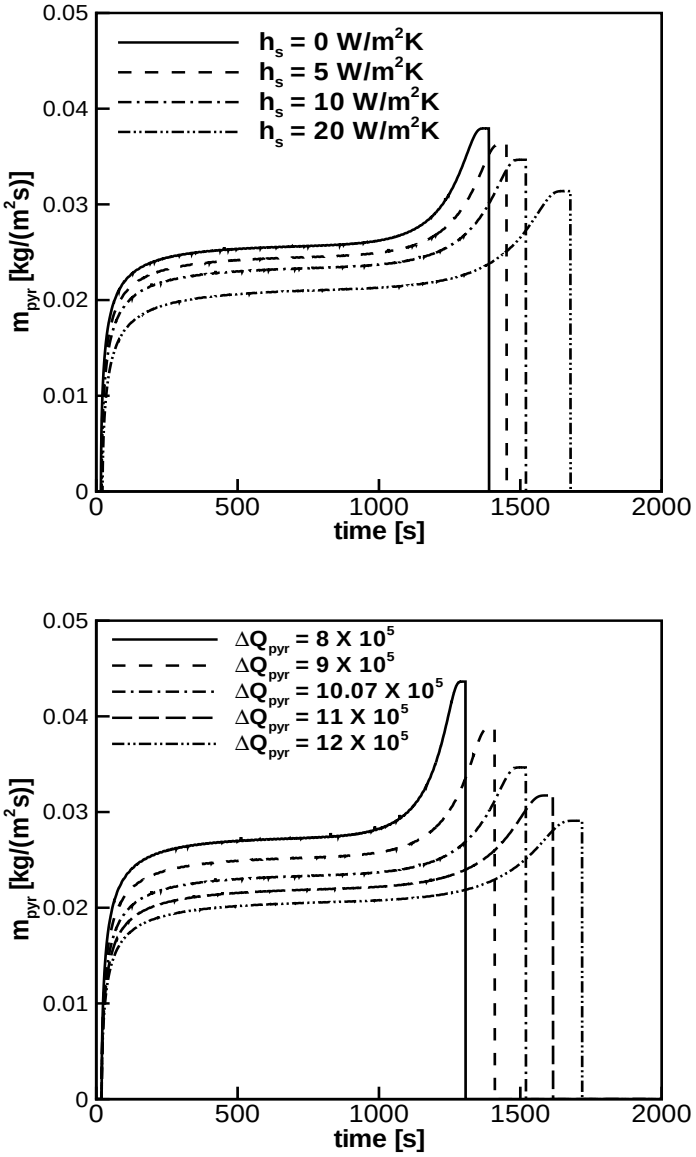

Figure 3.37: Top: effect of front side heat transfer coefficient h_s; bottom: heat of pyrolysis ΔQ_{pyr} on mass flow rate

3.4 Conclusions

In this chapter, the model was applied to dry- and wet-charring and non-charring materials in one-dimensional configurations. A sensitivity study was presented on numerical issues and model parameters. Provided these are chosen appropriately, good agreement with numerical and experimental results in the literature can be obtained.

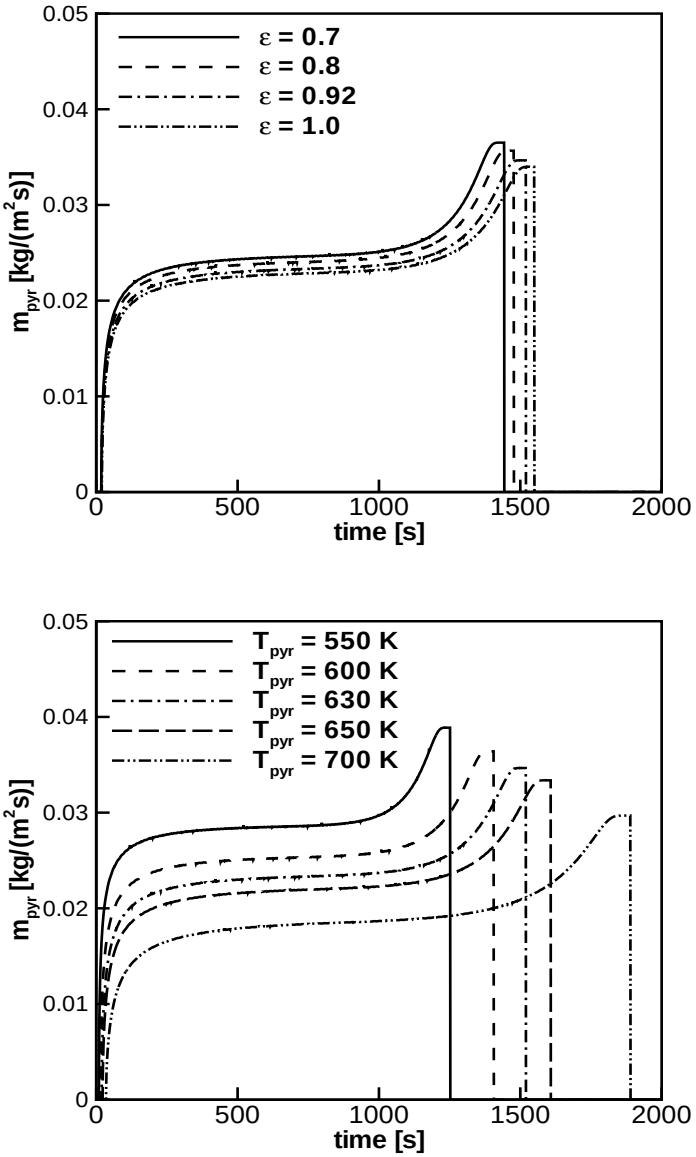

Figure 3.38: Top: effect of emissivity ϵ; bottom: pyrolysis temperature T_{pyr} on mass flow rate

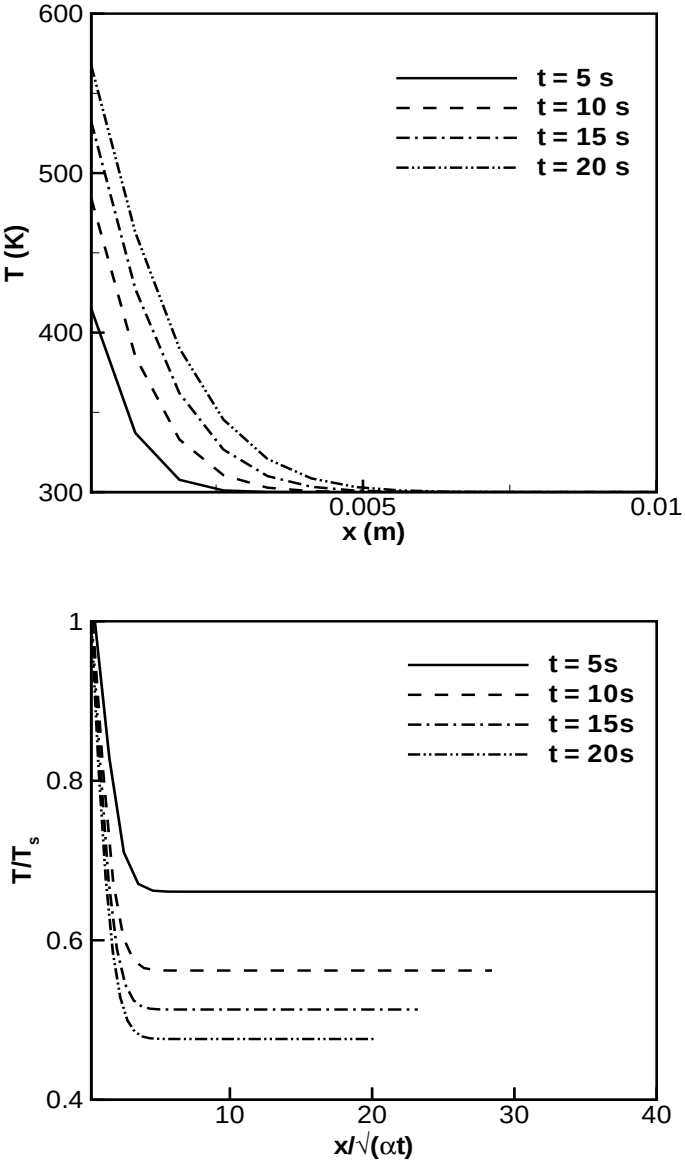

Figure 3.39: Top: temperature distribution along the length of the solid; bottom: Dimensionless temperature distribution along the dimensionless length at different time level for non-charring materials

4

Experimental study of one-dimensional configurations

4.1 Introduction

Many researchers around the globe have worked on the cone calorimeter or a similar apparatus of their choice to study the material behaviour under fire circumstances, for charring materials [37, 53, 72, 75, 102, 114] and non-charring materials [96]. V. Babrauskas and W. J. Parker [8] carried out solid flammability tests using cone calorimeter to understand the ignition of samples, the specimen size, thickness, air flow rates for controlled atmosphere studies, edge effects. The results are compared with empirical ignitability model results for charring and non-charring materials. Controlled atmosphere tests were performed in inert atmosphere [9] and for grain orientation [10, 115]. Rath et al. [90] worked on differential scanning calorimeter to study the importance of heat of pyrolysis on the course of thermal conversion of wood. According to them, the char formation is an exothermic process, while volatile formation is an endothermic process. This chapter reports on an experimental campaign, performed at the Lund University. Numerical simulation results are also discussed. This chapter is based on Wasan et al. [121, 122].

4.2 Experimental set-up

4.2.1 Cone calorimeter

Pyrolysis process that occurs in the solid is studied using the cone calorimeter, a product of Fire Testing Technology Ltd, provided by the University of Lund, Sweden. This set up is in accordance with ISO 5660 ASTM [2, 52]. The set up has a conical coil heater, mounted above the load cell, emits radiation of certain pre-set intensity. To that purpose, it is electrically heated to a temperature, corresponding to the desired emitted radiative heat flux towards the sample. The calibration is done by a total heat flux meter measuring total heat flux not only radiative. However in the cone the amount of radiative flux is about 90% so the convective part is small. This is established by a calibration curve, i.e. given the temperature of the coil, the heat flux emitted from the coil is controlled. A schematic

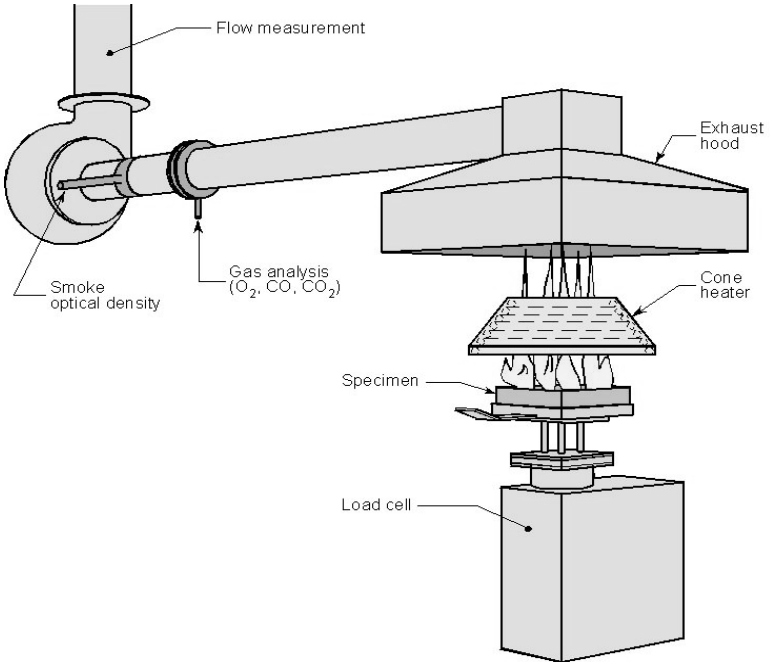

Figure 4.1: Schematic Cone Calorimeter apparatus

representation of the cone calorimeter is seen in figure 4.1. The load cell holds the retainer frame containing the sample. The retainer frame has dimensions of 10 cm × 10 cm (inner area). The major components of the cone calorimeter is shown in figure 4.2. The sample, containing the thermocouples at different depths to measure the temperatures, is wrapped in an aluminium foil. This foil is covered with glass wool from all sides while the front surface is kept open for the external heat flux to heat up the sample, in order to treat the pyrolysis process as a one-dimensional process. Experiments were carried on medium density fibre board (9.8 cm×9.8 cm×1.65 cm (thick)(effect area ×thickness)) mounted horizontally. In the cone calorimeter experiments, solid mass is continuously measured. Temperature

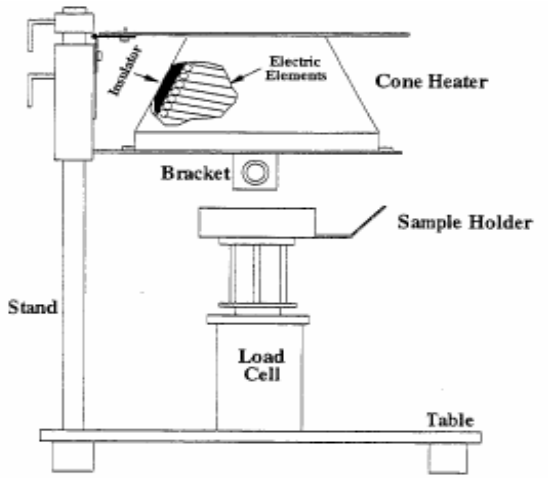

Figure 4.2: Schematic Cone Calorimeter apparatus

evolution at different depths is also measured. The solid is exposed to three different levels of external heat fluxes are investigated (20 kW/m^2, 30 kW/m^2 and 50 kW/m^2). Both the dry and wet medium density fibre board (MDF) are considered in the experiments.

The thermocouples used in the determination of temperatures is Type-K (Alumel and Chromel). A total of 8 thermocouples are mounted: one on the top and back surface and two at different depths (3 mm, 5 mm, and 8 mm) placed in a symmetric manner (roughly 1 cm from the center of the sample). The thermocouples, placed through drilled holes, are connected to a digital display via a converter. The thermocouples are joined by twisting them. Ofcourse, there is some amount of error and uncertainity involved during the temperature measurement. We do not know exact location of temperature measurement (error maybe around 0.3 mm). The cone calorimeter experiments are conducted in open atmosphere, with the normal oxygen concentration (21% by volume). Consequently, flames appear when the combustible gases are ignited with spark ignition located above the sample.

4.2.2 Results for dry samples

Already mentioned earlier, dry and wet samples were used in the cone calorimeter experiments. The MDF samples were first dried to drive out the moisture content. The samples are weighed to know the initial weight of the sample. Then, the samples are placed in the dryer for 24 hrs at 104^0C overnight. The sample weight was measured after 18 hrs and after 24 hrs in order to confirm that there was no futher change in the sample weight. This gives the final weight of the dry samples. The difference with the initial weight gives the amount of moisture driven out of the solid during the drying process. Initially, all dry samples weight was 110 gm. Several experiments have been conducted for each level of external heat flux, in order to obtain an impression on 'repeatability' of the results.

For a qualitative point of view, the following stages can be distinguished during the experiments:

- heat-up of the sample: a rise in surface temperature is observed;
- white smoke leaves the sample; this corresponds to moisture evaporation (even after carefully drying the samples, some water always remains);
- the sample surface becomes light brown;
- the sample surface becomes dark brown;
- dark smoke leaves the sample;
- first flashes of flames are seen;
- flames are established by ignition of a flammable gas/air mixture;
- cracks appear on the sample surfaces;
- the flames 'sit' on these cracks;
- tar is seen (not with 50 kW/m^2 heat flux);
- cracks, formed on the surface, widen and the flames form to full height and burn. volume shrinkage is obsevred as these flames cover the entire solid surface;
- the external heat flux is switched off, 3mins after the flames extinguish;
- the solid glows on its own until the entire solid has transformed into ash without any further external heat source.

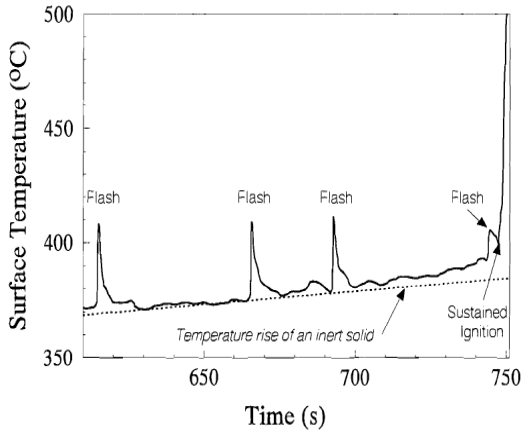

Figure 4.3: Surface temperature evolution during flashes and sustained ignition for a piloted ignition experiment on a horizontal red oak sample exposed to 18.8 kW/m^2 external heat flux, [7]

The above stages are very well discussed by A. Atreya [7]. The figure 4.3 shows the instances when the surface temperature rises to a higher value before a sustained ignition is established on the solid surface. These flashes are momentary unsustained flaming, reported by Atreya et al. [6].

The thermocouples used in the experiments have a uncertainity in temperature measurement around $\pm 3 \sim 5$. In principle, due to symmetry, the measurements at each of the depths must be 'identical'. There is no perfect symmetry in reality, but differences are not large.

Figures 4.4 through 4.6 reveal that there is some spreading in the temperature measurements, in particular when results from different tests are compared. Even though repeatability is not perfect, in general, the quality of the measurements as satisfactory to serve the purpose.

Figure 4.4 shows the temperature evolution in the solid at different depths, when the solid is exposed to 20 kW/m^2 external heat flux. The top left figure shows the front surface

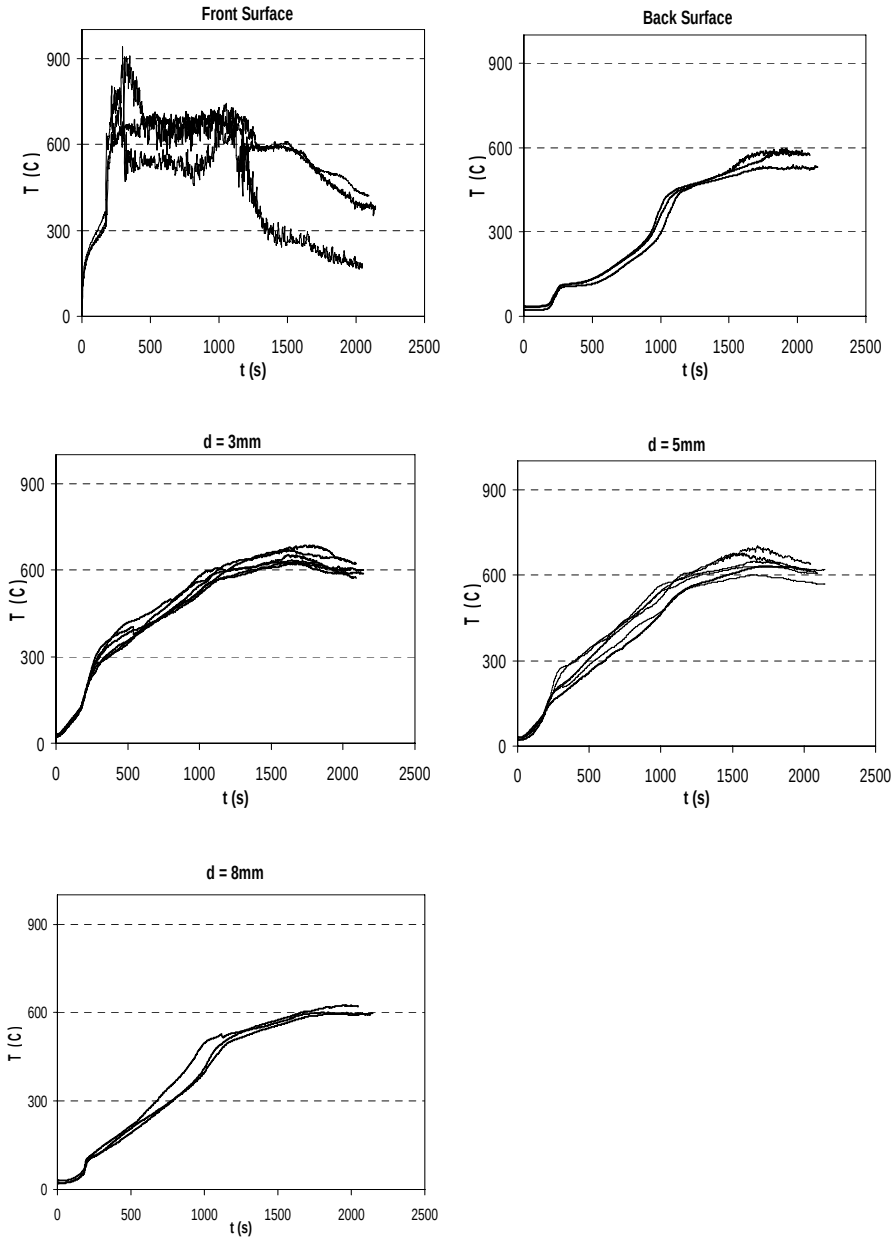

Figure 4.4: Evolution in time of temperature (dry sample). Top left: front surface temperature ; top right: back surface temperature; middle left: depth=3 mm; middle right: depth=5 mm; bottom left: depth=8 mm. Note: thermocouple at front surface detaches during the experiments. External heat flux=20 kW/m^2.

temperature evolution in time. The surface temperature starts to rise from the beginning. After reaching a certain temperature, a sudden temperature rise is observed. Depending on the external heat flux, this temperature varies in the range 300-350^{0}C. For 20 kW/m^2, this happens after about 200 s (for 30 kW/m^2, this already happens after 80 s and for 50 kW/m^2 already after 35 s). At this time, flames start to develop and the flame heat flux adds up to externally imposed heat flux. The flames formed tend to stay on the surface

untill the cracks develop, as the surface disintegrates. These cracks widen and the solid ruptures, making way for the flames to develop futher. Around 1200 s, there is a drop in the surface temperature indicating that pyrolysis process has reached its final stage. Around this time the flames weaken and start to extinguish. This is also seen with a decrease in the front surface temperature. Also, the other reason is the front surface thermocouple also detached from the surface due to the surface deformation.

Looking at the temperature distribution, there are some interesting things to observe. There is a plateau around 100^0C. This was observed even though the solid was dried. The plateau is more pronounced for the deeper temperatures. The reason for this is due to the remaining moisture that moves out of and into the solid during evaporation. The moisture that moves into the solid condenses, due to lower temperatures. When this zone is heated further, due to higher content, the evaporation leads to the plateau, also observed in the work of Fredlund [45].

It is also instructive to notice the different stages inside the material, e.g. at 5 mm depth. When the solid is exposed to external heat flux, the solid heats up. Until the onset of pyrolysis, the material heats up. Then, a steeper rise in temperature is observed, due to the added flames heat fluxes. This continues for some time until pyrolysis process lasts, i.e. there is mass flow rate of gases coming out of the solid undergoing pyrolysis. The temperature rise becomes weaker again when the flames become weaker (mentioned earlier). Finally, the temperature starts to decrease (as the flames extinguish and the external heat flux is switched off).

Figure 4.5 and 4.6 show similar results. Obviously, the end temperatures are higher and the pyrolysis process is faster as the external heat flux increases.

Figure 4.7 shows the evolution of the sample mass in time for the three imposed heat fluxes. From these results, the mass loss rate is computed as [107].

- For the first scan ($i = 0$):

$$-\left[\dot{m}\right]_{i=0} = \frac{25m_0 - 48m_1 + 36m_2 - 16m_3 + 3m_4}{12\Delta t} \tag{4.1}$$

- For the second scan ($i = 1$):

$$-\left[\dot{m}\right]_{i=1} = \frac{3m_0 + 10m_1 - 18m_2 + 6m_3 - m_4}{12\Delta t} \tag{4.2}$$

- For any scan for which ($1 < i < n - 1$):

$$-\left[\dot{m}\right]_{i} = \frac{-m_{i-2} + 8m_{i-1} - 8m_{i+1} + m_{i+2}}{12\Delta t} \tag{4.3}$$

- For the next to last scan ($i = n - 1$):

$$-\left[\dot{m}\right]_{i=n-1} = \frac{-3m_n - 10m_{n-1} + 18m_{n-2} - 6m_{n-3} + m_4}{12\Delta t} \tag{4.4}$$

- For the last scan ($i = n$):

$$-\left[\dot{m}\right]_{i=n} = \frac{-25m_n + 48m_{n-1} - 36m_{n-2} + 16m_{n-3} - 3m_{n-4}}{12\Delta t} \tag{4.5}$$

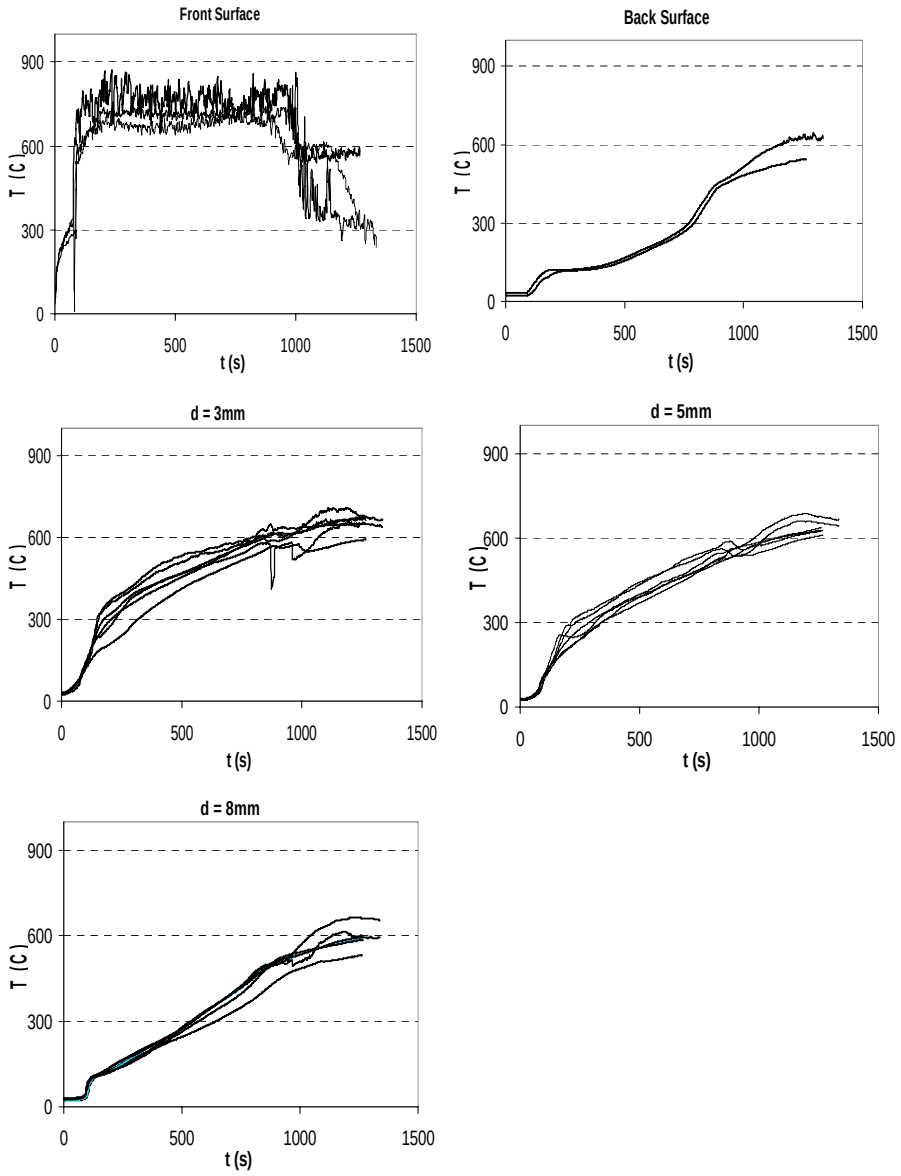

Figure 4.5: Evolution in time of temperature (dry sample). Top left: front surface temperature ; top right: back surface temperature; middle left: depth=3 mm; middle right: depth=5 mm; bottom left: depth=8 mm. Note: thermocouple at front surface detaches during the experiments. External heat flux=30 kW/m^2.

This, however, gives rise to quite large fluctuations, when this is directly applied to the instantaneous mass measurements. Therefore, we use a running average over 10 instantaneous values:

$$[\dot{m}]_{avg,i} = \frac{\sum_{i}^{i+9} \dot{m}_i}{10} \tag{4.6}$$

Figure 4.7 shows the evolution of the sample mass loss (left column) and the mass flow rate of volatiles (right column) for three different levels of heat flux (20 kW/m^2, 30 kW/m^2 and 50 kW/m^2). Qualitatively, all curves look similar. As seen earlier, the pyrolysis process is

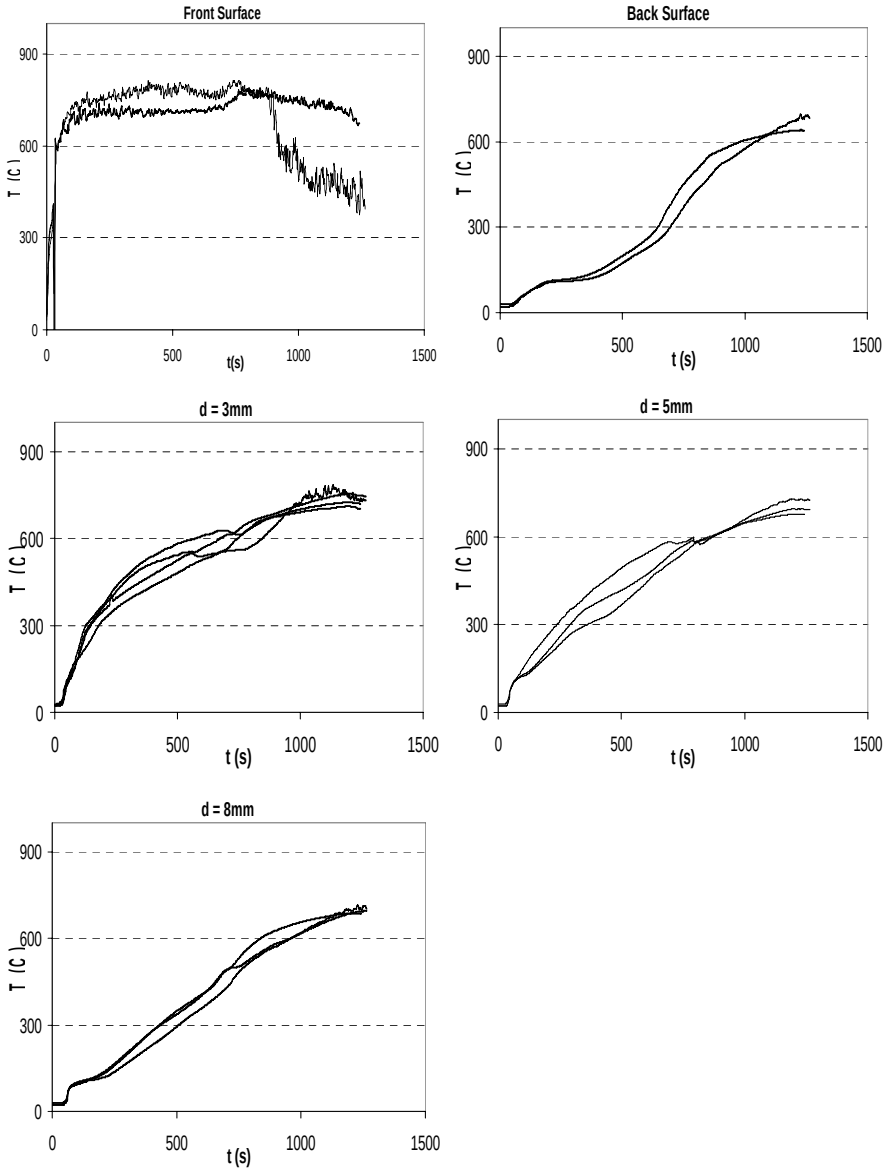

Figure 4.6: Evolution in time of temperature (dry sample). Top left: front surface temperature ; top right: back surface temperature; middle left: depth=3 mm; middle right: depth=5 mm; bottom left: depth=8 mm. Note: thermocouple at front surface detaches during the experiments. External heat flux=50 kW/m^2.

faster (and mass flow rates are higher) as the external heat flux is higher. At first, there is a slow decrease in the mass loss on the left column. This is mainly due to moisture evaporation that occurs at 100^0C. Even though the test sample was dried over night, there is still some remaining moisture in the solid that is driven out during the initial stage of pyrolysis process. Longer drying period was not taken in the experiments due to time restrictions of the author. When the surface temperature reaches about 320^0C, the solid undergoes a pyrolysis process. A steep decrease in mass or a sudden rise in the mass flow rate of volatiles is observed. During this stage, flames are formed. The mass flow rate decreases to a certain plateau as the endothermic pyrolysis process consumes energy. The developing char layer also acts as a resistance to the flow of volatiles. A quasi-steady state is observed, where heat is lost by conduction into the virgin solid. When the thermal front

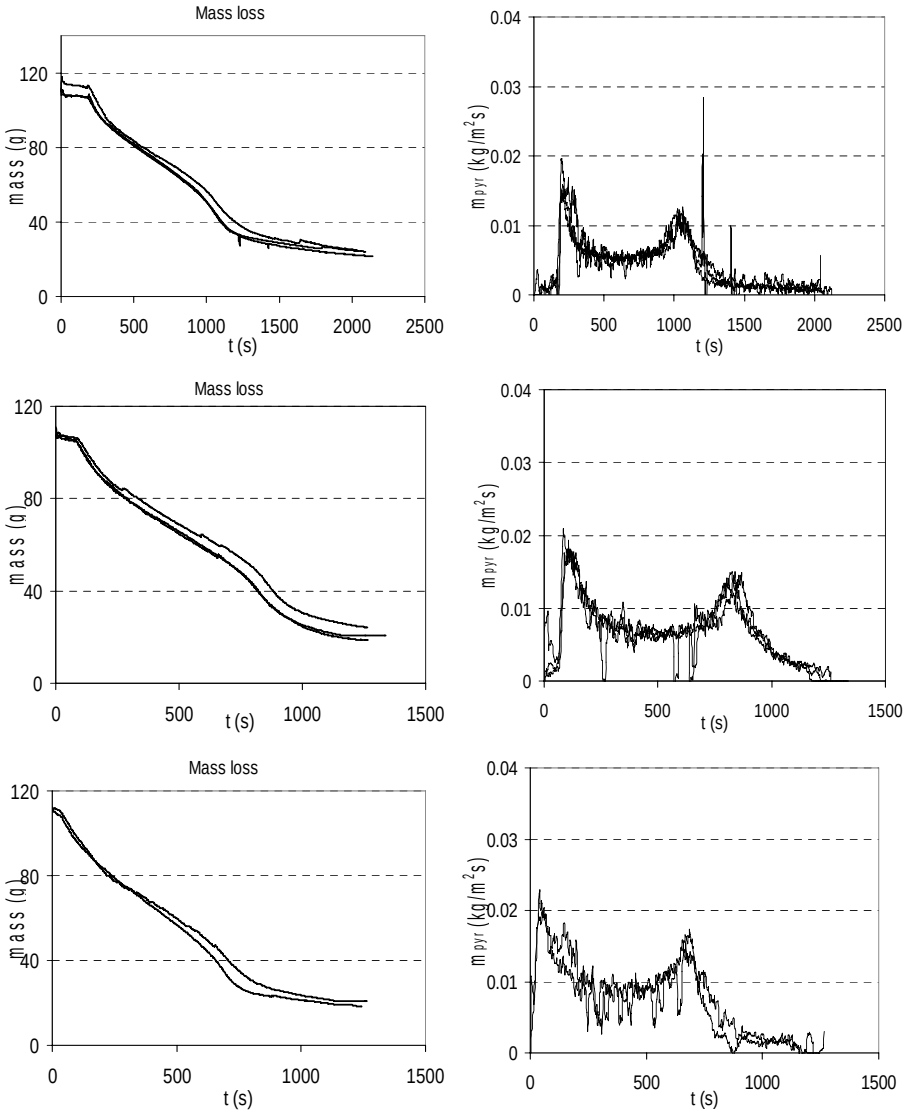

Figure 4.7: Evolution in time of mass (left column) and gas mass flow rate (right column). Top row: External heat flux=20 kW/m^2; middle row: External heat flux=30 kW/m^2; bottom row: External heat flux=50 kW/m^2.

approaches the well insulated back surface, a second peak is observed in the mass flow rate, known as the 'back effect' [103], as less heat is lost by conduction.

4.2.3 Results for Wet samples

The effect of unbound moisture on the pyrolysis process and the experimental observations are discussed. Only two levels of external heat flux (30 kW/m^2 and 50 kW/m^2) was applied on the (wet) solids. Qualitatively, the same stages are distinguished as reported in the previous section. More white smoke is released and this stage lasts longer when wet samples are exposed to heat flux. The solid samples has higher percentage of water compared to

dry samples around $6.5 \sim 7\%$. The moisture content was determined by comparison of the dried samples weight to the initial sample weight as:

$$MC\% = 100 \cdot \frac{\text{wt. of the original solid - wt. after drying}}{\text{wt. after drying}} \tag{4.7}$$

Figure 4.8 and 4.9 shows the temperature evolution in time. Apart from a larger flat

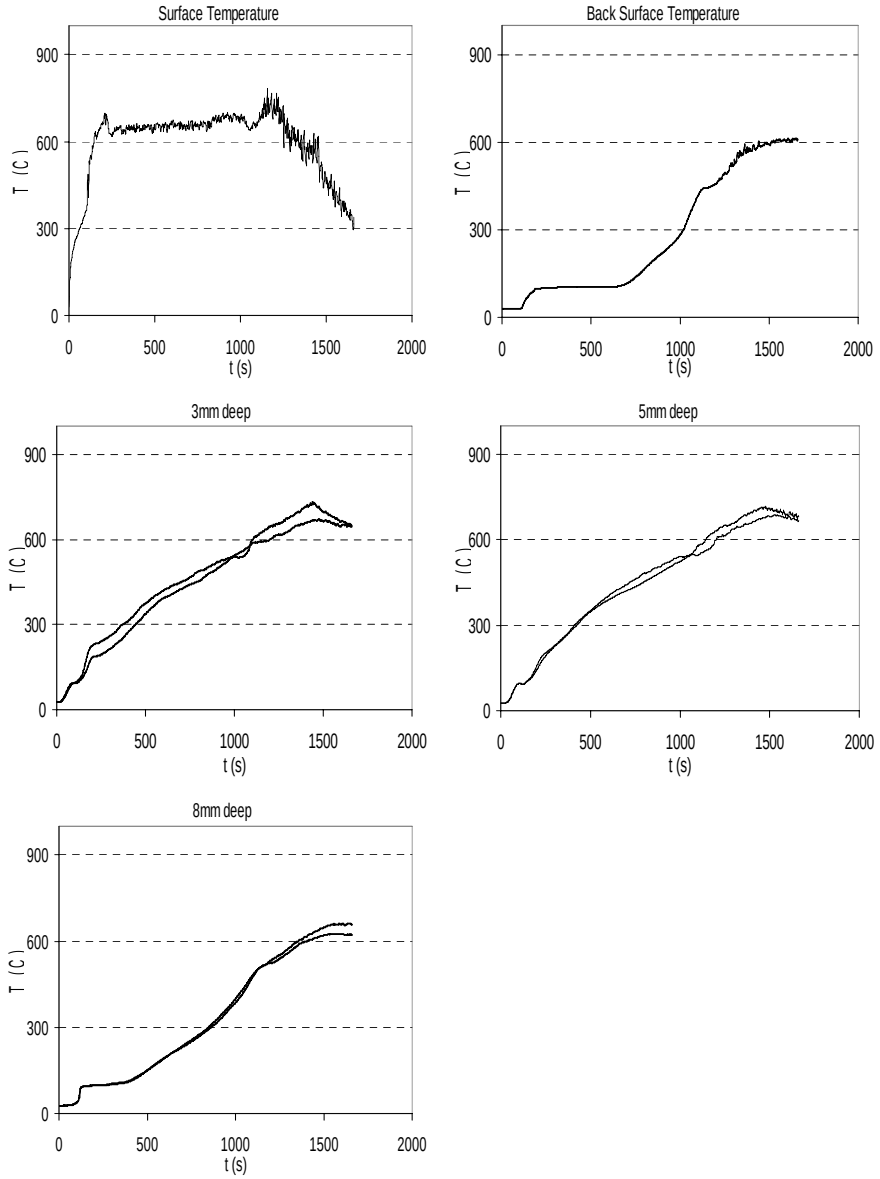

Figure 4.8: Evolution in time of temperature (wet samples, 6.5 ∼ 7% moisture). Top left: front surface temperature ; top right: back surface temperature; middle left: depth=3 mm; middle right: depth=5 mm; bottom left: depth=8 mm. Note: thermocouple at front surface detaches during the experiments. External heat flux=30 kW/m^2.

plateau around 100^0C, due to moisture evaporation, the profiles are very similar to what was described for the dry samples. In particular, the evolutions are very similar once the moisture is out of the sample. The duration of the pyrolysis process is increased.

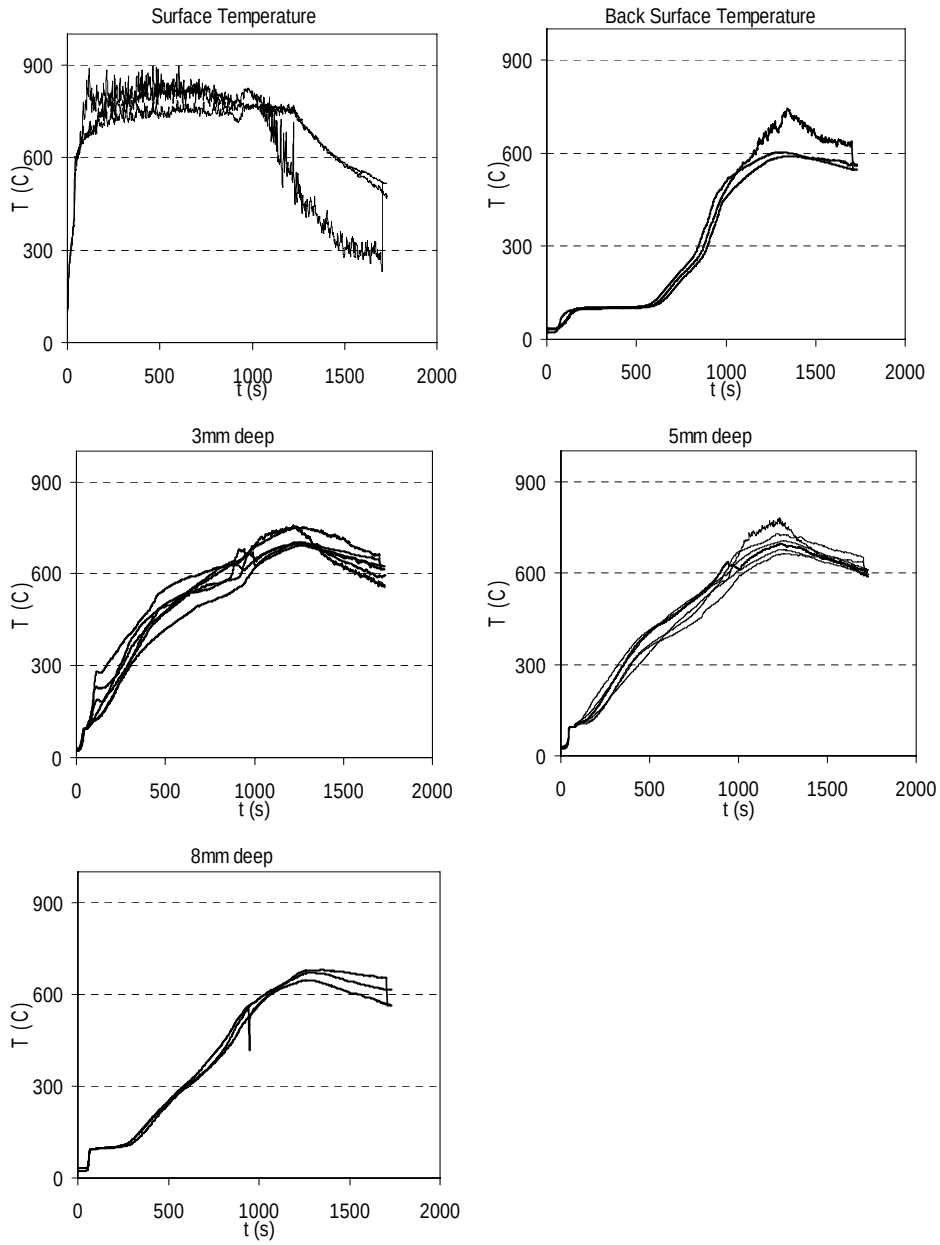

Figure 4.9: Temperature evolution in time (wet samples, 6.5 ∼ 7% moisture). Top left: front surface temperature ; top right: back surface temperature; middle left: depth=3mm; middle right: depth=5 mm; bottom left: depth=8 mm. Note: thermocouple at front surface detaches during the experiments. External heat flux=50 kW/m^2.

Figure 4.10 shows the mass loss (left) and mass flow rates (right). The initial mass loss is quick compared to dry samples, due to the moisture evaporation. When pyrolysis starts, also pyrolysis gases flow out leading to an increased mass loss rate. Here, the total mass flow rate (i.e. the sum of evaporation mass flow rate and the pyrolysis gases mass flow rate) is measured. When the pyrolysis front approach back surface, the back effect [102] is again observed, as in the case of dry MDF samples.

In general, the pyrolysis process takes somewhat longer time than for the dry samples. This

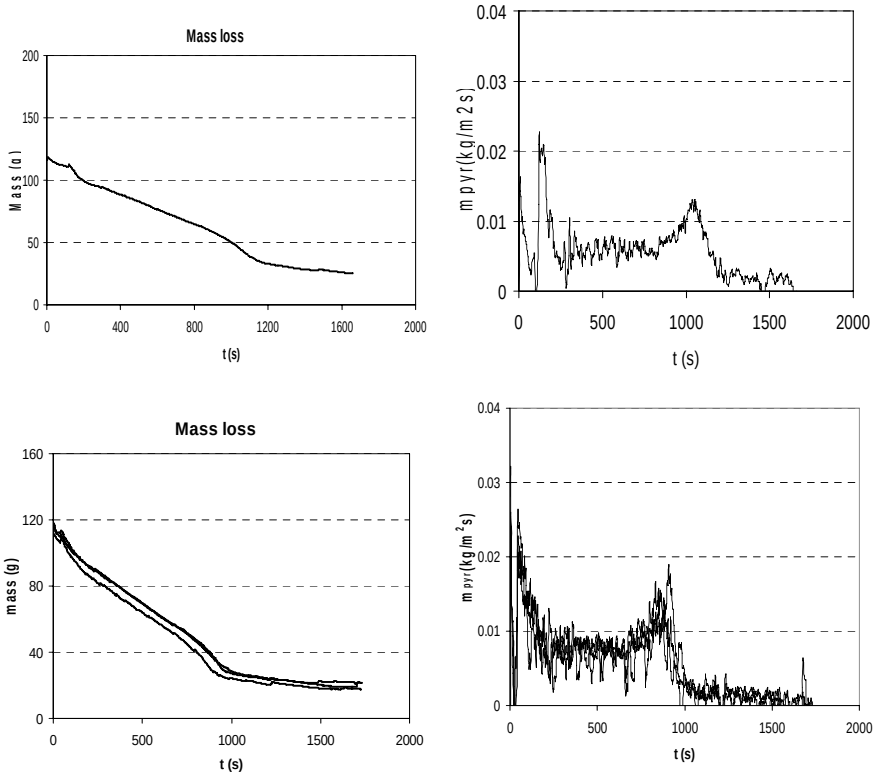

Figure 4.10: Evolution in time of mass (left) and gas mass flow rate (right). First row: External heat flux=30 kW/m^2; second row: External heat flux=50 kW/m^2.

is logical, as more water evaporates, which consumes energy that is otherwise available for the endothermic pyrolysis process. On the other hand, pyrolysis duration has decreased with the increase in the external heat flux. This is again similar to the dry MDF sample results.

4.3 Numerical simulation results

4.3.1 Cone calorimeter experiments

Now, the numerical simulation results for the cone calorimeter experiments are discussed. The experiments were performed in open atmosphere, so that flames are seen when the volatiles are ignited with a spark ignition placed above the retainer frame. These flames provide additional heat flux to the solid during pyrolysis. In the simulations, this is performed by means of an additional heat flux at the front surface. We assume this heat flux to be constant throughout the experiment. The rationale is that, even though the flame height varies during the experiments, the radiative flux need not change too much as long as the maximum temperature does not change significantly. The sides and back surface are perfectly insulated and impervious to pyrolysis gases. This resembles a one-dimensional heat transfer problem. The solid thickness is 1.65 cm. In numerical simulations, the computational mesh contains 33 cells ($\Delta x = 5.0 \times 10^{-2}$ m). The time step size of 0.5 s is used.

The external heat flux $\dot{q}''_{ext}$ of 20 kW/m^2, 30 kW/m^2 and 50 kW/m^2 is applied on the front surface.

The material properties for the medium density fibre (MDF) board samples [126] used in the simulations are put in table 4.1.

Properties	Value	Units
$\rho_{v,w}$	735	kg/m^3
$\rho_{v,d}$	690	kg/m^3
ρ_c	140	kg/m^3
$c_{v,l}$	4184	J/(kgK)
$c_{v,d}$	2000	J/(kgK)
c_c	2000	J/(kgK)
$k_{v,w}$	0.38	W/(mK)
$k_{v,d}$	0.36	W/(mK)
k_c	0.2	W/(mK)

Table 4.1: Thermo-physical properties of medium density fibre board [126]

The thermophysical properties obtained for the char is not easy to get. And it is not a fundamental property. The model parameters used in the simulations are: $\Delta Q_{pyr} = 4 \times 10^5$J/kg, T_{amb}=300 K, T_{pyr}=598 K. The convective heat transfer coefficient h = 5.0 W/m^{2}K, emissivity $\epsilon = 0.9$ and $\sigma = 5.67 \times 10^{-8}$ W/(m^{2}K^4).

The flame heat flux of 10 kW/m^2 is used as a rough estimate. For flames of 700 ^{0}C, this corresponds to a net absorption by the front surface of 20% of the black body emissive power of the flames. Note that the same value was reported for the experiments in [37] on pine samples. The radiation loss from the front surface to the surroundings is also explicitly considered.

The boundary conditions at the front surface are summarised as follows:

- prior to pyrolysis ($0 < t < t_{\text{start}}$)

$$\dot{q}''_{net} = \dot{q}''_{\text{ext}} - h(T_s - T_{\text{amb}}) - \epsilon\sigma T_s^4 \tag{4.8}$$

- during pyrolysis ($t_{\text{start}<t<t_{\text{end}}}$)

$$\dot{q}''_{net} = \dot{q}''_{\text{ext}} + \dot{q}''_{\text{flame}} - h(T_s - T_{\text{flame}}) - \epsilon\sigma T_s^4 \tag{4.9}$$

- immediately after pyrolysis ($t_{\text{end}} < t < t_{\text{end}} + 180s$)

$$\dot{q}''_{net} = \dot{q}''_{\text{ext}} + \dot{q}''_{\text{flame}} \cdot \exp\left(-\frac{t - t_{\text{end}}}{\tau_{\text{flame}}}\right) - h(T_s - T_{\text{flame}}) - \epsilon\sigma T_s^4 \tag{4.10}$$

- more than three minutes after the end of pyrolysis ($t > t_{\text{end}} + 180s$)

$$\begin{aligned}\dot{q}''_{net} = \dot{q}''_{\text{ext}} \cdot \exp\left(-\frac{t - t_{\text{end}} - 180}{\tau}\right) + \dot{q}''_{\text{flame}} \cdot \exp\left(-\frac{t - t_{\text{end}}}{\tau_{\text{flame}}}\right) \\ - h(T_s - T_{\text{flame}}) - \epsilon\sigma\left(T_s^4 - T_{\text{amb}}^4\right)\end{aligned} \tag{4.11}$$

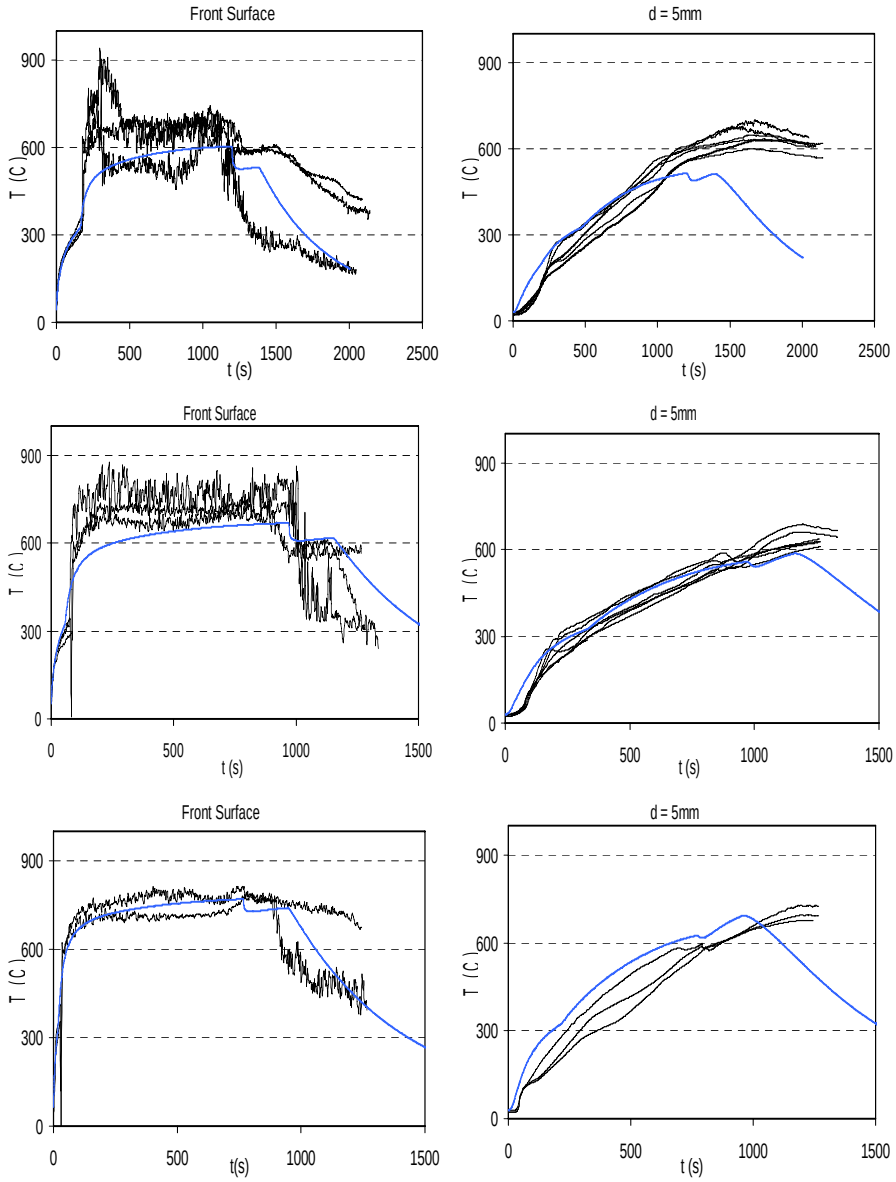

Figure 4.11: Evolution in time of temperature (dry sample). Left: front surface temperature; right: depth = 5 mm. top: external heat flux = 20 kW/m^2; middle: 30 kW/m^2; bottom: 50 kW/m^2. blue line: numerical simulations; black lines: experiments

Figure 4.11 shows the temporal evolution of the temperature, at the front surface (left) and at depth=5 mm (right) for the dry MDF samples. The smooth line is the simulation results from the enthalpy model. The surface temperature rise is mainly due to external radiation falling on the surface. As soon as the surface temperature reach the pyrolysis temperature, flames are generated. These flames add to the external heat flux leading to a sudden rise in the surface temperature. The model predicts all the events very well. The numerical simulation results in good agreement with the results from experiments.

Figure 4.12 shows the temperature evolution in time for wet MDF samples exposed to 30 kW/m^2 and 50 kW/m^2 external heat flux. There is no large difference between the dry and wet samples, except the plateau at 100^{0}C being more pronounced, due to moisture evapo-

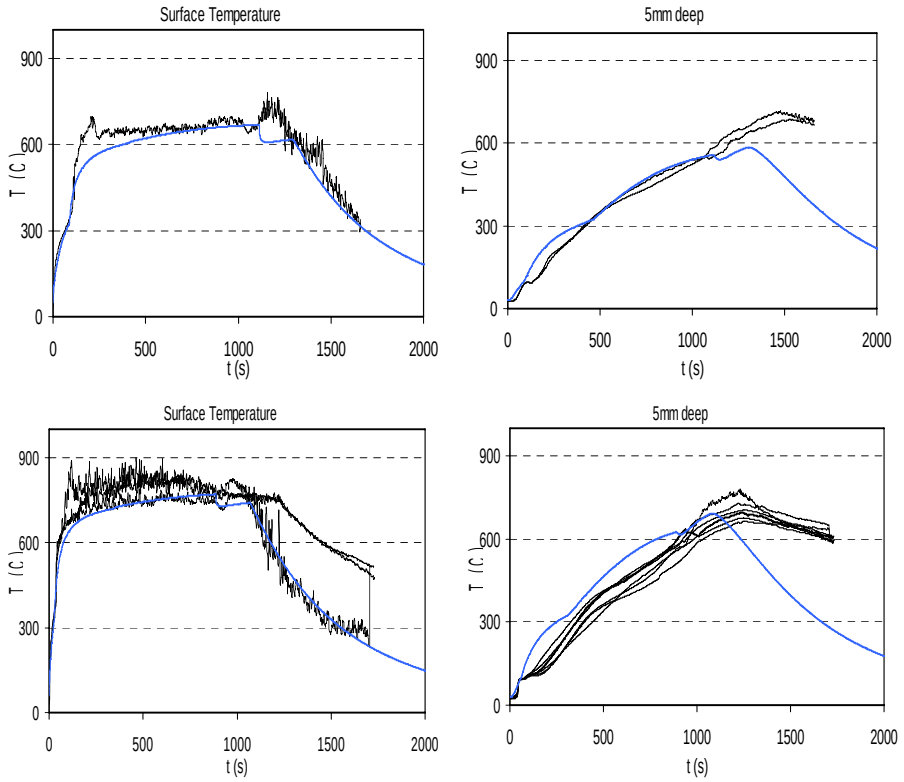

Figure 4.12: Evolution in time of temperature (wet sample). Left: front surface temperature; right: depth = 5mm. Top: external heat flux = 30kW/m^2; bottom: 50kW/m^2. blue lines: numerical simulations; black lines: experiments.

ration (moisture content-6.5 $\sim$ 7%). Again, the model predictions are in good agreement with the experiments.

Figure 4.13 shows the mass loss rate in time for the dry (left) and wet (right) samples when exposed to three different intensities of external heat flux 20, 30 and 50 kW/m^2. At the start of the simulation, the model shows the release of moisture from the solid in the form of water vapor for wet MDF samples (see figure 4.13, right column). The start of pyrolysis process in the solid is well predicted by the model. Note that the mass flow rate seen is the total mass flow rate of gases coming from the solid. This is the sum of the water vapour and the pyrolysis gases mass flow rates in case of wet charring materials. During the finite pyrolysis stage, the second peak is well predicted. When the evaporation front x_{evap} reaches the back surface, the mass flow rate drop as there is only the pyrolysis gases flow rate.

Till now, heat supplied from the external source and the flames was used for both evaporation and pyrolysis process. After the evaporation front reach the back surface, heat is only utilised for pyrolysis process. This accelerated the pyrolysis seen with the rise in the pyrolysis gases mass flow rate, also seen in chapter 3. All these events are well captured by the model. In the numerical simulations, volatiles mass flow rate drop to zero when the pyrolysis front reaches the back surface. But, in experiments the volatiles release continues longer, mainly due to char oxidation, etc.

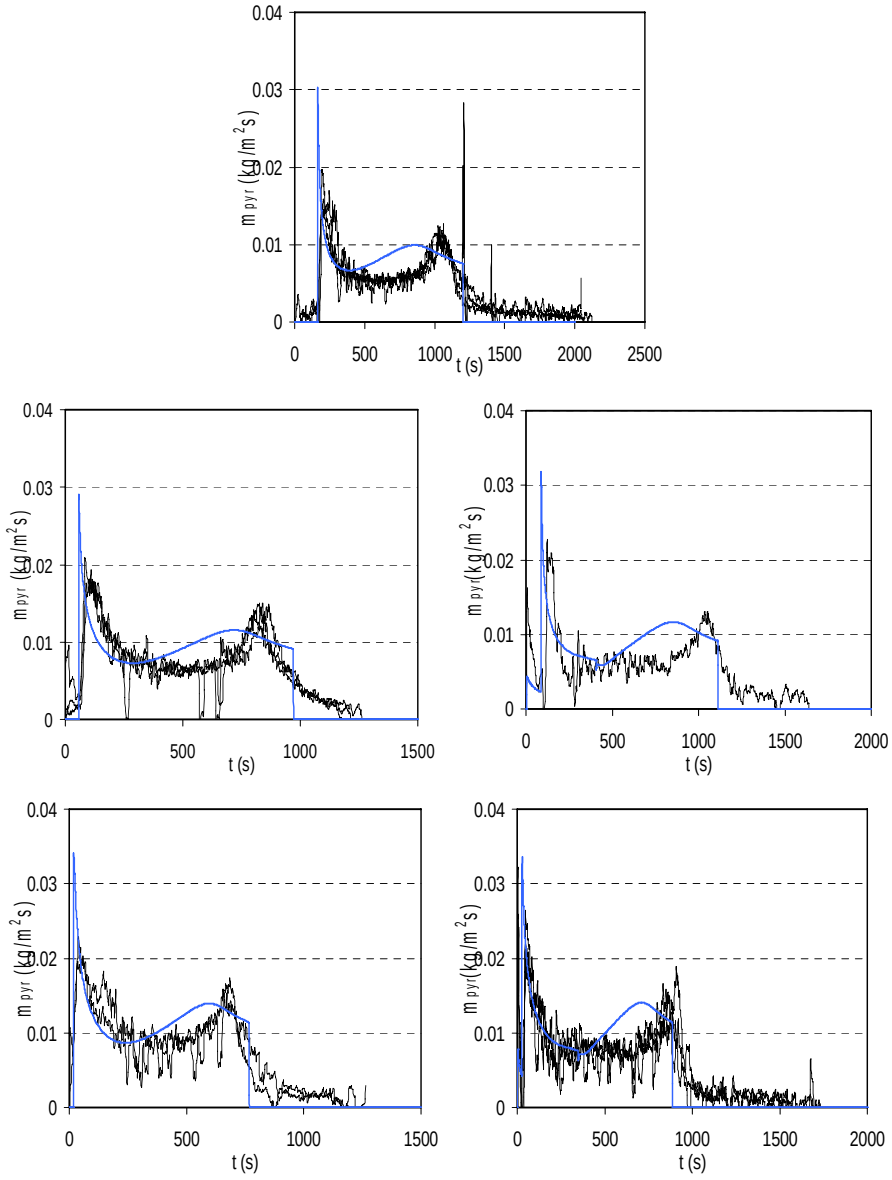

Figure 4.13: Evolution in time gas mass flow rate for dry samples (left) and wet samples (right). Top: external heat flux = 20 kW/m^2; middle: 30 kW/m^2; bottom: 50 kW/m^2

4.3.2 Sensitivity study

The effect of four different parameters: heat of pyrolysis, ΔQ_{pyr}, emissivity, ϵ, convective heat transfer coefficient, h and flame heat flux, q_{flame}, on mass flow rate of pyrolysis gases is studied. The material properties used in the numerical simulations are taken from table 4.1.

Figure 4.14 (top) shows the effect of heat of pyrolysis ΔQ_{pyr} on the mass flow rate. The mass loss rate increases with decrease in the heat of pyrolysis, because the heat required

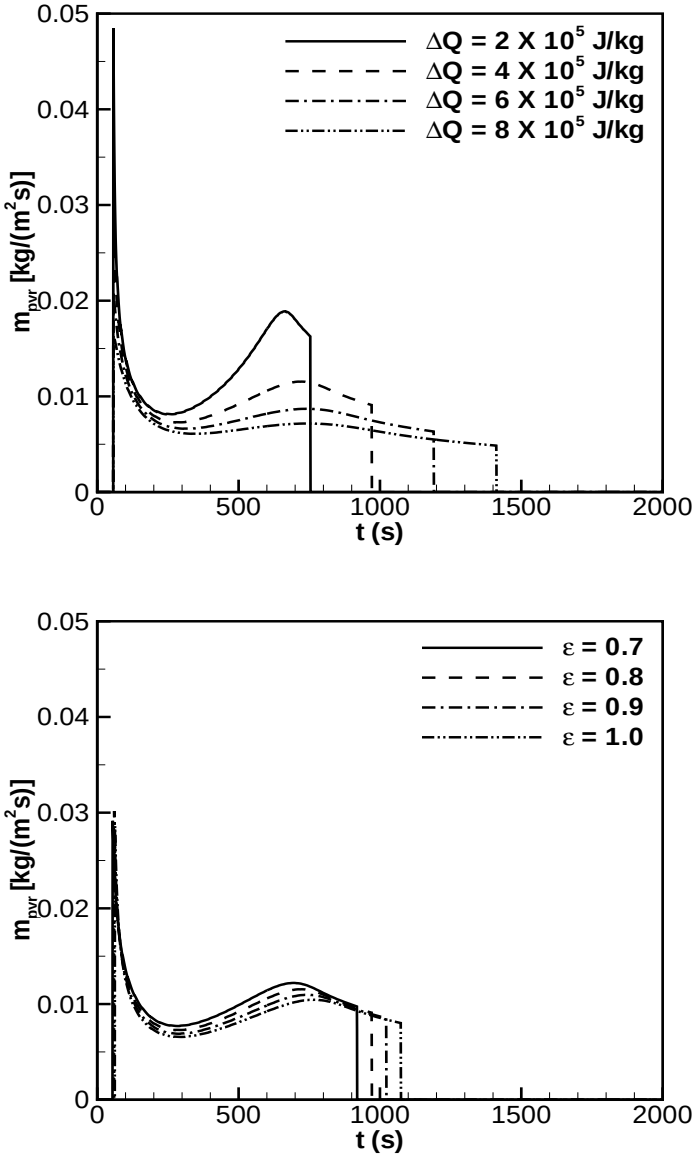

Figure 4.14: Pyrolysis gases mass flow rate in time. Top: Effect of heat of pyrolysis ΔQ_{pyr}; Bottom: Effect of epsilon ϵ

to pyrolyse the material is less and the pyrolysis temperature is reached quickly. This also results in a decrease in time taken to complete the pyrolysis process. The impact of this value is more pronounced in the second half of the pyrolysis process, during the finite pyrolysis stage (i.e., when thermal front has reached the back surface of the solid). The bottom figure shows the effect of emissivity. Obviously, increase in emissivity ϵ decreases the mass flow rate, and increases the duration of pyrolysis process, due to increase in the heat loss from the front surface in the form of radiation. This loss dominates if the surface temperature is high.

Figure 4.15 (top) shows the effect of front surface convective heat transfer coefficient h_s on

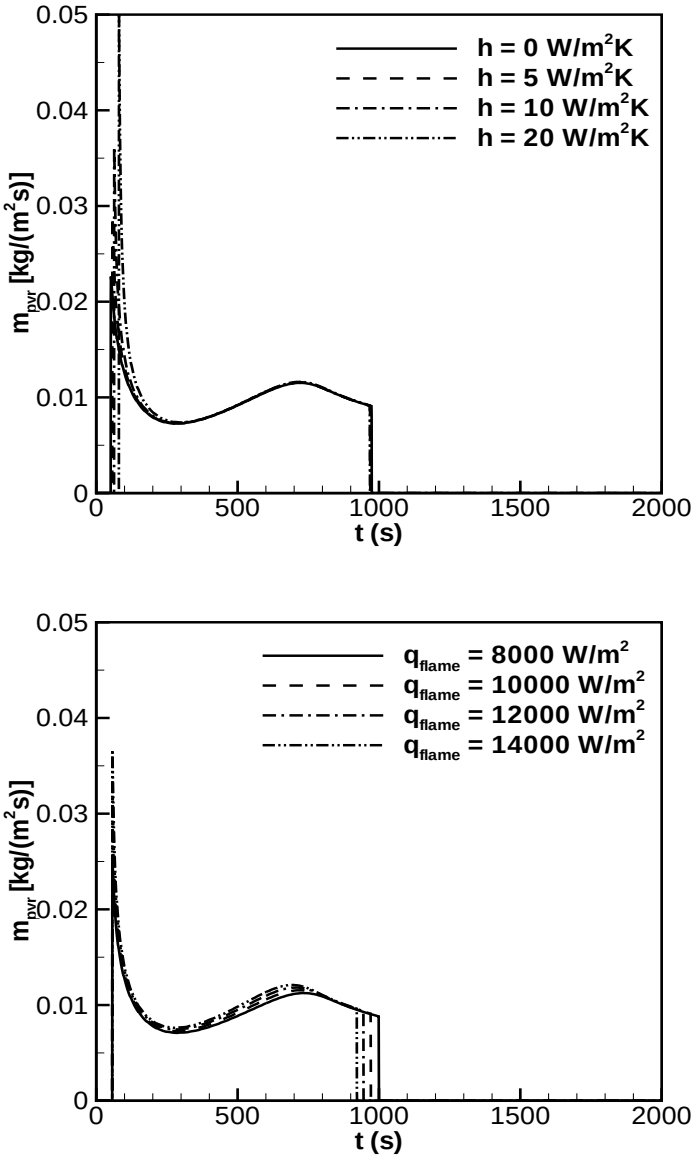

Figure 4.15: Pyrolysis gases mass flow rate in time. Left: Effect of heat transfer coefficient h; Right: Effect of flame heat flux q_{flame}

the mass flow rate. As seen in chapter 3, this value only affects the heat up phase and the infinite heating pyrolysis stage. Increase in the value of heat transfer coefficient will delay the start of the pyrolysis process, as heat is lost in the form of convection from the front surface, thus reducing the surface temperature. Figure 4.15 (bottom) shows the effect of flame heat flux on the mass flow rate of volatiles. Flame heat flux is only seen after pyrolysis starts; hence it does not alter the start of the process, but accelerates the pyrolysis process by providing additional heat to the solid. Increase in the flame heat flux decreases the duration of pyrolysis process.

Figure 6.10 shows the effect of pyrolysis temperature on mass flow rate of volatiles. With

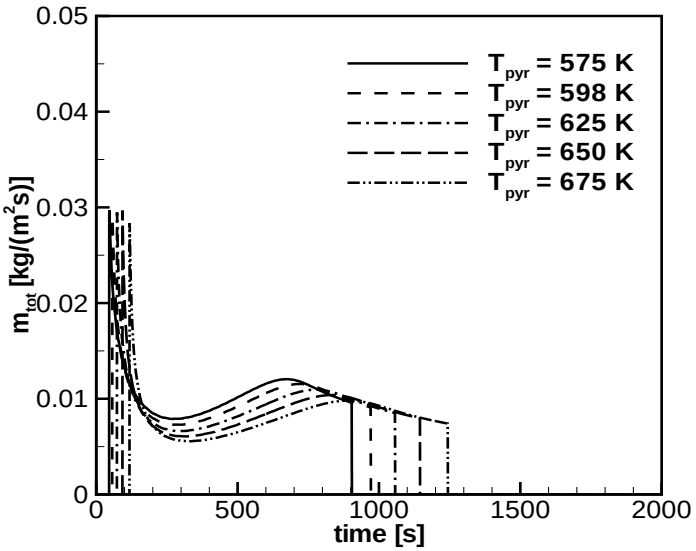

Figure 4.16: Effect of Pyrolysis temperature T_{pyr} on pyrolysis gases mass flow rate in time

the increase in the pyrolysis temperature T_{pyr}, the evolution of pyrolysis gases is delayed. Obviously the higher the pyrolysis temperature, the longer it takes for pyrolysis to begin. As seen in section 3.1.10, the mass flow rate peak value becomes lower, due to slower pyrolysis front motion. Also, the duration of pyrolysis process is long with higher T_{pyr}.

4.4 Conclusion

In this chapter, cone calorimeter experimental results for dry and wet MDF samples in the form of mass loss, mass flow rate of volatiles and the temperature distribution at different depths in the solid, were discussed. Numerical simulations were conducted to compare the model results with the experiments. Good agreement between the cone calorimeter experiments and numerical simulation results using enthalpy based model were observed.

5

Two-dimensional case study

5.1 Introduction

Flame spread over the surface of solid fuels is very important in the development of fire. For a flame to spread on the solid surface, it is essential that the flame provides sufficient heat to the unburnt solid ahead of the flame. The vaporised fuel mixes with the oxygen to oxidise, generating a flammable mixture ahead of the flame leading edge. The rate of flame spread is defined by the ability of the flame to heat the solid to pyrolyse and to ignite the combustible gases coming out of the heated solid. The shape of the flame also determines the heat that will be transferred to the unburnt solid ahead of the pyrolysing front. Flame spread is classified into 2 modes: co-current and counter current flame spread.

When the gas flow (either naturally induced or forced) opposes the direction of spread, the flow keeps the flame close to the surface downstream of the pyrolysis front, deterring the heat transfer by radiation and convection ahead of the flame. This type of spread, which is commonly known as 'opposed flow flame spread', is generally slow. This flame spread is controlled by the interaction between processes dominated by heat transfer from the flame to the solid and by gas phase chemical kinetics. For thermally thick solids, the spread rate increases with the flow velocity in the heat transfer dominated regime because the flame is pushed closer to the fuel surface enhancing the transfer of heat to the solid ahead of the flame.

On the other hand, if the gas flow is in the direction of spread, the flame is pushed forward ahead of the pyrolysis region, which favours the transfer of heat from the flame to the unburnt material, and results in a quick flame spread process. This is termed as the 'wind aided flame spread', seen in the upward flame spread in natural convection or forced flow moving in the direction of flame propagation. The gas flow pushes the flame ahead of the

pyrolysing region providing heat of the unburnt solid (radiation dominated).

Natural convection causes concurrent flow in upward flame spread and opposed flow in downward flame spread configurations. Heat transfer from the flame to the solid fuel ahead of the pyrolysis front is the controlling mechanism of flame spread and the gas phase has an effect on the flame spread rate primarily through the characteristics of the flame (length, temperature and soot) [33].

Flame spread is affected by the following parameters:

- Effect of turbulence: Turbulence enhances the fuel vapour/oxidiser mixing but could also cool the reacting gas by entrainment of ambient gas. In opposed flame spread, increasing turbulence should increase the flame spread in the solid heating dominated regime and decrease the flame spread rate in the chemical kinetics dominated regime. For concurrent flame spread, turbulence has a strong dependence on the surface heat flux and flame length. The surface heat flux is large in turbulent flow compared to laminar flow. A large surface heat flux not only reduces the heat up time but also increases the pyrolysis rate and through it the flame length.
- Effect of radiation: The incident radiation on the solids plays a major role during flame spread. The effect of the external radiation causes the surface temperature to rise to the pyrolysis temperature, which in turn influences the flame spread phenomena. In Quintiere's review paper [87], it is suggested that radiant heating from the fire, smoke and heated surface is the driving force behind fire growth on materials. The flammability diagram (incident heat flux(kW/m^2) vs. flame spread velocity (cm/s)) shows the behaviour of the material, presenting the time to ignite with a pilot ignition, peak or steady-state energy release rate per unit area and, upward and downward flame spread rate.
- Effect of charring: The development of char may reach a level at which the solid cannot sustain flame spread. The char has a lower thermal conductivity, which makes the heat conduction to the pyrolysis front difficult, thus decelerating the pyrolysis process within the solid.
- Effect of gravity: Flame spread through the buoyancy-driven flows generated by the density gradient in the flame vicinity plays a major role in radiation feedback. With increasing or decreasing gravity, the flow velocity varies; flame spread in low gravity is of particular interest in spacecraft safety. This is the case when the gas velocities are the same as the diffusion velocities.

There are other important parameters that contribute to some extend, such as the orientation, material aspects like grain boundary, oxygen content, presence of inert substances or fire retardants, etc.

5.2 Ignition criteria

The heat conduction into the solid results in the pyrolysis of the solid, leading to flame spread. The minimum intensity of heat flux required to achieve the ignition is called the 'critical flux for ignition'. Another concept refers to the 'ignition temperature', T_{ig}. The

basic theory behind these phenomena, which depends on the dimension and behaviour of the solid, i.e. thermally thin and thermally thick solids, is discussed in [86, 87].

5.2.1 Thermally thin solids

Thermally thin solids are those materials which show no spatial, internal temperature gradients. In other words, the solid reaches a uniform temperature before pyrolysis begins, as explained in chapter 3. The thickness of the solid is less than the thermal penetration depth ($\delta = \sqrt{\alpha t}$). The ignition time for the thermally thin materials is given by [86]:

$$t_{ig} \approx \frac{\rho c d \left(T_{ig} - T_{\infty}\right)}{\dot{q}''_{ext}} \tag{5.1}$$

5.2.2 Thermally thick solids

Thermally thick solids are those materials whose back boundary condition has a negligible effect on the numerical simulation results. The solid behaves as a semi-infinite solid during the early stage of the pyrolysis process. The ignition time for the thermally thick materials is given by [86]:

$$t_{ig} \approx \frac{\pi}{4} \rho c k \left(\frac{T_{ig} - T_{\infty}}{\dot{q}''_{ext}}\right)^2 \tag{5.2}$$

5.3 Flame spread velocity

After discussing the criteria responsible for the flame spread phenomena, the focus now lies on the development of flame spread modelling. The fundamental equation of flame spread, using the concept of 'surface of fire inception[1]', was given by Williams (1976) as:

$$\rho V_{pyr} \Delta h = \dot{q}''_f \tag{5.3}$$

where ρ is the density of the solid medium, V_{pyr} is the spread rate, $\Delta h = c_p(T_{ig} - T_s)$ is the enthalpy change per unit mass of medium from initial surface temperature T_s to ignition temperature T_{ig}, and $\dot{q}''_f$ is the net heat flux provided by the flames. The ignition temperature, T_{ig}, is the lowest surface temperature of the solid to sustain a piloted ignition.

To make the flame spread over the solid surface, enough heat has to be transferred to the unburnt solid to bring the solid to a higher temperature ahead of the flame to pyrolyse the solid. According to Williams [129], a material with lower density has a higher flame velocity

[1] This describes mass fires and defines the boundary between burning and non-burning fuel used by Emmons [33]

than the heavier one. Sibulkin and Kim [99], defined the steady flame spread rate V_{pyr} as the velocity of the moving ignition front on the combustible surfaces as:

$$V_{pyr} = \frac{\dot{q}_f^{''}\delta_f}{d\rho c_p(T_{ig}-T_s)} \qquad \text{thermally thin} \tag{5.4}$$

and

$$V_{pyr} = \frac{\dot{q}_f^{''2}\delta_f}{k\rho c_p(T_{ig}-T_s)^2} \qquad \text{thermally thick} \tag{5.5}$$

In the above equations (5.4) and (5.5), for thermally thick materials 'd' in the denominator of thermally thin materials, is replaced by $k\Delta T/\dot{q}_f^{''}$. Quintiere suggests another form of flame spread velocity for a continuous ignition. He considers a steady (or quasi-steady) situation and derives the movement over a heated length, δ_f, as the temperature rises from T_0 to T_{ig} in time t_{ig}. Here δ_f is the flame length $(y_f - y_{pyr})$. The flame spread velocity is:

$$V_{pyr} = \frac{\delta_f}{t_{ig}} \tag{5.6}$$

Hasemi [48] has offered a basic expression for upward flame spread for both thermally thin and thermally thick materials. The location of the pyrolysis front is given as a function of time by solving:

$$T_{ig} - T_0 = \int_0^t \dot{q}_w^{''}(x, t-\tau)\cdot\phi(\tau)d\tau \tag{5.7}$$

He uses the ignition temperature to begin with for a semi-infinite combustible wall. He proposes a term $\phi(\tau)$ which is an impulse response of the surface temperature to heat application. $\phi(\tau)$ depends on the wall conditions, but ignores the surface re-radiation just for simplicity. This impulse function is given by $\phi(\tau) = (\pi k\rho c_p\tau)^{-1/2}$. From equation (5.7) the above equation, assuming a constant $\dot{q}_w^{''}$ and steady flame spread velocity V_{pyr}, Hasemi replaces τ with y_{pyr}, where $y_{pyr} = -V_{pyr}\tau$. For a semi-infinite, thermally thick combustible wall, the flame spread velocity is:

$$V_{pyr} = \int_0^\infty \frac{\dot{q}_w^{''}(x-x_p+L_p)}{\sqrt{\pi k\rho c_p V_{pyr}(x-x_p)}}dx_p \tag{5.8}$$

For a thermally thin wall with Newtonian cooling, the impulse function can be represented as $\phi(t) = exp(-h_i t/\rho c_p d)$, where h_i is the heat transfer coefficient. The steady-state flame spread velocity is:

$$V_{pyr} = \frac{1}{\rho c_p d(T_{ig}-T_0)}\int_0^\infty \dot{q}_w^{''}(\xi + L_p)\cdot exp(\frac{-h_i\xi}{\rho c_p dV_{pyr}})d\xi \tag{5.9}$$

This equation is very similar to the equation proposed by Sibulkin (1977). It is thought that flame height is a function of the heat release rate or the mass flow rate of volatiles:

$$\dot{q}_w^{''} - \dot{q}_{rerad}^{''} = \Delta H_c\cdot\dot{m}_v^{''} \tag{5.10}$$

where $\dot{q}_{rerad}^{''}$ is the surface reradiation, which depends on the surface temperature and emissivity of the material.

5.4 Flame height correlations

Saito, Quintiere and Williams [94] studied upward flame spread of a flame along thermally thick charring and non-charring materials. They assumed steady flame spread over height,

i.e. $y_f - y_{pyr}$ remains approximately constant during the spread. Then the velocity of the pyrolysis front is given by:

$$V_{pyr} = \frac{y_f - y_{pyr}}{t_{ig}} \tag{5.11}$$

where t_{ig} is the characteristic ignition time for the material and y_f is the flame height/length. The value of y_{pyr} is unknown in the above equation, which is obtained from:

$$y_{pyr} = y_{pyr,0} + \int_0^t V_{pyr}(t_p)dt_p, \tag{5.12}$$

with $y_{pyr,0}$ being the initial value of y_{pyr} at time t=0. To find the value of y_f, a flame height correlation is required. The total rate of energy release per unit length is the sum $\left[\dot{Q}^{'} + q\int_0^y \dot{m}^{''}dx\right]$, where the pilot flame at the base of the wall releasing energy at the rate $\dot{Q}^{'}$ per unit length, $\dot{m}^{''}$ mass loss per unit area of the fuel, and q is the heat released per unit mass of fuel consumed. The basic equation used by Saito et al. for the flame height correlation is:

$$y_f = K\left(\dot{Q}^{'} + q\int_0^{y_{pyr}} \dot{m}^{''}dx\right)^n \tag{5.13}$$

Quintiere [84] proposed correlations to be able to interpret the wall heat flux from from the burner to the wall with, $\dot{q}^{'}$ and $y_f - y_{pyr}$, the flame heat flux and flame length, respectively. He proposed a correlation that is similar to Delichatsios et al. [39] for the flame height as:

$$y_f = 4.65\left(\frac{\dot{Q}_b^{'}}{c_p T_\infty \rho_\infty \sqrt{g}}\right)^{2/3} \tag{5.14}$$

where $c_p, T_\infty, \rho_\infty$ are the ambient air values, $\dot{Q}_b^{'}$ is the burner heat output and g is the acceleration due to gravity.

In general, flame height is defined as the length of the pre-heat zone from the flame tip to the pyrolysis front. The height of the wall flame is generally expressed in terms of the heat release rate as:

$$y_f = k_f(\dot{Q}^{'})^n, \tag{5.15}$$

with k_f is an empirical factor which depends on ambient conditions. Y. Hasemi [48] modified the above equation for unconfined turbulent diffusion flames.

$$Q^* = Q^{'}/(\rho_\infty c T_0 g^{1/2} D^{5/2}) \tag{5.16}$$

A similar relation was developed for line fire results in dependence of flame height on:

$$Q_l^* = Q_l^{'}/(\rho_\infty c T_0 g^{1/2} D^{3/2}) \tag{5.17}$$

Kokkala et al. [63] performed experiments on a non-combustible wall as a function of burner output, which showed a slope fit of $k_f = 0.043 m^{1/3}/kW^{-2/3}$ for n=2/3, and $k_f = 0.058 m^2/kW^{-1}$ for n=1.

The experiments and modelling procedure reported by Brehob et al. [22,24] are used in this study. They developed a model for estimating the heat feedback from the flame and the

mass loss rate at each location on the face of the burning surface to vary as a function of time. They applied a known external heat on the surface with a line burner placed at the bottom of the solid. When the surface temperature reaches a certain temperature, T_{ig}, the material starts pyrolysing significantly. The flames cover the solid above the pyrolysis front and y_f provides heat to the unburnt solid as $\dot{q}''_f$. In the model, the total heat feedback to the wall above the pyrolysis front helps to raise the surface temperature to the pyrolysis temperature:

$$\dot{q}''_{wall} = \dot{q}''_{flame} + \dot{q}''_{ext} - \dot{q}''_{rerad} \tag{5.18}$$

where $\dot{q}''_{flame}$ is the flame heat feedback, $\dot{q}''_{ext}$ is the external incident radiation and $\dot{q}''_{rerad}$ is the heat loss because of surface reradiation to the environment. The external radiation is known and the reradiation losses are calculated from the surface temperature and the ambient surrounding temperature.

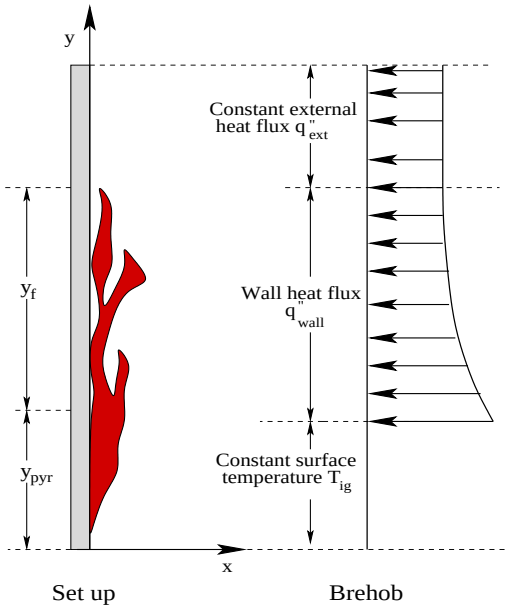

Figure 5.1: Flame spread settings in [22].

The above equation is true during the heat-up stage at the bottom section where the burner is placed. Brehob et al. [24] formulate a correlation to obtain the heat flux along the height as an exponential decay given by:

$$\dot{q}''_f = \dot{q}''_{f0} \cdot e^{\left(-C_0\left(\frac{y-y_p}{y_f-y_p}\right)\right)} \tag{5.19}$$

where $\dot{q}''_{f0}$ is the maximum forward heat flux of sustained flame spread for various materials (table 5.1) and the decay factor C_0 is -1.37.

The forward heat flux in the above equation (5.19) requires the flame height y_f. This is calculated by integrating the local mass flow rates over the entire pyrolysing region i.e. $y > y_b$ and $y < y_p$ on the combustible wall. Here y_b is the burnout height. This is a region where the solid has completely turned into char. Hence, the larger the total energy release

Material	Maximum forward heat flux, $\dot{q}''_{f0}$ (kW/m^2)
Hardboard	49
Poplar	43
Polymethylmethacrylate	35
Plywood	35
Cardboard	35
Particle board	32

Table 5.1: Maximum forward heat flux for sustained flame spread for various materials

rate, the taller the flames are, resulting in a greater area exposed to flames. The flame tip height is then determined as in [94]:

$$y_f(t) - y_{pyr}(t) = K\left[\dot{Q}'_b + \dot{Q}'_m\right]^n \tag{5.20}$$

where the sum within the brackets is the heat release rate per unit width in the fire, i.e. the sum of the energy per unit width by the burner ($\dot{Q}'_b$ in kW/m) and the energy release rate per unit width due to the pyrolysing surface ($\dot{Q}'_m$ in kW/m). Experimental correlation factors K and n are 0.0433 and 0.6667 respectively, taken from [22]. The transient mass loss rate or burning rate is calculated as:

$$\dot{Q}'_m = H_c \int_{x_b(t)}^{x_p(t)} \dot{m}''_{pyr} dx \tag{5.21}$$

The total energy release rate at any instant is obtained from the total mass loss rate of the burning slab multiplied by the heat of combustion, H_c, of the pyrolysed fuel. The value of heat of combustion (H_c) is 12000J/kg [23]. In [22], Brehob et al. assume convection loss on the back surface of the solid. They report that for a homogeneous material like PMMA, the rate of burning increases in the beginning because the heat loss to the interior decreases initially, goes through a maximum burning rate, and finally drops to zero due to heat loss from the back side of finite thickness. In the current settings, a perfectly insulated back surface is considered. In this case the mass flow rate abruptly goes to zero when the pyrolysis front reaches the back surface.

The important parameters and processes contributing to the upward flame spread are the heating of the unburnt fuel above the pyrolysis edge, the total heat feedback to the unburnt wall surface, $\dot{q}''_w(x,t)$, the flame height, x_f, and the local mass loss rate of the wall on the pyrolysing surface, $\dot{m}''_g$.

5.5 Case study

In the present work, the settings are illustrated in figure 5.2. The heat flux from the burner heats the solid to the pyrolysis temperature T_{pyr}. When the surface temperature has reached the pyrolysis temperature T_{pyr}, the pyrolysis process begins.

The heat applied at the bottom of the solid along with the heat losses is:

$$\dot{q}''_{wall} = \dot{q}''_{ext} + \dot{q}''_{f0} - h_s(T_s - T_{amb}) - \sigma\epsilon(T_s^4 - T_{amb}^4) \tag{5.22}$$

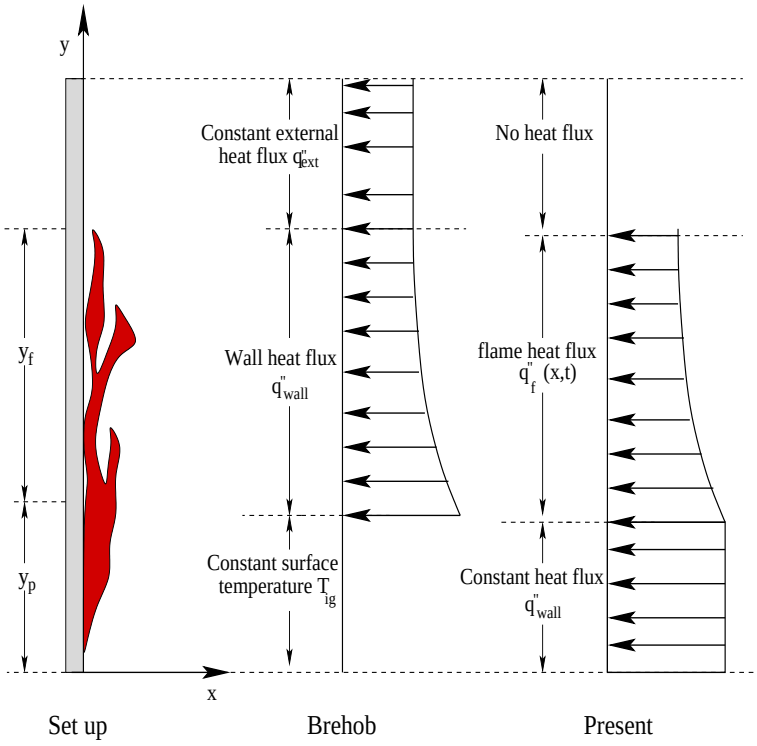

Figure 5.2: Numerical settings for flame spread in the present work.

The enthalpy-based model is extended to two dimensions in space to study the flame spread phenomena. A brief overview of the flame spread modelling theory is presented here. A schematic representation of a two-dimensional model is shown in figure 5.3. A 'pseudo-2D'(or 'pseudo-3D'): conduction inside the solid material is allowed in all directions, but the pyrolysis front in each row (or column) of computational cells is parallel to the solid material surface, exposed to the external heat flux, and moves perpendicular to that surface. The pyrolysis gases also flow out of the material, perpendicular to the exposed surface. These assumptions are most valid when the material thickness is much smaller than the other dimensions, as is mostly the case for fire (or flame spread) configurations. At first only the dry solid is tested, but extension to a wet solid can be performed.

5.5.1 Upward flame spread using a correlation for the flame height

When a solid is exposed to a radiant heat source, the solid temperature rises, albeit only in the region exposed to heat flux. When the surface temperature reaches the pyrolysis temperature T_{pyr}, the pyrolysis process begins, which causes the release of flammable pyrolysis gases. A pilot ignition is normally used to heat the solid and ignite the volatiles released after pyrolysis. Some materials auto-ignite on exposure to external heat flux (more information on auto-ignition can be found in Boonmee's PhD thesis of [21]). Upon ignition, the pyrolysis gases released from the solid mix with oxygen and burn to form flames. These flames develop to provide heat to the unburnt solid above, as they rise. In numerical simulations, this is performed by imposing a fixed external heat flux on the solid below this flame height x_f, computed from correlations [22, 31, 32, 51, 89, 126]. Once pyrolysis begins ($T_s = T_{pyr}$), a constant heat flux is applied below the flame height (y_f).

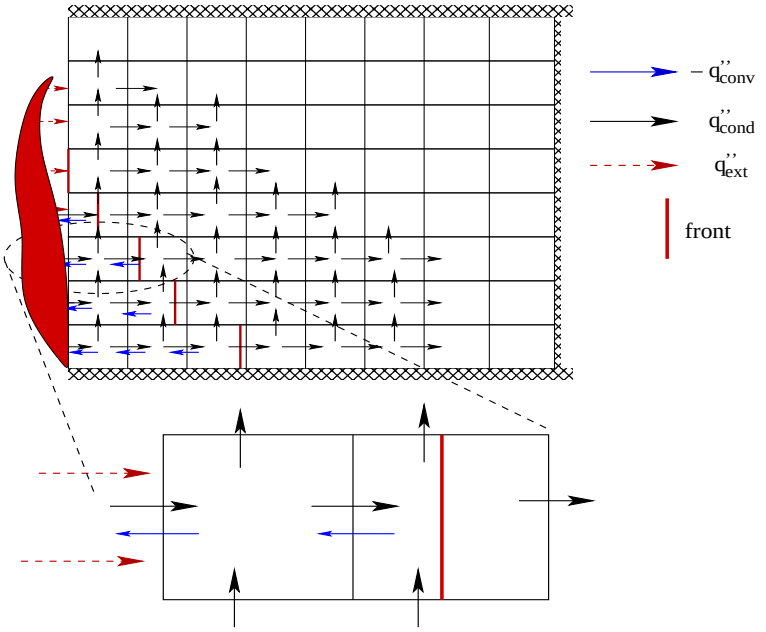

Figure 5.3: A two-dimensional schematic representation of flame spread

The results of this study are published in [120]. As basic upward flame spread test, a vertically oriented sample is considered, with the same material properties as in table 3.1. The sample is 10 cm high and three different thicknesses are considered, namely 3 mm, 5 mm and 1 cm. The model uses square cells of 0.5 mm x 0.5 mm. The physical time step size is set to 0.1 s. The back, top and bottom surfaces are perfectly insulated. An external heat flux of 40 kW/m^2 is imposed, in a region of 5 mm at the bottom of the front surface. By conduction, the material starts to heat up.

As soon as pyrolysis starts, the model uses a correlation for upward flame spread [22] to calculate the flame height $y_f(t)$ from the pyrolysis height $y_p(t)$ (i.e. the height over which the material has pyrolysed at its front surface or, alternatively, where the front surface temperature exceeds T_{pyr}):

$$y_f(t) = y_p(t) + k \left(\dot{Q}_b^{'} + \dot{Q}_m^{'} \right)^{2/3} \tag{5.23}$$

In this case, k is 0.0433, the igniter heat flux $\dot{Q}_b^{''}$ equals 40 kW/m$^2\times$ 0.005 m=0.2 kW/m. The heat release rate from pyrolysis is computed every time step as

$$\dot{Q}_m^{'} = \Delta H_c \int_0^{y_p} \dot{m}_{pyr}^{''} dy \tag{5.24}$$

using ΔH_c=16 MJ/kg. A constant value of 25 kW/m^2 is added to the external heat flux in the region $y < y_f(t)$, resembling radiative heat feedback from flames. Convective and radiative heat losses from the front surface can also be applied to dry charring materials, with ϵ =0.9, h=15.0 W/m^{2}K, which is explained in chapter 4.

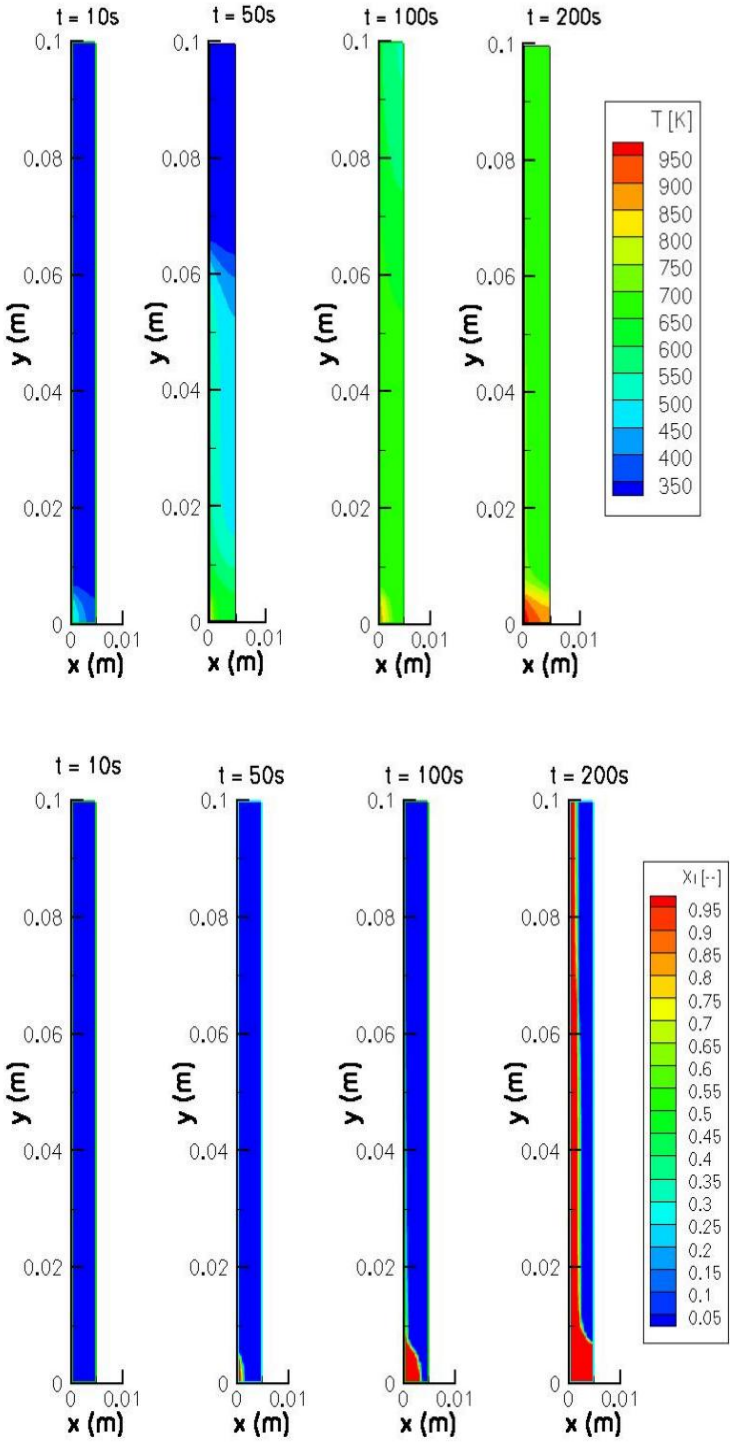

Figure 5.4: Temperature (top) and char fraction (bottom) fields after 10 s, 50 s, 100 s and 200 s.

Figure 5.4 shows the temperature and char fraction fields evolution in time for a material thickness of 5 mm. The multi-dimensionality in the fields is clearly observed. Obviously, the material heats up at the bottom (from the left surface) first. Pyrolysis also starts there. After the onset of pyrolysis, there is an acceleration in heating up and pyrolysis, because the flames rapidly cover a large part of the material.

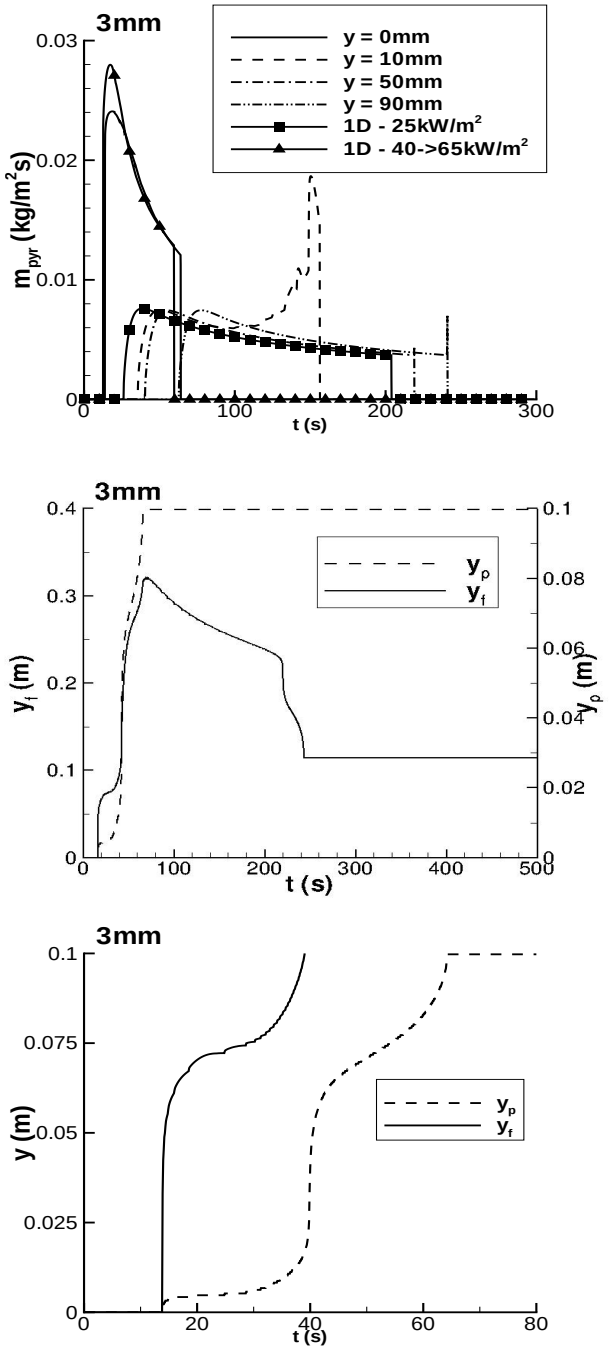

Figure 5.5: Top: Mass flow rate evolution in time at y=0 mm, y=1 cm, y=5 cm and y=9 cm. Middle: evolution of y_p and y_f. Bottom: Zoom of evolution of y_p and y_f for thickness=3 mm. 1D: one-dimensional results for comparison purposes

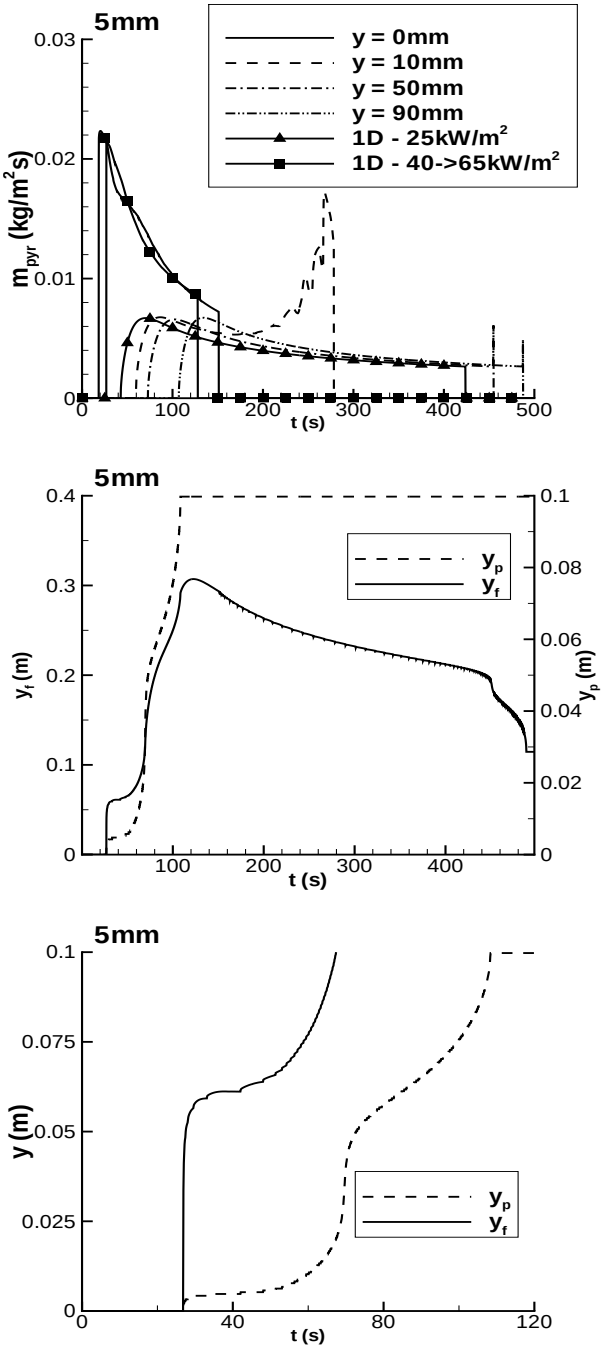

Figure 5.6: Top: Mass flow rate evolution in time at y=0mm, y=1cm, y=5cm and y=9cm. Middle: evolution of y_p and y_f. Bottom: Zoom of evolution of y_p and y_f for thickness=5 mm. 1D: one-dimensional results for comparison purposes

Figures 5.5, 5.6 and 5.7 provide a more quantitative illustration. In the top row, the mass flow rates evolutions in time of the pyrolysis gases are shown at different heights, for the different material thicknesses. For comparison purposes, one-dimensional configuration results are also shown, as explained below.

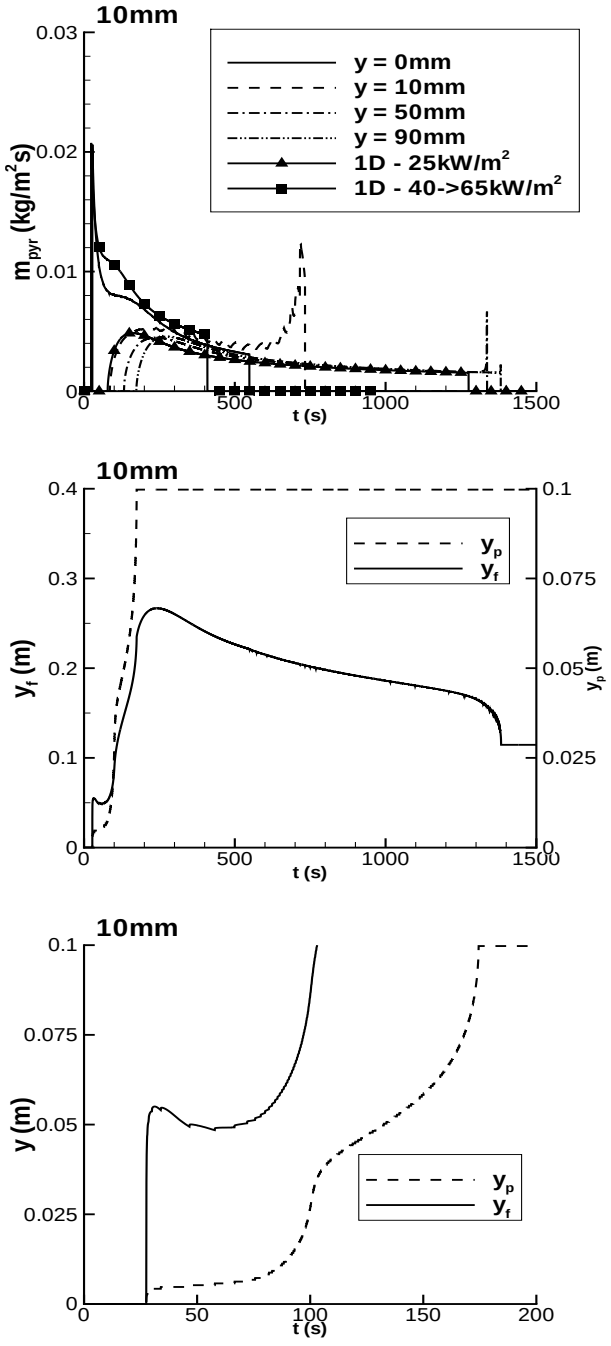

Figure 5.7: Top: Mass flow rate evolution in time at y=0mm, y=1cm, y=5cm and y=9cm. Middle: evolution of y_p and y_f. Bottom: Zoom of evolution of y_p and y_f for thickness=10mm. 1D: one-dimensional results for comparison purposes

At height y=0 mm (i.e. the bottom of the material), a heat flux of 25 kW/m^2 is added at the front surface as soon as pyrolysis starts, as mentioned above. The situation is treated as a one-dimensional heat conduction problem. This is reflected in the very small differences with the first one-dimensional result (for which the set-up is as discussed in chapter 4, adding

25 kW/m^2 at the front surface as soon as pyrolysis starts). As there are some conductive heat losses in the upward direction, the pyrolysis front motion is somewhat slower and the mass flow rates are somewhat lower than in the one-dimensional configuration [54]. This is true for all thicknesses. The thicker the material, the longer it takes for pyrolysis to start and the longer the pyrolysis process lasts.

At height y=5 cm and y=9 cm, the situation is also practically one-dimensional. Obviously, the higher the material, the longer it takes for pyrolysis to start, as radiative heat from the flames is required. Except for a shift in time, the results are very similar to the 1D results, with a constant external heat flux of 25 kW/m^2 imposed at the front surface. The temperature evolution in time (5.8, right) reveals that there is practically no pre-heating by conduction by the time pyrolysis starts. Thus, the simulation results confirm that radiative heat transfer from the flames is predominant. During the pyrolysis process, the net effect of conductive heat fluxes in the upward direction is small.

At height y=1 cm, on the other hand, the situation is more complex. There is pre-heating by conduction, which can also be seen in figure 5.8 (right) with the zoom of the first 100 s before the start of the pyrolysis in the material. Also, there is a second, high peak in the mass flow rate, again due to incoming conductive heat flux from below. Note that the igniter (burner) is active until the end of the simulation. This results in a higher temperature rise at the front surface (at y=0 cm and y=1 cm), compared to the value at higher locations (see figure 5.8).

The middle and bottom row of figures 5.5, 5.6 and 5.7 shows the evolution in time of the pyrolysis zone at the front surface (y_p) and the height of the flame tip (y_f). Clearly, at the onset of pyrolysis, the flames immediately cover a substantial part of the material, according to the applied correlation [22]. The flames are higher for the thinner material, as mass flow rates of the pyrolysis gases are higher. The radiative feedback from the flames heats up the material. Consequently, there is accelerating flame spread due to the positive feedback loop. Obviously, there is a delay in the evolution of y_p, compared to y_f. When the flames cover the entire front surface ($y_f = 0.1$ m, see right column of figures 5.5, 5.6 and 5.7), there is an evolution towards a more or less steady regime, with an almost linear increase of y_p. This is explained by the relatively constant incoming heat flux and outgoing total pyrolysis mass flow rates. As y_p approaches the top surface, an acceleration is observed again, as there are no conductive heat losses at the top surface and thus the pyrolysis front moves more rapidly than in a one-dimensional configuration, due to net incoming conductive heat fluxes from below. Note that y_f reaches a maximum value when y_p has reached the top surface and the total pyrolysis mass flow rate reaches its maximum value. As the material burns out, the flames become shorter and in fact disappear in the end. This is not seen here, because the igniter flux is kept in the correlation of [22], as mentioned above. The model assumes that the flames have their origin at y=0 mm at all times, even if the material is pure char after a while.

Figure 5.8, which shows the front surface temperature evolution in time, supports these findings. At heights where the situation resembles a one-dimensional configuration, three stages are normally observed: the heat-up phase before pyrolysis, the pyrolysis phase and the heat-up phase of char (up to the equilibrium end temperature). These stages are readily distinguished by sudden variations in the temperature evolution. At y=1 cm, however, we see the effect of conduction again: there is pre-heating before any flames are seen and in the

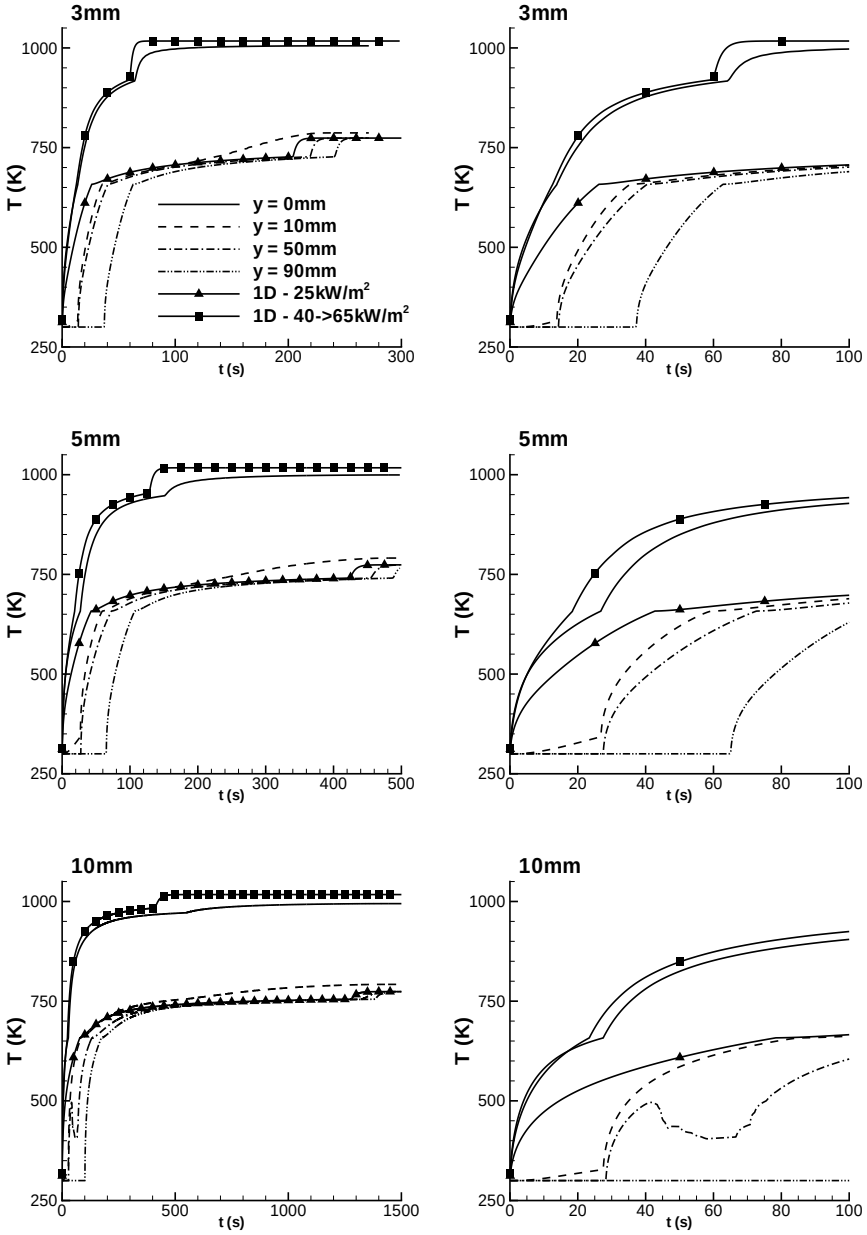

Figure 5.8: Right Column: Surface temperature evolution in time at y=0 mm, y = 1 cm,y = 5 cm and y = 9 cm. Left Column: Zoom from 0 to 100 s. Top: thickness = 3 mm; middle: thickness = 5 mm; bottom: thickness = 1 cm, 1D: one dimensional results for comparison purposes.

end, there is no sudden variation in the temperature evolution. Instead, there is a smooth transition to the equilibrium end temperature. Note that the equilibrium end temperature at y=5 cm and y=9 cm almost exactly matches the equilibrium end temperature: the configuration is practically one-dimensional, with negligible net effect of conductive fluxes in the upward direction. At y=0 cm, there are net conductive losses in the upward direction, so that the equilibrium end temperature is somewhat lower than in the purely one-dimensional

configuration.

Evidently, the temperature rise occurs later for higher positions in the material. In the bottom right column, the temperature at y=5 cm for the 1 cm thick material is quite remarkable. Before pyrolysis takes place at that height, there is a sudden decrease in the temperature evolution (between t=40 s and 80 s). This is due to the drop in y_f around y=5 cm in this period (see figure 5.5, 5.6 and 5.7)): when y_f drops below this height, there is no heat-up of the solid anymore and the net effect is 'cooling down', due to the convective and radiation losses from the front surface. This in turn leads to a decrease in temperature. However, this phenomenon is not observed for smaller material thicknesses, as the pyrolysis mass flow rates are higher. The present enthalpy based model predicts all these features.

5.5.2 Upward flame spread using CFD

Until now, only in the solid phase, simulations were performed. The flame development in the gas phase was modeled by means of correlations, predicting the flame height as a function of the pyrolysis front's position. In this paragraph, the empirical correlations are replaced by simulations in the gas phase. As such, the flame is predicted by solving equations for fluid motion and chemistry. The simulation in the gas phase is then coupled to the solid phase (or pyrolysis) simulation. That way, the gas phase simulation acts as a boundary condition for the solid phase, providing heat fluxes at the surface exposed to the flame. Conversely, the solid phase simulation acts as a boundary condition for the gas phase, providing pyrolysis gas mass fluxes (fuel inlet) and surface temperatures at the same interface. It is important to note that depending on the situation different parameters play their role. It can be the flow field, combustion model (e.g. lack of oxygen), radiation and soot. Primarily, you only need a good estimate for heat flux.

For the coupled simulations, we use the option of solving both phases with different codes. The solid phase is solved with the model, as described above. For the gas phase simulations, we use the commercially available CFD-package Fluent. The motivation to use Fluent is for the more freedom in model choices. The communication between the two codes is handled with the aid of the Tango Code [36]. This code essentially performs Gauss-Seidel iterations between the two codes. Every time step, several iterations are taken until convergence is achieved.

The purpose of this paragraph is to show that the pyrolysis model, developed here, is capable of being coupled to a CFD-simulation. Therefore, we use standard models in the CFD-simulation. A more appropriate choice of models, in order to quantitatively compare the simulation results to experimental data, is beyond the scope of the present work.

The turbulent flow is modeled using the standard $k-\epsilon$ model with enhanced wall treatment at the solid interface. The air and volatiles are treated as incompressible ideal gases at atmospheric pressure. We defined the volatiles as propane, which reacts with the oxygen in the air to form carbon dioxide and water vapor. The heat of combustion of propane is 50 MJ/kg.The reaction is treated as mixing-controlled, and the corresponding reaction depends on the turbulent quantities (Eddy Dissipation model). Radiation modeling is included with the Discrete Ordinates Model. The formation of soot is also considered with the Moss-

Brookes model. For the details of the models used in the gas phase simulation, we refer to appendix D.

As a test case, we consider a solid of dimension 3 mm thick x 10 cm high. This solid is exposed to an external constant heat flux of 40 kW/m^2 up to 6 mm high from the bottom. Initially, the entire set-up is at 295 K. The CFD-domain is 30 cm wide x 20 cm high. The solid interface is at the right boundary, which is composed of three pieces: The bottom and top 10 cm are treated as an adiabatic wall. The pyrolysing solid is placed in the middle 10 cm. The bottom, left and top boundary of the CFD-domain is considered open. A pressure-outlet boundary condition is applied, imposing a linearly varying pressure to incorporate the buoyancy. Where the pressure-outlet is in fact an inlet, the gas enters the domain normal to the boundary. A uniform Cartesian grid with spacing 2 mm is used in the gas phase. In the solid phase, the vertical grid spacing is 2 mm as well, resulting in a continuous grid at the interface. The grid spacing in horizontal direction is smaller (0.5 mm).

The results are shown in figures 5.9 to 5.12. Figure 5.9 and 5.10 shows the temperature distibution in the gas phase (left column) and solid phase (right column) at different time levels. The temperature in the solid rises first at the bottom where the external heat flux of 40 kW/m^2 is applied. This is the heat-up phase. When the surface temperature reaches the pyrolysis temperature, volatile gases are released from the surface of the solid.

The pyrolysis gases are treated as propane in the gas phase. Mixing with oxygen is required for combustion to take place. Thus, there is delay, resulting in a 'dead zone' of unburnt solid, namely where there is no temperature rise in the gas phase (see also figure 5.12). As flames form, they provide a radiant heat flux to the unburnt solid temperature rise of this unburnt solid leads to the solid degradation with further release of volatiles. These volatiles feed the growing flames, resulting in larger flames.

The final stages are seen in figure 5.10. The solid continues to burn for a while. At t=150 s, the flames reduce and the pyrolysis front motion comes to a stand-still, due to an insufficient heat flux from the flames for the pyrolysis front to proceed in the solid.

Figure 5.11 shows the upward velocity contour in the gas phase at time t=100s. We see the gas flow velocity increases in height with the release of volatile pyrolysis gases. These gases move in vertical direction to form flames.

Figure 5.12 shows the char fraction (ξ) in the solid at different time instants. At t=30 s, the solid has just started pyrolysing. When the flames develop, they provide heat on the unburnt solid above. We see in figure 5.12 (top right), the dead zone, as discussed above. After t=150 s, the entire process stops, as described above.

5.6 Conclusion

The enthalpy based pyrolysis model is extended to two-dimensions. The model performs well for the numerical test case using the correlation developed by Brehob et al. [22]. The results for a numerical reference case correlate well with 1D results. Differences were explained.

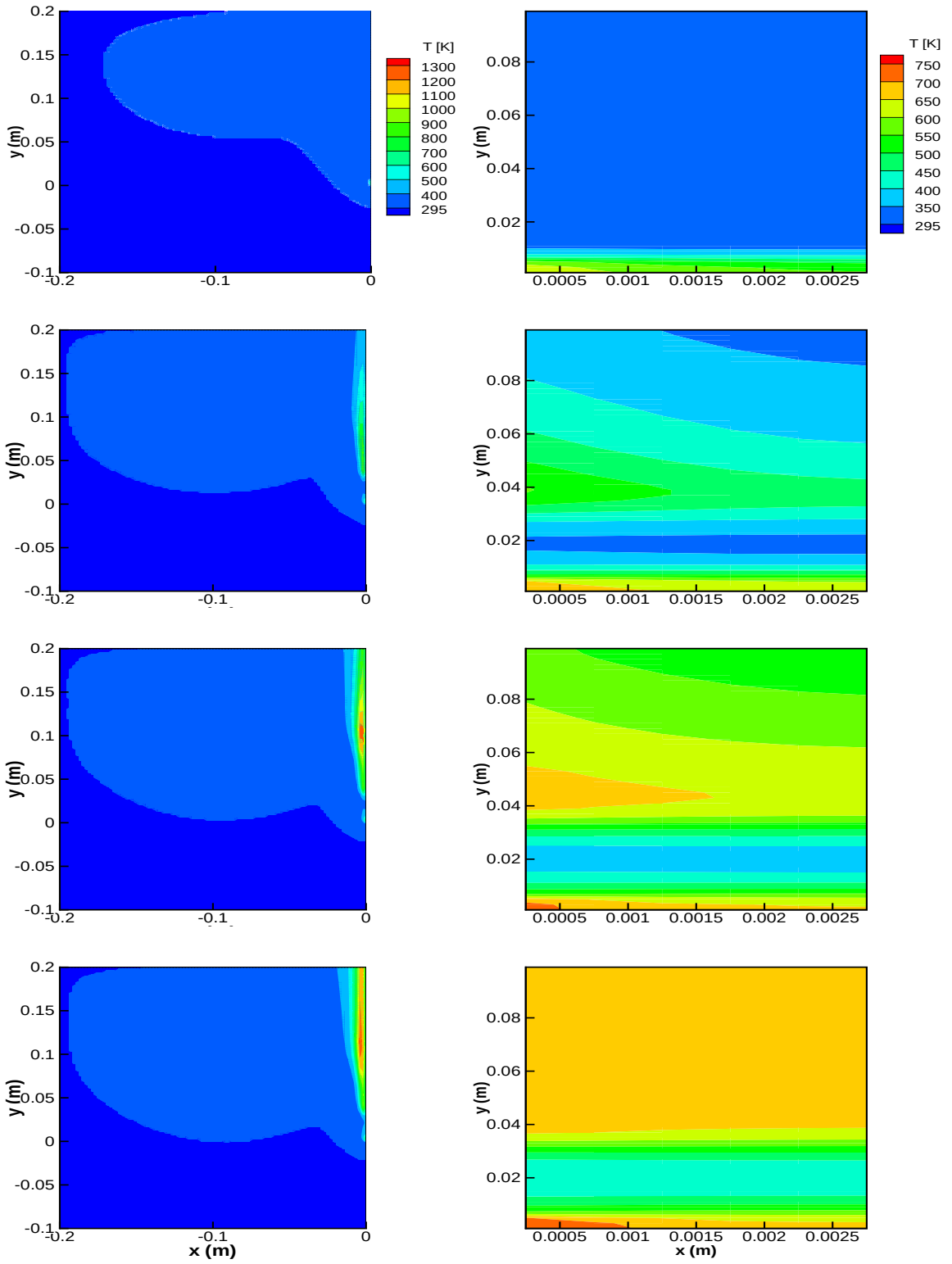

Figure 5.9: Temperature distribution in the gas phase (left column) and solid phase (right column) at different time levels; Top row: t=15 s; Second row: t=30 s; Third row: t=50 s; Bottom row: 75 s.

The potential of coupling to CFD for turbulent combustion, with radiative heat feedback, to fully simulate flame spread was illustrated.

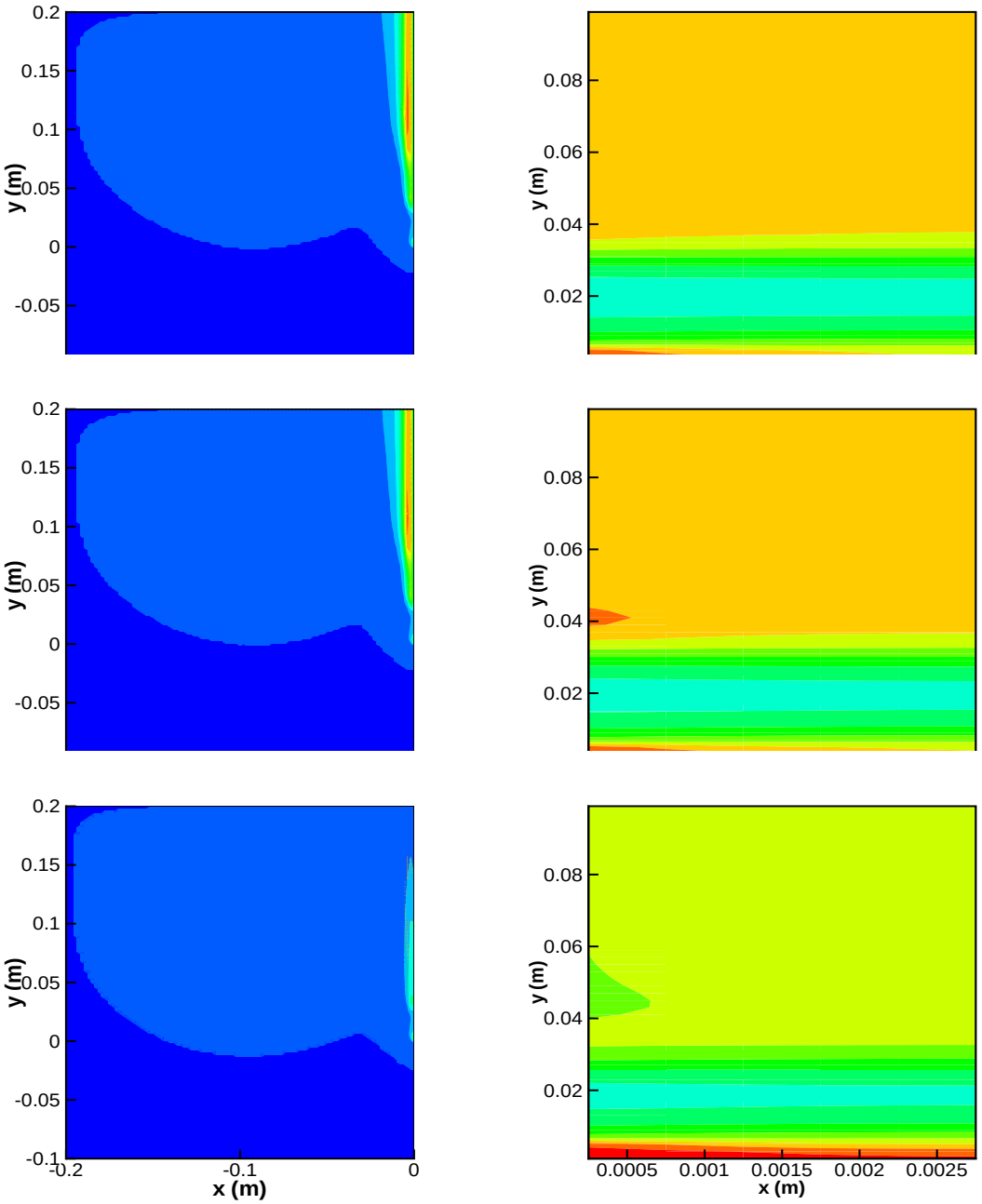

Figure 5.10: Temperature distribution in the gas phase (left column) and solid phase (right column) at different time levels; Top row: t=100 s; Middle row: t=125 s; Bottom row: t=150 s

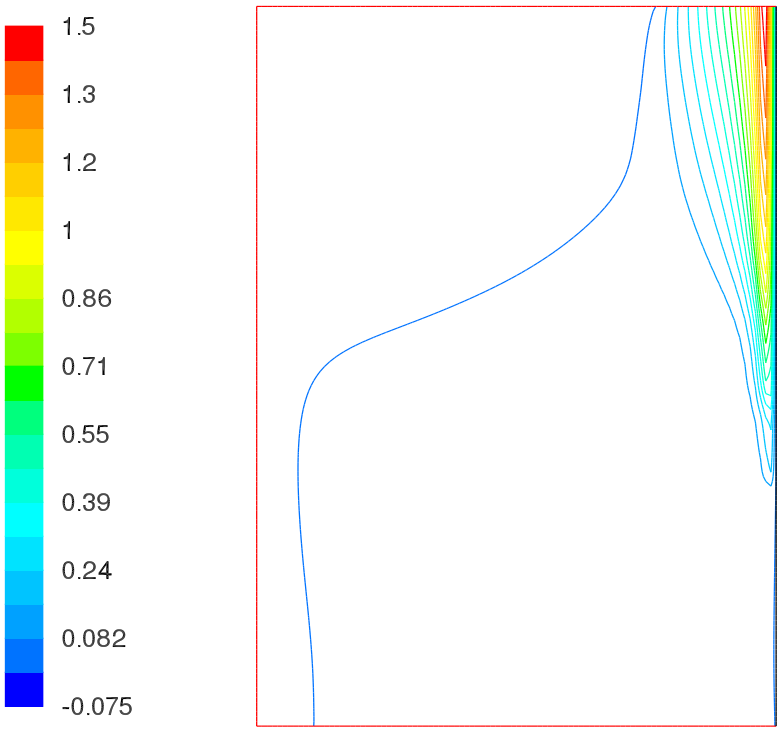

Figure 5.11: Upward velocity contour at time t=100s

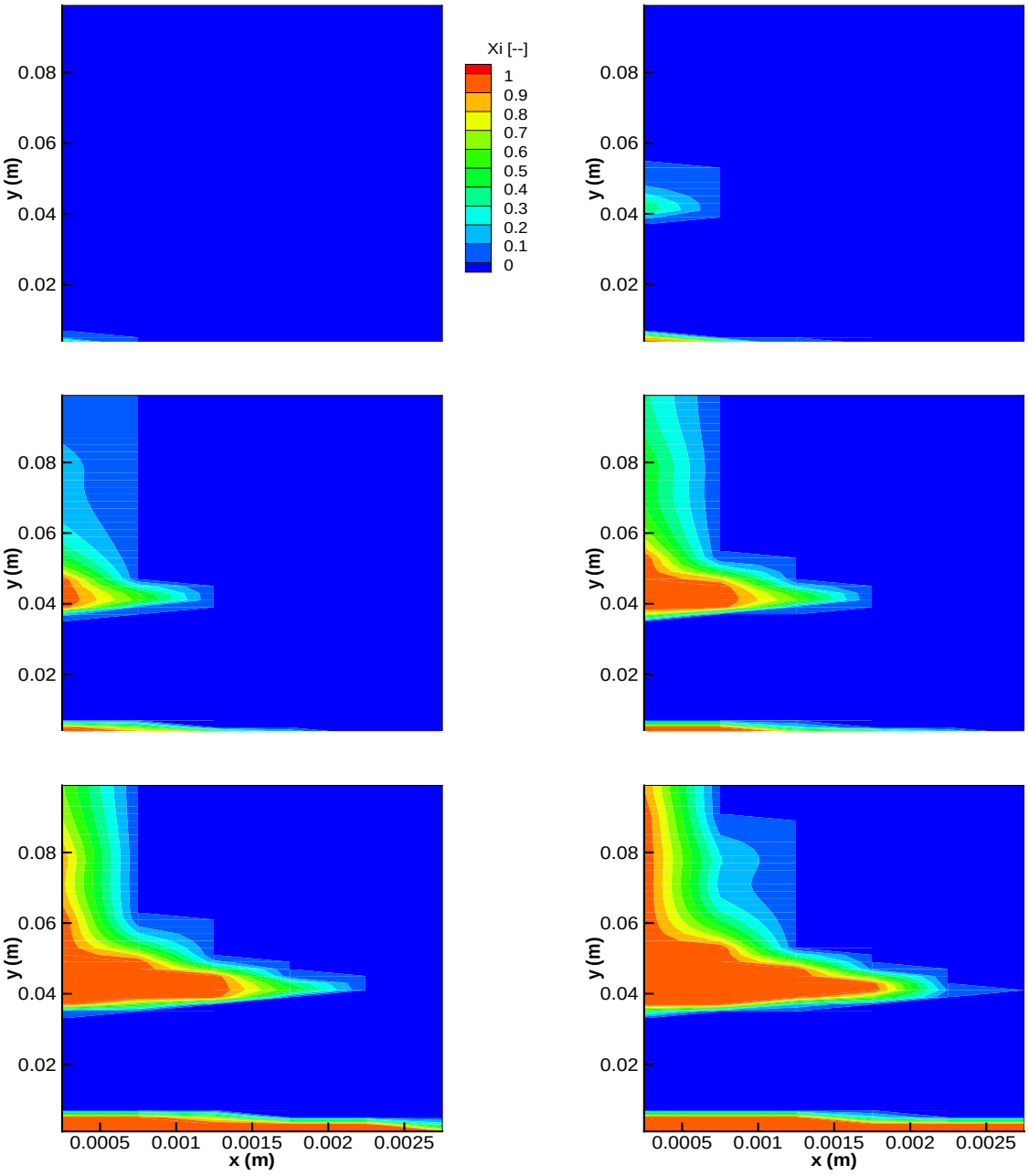

Figure 5.12: Char fraction (ξ) at different times, Top left: t=30 s; Top right: t=50 s; Middle left: t=75 s; Middle right: t=100 s; Bottom left: t=125 s; Bottom right: t=150 s.

6

Experimental study of upward flame spread - vertical parallel plates

6.1 Introduction

Theoretical correlations for the flame spread rate flame height and other related parameters, have been developed in [48, 50, 94]. Many laboratory scale flame spread experiments have been performed on charring [20, 24, 44, 46, 82, 88] and non-charring materials [20, 24, 89] to study these parameters.

Research on two parallel placed walls/boards [44], has drawn considerable interest in fire community. The experiments in [44] were conducted to measure the heat flux on the walls of two parallel boards, exposed to a line burner. The heat flux on the surface was observed to increase as the separation between the two walls decreased. The wall samples were incombustible boards of size 61 mm $\times$ 813 mm $\times$ 25 mm. A methane burner was used as igniter, with methane flow rates of 5 and 9 l/min ($\approx$ 7 and 12.5 kW heat output). The line burner used in this experiment was 600 mm long and 10 mm wide, with 1mm holes every 10mm. The separation between the two walls was 60mm or 100mm and the burner was placed centrally. Different distances between the two boards and different powers were examined to determine the heat flux from the flames to the walls.

FM Global has performed standard Parallel Panel Tests (PPT) [47] to study the materials fire propagation behavior, expressed as Fire Propagation Index (FPI), and Smoke Development Index (SDI). Khan et al. [62] used PPT tests conducted to study the fire propagation behavior of cables. Two vertical 0.61 m $\times$ 4.9 m high parallel panels separated by 0.3 m were used. These panels were a sandwich of 13 mm thick Marinate-I on 13mm plywood. A methane sand burner of 0.61 m $\times$ 0.3 m $\times$ 0.3 m was placed at the bottom of the panels,

act as an ignition source. The cables were fastened to the panels at every 0.61m length with 20 gauge thermocouple wires. The burner provided a heat flux to the surface of the cables in the order of 40-60 kW/m^2. The tests were conducted in a normally ventilated room.

de Ris [34] examined if the parallel panel tests can support a self-propagating fire. He used a fire resistant material and developed a model to study the fire propagation over parallel panels depending on the aspect ratio. The aspect ratio $\alpha = d/w$ (where d is the separation distance between the two panels, w is the width of each panel) is a very important parameter. The model predictions agreed with experimental test for PVC and CP-6. He found that both are fire resistive. He tested these fuels for aspect ratio equal to 0.5, 1.0, and 2.0.

This chapter reports on the experimental campaign I performed at the University of Lund, Sweden. Numerical simulation results are also discussed. This chapter is based on Wasan et al. [121, 122].

6.2 Experimental set-up

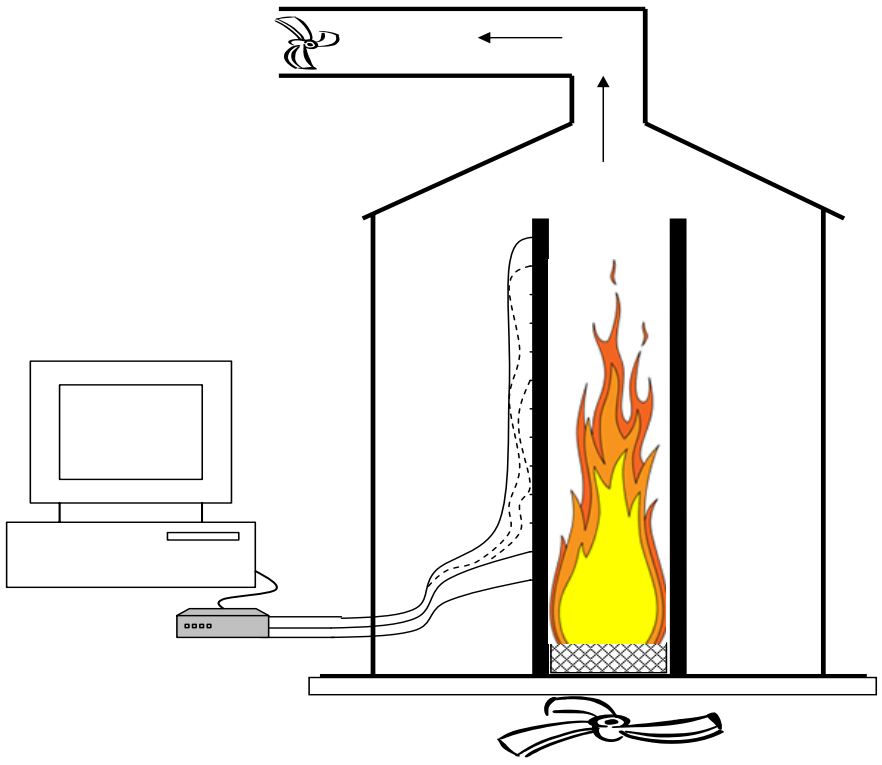

Figure 6.1: Experimental set-up for the vertical upward flame spread configuration

Flame spread experiments were conducted on particle boards, which have a low ignition time. Two particle boards of 2.5 m × 0.4 m × 0.025 m were used. Two different burners, with methane as fuel, are used: a sandstone burner (28.5cm × 30cm) and a honey comb burner (10 cm × 20 cm). The boards are placed vertically aside these burners, as shown in figure 6.1. The distance between the two boards is 30.5 cm with the sandstone burner and

10.5 cm with the honey comb burner. Using alignment of spirit (or bubble) level, care has been taken to keep the boards parallel to each other and vertical to the base.

The entire set up has been mounted on a test rig of 3 m $\times$ 3 m, provided with a fan for the air supply, through a porous material for even distribution and hence providing a vertically upward velocity of 0.3 m/s from the bottom. The set-up is surrounded by steel plate to reduce innluence from the surroundings and to create, as such, rather well defined boundary conditions for modelling afterwards (although this is not pursued in the present work). In order to visually keep track of the flame front, the board has been marked from bottom to top at every 10 cm. Thermocouples are installed on these markings to measure the surface temperature. The methane flow rate is maintained at 20 l/hr, to provide a power of 30 kW. The burner is operated manually. The flow is adjusted using a flow meter attached to the pipeline.

As reported by Foley and Drysdale [44], it was observed that the flame spread depends on the distance of separation between the two boards and the type of burner. Obviously, the amount of radiation falling on each surface is higher than in a single board configuration, because there is less radiative heat loss to the environment. The radiation loss becomes smaller as the distance between the plates decreases. Also, an additional heat flux is provided by the flames that are generated at the other plate.

Figure 6.2 shows pictures for the configuration with the sandstone burner (left) and the honey comb burner (right) at three different moments during the experiments. The top pictures were taken at the early stage of the experiments, not long after ignition of the methane fuel from the burner. The particle board has not started to pyrolyse yet (pre-heating stage). The second picture, taken when the experiment was going on for a while, reveals that, particularly for small distance between the plates, flames do not stay within the plates configuration. They move towards the back surface and tend to cover the back surface. This is a combination of the flow field and the fact that unburnt fuel finds oxygen in the sourrounding atmosphere. This is still more clearly seen in the bottom picture (particularly for the smallest plate distance again). The flames were extinguished by water mist shortly thereafter, as the flames reached the exhaust chimney and there was imminent danger of damage in the exhaust system.

The arrows indicate the flame height, obtained at different instants, by visual observation of flames. This visual information shown in figure 6.3 of flame height evolution in time for both configurations (sand and honeycomb burners) is used in the numerical simulations with the enthalpy based model.

Clearly, there is acceleration in the temporal evolution of the flame height for both the burners. A more of less quadratic behaviour is observed, as illustrated by the parabola in the figure, although a plateau is seen in the middle of the experiments. As excepted, the flame spread is much faster in the configuration with the smallest distance in between the plates (honeycomb), confirming that radiative heat transfer is prominent. In a short time, the flames rise and cover the solid, leading to an uncontrollable scenario.

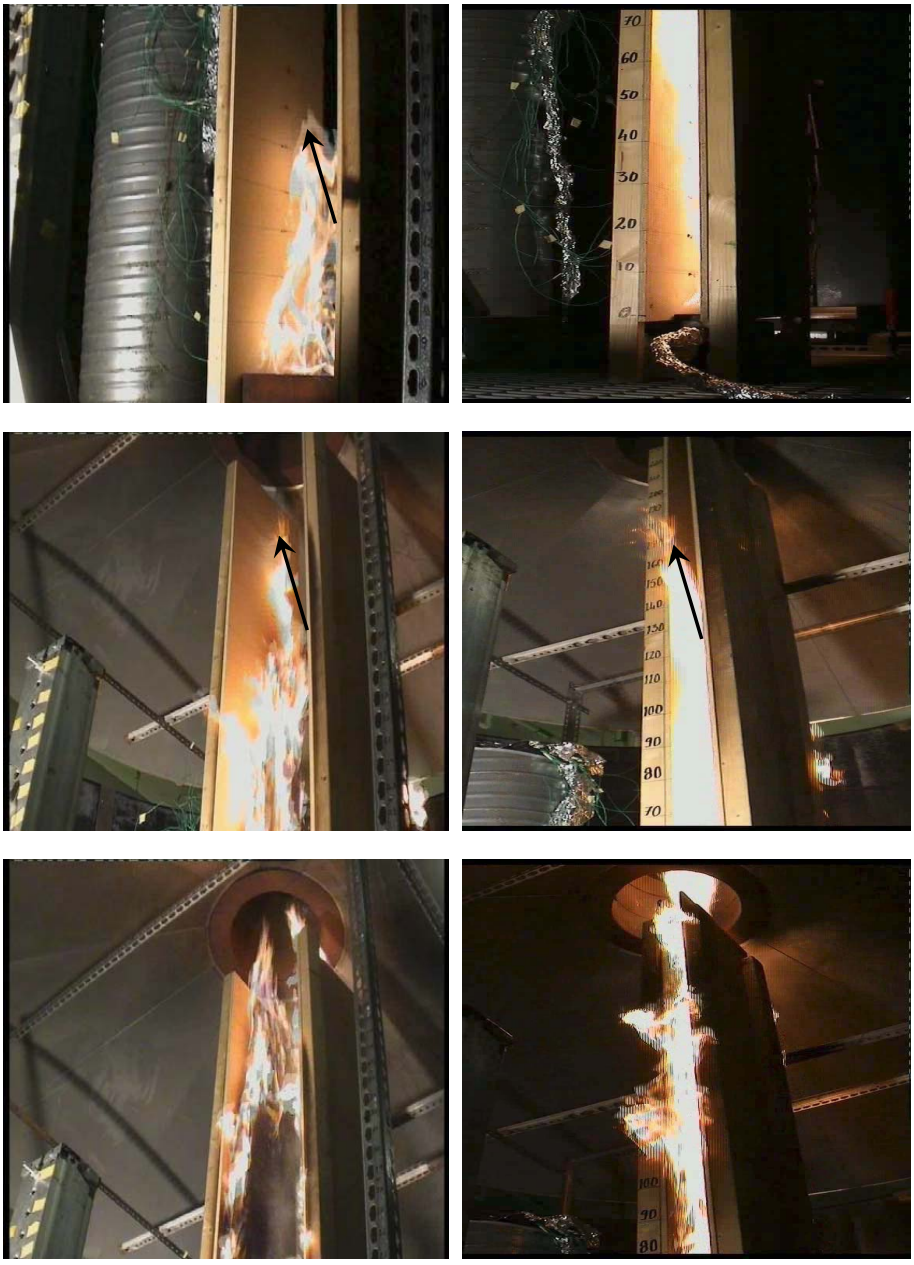

Figure 6.2: Three snapshots of the experiments. Left: sandstone burner (distance between plates is 30.5 cm); honey comb burner (distance between plates is 10.5 cm). Top: early stage (just after ignition of the burner); middle: intermediate stage; bottom: final stage(flames reach the exhaust chimney).

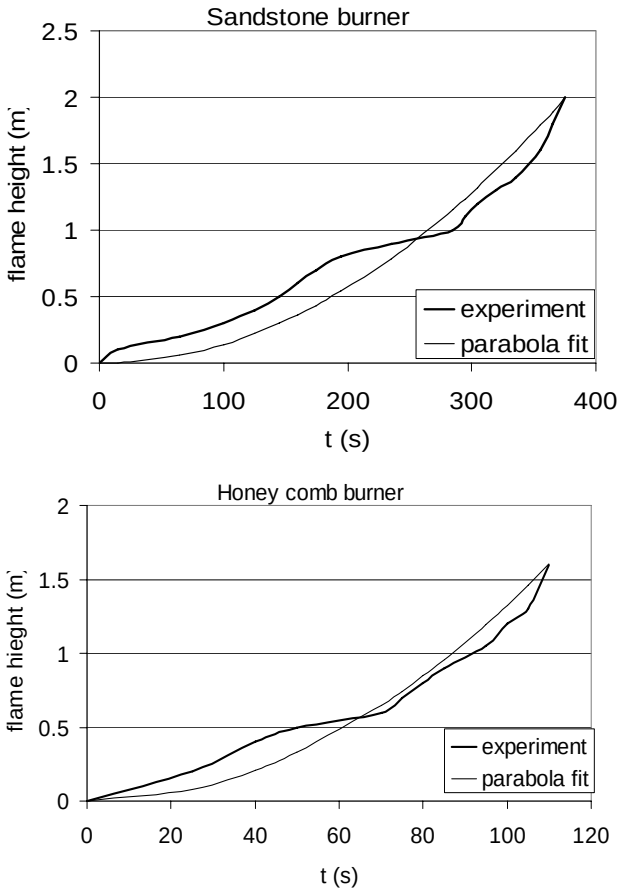

Figure 6.3: Flame height evolution in time. Top: 30.5 cm distance between the boards; Bottom:10.5 cm distance between the boards

6.3 Temperature field evolution

Figure 6.4 shows the evolution in time of the temperature in all thermocouples for the distance 30.5 cm between the plates. Clearly, ignition of the burner gases is almost immediately felt by all thermocouples at a height of 80cm or less. The flames from the burner rise above the sandstone burner to provide the heat to the particle board, immediately after the burner is ignited. This is deduced from the observed, almost instantaneous, temperature rise to 300^0C. Of course, this is well below typical flame temperatures, but the thermocouples are mounted on the surface, so that the measured temperature can be affected by heat loss by conduction into the virgin material. There are also radiation losses to the sourrounding. As the flames develop, the temperatures rise everywhere as time goes by, until the burner is extinguished by water mist (after about 500 s). Interestingly, the highest temperatures are not observed near the burner (y <50 cm), but somewhat higher. This is a direct consequence of the added heat flux from flames, stemming from the combustible pyrolysis gases and in addition the radiative heat flux provided by other burning board.

Figure 6.5 shows essentially the same information, but in an other way, as temperature profiles as function of height at different times. During the early stages ($t < 200\ s$), the thermocouples below 1 m indicate a temperature rise. As mentioned, this is primarily due to the flames from the burner. Then the high temperature region starts to extend (flame spread), until the entire region is at a quite uniform temperature (around 700^0C). Then the fire is extinguished by water mist, after 500 s, when the temperatures reduce to a lower

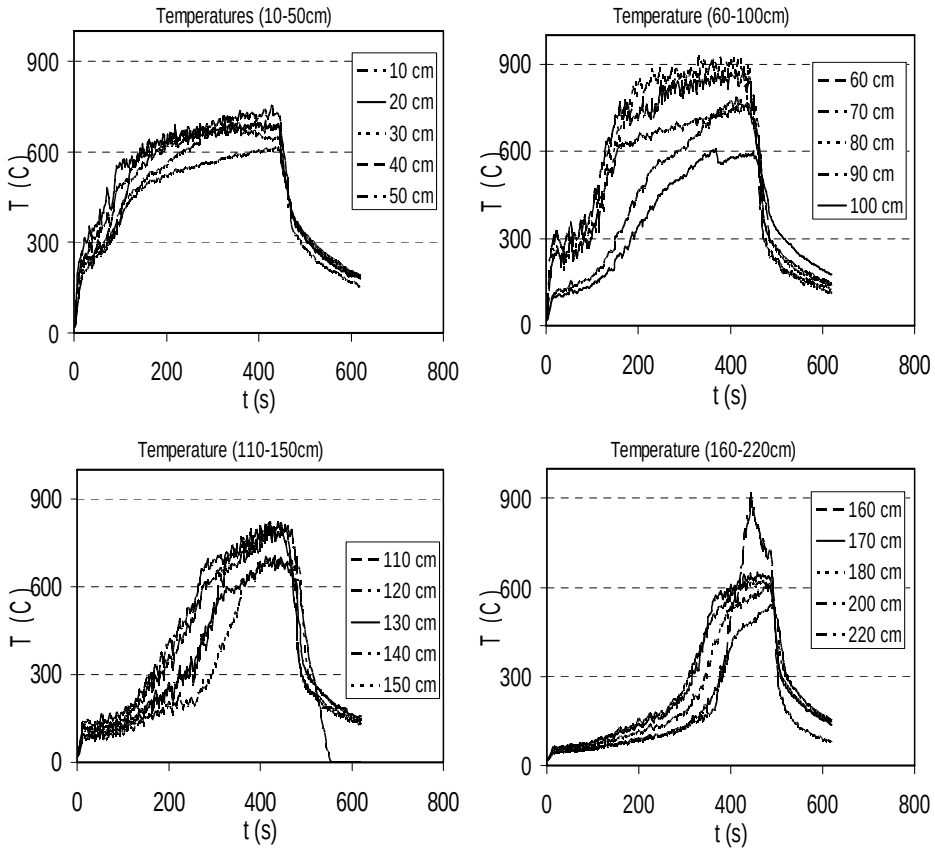

Figure 6.4: Temperature distribution over height at different times for 30.5 cm distance between plates

value seen in the lower row.

Figure 6.6 and 6.7 show the same information for the honey comb burner, where the distance between the plates (boards) is only 10.5 cm. The process is about 4 times faster than for the larger distance between the plates (30.5 cm apart, earlier test case). Apart from the speed of the flame spread, the curves are qualitatively very similar as shown in figures 6.4 and 6.5. Note that the measured temperatures are not higher. On the contrary, they are somewhat lower. This might be a consequence of incomplete combustion in between the plates, as the central flames might not receive enough oxygen from the surroundings. This is in line with the visual observation that the flames extend outside the plate configuration. Also, the duration of the experiment is short for this experiment.

6.4 Variable burner output

During one of the experiments, the burner started to run out of fuel (methane supply). This led to a reduction in burner power during the period 500 s $< t <$ 750 s.

Figure 6.8 reveals that this is clearly observed in the temporal evolution of temperature, except for the lower thermocouples ($y <$ 50 cm). The reduction in temperature is the most severe in the region 60 cm $< y <$ 1.2 m: flames that were present due to combustion of

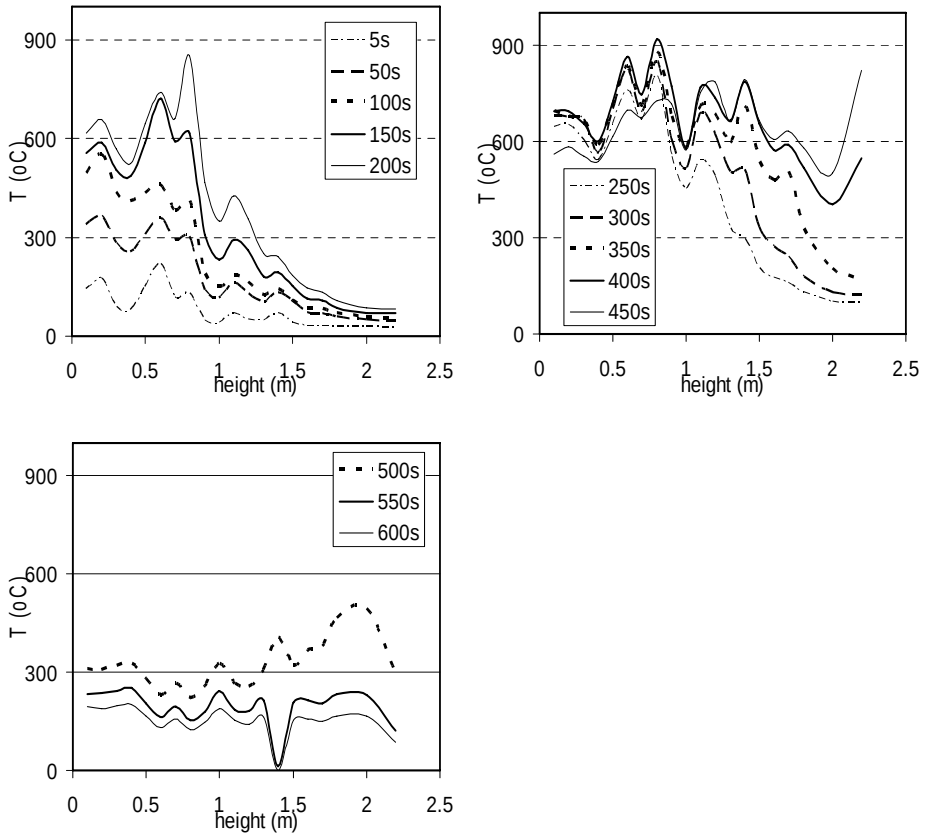

Figure 6.5: Temperature evolution in time at different heights for 30.5 cm distance between plates

the pyrolysis gases, disappear temporarily due to the reduced heat flux from the burner onto the plates. Once the burner is again at full power, the temperatures recover very rapidly. Interestingly, the temperature almost immediately reaches the level, it had before the reduction of the burner output power. In other words, the pyrolysis process seems to recover its latest stage very rapidly.

6.5 Numerical simulation

The particle board in the experiments had dimensions 2.5 m × 0.4 m × 2.5 cm . We simplify to a two dimensional case in numerical simulations, using 2.5 m × 0.4 m particle board with 100×40 cells for computation. A physical time step of 0.5 s is used. A constant heat flux is applied to resemble the burner flame heat flux falling on the particle board, up to 40 cm and 70 cm, for the sand burner and honeycomb burner respectively. The material properties for the particle board [126] are as follows:

The model parameters used in the simulations are: ΔQ_{pyr}=8.7 × 10^5 J/kg, T_{amb}=300 K, T_{pyr}=598 K.

The numerical simulations, performed for the parallel plate configuration with the sand

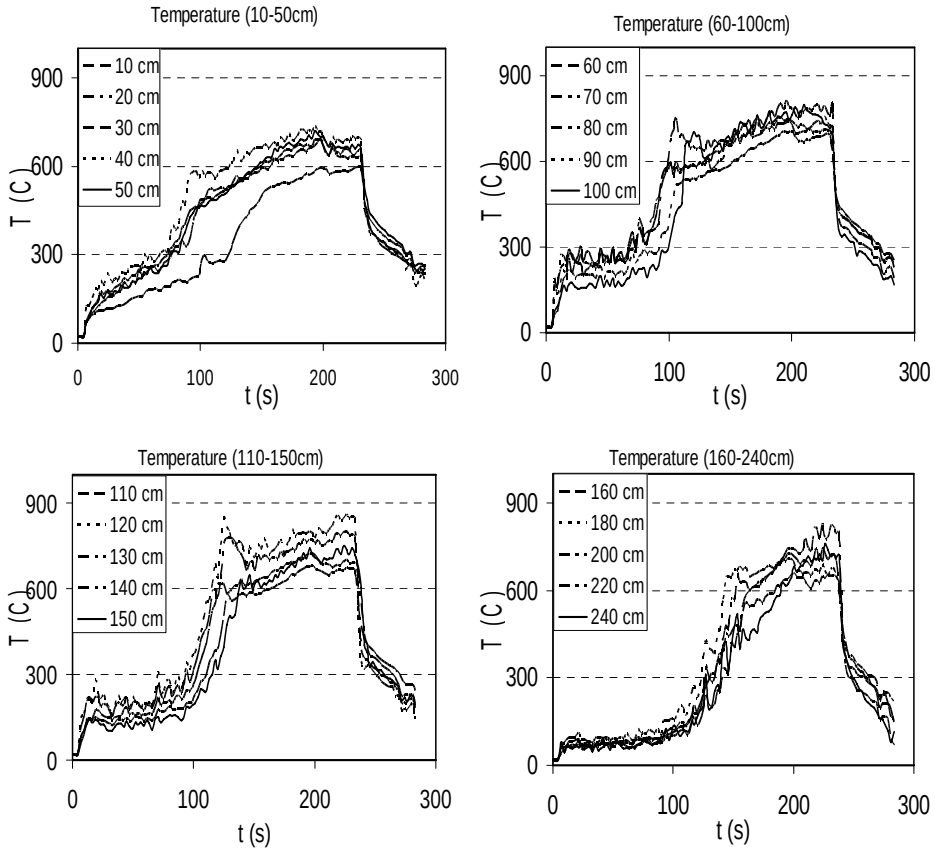

Figure 6.6: Temperature distribution over height at different times (10.5 cm distance between plates)-constant burner power

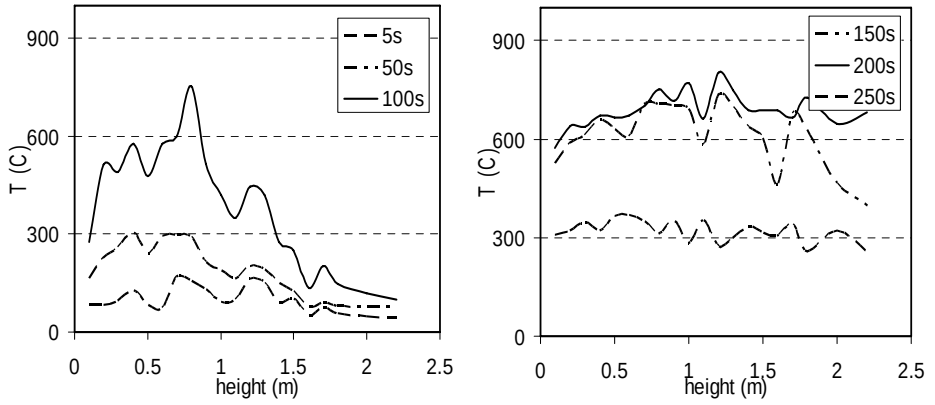

Figure 6.7: Temperature evolution in time at different heights for 10.5 cm distance between plates

burner, are discussed first. During the heat-up phase, the boundary conditions applied on

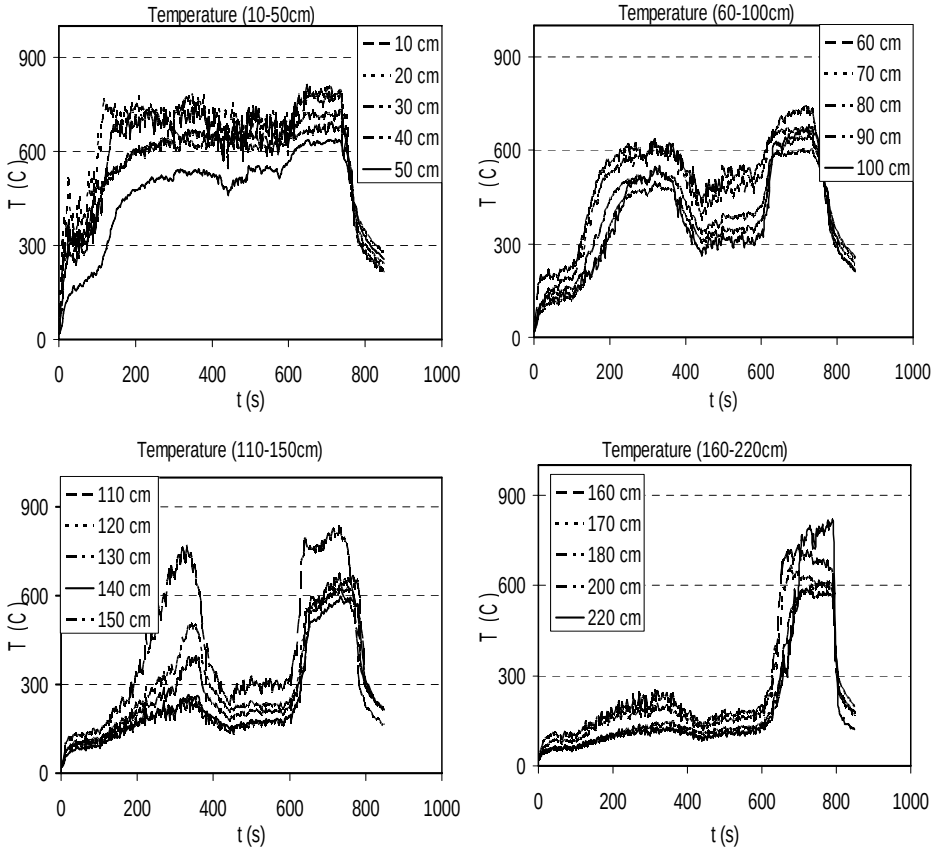

Figure 6.8: Temperature distribution over height at different times (30.5 cm distance between plates)- variable burner power

the particle board is implemented are:

$$\begin{aligned} (y < 0.4 \text{ m}) \quad & \dot{q}''_{net} = \dot{q}''_b - h_s(T_s - T_{amb}) - \epsilon\sigma(T_s^4 - T_\infty^4) \\ (y > 0.4 \text{ m}) \quad & \dot{q}''_{net} = \dot{q}''_b \cdot e^{(-C_0(y-y_f))} - h_s(T_s - T_{amb}) - \epsilon\sigma(T_s^4 - T_\infty^4) \end{aligned} \tag{6.1}$$

Up to a height of 0.4 m, the particle board is exposed to the burner power is $\dot{q}''_b$=37 kW/m^2 only. This is a persistent flame region.

At higher heights an exponential decay is introduced (decrease of radiation). The decay constant is set to $C_0 = 1.7$ by tuning with measured temperatures.

The material begins to pyrolyse as soon as $T_s = T_{pyr}$, with the release of volatiles. These volatiles form flames. The flame heat flux is considered constant in the numerical simulations, equal to $\dot{q}''_f$=55 kW/m^2, in the region 0.4 m $< y < y_f$, with y_f the vertical position of the pyrolysis front. Thus, a persistent flame region is assumed. An exponential decay is

Properties	Value	Units
$\rho_{v,d}$	600	kg/m^3
ρ_c	60	kg/m^3
$c_{v,d}$	2500	J/(kgK)
c_c	2500	J/(kgK)
$k_{v,d}$	0.36	$W/(mK)$
k_c	0.23	$W/(mK)$
h	15.0	$W/(m^2K)$
σ	$5.67 \cdot 10^{-8}$	$W/(m^2K^4)$
ϵ	0.3	$[-]$

Table 6.1: Thermo-physical properties of particle board [35]

assumed for $y < y_f$ again:

$$\begin{aligned} (y < 0.4 \text{ m}) \quad & \dot{q}''_{net} = \dot{q}''_b - h_s(T_s - T_{amb}) - \epsilon\sigma(T_s^4 - T_\infty^4) \\ (0.4 \text{ m} < y < y_f) \quad & \dot{q}''_{net} = \dot{q}''_f - h_s(T_s - T_{amb}) - \epsilon\sigma(T_s^4 - T_\infty^4) \\ (y > y_f) \quad & \dot{q}''_{net} = \dot{q}''_f \cdot e^{(-C_0(y-y_f))} - h_s(T_s - T_{amb}) - \epsilon\sigma(T_s^4 - T_\infty^4) \end{aligned} \tag{6.2}$$

The reradiation loss from the surface is relatively small for parallel plates exposed to fire, compared to single plate or single panel configuration. This is incoporated by applying an emissivity $\epsilon = 0.3$. The flame height is determined from the a parabolic fit as shown in figure 6.4 (top) for the sand burner.

$$y_f = 1.422 \times 10^5 (t)^2 \tag{6.3}$$

or from a piecewise linear reconstruction of the measured data.

$$y_f = y_0 + \frac{y_1 - y_0}{t_1 - t_0}(t - t_0) \tag{6.4}$$

where (y_0, y_1) are flame heights at time (t_0, t_1). And y_f is the flame height at time t.

Figure 6.9 shows the experimental and numerical simulation results for the constant power sand burner. Numerical simulations are performed using both parabolic and piecewise fits. Good agreement is observed. The agreement is better with the piecewise linear reconstruction. This shows the potential for flame spread simulations, provided the correct heat feedback can be computed from the gas phase. The results are split into subfigures to give a clear picture to the reader.

Similar findings are seen with the honeycomb burner. In the experiments, the flames, emerging from the burner, diverge, due to high flow rate of methane from narrow burner nozzle. The flames were observed up to h=0.8 m high. In numerical simulations, the heat flux from the burner flames is applied as a constant heat flux of $\dot{q}''_b$=15 kW/m^2 up to h=0.3 m and a higher heat flux of $\dot{q}''_b$=30 kW/m^2 up to h=0.8 m. The decay constant is set to C_0=1.3. The following boundary conditions are used during heat up:

$$\begin{aligned} (y < 0.3 \text{ m}) \quad & \dot{q}''_{net} = 15 \text{ kW/m}^2 - h_s(T_s - T_{amb}) - \epsilon\sigma(T_s^4 - T_\infty^4) \\ (0.3 \text{ m} < y < 0.8 \text{ m}) \quad & \dot{q}''_{net} = 30 \text{ kW/m}^2 - h_s(T_s - T_{amb}) - \epsilon\sigma(T_s^4 - T_\infty^4) \\ (y > 0.8 \text{ m}) \quad & \dot{q}''_{net} = \dot{q}''_b \cdot e^{(C_0(y-y_f))} - h_s(T_s - T_{amb}) - \epsilon\sigma(T_s^4 - T_\infty^4) \end{aligned} \tag{6.5}$$

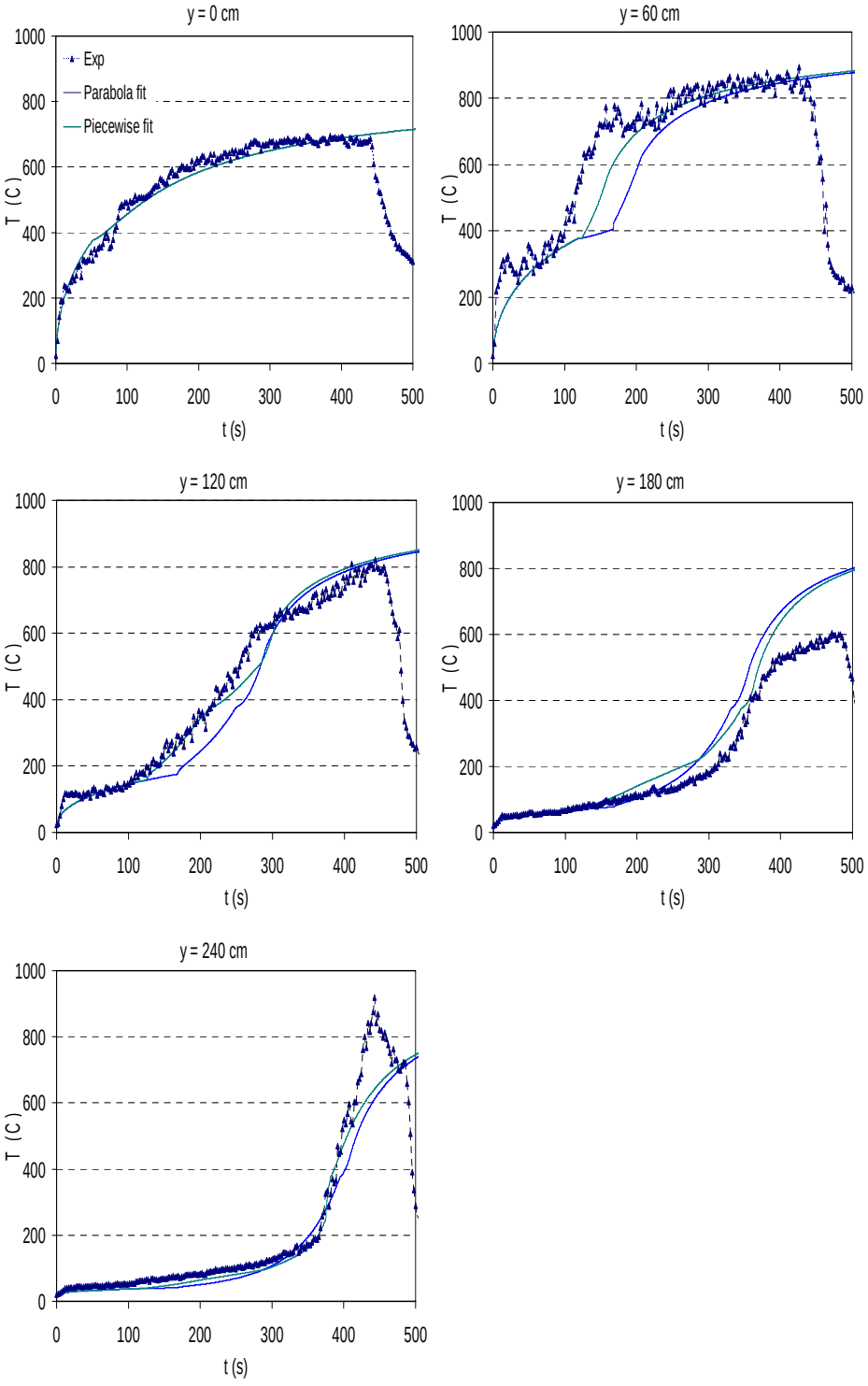

Figure 6.9: Temperature distribution for different heights using a constant sand burner

The flame heat flux is again $\dot{q}''_f$=55 kW/m^2 so that during pyrolysis:

$$\begin{aligned}
(y < 0.4 \text{ m}) \quad & \dot{q}''_{net} = 15 \text{ kW/m}^2 - h_s(T_s - T_{amb}) - \epsilon\sigma(T_s^4 - T_\infty^4) \\
(0.4 \text{ m} < y < 0.8 \text{ m}) \quad & \dot{q}''_{net} = \dot{q}''_b - h_s(T_s - T_{amb}) - \epsilon\sigma(T_s^4 - T_\infty^4) \\
(y < y_f) \quad & \dot{q}''_{net} = \dot{q}''_f - h_s(T_s - T_{amb}) - \epsilon\sigma(T_s^4 - T_\infty^4) \\
(y > y_f) \quad & \dot{q}''_{net} = \dot{q}''_f \cdot e^{(-C_0(y-y_f))} - h_s(T_s - T_{amb}) - \epsilon\sigma(T_s^4 - T_\infty^4)
\end{aligned} \tag{6.6}$$

The parabolic fit for the flame height now reads:

$$y_f = 1.323 \times 10^4 (t)^2 \tag{6.7}$$

Figure 6.10 shows the temperature distribution for the numerical simulation and experimental results. With the piecewise linear fit, agreement to the experimental results is better than with the parabolic fit. From these results we see that the enthalpy based model is capable to perform flame spread simulations even for large dimensions. Again, the results are split into subfigure to make the reader feel in ease. The results clearly point out the potential of the enthalpy based model to study flame spread.

6.6 Conclusions

In this chapter, original flame spread experiments have been performed in a vertical parallel particle board configuration. Two different distances between the very large plates (2.5 m high) have been considered (30.5 cm and 10.5 cm). The flame height evolution in time was visually recorded. For both configurations, an acceleration in the increase of the flame height in time was observed. The process is about 4 times faster for the smallest distance between the plates. Temperatures have been measured over the entire height. The most interesting observation is that the temperatures are somewhat lower, although the flame spread is much more rapid for the smaller distance between the plates due to increased radiative heat transfer (and possibly also due to higher upward convection of the flames). This is most likely due to incomplete combustion of the pyrolysis gases, as oxygen from the surrounding atmosphere might not be able to reach the centre in between the plates. The visual observation that flames extend outside of the parallel plate configuration supports this statement. Numerical simulation results show that the model predicts temperatures in good agreement with the experiments, when boundary conditions were are well tuned.

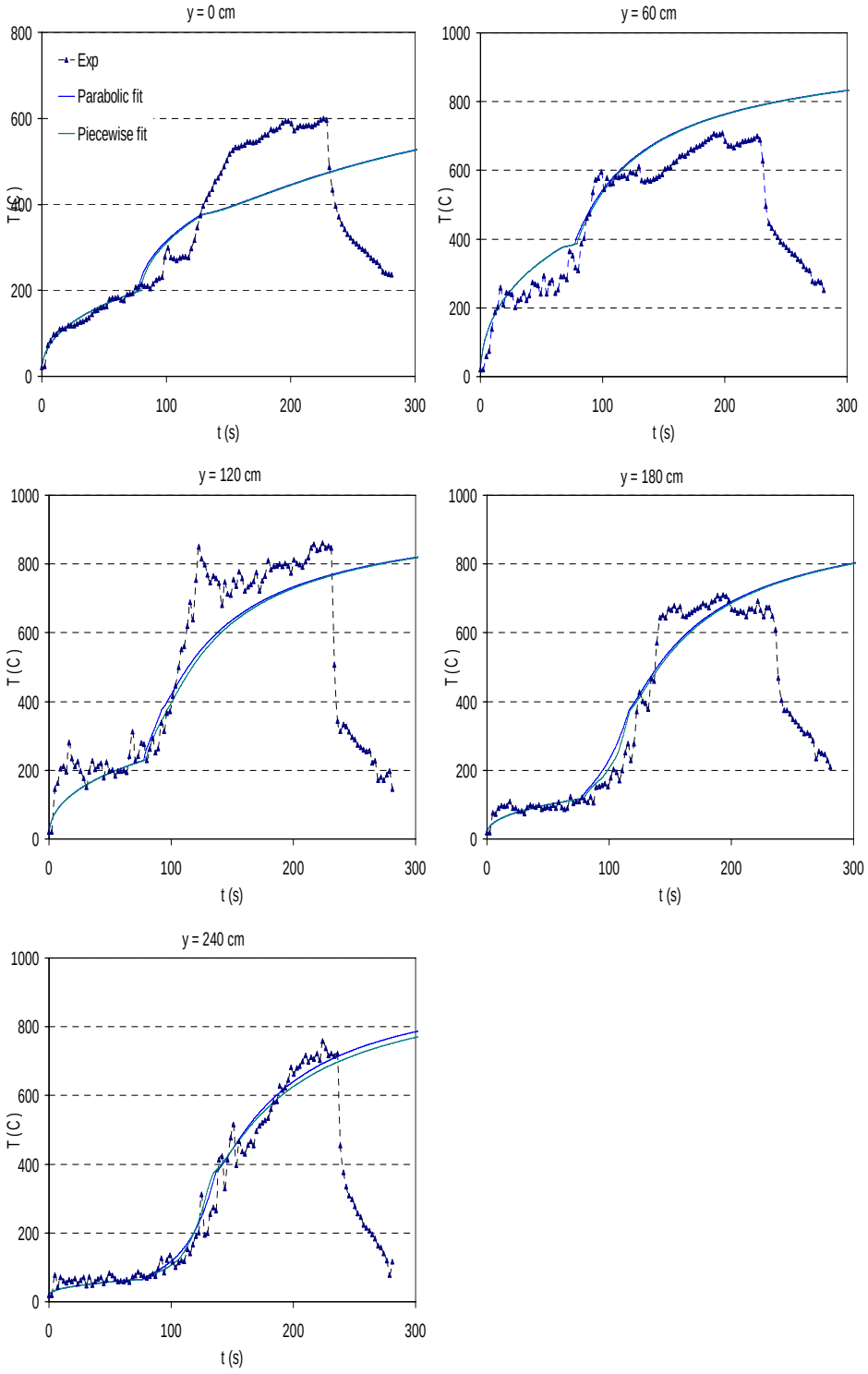

Figure 6.10: Temperature distribution for different heights using a constant honeycomb burner

7

Overall Conclusions

Starting from a basic thermodynamic description of pyrolysis phenomena, a simplified pyrolysis model has been described in detail. The basic model quantity is enthalpy, computed from the specific enthalpies of five constituents, namely dry virgin material, char, pyrolysis gases, liquid water and water vapour. Both the concept of pyrolysis heat and its relation to formation enthalpies of individual constituents have been revisited. It has also been explained how the developed model takes advantage of the use of pyrolysis heat to avoid the need for knowledge of the formation enthalpies of all individual constituents. The major assumption is that pyrolysis and evaporation are isothermal processes, taking place at infinitely thin fronts. The motion of each front is computed by means of a local mass and energy balance.

All equations have been solved on a fixed computational mesh, which makes the model appealing for general flame spread simulations. Indeed, it is easy to implement and applicable in three dimensions, for thermally thick or thin charring and non-charring materials, possibly containing moisture initially. The model can be combined with transport models for water liquid/vapour and pyrolysis gases in the solid material.

The numerical implementation and solution procedure have also been described. The model has then been applied to dry and wet charring materials, to non-charring materials and to a multi-dimensional configuration, resembling upward flame spread. Good agreement has been found for mass flow rates of pyrolysis gases in dry charring and non-charring materials (to which the model is directly applicable). The model formulation is robust with respect to several numerical aspects: the dependence of the results on the computational mesh cell's size and the physical time step size is small. Yet, in order to obtain continuous and smooth variations in time, it is essential to adopt a piecewise linear representation of the temperature field. With a constant temperature per computational cell, as is usually done, discontinuous evolutions of pyrolysis gases mass flow rates are obtained, regardless of the

physical time step and mesh size. The model is quick in terms of computational time already said in chapter 3.

The model has been applied to a series of test cases, illustrating that numerical reference results, obtained with the more complex moving mesh method, are well reproduced: the transient behaviour of the present model is good (no unphysical drops or peaks in the mass flow rates) and the effect of variable solid thickness and back surface boundary condition is well captured. In particular, the model performs well for the entire range of thermally thin through thermally thick materials. Moreover, possible interruption of the pyrolysis process due to insufficient incoming net heat fluxes, is automatically predicted.

Good agreement has again been found for the mass flow rate evolution in time of the pyrolysis gases, for plywood cone calorimeter experiments carried out in inert atmosphere. Furthermore, it has been explained how the model parameters (pyrolysis temperature and heat of pyrolysis) and boundary conditions (emissivity and back surface convective heat transfer coefficient) affect the mass flow rate, front and back surface temperatures and pyrolysis front position.

The effect of moisture is well captured : the pyrolysis process becomes slower as heat is consumed during the vaporisation process. The model can deal with multi-dimensional configurations by means of a test case, resembling upward flame spread. Many physical phenomena have been explained and automatically captured by the present, simplified model.

Cone calorimeter experiments have been conducted with different external heat flux intensities and for two different moisture contents (0 and 6.5%) of the sample. The results confirm that an increase in the intensity leads to higher volatiles mass flow rates and a shortened duration of the complete pyrolysis process. Presence of moisture in the solid obviously delays the pyrolysis process (i.e. causes a delay in ignition time of the solid) and increases the duration of the complete pyrolysis process. The enthalpy-based model for the pyrolysis process has predicted good agreement with the experiments. The mass flow rate peak value is very well captured, which is essential to predict the time of ignition.

Next, the extension of the model to two dimensions was discussed. Numerical reference test cases, with correlations from the literature to impose heat flux were considered first. The possibility to couple the developed pyrolysis model to CFD (Computational Fluid Dynamics). Simulations for gas phase turbulent combustion with radiation, was illustrated. From this we can conclude that the enthalpy based model can be easily be extended to higher dimensions, when the other existing models fail or are difficult to extend to higher dimensions. But, the model is limited to thermally thin materials, when the material thickness is much smaller than the other dimensions, as is mostly the case for fire (or flame spread) configurations.

In addition, original flame spread experiments have been performed in a vertical parallel particle board configuration. Two different distances between the very large plates (2.5m high) have been considered (30.5cm and 10.5cm). The flame height evolution in time was visually recorded. For both configurations, an acceleration in the increase of the flame height in time was observed. The process is about 4 times faster for the smallest distance between the plates. Temperatures have been measured over the entire height. The most interesting observation is that the temperatures are somewhat lower, although the flame

spread is much more rapid for the smaller distance between the plates due to increased radiative heat transfer (and possibly also due to higher upward convection of the flames). This is most likely due to incomplete combustion of the pyrolysis gases, as oxygen from the surrounding atmosphere might not be able to reach the centre in between the plates. The visual observation that flames extend outside of the parallel plate configuration supports this statement. Numerical simulation results show that the model predicts temperatures in good agreement with the experiments, when boundary conditions were are well tuned.

8

Future work

During pyrolysis, there are thermo-physical changes in the properties of the materials. These properties are temperature dependent. It is interesting to generate a model with thermo-physical properties which depend on temperature. The pyrolysis process is complex with various processes occurring at the same time. At present, the pyrolysis process is modelled for an inert atmosphere pyrolysis process. Oxidative pyrolysis process modelling has already been described for varying oxygen concentrations [65, 125]. This model can be applied to a pyrolysis process under an oxygen-controlled atmosphere.

Pyrolysis kinetics is deliberately not taken into account. This implies a limitation in applicability to situations where sharp fronts provide a good approximation for the pyrolysis and evaporation process. Note however, that multiple fronts (at different temperatures) can be easily be introduced, so that the pyrolysis process could be modelled by means of several fronts. At each front, a species of the pyrolysis gas mixture is then generated.

The effect of pores in the char need to be taken into account. In these pores, conduction in the gas phase can take place, possibly in combination with natural convection and, at sufficiently high temperatures, radiation.

Char oxidation and shrinkage also play a major role during the pyrolysis process [14, 18, 18, 90]. To capture these major events occurring during solid degradation, this process can be introduced into the model. Char oxidation is modelled by Weng et al. [126] assuming that it is an oxygen-controlled process, and the oxygen is diffused through the porous char according to Fick's law. During the pyrolysis process and char oxidation, a deformation takes place in the solid. This is incorporated in the form of a shrinkage factor discussed by Di Blasi [16]. Other factors like cracking and solid deformation can be included. Various models have been proposed in this part.

Incorporating the condensation of volatiles travelling in the direction of the pyrolysis and evaporation front motion. This can be done by giving a fraction of mass flow rate that cause condensation of volatiles in the lower temperature region of the virgin material.

Finally, for flame spread modelling, the approach was a pseudo-two dimensional model for the pyrolysis process. This can be turned into a complete model with the reconstruction method used in tracking the pyrolysis and evaporation fronts.

A

Enthalpy model - Zeroth order

A.1 Introduction

The development of the enthalpy based model (zero-th order) for the pyrolysis of charring materials is dealt. For the numerical solution of the model equations, VOF (Volume of Fluid) approach is followed, in order to avoid explicit front tracking. The pyrolysis process is treated as a endothermic, isothermal process occuring at the prescribed pyrolysis temperature T_{pyr}. Chemical kinetics is not taken into account. To make the model as simple as possible, moisture content and other effects occuring during the pyrolysis process are neglected at the moment. The configuration under consideration is one-dimensional, so that e.g. anisotropy in material properties is not taken into account. As seen in chapter 2 enthalpy based model is developed using enthalpy as the basic quantity.

A.2 Model development

Figure A.1 shows a schematic one-dimensional representation of the enthalpy based model (zero-th order). The figure also shows the different zones during the pyrolysis process. A constant external radiative heat flux is applied on the left boundary of the solid, while the right boundary is completely insulated. Initially the solid is at the ambient temperature. When the solid is exposed to heat flux, the temperature in solid rises. When the temperature becomes sufficiently high, the pyrolysis process starts. Solid (virgin) material degrades and volatile combustible gases are released. These volatiles move out of the solid as soon as they are produced. There is also inward movement of these volatiles, which is ignore. In general the solid is divided into three different zones:

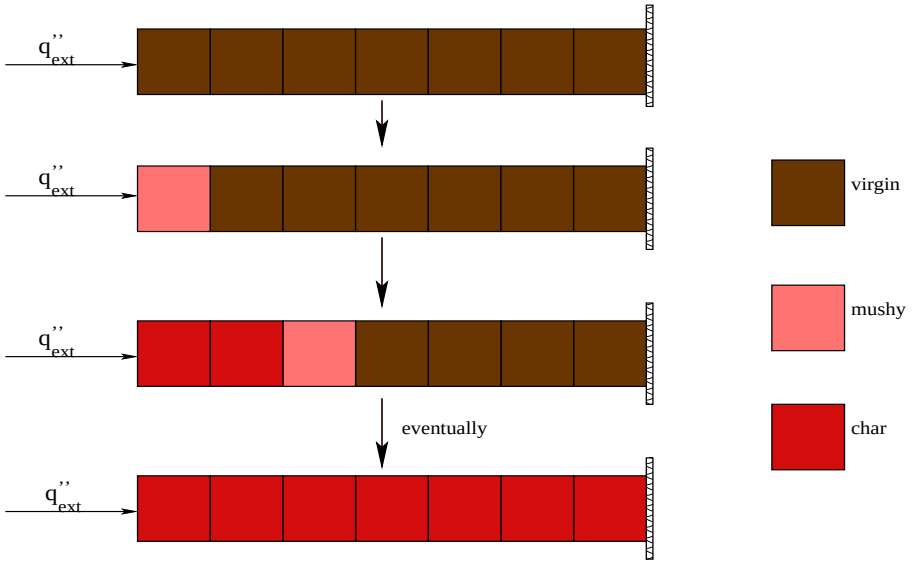

Figure A.1: Enthalpy based model representation

- virgin material: cells with char fraction ξ equal to zero;
- a single mushy cell, where $0< \xi <1$;
- char material: cells where ξ equal to 1.

The quantities $((\tilde{\rho}h)_i, T_i)$ in the model are stored in the cell centers. In the zero-th order, the temperature is assumed uniform in each cell. Enthalpy is the basic quantity of the model. The thermodynamic definition of enthalpy is made in chapter 2.

The thick vertical line with arrow represents the pyrolysis process. During pyrolysis, there is a monotonous rise in enthalpy at a constant temperature, equal to T_{pyr}. Pyrolysis takes place in the mushy cell when the following conditions are fulfilled at the same time:

- temperature at the pyrolysis front equals pyrolysis temperature T_{pyr};
- char fraction ξ in the cell is below 1;
- there is a rise in enthalpy $(\tilde{\rho}h)_i$ in the cell.

If any of these conditions is not fulfilled, a variation in enthalpy in the mushy cell is transformed into a variation in temperature. This is shown as inclined dashed lines in figure A.2.

In case of a constant external heat flux imposed on the virgin solid material, as is the case in the present study, the pyrolysis front (mushy cell) advances into the virgin solid material, leaving behind char, which has a lower density ($\rho_c < \rho_v$). Note that pyrolysis, a transition of virgin material into char, is irreversible: once char has been formed, it cannot be transformed back into virgin material.

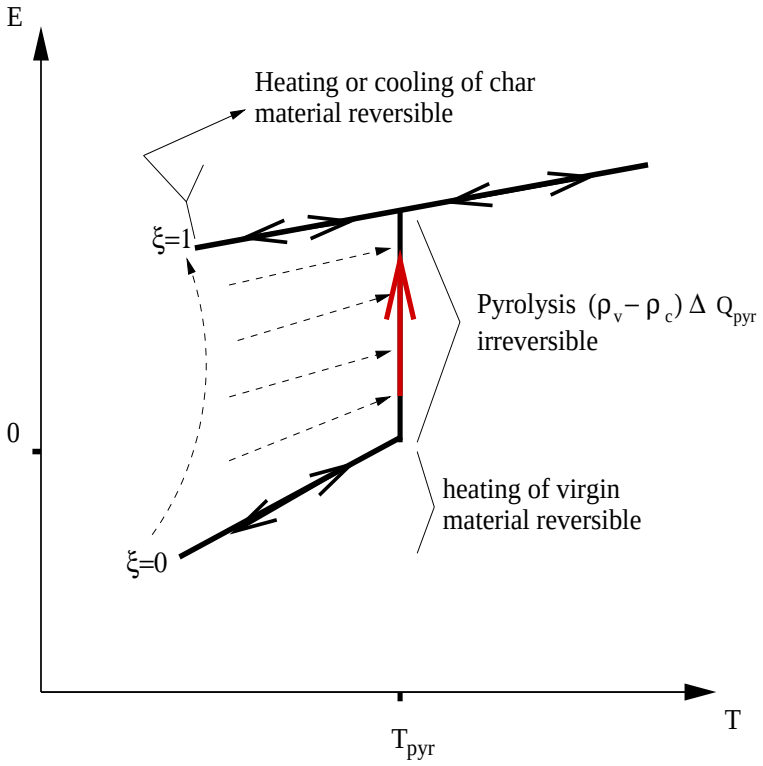

Figure A.2: Relation between enthalpy, char fraction and temperature

The basic equation is the energy conservation equation, yielding the update in energy density in cell i as follows:

$$(\tilde{\rho}h)_i^{n+1} = (\tilde{\rho}h)_i^n + \frac{\Delta t}{\Delta x_i}[(\dot{q}''^n_{cond,i-1/2} + \dot{q}''^n_{cond,i+1/2}) + (\dot{q}''^n_{conv,i-1/2} + \dot{q}''^n_{conv,i+1/2})] \tag{A.1}$$

The sign convention in equation (A.1) is such that heat fluxes $\dot{q}''$ are positive when they remove energy from cell 'i'. The subscript 'cond' refers to heat conduction, while 'conv' denotes convection of heat by the pyrolysis gases, generated in the mushy cell and flowing out of the solid material where the external heat flux is imposed. The superscript refers to the physical time level: $t^{n+1} = t^n + \Delta t$. A Cartesian grid of N number of cells with Δx_i as cell dimension is used in the numerical simualtions.

The sum of the conductive and convective heat flux is responsible for the increase in the enthalpy level at every time step. The enthalpy change gives rise to the new enthalp level at the new time step. The conductive heat flux is given by Fourier's law. This is straightforward for an interface between two similar cells, i.e. between two char or two virgin cells, with central discretisation:

$$\dot{q}''_{cond,i-1/2} = -\frac{T_i - T_{i-1}}{R_{i-1/2}}; R_{i-1/2} = \frac{\frac{1}{2}\Delta x_{i-1}}{k_{i-1}} + \frac{\frac{1}{2}\Delta x_i}{k_i} \tag{A.2}$$

Obviously, the expression at face $i + 1/2$ is similar. 'k' is the effective thermal conductivity, which is equal to the thermal conductivity of the pure material here. This quantity can depend on temperature.

The thermal conductivity for a mushy cell with a sharp front is given as:

$$\frac{1}{k_i} = \frac{\xi_i}{k_c} + \frac{(1-\xi_i)}{k_v} \tag{A.3}$$

The discretised conductive heat flux at the face of a mushy cell, with a sharp front is:

$$q''_{cond,i-1/2} = \frac{T_{i-1} - T_{pyr}}{(\frac{1}{2}\Delta x_i + \frac{1}{2}\Delta x_{i-1})/k_{i-1}} + \frac{T_{pyr} - T_i}{(\frac{1}{2}\Delta x_i + \frac{1}{2}\Delta x_{i-1})/k_i} \tag{A.4}$$

The convective heat fluxes depend on the mass flow rates of pyrolysis gases through faces $i+1/2$ and $i-1/2$. These mass flow rates are related to variations in char fraction in the mushy cell: as pyrolysis takes place, this char fraction evolves from 0 to 1 and pyrolysis gases are generated as virgin material is transformed into char. This can be expressed as follows. The variation in total mass of the solid determines the amount of volatiles that evolved out of the solid. It is assumed that the pyrolysis gases leave the solid material instantaneously. The total mass of the solid is given by:

$$\dot{m}''_{tot} = \sum_i \left(\rho_c \xi_i + \rho_v (1-\xi_i)\right) \Delta x_i \tag{A.5}$$

Thus, the pyrolysis gases mass flow rate is:

$$\dot{m}''_g = -\frac{d\dot{m}''_{tot}}{dt} = \sum_i (\rho_v - \rho_c) \Delta x_i \frac{d\xi_i}{dt} \tag{A.6}$$

From this mass flow rate, the convective heat fluxes can be computed, with upwind differencing:

$$\dot{q}''_{conv,i-1/2} = \dot{m}''_{g,i-1/2} \cdot c_{pyr}(T_i) \cdot T_{i-1/2} \tag{A.7}$$

In equation A.7, c_{pyr} is the thermal heat capacity of the pyrolysis gases. From the above equations, it is clear that the temperature and char fraction fields need to be determined from the basic variable, enthalpy $(\tilde{\rho}h)_i$, in order to determine the fluxes that govern the evolution of enthalpy in equation A.1. Still under the assumption of a zero-th order temperature representation and first assuming that there is no cooling down phase, and recalling that the enthalpy equals zero when the virgin material temperature is equal to the pyrolysis temperature, the following relations are valid for char fraction as function of enthalpy (see figure A.2):

$$\begin{aligned} (\tilde{\rho}h)_i \leq 0 &\rightarrow \xi_i = 0 \\ 0 \leq (\tilde{\rho}h)_i \leq (\rho_v - \rho_c)\Delta Q_{pyr} &\rightarrow \xi_i = \frac{(\tilde{\rho}h)_i}{(\rho_v - \rho_c)\Delta Q_{pyr}} \\ (\tilde{\rho}h)_i \geq (\rho_v - \rho_c)\Delta Q_{pyr} &\rightarrow \xi_i = 1 \end{aligned} \tag{A.8}$$

Here, ΔQ_{pyr} is the pyrolysis energy. If a mushy (or char) cell cools down, the char fraction must remain unchanged, as pyrolysis is an irreversible process. An increase of char fraction beyond 1 must be avoided. This can then be summarised for the mushy cell as:

$$0 < \xi_i < 1 \Rightarrow \xi_i^{n+1} = min\left(max\left(\xi_i^n; \frac{(\tilde{\rho}h)_i}{(\rho_v - \rho_c)\Delta Q_{pyr}}\right); 1\right) \tag{A.9}$$

The general relation between temperature and enthalpy contains the char fraction of cell i:

$$\begin{aligned}(\tilde{\rho}h)_i = (1-\xi_i)\int_{T_{pyr}}^{T_i} \rho_v c_v(T)dT \\ + \xi_i \int_{T_{pyr}}^{T_i} \rho_c c_c(T)dT + \xi_i(\rho_v - \rho_c)\Delta Q_{pyr}\end{aligned} \tag{A.10}$$

The determination of temperature from the enthalpy is less straightforward and depends on the char fraction of cell i. Simplifying, primarily for ease of notation, to constant thermal capacities c_v and c_c, this becomes:

- Virgin cell:

$$\xi_i = 0 \Rightarrow T_i = T_{pyr} + \frac{(\tilde{\rho}h)_i}{\rho_v c_v} \tag{A.11}$$

- Pyrolysing mushy cell:

$$\xi_i = \frac{(\tilde{\rho}h)_i}{(\rho_v - \rho_c)\Delta Q_{pyr}} \Rightarrow T_i = T_{pyr} \tag{A.12}$$

- Non-pyrolysing mushy cell:

$$\begin{aligned}\xi_i > \frac{(\tilde{\rho}h)_i}{(\rho_v - \rho_c)\Delta Q_{pyr}} \Rightarrow \\ T_i = T_{pyr} + \frac{(\tilde{\rho}h)_i - \xi_i(\rho_v - \rho_c)\Delta Q_{pyr}}{\xi_i \rho_c c_c + (1-\xi_i)\rho_v c_v}\end{aligned} \tag{A.13}$$

- Char cell:

$$\xi_i = 1 \Rightarrow T_i = T_{pyr} + \frac{(\tilde{\rho}h)_i - \rho_v - \rho_c)\Delta Q_{pyr}}{\rho_c c_c} \tag{A.14}$$

A.3 Implementation and solution procedure

The model falls in the category of VOF (Volume of Fluid). Pyrolysis process occurs when the cell temperature reach the predefined pyrolysis temperature T_{pyr}. This temperature is stored in the cells center along with the enthalpy. The model assumes that volatiles reach the surface as soon as they are produced. There is a thermal equilibrium established between the pyrolysis gases and the char matrix.

The flow chart in figure A.3 illustrates the solution procedure for zeroth order enthalpy based model. Starting from the initial conditions, physical time steps $\Delta t = t^{n+1} - t^n$ are taken till the end of the simulation. From the initial condition, the enthalpy in the cell is computed by $\rho_v c_v (T_{ref} - T_{pyr})$. Stepping from time t^n to t^{n+1} occurs in an iterative manner. From the new enthalpy level, char fraction ξ is computed. The mass flow rate of pyrolysis gases is computed with the increase in the char fraction. From the new char fraction ξ^{n+1} and enthalpy $(\tilde{\rho}h)^{n+1}$, the cell temperature is computed as in A.11 to A.14. Care is taken to keep the char fraction below unity in the mushy cell i.e. $0 < \xi < 1$. Once all the variable are computed, fluxes are computed at the cell face. Conductive flux is computed using

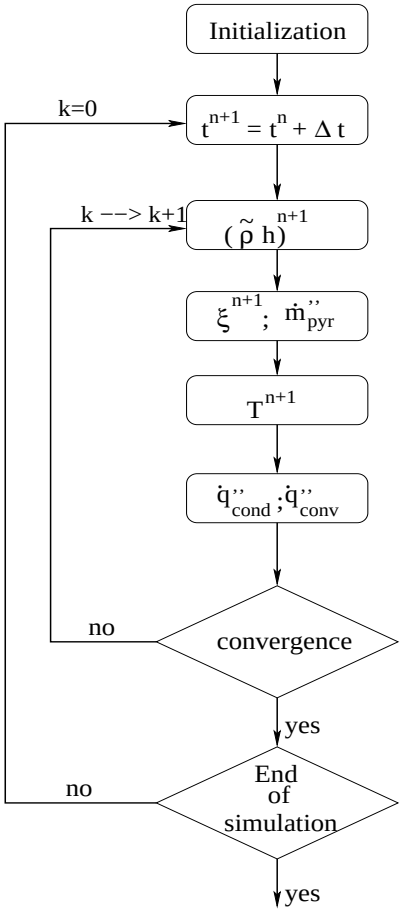

Figure A.3: Flow chart: Solution procedure for dry charring materials (mushy cell) - Zeroth order

the Fourier law, while convective flux concerns to the flow of volatiles from the solid. The convergence is checked for the iterative procedure. This is done by means of an L_∞ residual $res = log\left(\underbrace{max}_{i}|res_i|\right)$, where res_i is defined for each cell as:

$$res_i = -\frac{(\tilde{\rho}h)_i^{n+1} - (\tilde{\rho}h)_i^n}{\Delta t} + \frac{q_{i-1/2}^{n+1} - q_{i+1/2}^{n+1}}{\Delta x_i} \tag{A.15}$$

Residuals at $k+1$ are compared to the residuals at $k=0$ and assume convergence when the residual drops to 5 orders of magnitude. If the convergence level is met, the next time level $n+1$ is achieved. If not, the next iteration is performed.

A.4 Discussion of Results

A one-dimensional test case, as depicted in figure A.1, is considered. The material thickenss L is 3 cm. A total of 40 cells are used in the simulations with a time step size of 0.1 s. Possible shrinking and cracking due to pyrolysis process are not taken into account.

The following table shows the thermo-physical properties used in the numerical simulation are taken from [109] is put in table A.1. The convection heat transfer coefficient h = 5.0

Properties	*Value*	*Units*
ρ_v	650.0	kg/m^3
ρ_c	350.0	kg/m^3
c_v	1257.0	J/(kgK)
c_c	1257.0	J/(kgK)
c_{pyr}	2000.0	J/(kgK)
k_v	0.1257	W/(mK)
k_c	0.1257	W/(mK)

Table A.1: Thermo-physical properties [92]

W/(m^{2}K), emissivity $\epsilon = 0.9$ and stefan boltzmann constant equal to $5.67 \cdot 10^{-8}$ W/(m^{2}K^4). The model parameters are T$_{pyr}$ = 570 K, heat of pyrolysis $\Delta Q_{pyr} = 7.54 \cdot 10^5$ J/kg.

Three different boundary conditions are applied on the solid under study. Case a and b are constant heat fluxes, while case c is a simplified radiation and convection combination, with a constant ambient temperature:

- case a: $\dot{q}''_{ext} = 50$ kW/m^2
- case b: $\dot{q}''_{ext} = 20$ kW/m^2
- case c: $\dot{q}''_{net} = 50$ kW/m^2 $- h(T_0 - T_\infty) - \epsilon\sigma(T_0^4 - T_\infty^4)$

For case c, T_0 denoted the temperature of the first cell (in the zero-th order temperature representation) or the front surface temperature. Ambient and reference temperature is T_∞=300 K. The other values are as shown in table A.1. For all three cases, the rear surface is perfectly insulted:

$$- k_{v/c} \frac{dT}{dx}\bigg|_{x=L} = 0 \tag{A.16}$$

Results are compared on three different grid sizes containing 40, 100, and 160 cells respectively in a one dimensional configuration. The meshes are equidistant Cartesian form.

Case a: $\dot{q}''_{ext} = 50$ kW/m^2

As mentioned, an external heat flux of 50 kW/m^2 is imposed on the front surface of the solid. The pyrolysis gases mass flow rate is shown in figure A.4 for the three meshes considered. The first, and maybe the most important observation is that the mass flow rate is not continuous in time. The mass flux always drops to zero when the char fraction in the mushy cell becomes equal to 1. This is due to the zero-th order temperature approximation, with uniform temperature in each cell. Indeed, as long as the mushy cell is pyrolysing, its temperature is kept constant equal to pyrolysis temperature T_{pyr}. The only heat transfer mechanism towards the virgin material is through conduction. Thus, it is inevitable that, at the moment where the mushy cell becomes pure char, the temperature of the neighbouring virgin cell is below pyrolysis temperature. This cell then first needs to heat up to the pyrolysis temperature, before it can start pyrolysing. During this heat up phase, the char

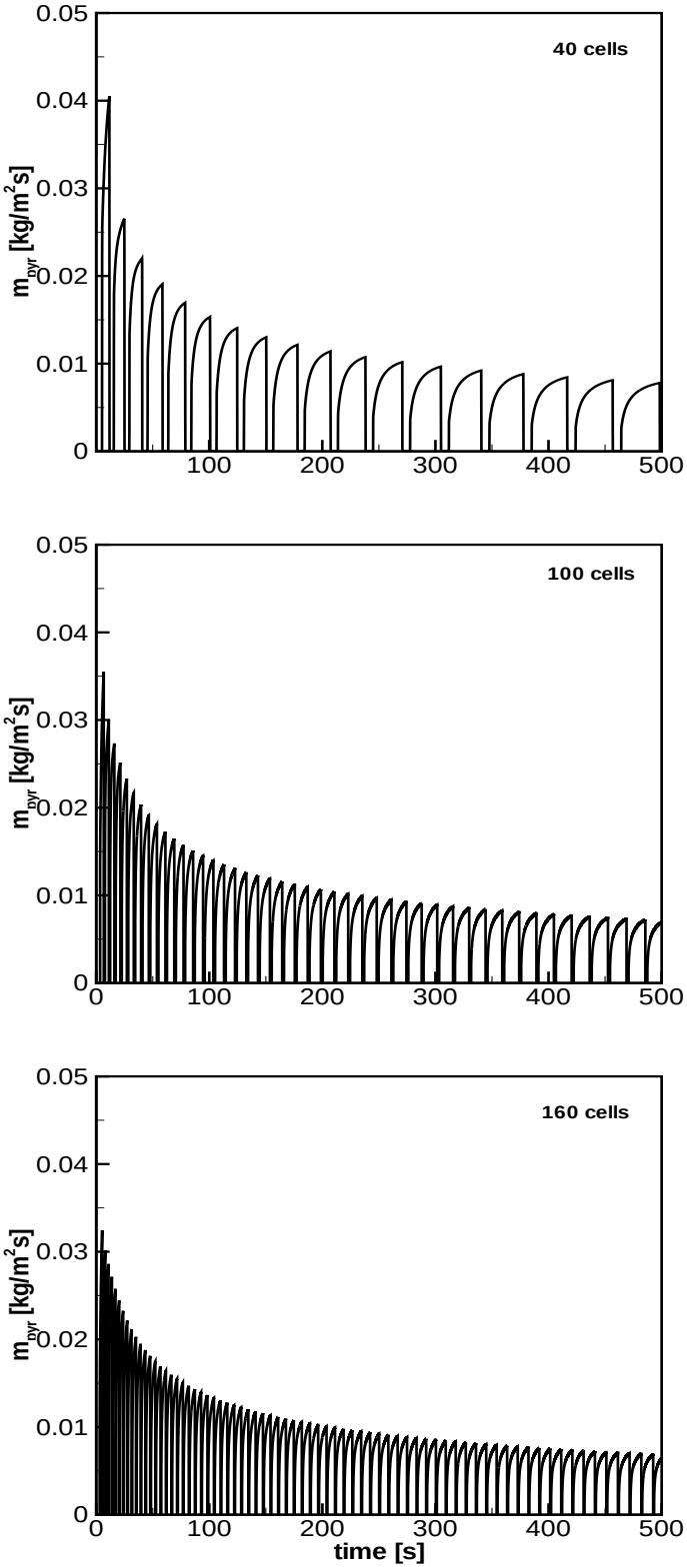

Figure A.4: Pyrolysis gases mass flow rate for case a (top left: 40 grid cells; top right: 100 cells; bottom: 160 cells)

fraction remains equal to zero, so that, through equation(A.6), the mass flux inevitably drops to zero. Clearly, this behaviour is not physical. More advanced temperature representation will cure this problem. This part is discussed at the end of this chapter and in chapter 2.

The second observation is that the intervals of pyrolysis, i.e. non-zero mass flow rate, become shorter as the number of cells increases. This is logical: as the cell become smaller, the time of evolution of char fraction from zero to one, becomes shorter for the same heat fluxes.

The third observation is that, if the peak values of pyrolysis mass flow rate in all intervals were connected, differences between the 100 cells and 160 cells meshes become small, but there is a clear distinction in comparison to the use of only 40 cells. For this coarse mesh, the maximum peak pyrolysis mass flow rate is met in the first interval and the peak value is higher than for the other two meshes. The decrease of the peak values in time is due to the higher heat losses at the front surface with the volatile components (eq. A.7).

Finally, we discuss the pyrolysis mass flow rate evolution in each pyrolysis interval. This is most clearly visualised for the coarse mesh, but the behaviour is similar for the other meshes. There is an increase in time of mass flow rate in each cell, primarily due to a decrease of conductive heat loss to the neighbouring virgin cell. This neighbour cell heats up, while the mushy cell remains at pyrolysis temperature with the zero-th order temperature representation. Again, this will be remedied with the more advanced temperature representation.

Case b: $\dot{q}''_{ext} = 20$ kW/m^2

This test case is very similar to case a, but the imposed external heat flux is lower, equal to 20 kW/m^2. Consequently, it takes longer for the first cell to become mushy. The pyrolysis intervals also become longer and the peak values lower, for the same reason. Again, differences between the 100 cells and 160 cells meshes are small, but there is a discrepancy with the 40 cells grid. In general, all the observations and explanations, described for case a, remain valid.

Case c: $\dot{q}''_{ext}$=50 kW/m^2 $- h(T_0 - T_\infty) - \epsilon\sigma(T_0^4 - T_\infty^4)$

For this case, the external heat flux of 50 kW/m^2 is counteracted by radiative and external convective heat losses. The latter must not be confused with the 'convective' heat losses by the pyrolysis gases from the solid material. Figure A.6 shows the results for case c. It is interesting to make the comparison to figure A.4, in order to judge upon the impact of radiation and convection for the present configuration. The global observations are the same as described above. The major difference is that the length of the pyrolysis intervals becomes longer and the peak value becomes lower as time proceeds. The reason is that the front face temperature decreases, so that radiative and convective heat losses increase and the net incident heat flux decreases. In the early stages, differences between figure A.6 (top) and A.4 (top) are small. As was observed in cases a and b, differences between the 100 cells and 160 cells meshes are small, but the discrepancy for the 40 cells mesh is substantial.

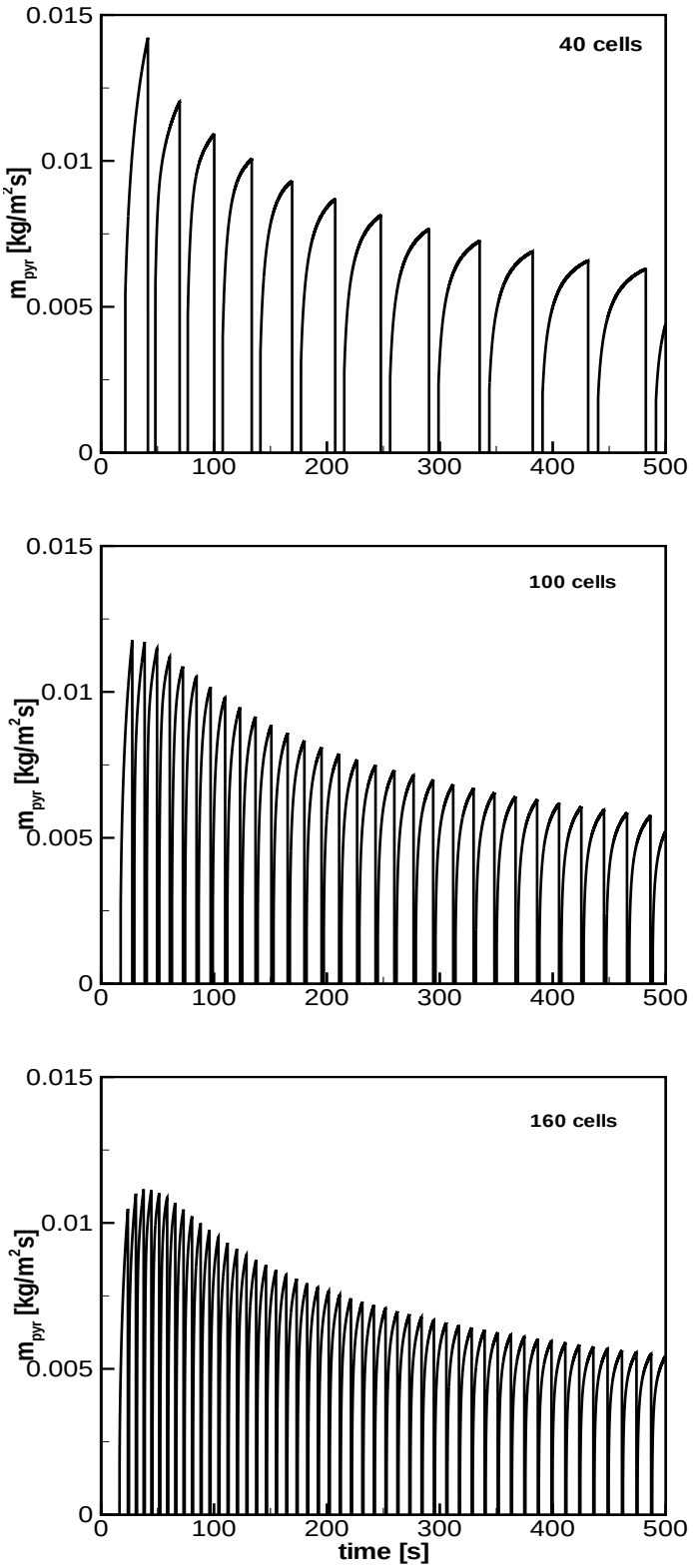

Figure A.5: Pyrolysis gases mass flow rate for case b (top left: 40 grid cells; top right: 100 cells; bottom: 160 cells)

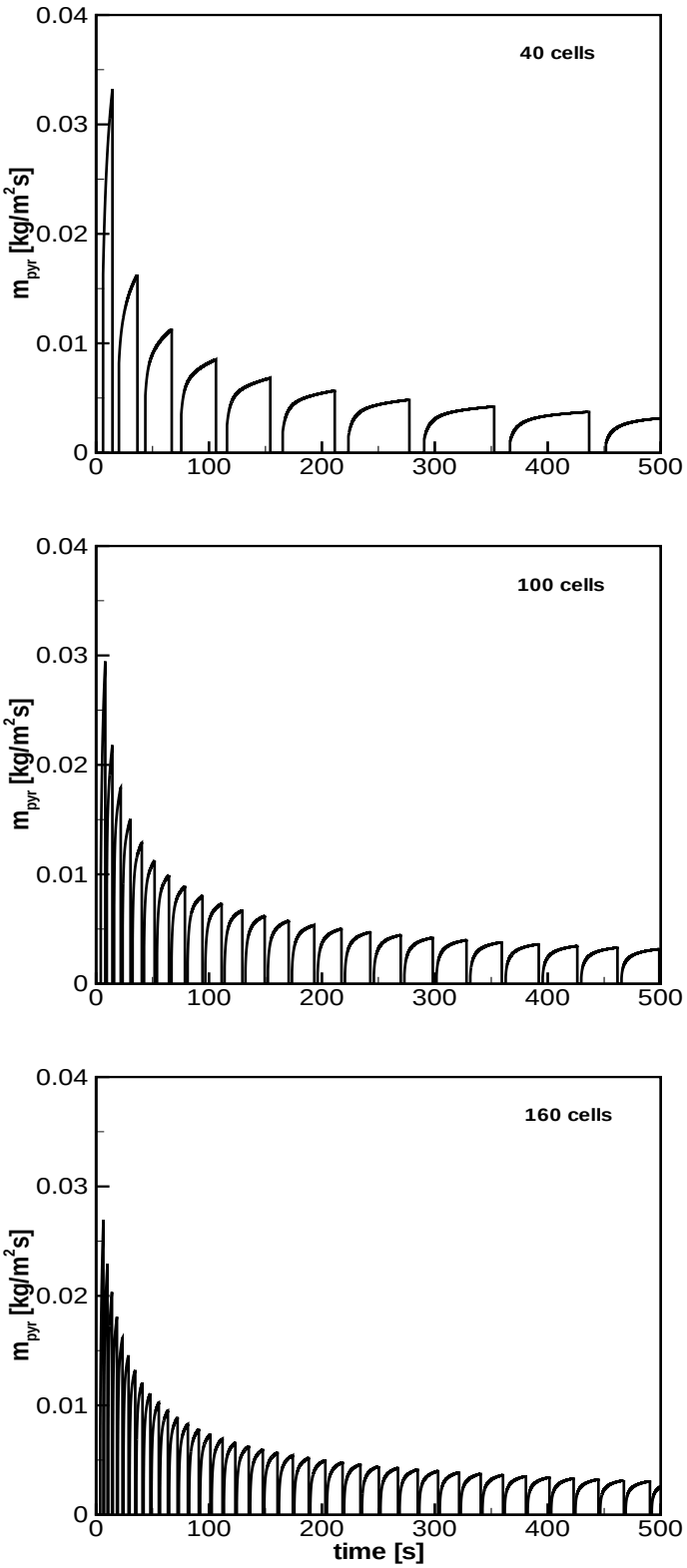

Figure A.6: Pyrolysis gases mass flow rate for case c (top left: 40 grid cells; top right: 100 cells; bottom: 160 cells)

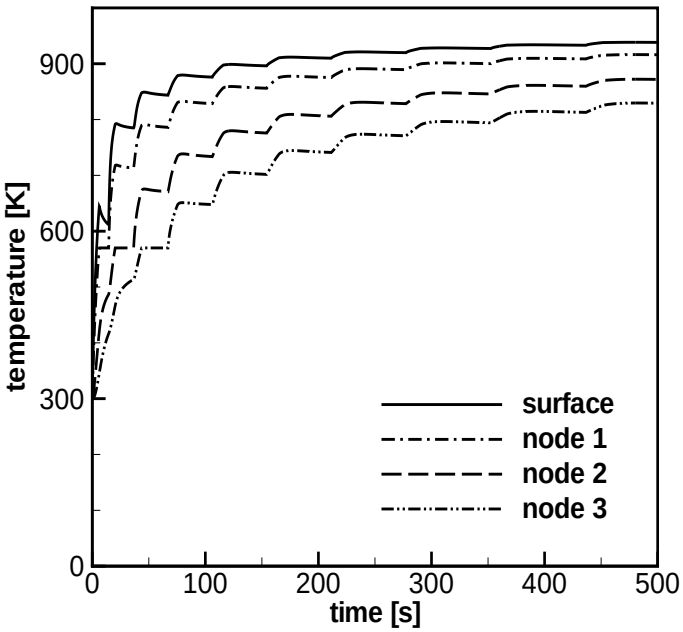

Figure A.7: Temperature evolution in time

A.5 Surface temperature

Finally, the front surface temperature evolution in time is shown in figure A.7. The front surface is exposed to external heat flux and the back surface is perfectly insulated. When external radiative and convective heat losses are taken into account at the front surface, there is a temperature evolution to an equilibrium temperature after 450 s. The surface temperature drops at the start of the pyrolysis process. This is due to the extrapolation of the temperatures. The extrapolation formula is:

$$T_s = T_o + \frac{1}{2}(T_0 - T_1) \tag{A.17}$$

When the first cell pyrolysis (mushy), its temperature is constant equal to pyrolysis temperature, while the neighbouring (second) cell temperature keeps rising due to conduction into the virgin solid. This leads to a lower surface temperature.

A.6 Enthalpy distribution

Figure A.8 shows the enthalpy distribution in the solid at different time levels. After 100 s, the pyrolysis front has crossed 0.003 m. There is a sharp rise in the enthalpy level at the pyrolysis front (mushy cell). The enthalpy at 0 level, when the cell temperature reach the pyrolysis temperature and char fraction $\xi = 0$. But increases rapidly with increases in ξ. Ofcourse, enthalpy in the solid increases due to the heating of pure virgin and char. It is below 0 value in virgin material and a very high value in the char layer.

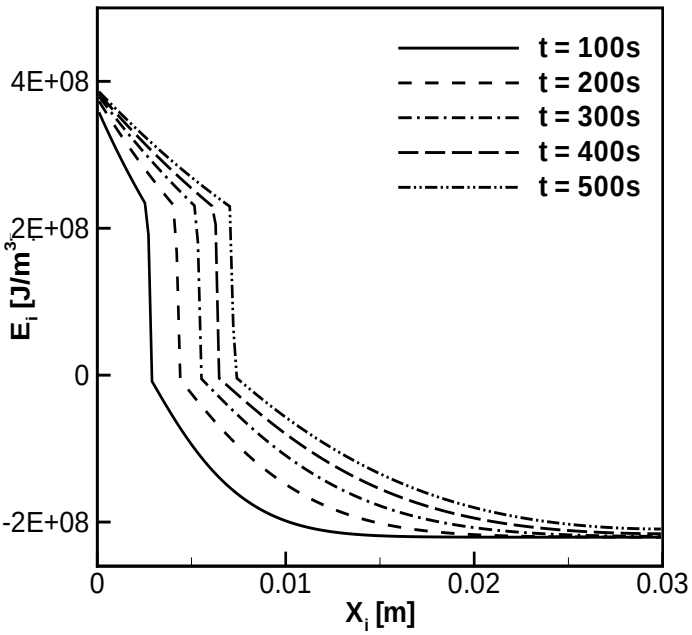

Figure A.8: Enthalpy distribution in the solid

A.7 Model improvement

The major limitation of this zero-th order enthalpy based model is the unphysical drop of pyrolysis mass flow rate to zero, when the mushy cell becomes pure char (i.e. ξ_i=1). As explained above, this is a direct consequence of the zero-th order temperature representation. This simple model can be improved by a higher order temperature field representation. The general idea is to construct piecewise linear temperature representation rather than a piecewise constant per cell. The modified enthalpy based model is modelled, instead of assuming a constant mushy cell temperature, equal to the pyrolysis temperature but in an infinitely thin pyrolysis front maintained at the pyrolysis temperature T_{pyr}. Details on the modelling and development of the modified model is described in chapter 2.

A.8 Conclusions

In this appendix, the enthalpy based model was applied to one-dimensional test cases. Some unphysical aspects observed have been explained and a model improvement, in order to remedy these shortcomings, has been suggested, based on piecewise linear temperature representation.

B

Solution procedure - Piecewise linear approach

B.1 Implementation and solution procedure

As described in the chapter 2, the model considers enthalpy as the basic variable, for which a transport equation is solved. Here, enthalpy alone is not only important, but rather focus is made in temperature distribution and volatile production. The latter is related to the motion of the pyrolysis front, which is assumed infinitely thin in the present model formulation. So, it is required to generate a procedure to reconstruct temperature and front position from the basic enthalpy variable. This is done, using the relationships between these variables, as described earlier in chapter 3. Note that pyrolysis is treated as an endothermic process, taking place infinitely fast at $T = T_{pyr}$, which effectively reduces the pyrolysis region to an infinitely thin front. The same is true for the evaporation process, being infinitely fast at $T = T_{evap}$. Some further assumptions are made in the applications below: the model assume that water vapour and pyrolysis gases leave the solid material at the side of the imposed external heat flux as soon as they are generated. This is the simplest possible transport model. The vapour and volatiles are further assumed to take the local temperature of the solid material (local thermal equilibrium throughout the solid).

B.1.1 Solution procedure

The flow chart in figure B.1 illustrates the solution procedure for dry charring materials. The treatment of the vaporisation front (at T=373 K) is similar to the treatment of the pyrolysis front and will therefore not be discussed. Starting from the initial conditions, physical time steps $\Delta t = t^{n+1} - t^n$ are taken until the end of the simulation. From the most recent situation, the conduction and convection fluxes are computed first for the enthalpy

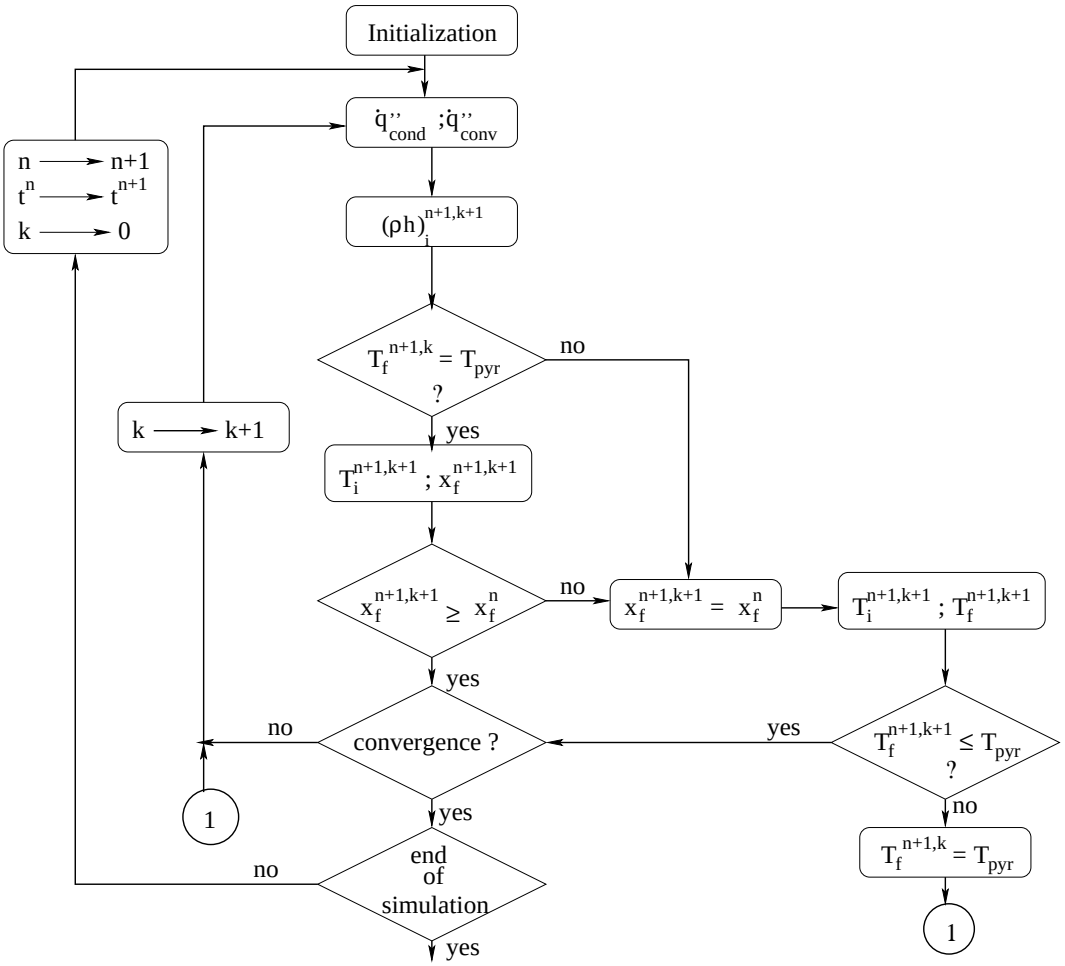

Figure B.1: Flow chart: Solution procedure for dry charring materials (mushy cell) - Piecewise linear

equation to be solved for each computational cell. Stepping from time t^n to t^{n+1} occurs in an iterative manner. The pseudo-time levels, for the evolution from t^n to t^{n+1} is denoted as $t^{n+1,k}$ or $t^{n+1,k+1}$, where the index k or $k+1$ indicates what values are used within this iterative procedure. From the fluxes, the enthalpy update is computed:

$$(\tilde{\rho}h)_i^{n+1,k+1} = (\tilde{\rho}h)_i^n + \frac{\Delta t}{\Delta x_i}\Big[\left(\dot{q}''^{n+1,k+1}_{cond,i-1/2} - \dot{q}''^{n+1,k+1}_{cond,i+1/2}\right) + \left(\dot{q}''^{n+1,k}_{conv,i-1/2} - \dot{q}''^{n+1,k}_{conv,i+1/2}\right)\Big] \tag{B.1}$$

In B.1, $\widetilde{\rho} = \sum_i \widetilde{\rho}_i$, the local mass concentration. In fact, only the central node is treated point-implicitly in the conductive fluxes in the subiterations described below. From the new enthalpy field, the temperature field, the position of the pyrolysis front and the pyrolysis front temperature must be reconstructed. As long as no pyrolysis process is taking place, only the temperature field must be reconstructed. Here, it is important to describe what must be done when there is a pyrolysis front.

If the pyrolysis process is ongoing, the pyrolysis front temperature is constant, equal to $T_f^{n+1,k+1} = T_f^{n+1,k} = T_{pyr}$. Thus, if $T_f^{n+1,k} = T_{pyr}$, the enthalpy update leads to a new temperature field $T_i^{n+1,k+1}$ and a movement of the pyrolysis front to a new position $x_f^{n+1,k+1}$. The front is allowed to move backwards during the iterative procedure, but it must not move back to a position $x_f^{n+1,k+1} < x_f^n$, as pyrolysis is an irreversible process. This is checked. If

$x_f^{n+1,k+1} \geq x_f^n$, there is no problem and convergence is checked for the iterative procedure. This is done by means of an L_∞ residual $res = log\left(\underbrace{max}_{i}(|res_i|)\right)$, where res_i is defined for each cell as:

$$res_i = -\frac{(\tilde{\rho}h)_i^{n+1,k} - (\tilde{\rho}h)_i^n}{\Delta t} + \frac{q_{i-1/2}^{n+1,k} - q_{i+1/2}^{n+1,k}}{\Delta x_i} \tag{B.2}$$

The latest residual is compared with the residual for $k = 0$ and we assume convergence when the residual dropped 5 orders of magnitude. If the convergence criterion is met, the next time level $n + 1$ is achieved. If not, the next iteration is performed. Now, when any of the above mentioned tests is *not true*, the following procedure is employed. First, it is possible that $T_f^{n+1,k} < T_{pyr}$, which means that previously, there has already been pyrolysis, but the pyrolysis process stopped (e.g. due to insufficient incoming heat flux for the pyrolysis process to continue). Then the pyrolysis front does not move and the new temperature field $T_i^{n+1,k+1}$ and the new pyrolysis front temperature $T_f^{n+1,k+1}$ are computed from the new enthalpy field. In the case of heating, it is possible that $T_f^{n+1,k+1} > T_{pyr}$. On the other hand, in our model the front temperature cannot exceed T_{pyr}. Thus, if $T_f^{n+1,k+1} > T_{pyr}$ is true, we clip the front temperature to $T_f^{n+1,k+1} = T_{pyr}$ and go to the next iteration. In this next iteration, the test $T_f^{n+1,k+1} = T_{pyr}$ will be true and the pyrolysis front will be allowed to move. Thus, it is possible that, within one physical time step from t^n to t^{n+1}, the pyrolysis front heats up to T_{pyr} and moves.

The second test fails if $x_f^{n+1,k+1} < x_f^n$. If so, the front position is clipped to $x_f^{n+1,k+1} = x_f^n$ and the front temperature is computed. Indeed, if the solution for the front position were a backward motion due to the enthalpy update, this is prohibited and cooling of the pyrolysis front is computed instead. From that point onwards, the numerical simulation proceeds further.

C

PDE formulations

C.1 Mass equations for the constituents

The mass equations for each of the five constituents are considered. The equations read (for a one-dimensional configuration):

$$\begin{cases} \dfrac{\partial \tilde{\rho}_v}{\partial t} = -\dot{\omega}_g(x)\dfrac{\rho_v}{\rho_v - \rho_c} \\ \dfrac{\partial \tilde{\rho}_c}{\partial t} = \dot{\omega}_g(x)\dfrac{\rho_v}{\rho_v - \rho_c} \\ \dfrac{\partial \tilde{\rho}_g}{\partial t} + \dfrac{\partial \tilde{\rho}_g u_g}{\partial x} = \dot{\omega}_g(x) \\ \dfrac{\partial \tilde{\rho}_{w,l}}{\partial t} = -\dot{\omega}_{w,v}(x) \\ \dfrac{\partial \tilde{\rho}_{w,v}}{\partial t} + \dfrac{\partial \tilde{\rho}_{w,v} u_{w,v}}{\partial x} = \dot{\omega}_{w,v}(x) \end{cases} \tag{C.1}$$

Processes only take place at the pyrolysis front ($x_{f,pyr}$) and the evaporation front ($x_{f,evap}$), so that the RHS in C.1 is zero in all equations elsewhere.

Note that virgin material, char and water as a liquid do not move in the model formulation, so that theit velocities are zero. The notation refers to local densities. For char, e.g., the local density can only take 2 values:

$$\begin{aligned} \tilde{\rho}_c &= \rho_c \quad \text{if } x < x_{f,pyr} \\ \tilde{\rho}_c &= 0 \quad \text{if } x > x_{f,pyr} \end{aligned} \tag{C.2}$$

The convective velocities u_g and $u_{w,v}$ stem from a transport model. In the model, their

values equals infinity, i.e. pyrolysis gases and water vapour immediately leave the solid matrix, as soon as they are created. However, the product remain finite.

The production rates of gases and water vapour are related to the speed of the front motion, as is discussed next.

C.2 Motion of pyrolysis front and evaporation front

The motion of the pyrolysis front is determined from a local mass balance equation:

$$\dot{\omega}_g(x) = (\rho_v - \rho_c)\,\frac{dx_{f,pyr}}{dt}\delta\left(x - x_{f,pyr}\right) \tag{C.3}$$

where $\delta\,()$ is Dirac-functional, defined as:

$$\begin{cases} \delta\left(x-a\right) = \begin{cases} 0 & \text{if x}\neq \text{ a} \\ \infty & \text{if x=a} \end{cases} \\ \int_{-\infty}^{+\infty} \delta\left(x-a\right) dx = 1 \end{cases} \tag{C.4}$$

Indeed: omtegrating expression (refapp3eq3) over a control volume around the pyrolysis front yields:

$$\begin{aligned} \int_{CV} \dot{\omega}_g dV &= \int_{CV} (\rho_v - \rho_c)\,\frac{dx_{f,pyr}}{dt}\delta\left(x - x_{f,pyr}\right) dV \\ &= (\rho_v - \rho_c)\,\frac{dx_{f,pyr}}{dt} S \underbrace{\int \delta\left(x - x_{f,pyr}\right) dx}_{1} \end{aligned} \tag{C.5}$$

which exactly corresponds to a mass balance over the pyrolysis front (also refer to equation 2.19).

A similar expression can be derived for the motion of the evaporation front:

$$\dot{\omega}_{w,v}(x) = \rho_{w,l}\frac{dx_{f,evap}}{dt}\delta\left(x - x_{f,evap}\right) \tag{C.6}$$

C.3 Enthalpy equation

The enthalpy equation reads:

$$\frac{\partial \tilde{\rho} h}{\partial t} + \frac{\partial \tilde{\rho} h u}{\partial x} = -\frac{\partial}{\partial x} q_{cond} \tag{C.7}$$

Using 2.1 and 2.16, C.7 becomes:

$$\sum_{\alpha} \frac{\partial \tilde{\rho}_\alpha h_\alpha}{\partial t} + \sum_{\alpha} \frac{\partial \tilde{\rho}_\alpha h_\alpha u_\alpha}{\partial x} = +\frac{\partial}{\partial x}\left(k\frac{\partial T}{\partial x}\right) \tag{C.8}$$

In the convection term, the velocity of the constituents must be taken. Thus, the convection term only appears for gas and water vapour in the model. Further elaboration yields:

$$\underbrace{\sum_{\alpha} \tilde{\rho}_\alpha \left[\frac{\partial h_\alpha}{\partial t} + u_\alpha \frac{\partial h_\alpha}{\partial x} \right]}_{I} + \underbrace{\sum_{\alpha} h_\alpha \left[\frac{\partial \tilde{\rho}_\alpha}{\partial t} + \frac{\partial \tilde{\rho}_\alpha u_\alpha}{\partial x} \right]}_{II} = + \frac{\partial}{\partial x} \left(k \frac{\partial T}{\partial x} \right) \tag{C.9}$$

The two terms in the LHS are now discussed. Using 2.2, the dependency on formation enthalpies disappears:

$$\sum_{\alpha} \tilde{\rho}_\alpha \left[\frac{\partial}{\partial t} \int_{T_{ref,\alpha}}^{T} c_\alpha(T) dT + u_\alpha \frac{\partial}{\partial x} \int_{T_{ref,\alpha}}^{T} c_\alpha(T) dT \right] \tag{C.10}$$

For term II, expression C.1 yields:

$$\begin{aligned} &\dot{\omega}_g(x) h_g\left(T\right) + \frac{\rho_c}{\rho_v - \rho_c} \dot{\omega}_g(x) h_c\left(T\right) - \frac{\rho_c}{\rho_v - \rho_c} \dot{\omega}_g(x) h_v\left(T\right) \\ &+ \dot{\omega}_{w,v}(x) h_{w,v}\left(T\right) - \dot{\omega}_{w,v}(x) h_{w,l}\left(T\right) \end{aligned} \tag{C.11}$$

Term II only differs from zero at the two fronts, which are at pyrolysis or evaporation temperature:

$$\begin{aligned} &\dot{\omega}_g(x) \left[h_g\left(T_{pyr}\right) + \frac{\rho_c}{\rho_v - \rho_c} h_c\left(T_{pyr}\right) - \frac{\rho_c}{\rho_v - \rho_c} h_v\left(T_{pyr}\right) \right] \\ &+ \dot{\omega}_{w,v}(x) \left[h_{w,v}\left(T_{evap}\right) - h_{w,l}\left(T_{evap}\right) \right] \end{aligned} \tag{C.12}$$

or, with 2.4 and 2.8:

$$\dot{\omega}_g(x) \Delta Q_{pyr} + \dot{\omega}_{w,v}(x) \Delta L_v \tag{C.13}$$

As such, the enthalpy equation C.9 reads:

$$\begin{aligned} &\tilde{\rho}_v \frac{\partial}{\partial t} \int_{T_{ref,v}}^{T} c_v(T) dT + \tilde{\rho}_c \frac{\partial}{\partial t} \int_{T_{ref,c}}^{T} c_c(T) dT + \tilde{\rho}_g \frac{\partial}{\partial t} \int_{T_{ref,g}}^{T} c_g(T) dT \\ &+ \tilde{\rho}_{w,l} \frac{\partial}{\partial t} \int_{T_{ref,w,l}}^{T} c_{w,l}(T) dT + \tilde{\rho}_{w,v} \frac{\partial}{\partial t} \int_{T_{ref,w,v}}^{T} c_{w,v}(T) dT \\ &+ \tilde{\rho}_g u_g \frac{\partial}{\partial x} \int_{T_{ref,g}}^{T} c_g(T) dT + \tilde{\rho}_{w,v} u_{w,v} \frac{\partial}{\partial x} \int_{T_{ref,w,v}}^{T} c_{w,v}(T) dT \\ &+ \dot{\omega}_g(x) \Delta Q_{pyr} + \dot{\omega}_{w,v}(x) \Delta L_v = \frac{\partial}{\partial x} \left(k \frac{\partial T}{\partial x} \right) \end{aligned} \tag{C.14}$$

The enthalpy equation can be simplified at positions where no front is present. In that case the heat input by conduction and conveciton is used to modify the temperature:

$$\begin{aligned} &\tilde{\rho}_v \frac{\partial}{\partial t} \int_{T_{ref,v}}^{T} c_v(T) dT + \tilde{\rho}_c \frac{\partial}{\partial t} \int_{T_{ref,c}}^{T} c_c(T) dT + \tilde{\rho}_g \frac{\partial}{\partial t} \int_{T_{ref,g}}^{T} c_g(T) dT \\ &+ \tilde{\rho}_{w,l} \frac{\partial}{\partial t} \int_{T_{ref,w,l}}^{T} c_{w,l}(T) dT + \tilde{\rho}_{w,v} \frac{\partial}{\partial t} \int_{T_{ref,w,v}}^{T} c_{w,v}(T) dT \\ &= \frac{\partial}{\partial x} \left(k \frac{\partial T}{\partial x} \right) - \left[\tilde{\rho}_g u_g \frac{\partial}{\partial x} \int_{T_{ref,g}}^{T} c_g(T) dT + \tilde{\rho}_{w,v} u_{w,v} \frac{\partial}{\partial x} \int_{T_{ref,w,v}}^{T} c_{w,v}(T) dT \right] \end{aligned} \tag{C.15}$$

At the front positions, during evaporation or pyrolysis, the heat front motion is governed by the heat balance. Consider e.g. the evaporation front. Introducing the notation $h_{s,i} = \int_{T_{ref}}^{T} c_i dT$ for the sensible enthalpy of a constituent, and $\dot{x}_{f,evap} = dx_{f,evap}/dt$ equation C.14 becomes:

$$\begin{aligned} &\tilde{\rho}_v \frac{\partial h_{s,v}}{\partial t} + \tilde{\rho}_c \frac{\partial h_{s,c}}{\partial t} + \tilde{\rho}_g \frac{\partial h_{s,g}}{\partial t} + \tilde{\rho}_g u_g \frac{\partial h_{s,g}}{\partial x} \\ &+ \tilde{\rho}_{w,l} \frac{\partial h_{s,w,l}}{\partial t} + \tilde{\rho}_{w,v} \frac{\partial h_{s,w,v}}{\partial t} + \tilde{\rho}_{w,v} u_{w,v} \frac{\partial h_{s,w,v}}{\partial x} \\ &+ \rho_{w,l} \dot{x}_{f,evap} \delta\left(x - x_{f,evap}\right) L_v = \frac{\partial}{\partial x}\left(k \frac{\partial T}{\partial x}\right) \end{aligned} \tag{C.16}$$

According to the model, the temperature remains 373K. So, for an observer moving with the evaporation front, $\frac{Dh_s}{Dt} = \frac{dh_s}{dT}\frac{DT}{dt}$=0 for each of the constituents, with $\frac{D}{Dt}$:

$$\frac{D\bullet}{Dt} = \frac{\partial \bullet}{\partial t} + \dot{x}_{f,evap} \frac{\partial \bullet}{\partial x} \tag{C.17}$$

Introducing this in equation C.16, yields:

$$\begin{aligned} &- \tilde{\rho}_v \dot{x}_{f,evap} \frac{\partial h_{s,v}}{\partial x} - \tilde{\rho}_c \dot{x}_{f,evap} \frac{\partial h_{s,c}}{\partial x} + \tilde{\rho}_g \left(u_g - \dot{x}_{f,evap}\right) \frac{\partial h_{s,g}}{\partial x} \\ &- \tilde{\rho}_{w,l} \dot{x}_{f,evap} \frac{\partial h_{s,w,l}}{\partial x} + \tilde{\rho}_{w,v} \left(u_{w,v} - \dot{x}_{f,evap}\right) \frac{\partial h_{s,w,v}}{\partial x} \\ &+ \rho_{w,l} \dot{x}_{f,evap} \delta\left(x - x_{f,evap}\right) L_v = \frac{\partial}{\partial x}\left(k \frac{\partial T}{\partial x}\right) \end{aligned} \tag{C.18}$$

At the front, $x = x_{f,evap}$, temperature is a continuous function and its derivative is piecewise continuous, with a step at the front position. The local densities of water as a liquid and as a vapour are also piecewise continuous, with a step at the front. Thus, the sum of the first five terms is a step function at the evaporation front and the leading term is the sixth term:

$$\begin{aligned} LHS = &\rho_{w,l} \dot{x}_{f,evap} \delta\left(x - x_{f,evap}\right) L_v \\ &+ \theta\left(H\left(x - x_{f,evap}\right)\right) + \theta\left(continuous\right) \end{aligned} \tag{C.19}$$

The notation $H(x-a)$ refers to the Heaviside function: $H(x-a) = 0$ for $x < a$; $H(x-a) = 1$ for $x \geq a$.

For the temperature derivative at the front (in the RHS), the indices l for the left front value limit and r for the right front value limit:

$$k \frac{\partial T}{\partial x} = \left(k \frac{\partial T}{\partial x}\right)_l + H(x - x_{f,evap}) \left[\left(k \frac{\partial T}{\partial x}\right)_r - \left(k \frac{\partial T}{\partial x}\right)_l\right] \tag{C.20}$$

so that:

$$\begin{aligned} RHS = \frac{\partial}{\partial x}\left(k \frac{\partial T}{\partial x}\right) &= \left(k \frac{\partial T}{\partial x}\right)_l + H(x - x_{f,evap}) \left[\left(k \frac{\partial T}{\partial x}\right)_r - \left(k \frac{\partial T}{\partial x}\right)_l\right] \\ &+ \left[\left(k \frac{\partial T}{\partial x}\right)_r - \left(k \frac{\partial T}{\partial x}\right)_l\right] \delta\left(x - x_{f,evap}\right) \\ &= \left[\left(k \frac{\partial T}{\partial x}\right)_r - \left(k \frac{\partial T}{\partial x}\right)_l\right] \delta\left(x - x_{f,evap}\right) \\ &+ \theta\left(H\left(x - x_{f,evap}\right)\right) + \theta\left(continuous\right) \end{aligned} \tag{C.21}$$

Thus, to leading order, equation C.18 becomes:

$$\rho_{w,l}\dot{x}_{f,evap}L_v = \left(k\frac{\partial T}{\partial x}\right)_r - \left(k\frac{\partial T}{\partial x}\right)_l \tag{C.22}$$

For the pyrolysis front, a similar expression can be derived:

$$\left(\rho_v - \rho_c\right)\dot{x}_{f,pyr}\Delta Q_{pyr} = \left(k\frac{\partial T}{\partial x}\right)_r - \left(k\frac{\partial T}{\partial x}\right)_l \tag{C.23}$$

Equations C.22 and C.23 are derived from the finite volume in this work, yielding the same expressions 2.18 and 2.20.

D

Simulation and modelling gas phase

D.1 Conservation equations

The equation of continuity for a mixture is derived by considering an infinitesimal particle, with a infinitely small control volume ($\Delta x \Delta y \Delta z$) is given by:

$$\frac{\partial \rho}{\partial t} + (\nabla \cdot \rho \mathbf{v}) = 0 \tag{D.1}$$

For a binary mixture, or multicomponent system, the above equation can be written as:

$$\begin{aligned} &\frac{\partial \rho_i}{\partial t} + \nabla \cdot (\rho_i \bar{v}_i) = \omega_i \\ &\text{or} \\ &\rho \frac{\partial Y_i}{\partial t} + \rho v \cdot \nabla Y_i + \nabla \cdot \rho Y_i V_i = \omega_i \qquad i = 1, 2, 3, \cdots N \end{aligned} \tag{D.2}$$

Here, Y_i is the mixture fraction i.e. $Y_i = \rho_i / \rho$, ω_i is the rate of reaction for component i, v is the mass average velocity and V_i is the mass diffusion velocity [64]. The conservation of momentum for a Newtonian fluid (a fluid exhibiting a linear relationship between shear stress and rate of deformation), leads to a Navier-Stokes equation. Conservation of momentum for an infinitesimal control volume is given as:

$$\rho \left[u_j \bar{\nabla} \cdot u_i + \frac{\partial u_i}{\partial t} \right] = \frac{\partial \sigma_{ji}}{\partial x_j} + B_i \tag{D.3}$$

The surface force is split into a surface force df_i and a body force(per unit volume) B_i. For a mixture of N species, the body forces acting on the species may differ. Thus for a

multicomponent system:

$$B_i = \rho \sum_{k=1}^{N} (Y_k f_k)_i \tag{D.4}$$

where f_k is the force per unit mass on the kth species. And the stress tensor σ_{ij} is given as:

$$\sigma_{ij} = -p\delta_{ij} + \left(-\frac{2}{3}\mu\right)\frac{\partial u_k}{\partial x_k}\delta_{ij} + \mu\left(\frac{\partial u_i}{\partial x_j} + \frac{\partial u_i}{\partial x_i}\right) \tag{D.5}$$

replacing the value of B_i and σ_{ij} from D.4 and D.5, respectively in equation D.3 gives:

$$\begin{aligned}
\rho\left[u_j\frac{\partial u_i}{\partial t} + \frac{\partial u_i}{\partial t}\right] &= \frac{\partial \sigma_{ji}}{\partial x_j} + B_i \\
&= \frac{\partial \sigma_{ji}}{\partial x_j} + \rho\sum_{k=1}^{N}(Y_k f_k)_i \\
&= \frac{\partial}{\partial x_j}\left[-p\delta_{ij} + \left(-\frac{2}{3}\mu\right)\frac{\partial u_k}{\partial x_k}\delta_{ij} + \mu\left(\frac{\partial u_i}{\partial x_j} + \frac{\partial u_i}{\partial x_i}\right)\right] \\
&\qquad + \rho\sum_{k=1}^{N}(Y_k f_k)_i
\end{aligned} \tag{D.6}$$

The conservation of energy for a infinitesimal control volume is given by:

$$\rho\frac{Dh}{Dt} - \frac{Dp}{Dt} = -\nabla\cdot\mathbf{q} + \Phi + \dot{Q} + \rho\sum_{k=1}^{N} Y_k f_k \cdot V_k \tag{D.7}$$

where D/Dt is the material derivative, h is the total enthalpy in the system, $\dot{Q}$ is the heat input, p is the pressure in the system, Φ is the disspation by viscous stress and the final term is the work done by the body forces. Here, Φ is given by:

$$\begin{aligned}
&\Phi = \tau_{ij}\frac{\partial u_i}{\partial x_j} \\
\text{with} \qquad &\tau_{ij} = -\frac{2}{3}\mu\frac{\partial u_k}{\partial x_k}\delta_{ij} + \mu\left(\frac{\partial u_i}{\partial x_j} + \frac{\partial u_j}{\partial x_i}\right) = \sigma_{ij} + p\delta_{ij}
\end{aligned} \tag{D.8}$$

The total enthalpy is given by:

$$h = \Delta h^0_{f,i} + \int_{T_{ref}}^{T} C_{p,i}dT \tag{D.9}$$

The total enthalpy is defined as the sum of the formation enthalpy at the reference temperature T_{ref} and the thermal enthalpy.

Turbulence and combustion play an important role in the event of flame generation and flame spread phenomena. The flow phenomenon is charaterised into laminar, turbulent and transition regime depending on the value of the Reynolds number (Re). Reynolds number of a flow gives a measure of the relative importance of inertia forces and the viscous forces. For low Reynolds number, the flow is smooth and adjacent layers of fluid slide past each

other in a orderly fashion. Mixing is possible only due to molecular diffusion. This regime is called laminar flow.

Above critical Reynolds number Re_{crit}, there are some radical change in the flow behaviour. The flow pattern is not in order, velocity distribution vary from center to the wall. In other words there is a chaotic behaviour in the fluid particles. This regime is called turbulent flow. This chaotic behaviour is due to the formation of eddies in the flow regime. These eddies move randomly back and forth and across the adjacent fluid layers. Different characteristics of turbulent flows [64] are: irregularity, diffusivity, large Reynolds number, three dimensional vorticity fluctuations, dissipation.

Between these two flow regime lies the transition regime, mainly due to the occurance of small disturbances initially. The change from transition to turbulent is associated with the shear flow. Hydrodynamic stability theory seeks to identify conditions which give rise to the amplification of diturbances [116].

D.2 Direct Numerical Simulation

The approach of direct numerical simulation (DNS) started in the 1980s for non-reacting flows and in the 1990s for reacting flows [67]. DNS studies reveal the fine scale physics is captured with utmost realism. It yields first principle solution free from turbulence modelling errors. The above discussed Navier Stokes equations are employed in the direct numerical simulation. The superior accuracy of DNS comes at the expense of enormous computational demand, such an approach is not applicable to most practical engineering simulations. Some compromises in resolution must be made and the fine-scale details have to be modelled.

D.3 Reynolds-Averaged Navier-Stokes models

Deviating from the laminar to turbulent flow regime, there are fluctuations in velocity component. It is important to know that the velocity component is decomposed of a steady mean value $\bar{u}$ and a fluctuating value u'. If these instantenous values are solved in the numerical calculations, a vast amount of computational time is required. Hence, it is necessary to average these instantenous fluctuations, that are not very important. There are two averaging procedures commonly used:

Reynolds averaging

The conventional time-averaging procedure, also called Reynolds averaging for velocity component as:

$$\bar{u} = \frac{1}{\Delta t} \int_{t_0+\Delta t}^{t_0} u(t) \cdot dt \tag{D.10}$$

where Δt is the time scale, sufficiently larger than the turblent time scale and small enough to be resolved. This can now be put into two part i.e. the mean motion and the fluctuation, or eddy as

$$u = \bar{u} + u' \tag{D.11}$$
$$p = \bar{P} + p' \tag{D.12}$$
$$\rho = \bar{\rho} + \rho' \tag{D.13}$$
$$h_t = \bar{h_t} + h_t' \tag{D.14}$$
$$T = \bar{T} + T' \tag{D.15}$$

where the fluctuating terms ρ', h_t', T' are zero. This type of averaging is used for constant density flows.

Mass-weighted averaging (Favre averaging)

The mass-weighted velocity can be defined as:

$$\tilde{u} = \frac{\overline{\rho u}}{\bar{\rho}} \tag{D.16}$$

The velocity can then be written as:

$$u \equiv \tilde{u} + u'' \tag{D.17}$$

where u'' is the superimposed velocity fluctuation.

D.4 Continuity equation for compressible system

Navier-Stokes equations for a compressible, viscous, heat conducting perfect gas with averaging for the mean-continuity equation can be written as:

$$\frac{\partial \bar{\rho}}{\partial t} + \frac{\partial}{\partial x_j}\left(\bar{\rho}\tilde{u}_j\right) = 0 \tag{D.18}$$

the mean-momentum equation is:

$$\frac{\partial}{\partial t}\left(\bar{\rho}\tilde{u}_j\right) + \frac{\partial}{\partial x_j}\left(\bar{\rho}\tilde{u}_i\tilde{u}_j\right) = -\frac{\partial \bar{p}}{\partial x_i} + \frac{\partial}{\partial x_j}\left(\bar{\tau}_{ij} - \overline{\rho u_i'' u_j''}\right) + \bar{\rho} g_i \tag{D.19}$$

and the mean-energy equation is:

$$\frac{\partial}{\partial t}\left(\bar{\rho}\tilde{h}\right) + \frac{\partial}{\partial x_j}\left(\bar{\rho}\tilde{h}\tilde{u}_j\right) = \frac{\partial \bar{p}}{\partial t} + \frac{\partial}{\partial x_j}\left(\frac{k}{c_p}\frac{\partial \tilde{h}}{\partial x_j} - \overline{\rho h'' u_j''}\right) - \frac{\overline{\partial \dot{q}_j^R}}{\partial x_j} \tag{D.20}$$

The species conservation equation:

$$\frac{\partial}{\partial t}\left(\bar{\rho}\tilde{Y_k}\right) + \frac{\partial}{\partial x_j}\left(\bar{\rho}\tilde{Y_k}\tilde{u}_j\right) = \left(\overline{\rho D \frac{\partial Y_k}{\partial x_j}} - \overline{\rho u_i'' Y_k''}\right) + \bar{S}_k \tag{D.21}$$

The left hand side of the equation D.20 is the average change in ρh per unit volume per unit time, the first term on the right hand side denote the pressure work due to macroscopic motion, the term within the brackets is the heat transport due to conduction and the turbulent diffusion of ρh, and the last term is due to the radiation loss during fire.

From the above three equations D.18 to D.20, the averaging has generated two extra terms describing the fluctuating quantities from the inertial terms. These terms are the turbulent flux term involve the Reynolds stress for $\overline{\rho u_i'' u_i''}$ and Reynolds flux for $\overline{\rho h'' u_j''}$. Since there are more unknowns than equations, the system is not closed. Turbulence modelling gives closure to this problem. In the same way for the turbulent combustion a closure is reguired for the averaged reaction rate term $\bar{S}_k$. The models must be capable to serve the purpose, possess a wide applicability, be accurate, simple and economical to run in terms of computational costs.

D.5 Gradient transport models

Analogy is drawn between the turbulent transport of a flow property and the corresponding molecular diffusion transport, due to the diffusive and dissipative nature of turbulence. The gradient transport approach assumes that the turbulent transport term of a property is proportional to the negative of the gradient of the mean value of that property, with proportionality being the corresponding turbulent transport coefficient. This is done by Reynolds flux term for the reaction scalar ϕ as

$$\overline{\rho u_i'' \phi''} = -\frac{\mu_T}{\sigma_\phi} \frac{\partial \tilde{\phi}}{\partial x_i} \tag{D.22}$$

where μ_t is the turbulent viscosity coefficient, and σ_ϕ is the turbulent Prandtl or Schmidt number. To prescribe, Reynolds stress term $\overline{\rho u_i'' u_j''}$, the transport should not involve the symmertical term $\overline{\rho u_i'' u_i''}$ in the momentum transport equation D.19. With new turbulent kinetic energy, based on Favre-averaged quantities, Reynolds stress term is expressed as:

$$\overline{\rho u_i'' u_j''} = \frac{2}{3}\delta_{ij}\left(\rho_k + \mu_T \frac{\partial \tilde{u}_\alpha}{\partial x_\alpha}\right) - \mu_T \left(\frac{\partial \tilde{u}_i}{\partial x_j} + \frac{\partial \tilde{u}_j}{\partial x_i}\right) \tag{D.23}$$

Two equation model: k-ϵ model

In the $k-\epsilon$ model, two additional equaitons are solved for k and ϵ, where ϵ is the viscous dissipation rate of the turbulent kinetic energy k, defined as

$$k = \frac{\overline{u_i'' u_i''}}{2} \tag{D.24}$$

from k and ϵ, the turbulent viscosity can be calculated:

$$\mu_T = C_\mu \bar{\rho} \frac{k^2}{\epsilon} \tag{D.25}$$

where C_μ is the proportionality constant, equal to 0.09.

The determination of turbulent kinetic energy k and viscous dissipation rate ϵ, are discussed. The extra terms generated after averaging are subseguently modelled to effect closure. For the standard $k-\epsilon$ model [80], the equations read:

$$\frac{\partial}{\partial t}\left(\bar{\rho}k\right)+\frac{\partial}{\partial x_i}\left(\bar{\rho}\tilde{u}_i k\right)=\frac{\partial}{\partial x_i}\left[\left(\mu+\frac{\mu_T}{\sigma_k}\right)\frac{\partial k}{\partial x_i}\right]+P_k-\bar{\rho}\epsilon \tag{D.26}$$

$$\frac{\partial}{\partial t}\left(\bar{\rho}\epsilon\right)+\frac{\partial}{\partial x_i}\left(\bar{\rho}\tilde{u}_i \epsilon\right)=\frac{\partial}{\partial x_i}\left[\left(\mu+\frac{\mu_T}{\sigma_\epsilon}\right)\frac{\partial \epsilon}{\partial x_i}\right]+C_{\epsilon 1}\frac{\epsilon}{k}P_k-C_{\epsilon 2}\bar{\rho}\frac{\epsilon^2}{k} \tag{D.27}$$

where the source term P_k is given by:

$$P_k=-\overline{\rho u_i'' u_j''}\frac{\partial \tilde{u}_i''}{\partial x_j} \tag{D.28}$$

and the Reynolds stress $\overline{\rho u_i'' u_j''}$ are determined from Boussinesq equation D.23.

In Fluent, the standard $k-\epsilon$ model , the turbulent kinetic energy, k and its rate of dissipation, ϵ, are obtained from the following transport equations:

$$\begin{aligned}\frac{\partial}{\partial t}\left(\rho k\right)+\frac{\partial}{\partial x_i}\left(\rho u_i k\right)=&\frac{\partial}{\partial x_i}\left[\left(\mu+\frac{\mu_T}{\sigma_k}\right)\frac{\partial k}{\partial x_i}\right]\\&+G_k+G_b-\rho\epsilon-Y_M+S_k\end{aligned} \tag{D.29}$$

$$\begin{aligned}\frac{\partial}{\partial t}\left(\rho \epsilon\right)+\frac{\partial}{\partial x_i}\left(\rho u_i \epsilon\right)=&\frac{\partial}{\partial x_i}\left[\left(\mu+\frac{\mu_T}{\sigma_\epsilon}\right)\frac{\partial \epsilon}{\partial x_i}\right]\\&+C_{1\epsilon}\frac{\epsilon}{k}(G_k+C_{3\epsilon}G_b)-C_{2\epsilon}\rho\frac{\epsilon^2}{k}+S_\epsilon\end{aligned} \tag{D.30}$$

where, G_k represents the generation of turbulence kinetic energy due to the mean velocity gradients, G_b is the generation of turbulent kinetic energy due to buoyancy, Y_M represents the contribution of the fluctuating dilation in compressible turbulence to the overall dissipation rate, $C_{1\epsilon}$, $C_{2\epsilon}$ and $C_{3\epsilon}$ are constants. ρ_k and ρ_ϵ are the turbulent Prandtl numbers for k and ϵ. S_k and S_ϵ are user defined source terms.

Modelling the turbulent production is discussed now. The generation of turbulence kinetic energy, G_k, is evaluated in a consistent manner as:

$$G_k=\mu_t\sqrt{2S_{ij}S_{ij}} \tag{D.31}$$

where S is the modulus of the mean rate-of-strain tensor.

The genration of turbulence due to buoyancy is given by:

$$\begin{aligned}G_b&=\beta g_i\frac{\mu_t}{\mathrm{Pr}_t}\frac{\partial T}{\partial x_i}\\&\text{where}\\\beta&=-\frac{1}{\rho}\left(\frac{\partial \rho}{\partial T}\right)_p\end{aligned} \tag{D.32}$$

where Pr_t is the turbulent Prandtl number for energy and g_i is the component of the gravitational vector in the ith direction.

The contribution of the fluctuating dilation dissipation term in k equation is modelled as:

$$\begin{aligned} Y_M &= 2\rho\epsilon M_t^2 \\ &\text{where} \\ M_t^2 &= \sqrt{\frac{k}{a^2}} \end{aligned} \tag{D.33}$$

where $a \equiv \sqrt{\gamma RT}$ is the speed of sound.

The default set of constants in turbulence calculations presented in table D.1.

Constants	Value
C_μ	0.09
$C_{\epsilon 1}$	1.44
$C_{\epsilon 2}$	1.92
σ_k	1.0
σ_ϵ	1.30
σ_T	0.7

Table D.1: Constants for $k-\epsilon$ model

The $k-\epsilon$ model is simple, complete model to describe turbulent flows and is acceptable for simple flows.

D.6 Reynolds stress equation model

In the gradient transport models, the Reynolds stress and flux are limited to gradient transport. But, in Reynolds stress models moments of the Navier-Stokes equations are generated to model the Reynolds stress, and describe the turbulent transport. Turbulence models e.g. $k-\epsilon$ model assume a isotropic turbulence, but practical flows show anisotropic behaviour. This approach are known as Algebraic Stress Models (ASM). Algrbraic expressions are derived for the Reynolds stresses, $\bar{\rho}\widetilde{u_i''u_j''}$, which depend on turbulent kinetic energy, dissipation rates, mean strain tensor $\tilde{S}$ or mean rotational tensor. Another approach is to derive and close the balance equations for the Reynolds stresses. This is the Reynolds stress model (RSM), is a second order modelling.

D.7 Large Eddy Simulations

With steady RANS, it is impossible to capture highly transient phenomena or detailed structures of the turbulent flow. While, DNS is computationaly expensive. Large eddy

simulation (LES) gives a way by resolving the large scale structures while modelling the dissipative small scale processes. In LES, all the conservation equations are spatially filtered with a filter of size Δ, which is in general equivalent to the grid size (called grid filter) of the LES simulation.

D.8 Near wall treatments

The mean flow field is affected through the no-slip condition at the wall. Very close to the wall, viscous damping reduces the tangential velocity fluctuations, while kinematics blocking reduces the normal fluctuations.

The near wall region can be divided into three layers. The inner most layer, called the viscous sublayer, the flow is almost laminar, and the viscosity plays the major role in heat and momentum or mass transfer. The outer layer is the fully turbulent layer where turbulence play a major part. In between these two in an interim region, where the effects of molecular viscosity and turbulence are equally important. One way is to introduce wall functions. Wall functions are used to bridge the viscosity affected region between the wall and the fully turbulent region. This kind of approach save computational costs for high Reynolds numbers. The other approach is to modify the turbulence models by resolving the flow all the way to the wall. This is called near wall modelling approach valid for low Reynold number flows.

Wall functions comprise of two quantities:

- laws of the wall for the mean velocity and temperature.
- formulae for the near wall turbulent quantities.

Different approach have been used in the literature. Some of the prominent are: a. standard wall function, b. non-equilibrium wall function, c. enhanced wall function.

Sandard wall function: is the most widely used in industrial applications, was developed by Launder and Spalding. Here the boundary condition is applied some distance away from the wall, so that the turbulence-model equation are not solved close to the wall [81]. The wall function boundary condition is applied at a location $y = y_p$ in the log-law region (e.g. where y^+ is around 50). Subscript 'p' indicate quantities evaluated at y_p e.g. $\langle U \rangle_p$, k_p and ϵ_p.

The law of the wall for mean velocity is

$$\begin{aligned} u^+ &= \frac{1}{\kappa} ln\left(Ey^+\right) \\ \text{where} \quad u^+ &= \frac{y_p C_\mu^{1/4} k_p^{1/2}}{\tau_w/\rho} \\ y^+ &= \frac{\rho C_\mu^{1/4} k_p^{1/2} y_p}{\mu} \end{aligned} \tag{D.34}$$

here u^+ is the dimensionless velocity and y^+ is the dimensionless distance from the wall. The constants $C_\mu = 0.09$. The logarithmic law for the mean velocity is known to be valid for $30 < y^+ < 300$. Below this region i.e. $y^+ <$30, we assume $u^+ = y^+$.

Reynolds analogy between momentum and energy transport gives similar logarithmic law of mean temperature. The law-of-the wall implemented in Fluent is:

$$T^+ = \frac{(T_w - T_p)\,\rho c_p k_p^{1/2}}{\dot{q}} = \begin{cases} Pr \cdot y^+ & (y^+ < y_0^+) \\ \\ Pr_t \left[\frac{1}{\kappa} ln(Ey^+) + P\right] & \\ +\frac{1}{2}\rho \frac{C_\mu^{1/4} k_p^{1/2}}{\dot{q}} \left(Pr_t u_p^2 + (Pr - Pr_t)\, u_c^2\right) & (y^+ > y_0^+) \end{cases} \tag{D.35}$$

with P computed by using the formula given by Jayatilleke:

$$P = 9.24 \left[\left(\frac{Pr}{Pr_t}\right)^{3/4} - 1\right] \left[1 + 0.28 e^{-0.007 Pr/Pr_t}\right] \tag{D.36}$$

where Pr and Pr_t is molecular Prandtl number and turbulent Prandtl number respectively. The boudary value for k imposed at the boundary is:

$$\frac{\partial k}{\partial n} = 0 \tag{D.37}$$

where n is the local coordinate normal to the wall. The production of kinetic energy G_k, and its dissipation rate, ϵ are source terms in k equation. The production of k is based on the logarithmic law and is computed from:

$$G_k \approx \tau_w \frac{\partial u}{\partial y} = \tau_w \frac{\tau_w}{\kappa \rho k_p^{1/2} y_p}$$

$$\text{with } \epsilon \text{ is computed from} \tag{D.38}$$

$$\epsilon_p = \frac{C_\mu^{3/4} k_p^{3/2}}{\kappa y_p}$$

The dissipation ϵ equation is not solved at the wall-adjacent cells, but instead is computed using above equation D.38.

D.9 Enhanced wall treatment

Enhanced wall treatment is a near wall modelling method that combines a two-layer model with so called wall functions. The two layer approach is an integral part of the enhanced wall treatment and is used to specify both ϵ and the turbulent viscosity in the near wall cells. The system is divided into a viscosity-affected region and a fully turbulent region. The separation between the two regions is determined by a wall distance-based, turbulent Reynolds number, Re_y, defined as:

$$Re_y \equiv \frac{\rho y \sqrt{k}}{\mu} \tag{D.39}$$

where y is the wall-normal distance calculated at the cell center. In FLUENT, y is interpreted as the distance to the nearest wall:

$$y \equiv \underbrace{\min}_{\vec{r}\in\Gamma_w} \|\vec{r} - \vec{r}_w\| \tag{D.40}$$

where $\vec{r}$ is the position vector at the field point, and $\vec{r}_w$ is the position vector of the wall boundary. Γ_w is the union of all the wall boundaries involved. $k-\epsilon$ models are used in the fully turbulent region. In the viscosity-affected near wall region, the two-layer approach is used for the high-Reynolds-number along with the enhanced wall treatment [43]:

$$\mu_{t,enh} = \lambda_\epsilon \mu_t + (1-\lambda_\epsilon)\mu_{t,2layer} \tag{D.41}$$

where μ_t is the turbulent viscosity. A blending function, λ_ϵ, is defined in such a way that it is equal to unity away from walls and is zero in the vicinityof the walls. This blending function has the following form:

$$\lambda_\epsilon = \frac{1}{2}\left[1 + \tanh\left(\frac{Re_y - Re_y^*}{A}\right)\right] \tag{D.42}$$

Here, A determines the width of the blending function. The ϵ field of the velocity-affected region is computed from:

$$\epsilon = \frac{k^{3/2}}{l_\epsilon} \tag{D.43}$$

the length scales are computed as:

$$l_\epsilon = yC_l^*(1 - e^{-Re_y/A_\epsilon}) \tag{D.44}$$

The constants in the above equations are:

$$C_l^* = \kappa C_\mu^{-3/4'}, \qquad A_\epsilon = 2C_l^* \tag{D.45}$$

In Fluent, the near wall region is formulated by a single wall law for the entire wall region (i.e., viscous sublayer, buffer region and fully turbulent outer region) by blending the linear (laminar) and logarithmic (turbulent) laws-of-the-wall using a function as:

$$u^+ = e^\Gamma u^+_{\text{lam}} + e^{1/\Gamma} u^+_{\text{lam}} \tag{D.46}$$

where the blending function is given by:

$$\Gamma = -\frac{a(y^+)^4}{1+by^+} \tag{D.47}$$

where a=0.01 and b=5. The general equation for the derivative $\frac{du^+}{dy^+}$ is:

$$\frac{du^+}{dy^+} = e^\Gamma \frac{du^+_{\text{lam}}}{dy^+} + e^{1/\Gamma}\frac{du^+_{\text{turb}}}{dy^+} \tag{D.48}$$

The enhanced wall functions are developed by combining an enhanced turbulent wall law with the laminar wall law. The enhanced turbulent law of the wall for compressible flow with heat transfer and pressure gradients is:

$$\frac{du^+_{\text{turb}}}{dy^+} = \frac{1}{\kappa y^+}\left[S'\left(1 - \beta u^+ - \gamma(u^+)^2\right)\right]^{1/2} \tag{D.49}$$

where:

$$S = \begin{cases} 1 + \alpha y^+ & \text{for } y^+ < y_s^+ \\ 1 + \alpha y_s^+ & \text{for } y^+ \geq y_s^+ \end{cases} \tag{D.50}$$

and

$$\begin{aligned} \alpha &\equiv \frac{\nu_w}{\tau_w u^*}\frac{dp}{dx} &= \frac{\mu}{\rho^2 (u^*)^3}\frac{dp}{dx} \\ \beta &\equiv \frac{\sigma_t q_w u^*}{c_p \tau_w T_w} &= \frac{\sigma_t q_w}{\rho c_p u^* T_w} \\ \gamma &\equiv \frac{\sigma_t (u^*)^2}{2 c_p T_w} \end{aligned} \tag{D.51}$$

where y_s^+ is the location at which the log-law slope is fixed. By default in Fluent it is fixed, $y_s^+ = 60$. The coefficient α represents the influences of pressure gradients while the coefficients β and γ represent the thermal effects. If these values are put to zero, then a classical turbulent logarithmic law of the wall is seen.

The laminar law of the wall is determined from the following expression:

$$\frac{du_{\text{lam}}^+}{dy^+} = 1 + \alpha y^+ \tag{D.52}$$

In the above expression the effects of pressure gradients through α are included, while other effects like the effects of variable properties due to heat transfer and compressibility on the laminar wall law are neglected. Intragrating the above equation yields:

$$u_{\text{lam}}^+ = y^+ \left(1 + \frac{\alpha}{2} y^+\right) \tag{D.53}$$

Enhanced thermal wall functions follow the same approach developed for the profile of u^+. This also follows with a blend between the laminar and logarithmic profiles as:

$$T^+ \equiv \frac{(T_w - T_P)\, \rho c_p u_T}{\dot{q}} = e^{\Gamma} T_{\text{lam}}^+ + e^{1/\Gamma} T_{\text{turb}}^+ \tag{D.54}$$

where T_p and $\dot{q}$ are the values as in standard wall functions. The blending factor Γ is defined as:

$$\Gamma = -\frac{a\,(\text{Pr}\; y^+)^4}{1 + b\text{Pr}^3 y^+} \tag{D.55}$$

Here, Pr is the molecular Prandtl number, and the coefficients a and b are defined earlier, refer equation D.47. The definition for the turbulent and laminar thermal wall functions is:

$$T_{\text{lam}}^+ = \text{Pr}\left(u_{\text{lam}}^+ + \frac{\rho u_*}{2\dot{q}} u^2\right) \tag{D.56}$$

$$T_{\text{turb}}^+ = \text{Pr}_t \left(u_{\text{turb}}^+ + P + \frac{\rho u_*}{2\dot{q}} \left[u^2 - \left(\frac{\text{Pr}}{\text{Pr}_t} - 1\right)\left(u_c^+\right)^2 (u_*)^2\right]\right) \tag{D.57}$$

where the quantity u_c^+ is the value of u^+ at the crossover between the laminar and turbulent region. A similar procedure is used for the species wall functions when the enhanced wall treatment is used. Here, instead of Prandtl numbers in the above equations, Schmidt numbers are used. The production of turbulence kinetic energy, G_k, is computed using the velocity gradients that are stable with the enhanced law of the wall.

D.10 Combustion modelling

Till now only the non-reacting turbulent flows were considered. Modelling reacting flows has significant challenges in the closure of the highly nonlinear chemical source terms in equation D.20 and D.21 for $\overline{\partial \dot{q}_j^R}/\partial x_j$ and $\bar{S}_k$, respectively. Since both these terms are highly non-linear in local instantaneous gas temperature, many other extra terms are generated during the time averaging process.

Turbulent chemistry interactions

Consider a simplified chemical reaction of the form:

$$\mathrm{F} + \nu\mathrm{O} \xrightarrow{k} \mathrm{P} \tag{D.58}$$

where k is the rate constant for the reaction, F, O, and P are the fuel, oxygen and products respectively, with ν being the shoichiometric ratio of the oxygen supply.

$$k = Ae^{-T_a/T} \tag{D.59}$$

A and T_a are the frequency factor and activation temperature for the reaction. The instantaneous fuel disappearance rate

$$S_f = -\rho^2 k Y_f Y_o \tag{D.60}$$

where Y_f and Y_o are the mass fractions of fuel and oxidant, respectively. Each variable on the right side of the above equation has its own fuctuations and the time mean fuel disappearance as:

$$\begin{aligned} -\bar{S}_f = \tilde{\rho k}\left(\bar{\rho}\tilde{Y}_f\tilde{Y}_o + \overline{\rho Y_f'' Y_o''}\right) + \overline{\rho\,(\rho k)\,Y_o''}\cdot\tilde{Y}_f \\ + \overline{\rho\,(\rho k)\,Y_f''}\cdot\tilde{Y}_o + \overline{\rho\,(\rho k)\,Y_o''Y_f''} \end{aligned} \tag{D.61}$$

Except the first term in the above equation D.61, which is for the mean chemical production with no turbulent fluctuations, all other terms contain the fluctuations in rate constants and reactants concentrations. Fluctuations in the rate constant can be examined by expanding the Arrhenius expression in terms of the time mean and fluctuating temperatures. The instantaneous scalar variables split into Favre mean and fluctuating parts, where the fundamental turbulent closure problem introduced by time averaging is highly non-linear form of chemical source term. Different types of approach are employed to find a closure for this chemical source term proposed, are mentioned below. These model are relevent only when chemical time scales are larger than turbulent time scales ($\tau_c \gg \tau_t$, i.e. low Damköhler number limit).

- Arrhenius approach
  This model is evaluated by local mean properties with a simple closure, developed in terms of principle dependent variables. Turbulent fluctuations are neglected and the turbulent chemistry is not touched. The mean rate constant is:

  $$k\left(\bar{T}\right) = Ae^{-T_a/\bar{T}} \tag{D.62}$$

  The correct value, however, is $\overline{k\,(T)}$.

- The Eddy break up (EBU) model
  One of the earlier attempts to provide a reaction term closure is to assume that the reaction term is controlled by the mixing process only. The eddy-breakup (EBU) model, developed by Spalding, the mean reaction rate is proportional to the variance of the fuel and mixing time determined from the turbulence characteristics, namely k/ϵ as

$$\bar{\omega}_f = \bar{\rho} C_{EBU} \left(\frac{\epsilon}{k}\right) \left(\overline{Y_f''^2}\right)^{1/2} \tag{D.63}$$

  where C_{EBU} is an empirical constant in the order of unity [80]. Since k and ϵ are used in the model, the Eddy breakup closure is generally used together with the $k-\epsilon$ turbulence model. This approach originally developed for non-premixed flames was applied by Magnussen and Hjertager (1976) to turbulent diffusion flames. From the above equation D.58, the mean reaction rate is given by:

$$\bar{\omega}_f = \bar{\rho} C_{EBU} \left(\frac{\epsilon}{k}\right) \min\left[\overline{Y}_f, \frac{\overline{Y}_o}{\nu}, B_{EB}\frac{\overline{Y}_p}{(1+\nu)}\right] \tag{D.64}$$

  Here, $\overline{Y}_f$, $\overline{Y}_o$, and $\overline{Y}_p$ are the time mean mass fractions of fuel, oxygen and products respectively, which ever is the smaller. This equation do not consider the fluctuations and does not take into account the influence of chemistry. The model limits itself when it comes to multicomponent mixtures, and most notably that of temperatures on reaction rates is completely neglected [33].

  Fluent uses a turbulence-chemistry interaction model called the eddy dissipation model based. The net rate of production of species i due to reaction r. $R_{i,r}$ is given by the smaller (i.e., limiting value) of the two expressions below:

$$R_{i,r} = \nu_{i,r}^{'} M_{i,r} A \rho \frac{\epsilon}{k} \underbrace{\min}_{R} \left(\frac{Y_R}{\nu_{R,r}^{'} M_{w,\Re}}\right) \tag{D.65}$$

$$R_{i,r} = \nu_{i,r}^{'} M_{i,r} A B \rho \frac{\epsilon}{k} \frac{\sum_P Y_P}{\sum_j^N \nu_{j,r}^{''} M_{w,j}} \tag{D.66}$$

  where, Y_P is the mass fraction of any product species, P; Y_R is the mass fraction of a particular reactant, R; A and B are an empirical constants equal to 4.0 and 0.5 respectively. Here, k/ϵ is as in the eddy-breakup model discussed above. Combustion proceeds whenever turbulence is present ($k/\epsilon > 0$), and an ignition source is not required to initate combustion.
- Mixture fraction methods
  The mean velocity $\bar{u}_i$ and Reynolds stresses $\overline{u_i'' u_j''}$ are just the first and second moments of the probability density function of the velocity is P(u;x,t). Probability density functions (*pdf*) contains not only on the mean value of the variable but also on its variance (first moment) and on all higher moments. The information contained in a *pdf* is essential for combustion phenomena. The reaction in equation D.58, even though it is a simplified representation, is a complex function of the composition variables (Y_f and Y_o), the mixture denisty ρ and the temperature T, whence:

$$\bar{S}_f = \int S_f\left(Y_f, Y_o, \rho, T\right) P\left(Y_f, Y_o, \rho, T\right) dY_f dY_o d\rho dT \tag{D.67}$$

  where $P\left(Y_f, Y_o, \rho, T\right)$ is a joint probability density function for these scalar variables.

Pdf for mixture fraction

Probability density function has some common features for many combustion applications, describing a limited number of parameters. A possible approach is that pdf has a fixed shape, parameterized using, only one or two parameters. This is done by using the moments of the variable: mean quantities and first moment i.e. variance.

D.11 Radiation modelling

Radiation is particularly interesting when it comes to fire, where it usually determines the rate at which neighbouring material surfaces are drawn into a developing fire. Radiation heat transfer from the flames to the unburnt solid plays a vital role in the flame spread phenomena or fire development. During fire, two types of radiations are experienced, luminous radiation from particulate soot, and non-luminous radiation from hot product gases and unburnt fuel, participate in energy transfer. Nearly all flames are visible to human eye and are, therefore, called luminous (giving out light). This luminous emission known to come from tiny char (almost pure carbon) particles, called soot, which are generated during the combustion process. A description of the scalar fields for temperature, species and soot concentration in the turbulent flame along with the complete radiation properties is required in the thermal radiation model. The fluctuating, inhomogeneous nature of combustion process, makes the difficulty in evaluating the model.

Thermal radiation is seen through the divergence of the mean radiative energy flux $\frac{\partial \dot{q}_j^R}{\partial x_j}$ in the energy conservation equation D.20. This is determined by considering a radiation transfer equation for an idealized continuous, homogeneous, isotropic medium. If the emitting, absorbing and scattering medium at position $(\vec{r})$ can be considered to be in thermal equilibrium, then a radiation balance for an infinitesimal pensil of ray of wavelength λ and intensity I_λ passing through an elementary control volume in the direction $\vec{s}$ is the equation of transfer, or radiative transfer equation (RTE) as [76]:

$$\frac{1}{C}\frac{\partial I_\lambda(\vec{r},\vec{s})}{\partial t} + \frac{dI_\lambda(\vec{r},\vec{s})}{d\vec{s}} + (k_a + k_s)\, I_\lambda(\vec{r},\vec{s}) = k_a \frac{\sigma T^4}{\pi} + \frac{k_s}{4\pi}\int_0^{4\pi} \Phi\left(\vec{s},\vec{s}^{\,\prime}\right) I(\vec{r},\vec{s}) d\Omega^{'} \tag{D.68}$$

where $\vec{r}$ is the position vector, $\vec{s}$ is the direction vector, $\vec{r}^{\,\prime}$ is the scattering direction vector, k_a is the absorption coefficient, k_s is the scattering coefficient, Φ is the scattering phase function and $\Omega^{'}$ is the scatter angle. The change in the intensity over the length s is the sum of the energy absorption together with energy scattered outside into the gas with the heat absorbed into the element and the gain by scattering in the S direction. The last term in equation D.68 is complicated, because it accounts for the radiative transfer in all directions and all wavelengths for each control volume.

For engineering applications, the speed of light is so large compared to local time and length scales that the first term in equation D.68 can be neglected [73].

In fluent, the discrete ordinates (DO) radiation model use the RTE for a definite number of discrete solid angles, each associated with a vector direction $\vec{s}$ fixed in the global cartesian system (x, y, z). The DO model transforms equation D.68 into a transport equation for radiation intensity in the spatial coordinates (x, y, z). The DO model solves as many transport equations as there are directions $\vec{s}$.

The DO model considers the radiation transfer equation (RTE) (equation D.68) in the direction $\vec{s}$ as a field equation is written as:

$$\nabla \cdot \left(I\left(\vec{r}, \vec{s}\right)\vec{s}\right) + (a + \sigma_s) I\left(\vec{r}, \vec{s}\right) = an^2 \frac{\sigma T^4}{\pi} + \frac{\sigma_s}{4\pi} \int_0^{4\pi} \Phi\left(\vec{s}, \vec{s}^{'}\right) I(\vec{r}, \vec{s}) d\Omega^{'} \tag{D.69}$$

where $\vec{r}$ is a position vector, $\vec{s}$ is the direction vector, $\vec{s}^{'}$ is the scattering direction vector, s is the path length, a is the absorption coefficient, n is the refractive index, σ_s is the scattering coefficient, σ represents Stefan-Boltzmann constant $(5.668) \times 10^{-8}$ W/m^2-K^4, I is the radiation intensity, which depends on position $\vec{r}$ and direction $\vec{s}$, T is the local temperature, Φ is the phase function, and $\Omega^{'}$ is the solid angle.

The RTE for the spectral intensity $I_\lambda\left(\vec{r}, \vec{s}\right)$ is written as:

$$\nabla \cdot \left(I_\lambda\left(\vec{r}, \vec{s}\right)\vec{s}\right) + (a_\lambda + \sigma_s) I_\lambda\left(\vec{r}, \vec{s}\right) = a_\lambda n^2 T_{b\lambda} + \frac{\sigma_s}{4\pi} \int_0^{4\pi} \Phi\left(\vec{s}, \vec{s}^{'}\right) I_\lambda(\vec{r}, \vec{s}) d\Omega^{'} \tag{D.70}$$

In here, λ is the wavelength, a_λ is the spectral absorption coefficient, and $I_{b\lambda}$ is the black body intensity given by the Planck function. The scattering coefficient, the scattering phase function, and the refractive index n are assumed independent of wavelength.

D.12 Soot modelling

A generalised features of soot formation is uncertain as it is difficult to detail out the chemical mechanisms in relation to the more complex hydrocarbons contained in fuels and flammable materials. Soot formation is due to cyclization, creation of aromatic rings, which grow into polynuclear aromatics by the successive addition of alkyl groups. Beyond a certain size these rings act as a condensed phase nuclei to continue to grow into particles by surface reactions and the physical processes of coagulation and agglomeration.

J. B. Moss [33] proposed the work done by Khan (1979) for a global expression for soot mass concentration as

$$\left(\frac{ds}{dt}\right) = C\Phi^3 P_{fu} e^{(E/RT)} \tag{D.71}$$

for use in direct injection diesel engine simulation, where Φ is the local equivalence ratio, P_{fu} is the partial pressure of unburnt fuel; C is the soot formation constant and the activation temperature, E/R, is 20000 K.

A recent soot model used by Yeoh et al. [134] originally developed by Moss, Stewart and Syed, incorporates the essential physical processes of nucleation, coagulation and surface growth. The representation of soot properties involves just two properties - soot volume fraction, f_v, and the particulate number density or radical nuclei, n.

The transport equations for the soot particulate number density and soot fraction can be written as:

$$\begin{aligned}
&\frac{\partial(\rho\zeta_n)}{\partial t}+\frac{\partial(\rho\tilde{u}_i\zeta_n)}{\partial x_j}+\frac{\partial(\rho U_{th}\zeta_n)}{\partial x_j}-\frac{\partial}{\partial x_j}\left[\left(\frac{\mu_t}{\sigma_{n,pr}}\right)\frac{\partial\zeta_n}{\partial x_j}\right]\\
&\qquad=\underbrace{C_\alpha\rho^2T^{1/2}X_{fu}e^{(-T_a/T)}}_{\text{nucleation}}-\underbrace{\rho^2C_\beta T^{1/2}\zeta_n^2}_{\text{coagulation}}\\
&\frac{\partial(\rho\zeta_s)}{\partial t}+\frac{\partial(\rho\tilde{u}_i\zeta_s)}{\partial x_j}+\frac{\partial(\rho U_{th}\zeta_s)}{\partial x_j}-\frac{\partial}{\partial x_j}\left[\left(\frac{\mu_t}{\sigma_{s,pr}}\right)\frac{\partial\zeta_s}{\partial x_j}\right]\\
&\qquad=\underbrace{144C_\alpha\rho^2T^{1/2}X_{fu}e^{(-T_a/T)}}_{\text{nucleation}}\\
&\qquad-\underbrace{N_o^{1/3}\rho^2C_\gamma T^{1/2}X_{fu}e^{(-T_a/T)}\zeta_s^{2/3}\zeta_n^{1/3}}_{\text{surface growth}}-\underbrace{w_{ox}}_{\text{oxidation}}
\end{aligned}\tag{D.72}$$

where $\zeta_n=\frac{n}{\rho}N_o$ and $\zeta_s=\frac{\rho-s}{\rho}f_v$. N_o is the Avagadro number. As in other models of turbulent combustion, the mean source terms present the greatest closure difficulty as a result of their non-linear dependence on temperature. The source term in equation D.72 for soot oxidation w_{ox} by O_2 and mean thermphoretic velocity component U_{th} is given by:

$$\begin{aligned}
w_{ox}&=1.085\times10^5P_{O_2}T^{-1/2}e^{(-E/RT)}\\
U_{th}&=-0.54\nu\nabla(\ln T)
\end{aligned}\tag{D.73}$$

A detailed discussion was made by Ian Kennedy [61] on the various models of soot formation and oxidation. There, he describes the various models developed based on empirical correlations, semi-empirical models, and models with detailed chemistry. He classified the model developed by Moss as a semi-empirical. An equation for the mass fraction of soot in the laminar diffusion flame, which is a detailed model, is written as:

$$\frac{\partial(\rho u_jY_s)}{\partial x_j}=\frac{\partial}{\partial x_j}\left[\rho\mathrm{D}\frac{dY_s}{dx_j}\right]+\frac{\partial}{\partial x_j}\left[0.54\eta\frac{1}{T}\frac{dT}{dx_j}Y_s\right]+\left[\frac{d}{dt}(\rho_sf_v)\right]\tag{D.74}$$

The first term on the right hand side accounts for soot diffusion, the second term for thermophoresis and the final term is the net source term that is derived from flamelet theory. Due to the source term in the above equation, moments are required for the aerosol size distribution, the first moment being the soot volume. Fractional moments such as the soot aerosol surface area can be found by interpolation.

Fluent uses the Moss-Brookes model for soot modelling. This model solves transport equations for normalized radical nuclei concentration b^*_{nuc} and soot mass fraction Y_{soot}:

$$\begin{aligned}
\frac{\partial(\rho Y_{\mathrm{soot}})}{\partial t}+\nabla\cdot(\rho\vec{\nu}Y_{\mathrm{soot}})&=\nabla\cdot\left(\frac{\mu_t}{\sigma_{\mathrm{soot}}}\nabla Y_{\mathrm{soot}}\right)+\frac{dM}{dt}\\
\frac{\partial(\rho b^*_{\mathrm{nuc}})}{\partial t}+\nabla\cdot(\rho\vec{\nu}b^*_{\mathrm{nuc}})&=\nabla\cdot\left(\frac{\mu_t}{\sigma_{\mathrm{nuc}}}\nabla b^*_{\mathrm{nuc}}\right)+\frac{1}{N_{\mathrm{norm}}}\frac{dM}{dt}
\end{aligned}\tag{D.75}$$

where, Y_{soot} is the soot mass fraction, M is the soot mass concentration (kg/m^3), b^*_{nuc} is the normalized radical nuclei concentration (particle $\times$ 10^{-5} /kg) $= \frac{N}{\rho N_{\text{norm}}}$, N is the soot particle number density (particle/m^3), and N_{norm} is equal to 10^{15} particles.

The instanteneous production rate of soot particles, subject to nucleation from the gas phase and coagulation in the free molecular regime, is given by:

$$\frac{dN}{dt} = \underbrace{C_\alpha N_A \left(\frac{X_{\text{prec}} P}{RT}\right)^l e^{(-T_\alpha/T)}}_{\text{Nucleation}} - \underbrace{C_\beta \left(\frac{24RT}{\rho_{\text{soot}} N_A}\right)^{1/2} d_p^{1/2} N^2}_{\text{Coagulation}} \tag{D.76}$$

where C_α, C_β and l are model constants. N_A is the Avogadro number (=6.022045 $\times$ 10^{26} k/mol) and X_{prec} is the mole fraction of soot precursor.

The source term for soot mass concentration is modelled by the expression:

$$\begin{aligned}\frac{dM}{dt} = & \underbrace{C_\alpha M_P \left(\frac{X_{\text{prec}} P}{RT}\right)^l e^{(-T_\alpha/T)}}_{\text{Nucleation}} \\ & + \underbrace{C_\gamma \left(\frac{X_{\text{sgs}} P}{RT}\right)^m e^{(-T_\gamma/T)} \left[(\pi N)^{1/3} \left(\frac{6M}{\rho_{\text{soot}}}\right)^{2/3}\right]}_{\text{Surface Growth}} \\ & - \underbrace{C_{\text{oxid}} C_\omega \eta_{\text{coll}} \left(\frac{X_{\text{OH}} P}{RT}\right) \sqrt{T} (\pi N)^{1/3} \left(\frac{6M}{\rho_{\text{soot}}}\right)^{2/3}}_{\text{Oxidation}}\end{aligned} \tag{D.77}$$

where C_γ, C_{oxid}, C_ω, m and n are additional model constants. The constant M_P (=144 kg/kgmol) is the mass of an incipient soot particle, η_{coll} is 0.04 and the mean density of soot particle is 2000 kg/m^3.

References

[1] The SFPE Handbook of Fire Protection Engineering. Society of Fire Protection Engineers, 2002.

[2] ASTM E1354 09. Standard test method for heat and visible smoke release rates for materials and products using an oxygen consumption calorimeter. Technical report, ASTM International, West Conshohocken, PA, 2003, DOI: 10.1520/E1354-09, www.astm.org, 2003.

[3] V. Alexiades and A. D. Solomon. Mathematical modelling of melting and freezing processes. Hemisphere Publishing Coporation, 1993.

[4] S. S. Alves and J. L. Figueiredo. A model for pyrolysis of wet wood. Chemical Engineering Science, 44:2861–2869, 1989.

[5] A. Atreya. Pyrolysis, ignition and fire spread on horizontal surfaces of wood. Ph.D Thesis, Harvard University, 1984.

[6] A. Atreya and I. S. Wichmann. Heat and mass transfer during piloted ignition of cellulosic solids. Journal of Heat Transfer, 111:719–725, 1989.

[7] Arvind Atreya. Ignition of fires. Phil. Trans. R. Soc. London. A, 356:2787–2813, 1998.

[8] V. Babrauskas and W. J. Parker. Ignitability mesurements with the cone calorimeter. Fire and Materials, 11:31–43, 1987.

[9] V. Babrauskas, W. H. Twilley, M. Janssens, and S. Yusa. A cone calorimeter for controlled-atmosphere studies. Fire and Materials, 16:37–43, 1992.

[10] V. Babrauskas, W. H. Twilley, and W. J. Parker. The effect of specimen edge conditions on heat release rate. Fire and Materials, 17:51–63, 1993.

[11] C. H. Bamford, J. Crank, and D. H. Malan. The combustion of wood. part i. Mathematical Proceedings of the Cambridge Philosophical Society, 42:166–182, 1945.

[12] B. Benkoussas, J. L. Consalvi, B. Porterie, N. Sardoy, and J. C. Loraud. Modelling thermal degradation of woody fuel particles. International Journal of Thermal Sciences, 46:319–327, 2007.

[13] R. Bilbao, J. F. Mastral, J. Ceamanos, and M. E. Aldea. Modelling of the prolysis of wet-charring materials. J. of Analytical and Applied Pyrolysis, 36:81–97, 1996.

[14] Colomba Di Blasi. Modelling and simulation of combustion processes of charring and non-charring solid fuels. Prog. Energy Combust. Sci., 19:71–104, 1993.

[15] Colomba Di Blasi. Processes of flames spreading over the surfaces of charring fuels: effect of the solid thickness. Combustion and Flame, 97:225–239, 1994.

[16] Colomba Di Blasi. Heat, momentum and mass trasport through a shrinking biomass particle exposed to thermal radiation. Chemical Engineering Science, 51:1121–1132, 1996.

[17] Colomba Di Blasi. The state of the art of transport models for charring solid degradation. Polymer International, 49:1133–1146, 2000.

[18] Colomba Di Blasi. Modeling chemical and physical processes of wood and biomass pyrolysis. Prog. Energy Combust. Sci., 34:47–90, 2008.

[19] Colomba Di Blasi. Combustion and gasification rates of lignocellulosic chars. Prog. Energy Combust. Sci., 35:121–140, 2009.

[20] P. Blomqvist and P. Van Hees. Upward flame spread experiments - a preparatory study. Technical report, SP AR, Boras 2001, Sweden, 2001.

[21] N. Boonmee. Theoretical and experimental study of autoignition of wood. Ph.D Thesis, University of Maryland, 2004.

[22] E. G. Brehob, C. I. Kim, and A. K Kulkarni. Numerical model of upward flame spread on practical wall materials. Fire Safety Journal, 36:225–240, 2001.

[23] E. G. Brehob and A. K Kulkarni. Time-dependent mass loss rate behavior of wall materials under external radiation. Fire and Materials, 17:249–254, 1993.

[24] E. G. Brehob and A. K Kulkarni. Experimental measurements of upward flame spread on a vertical wall with external radiation. Fire Safety Journal, 31:181–200, 1998.

[25] K. M. Bryden and M. J. Hagge. Modelling the combined impact of moisture ad char shrinkage on the pyrolysis of a biomass fuel. Fuel, 82:1633–1644, 2003.

[26] K. M. Bryden, K. W. Ragland, and C. J. Rutland. Modelling thermally thick pyrolysis of wood. Biomass and Bioenergy, 22:41–53, 2002.

[27] Y. Chen, M. A. Delichatsios, and V. Motevalli. Material pyrolysis properties, part 1: An integral model for one-dimensional transient pyrolysis of charring and non-charring materials. Comb. Sci. and Tech., 88:309–328, 1993.

[28] Y. Chen, M. A. Delichatsios, and V. Motevalli. Material pyrolysis properties, part 2: Methodology for the derivation of pyrolysis properties for charring materials. Comb. Sci. and Tech., 104:401–425, 1995.

[29] Hsiang cheng Kung. A mathematical model of wood pyrolysis. Combustion and Flame, 18:185–195, 1972.

[30] Hsiang cheng Kung and A. S. Kalelkar. On the heat of reaction in wood pyrolysis. Combustion and Flame, 20:91–103, 1973.

[31] J. L. Consalvi, Y. Pizzo, and B. Porterie. Numerical analysis of the heating process in upward flame spread over thick pmma slabs. Fire Safety Journal, 43:351–362, 2008.

[32] J. L Consalvi, Y. Pizzo, B. Porterie, and J. L. Torero. On the flame height definition for upward flame spread. Fire Safety Journal, 42:384–392, 2007.

[33] G. Cox. Combustion fundamentals of fire. Academic Press, 1995.

[34] J. L. de Ris. Will it support a self-propagating fire? In NIST workshop on fire growth and spread on objects, 2002.

[35] J. L. de Ris and Z. Yan. Modeling ignition and pyrolysis of charring fuels. In Proceedings of the 5th International Conference on Fire and Materials, pages 111–121, 1998.

[36] J. Degroote, K. Bathe, and J. Vierendeels. Performance of a new partitioned procedure versus a monolithic procedure in fluid-structure interaction. Computers and Structures, 87:793–801, 2009.

[37] M. Delichatsios, B. Paroz, and A. Bhargava. Flammability properties for charring materials. Fire Safety Journal, 38:219–228, 2003.

[38] M. A. Delichatsios. Heinz tomato paste plywood bin storage. Technical report, FMRC data file '17dec961', December 1996.

[39] M. A. Delichatsios, Mary Delichatsios, Y. Chen, and Y. Hasemi. Similarity solutions and applications to turbulent upward flame spread on noncharring materials. Combustion and Flame, 102:357–370, 1995.

[40] M. M. Delichatsios, P. Wu, M. A. Delichatsios, and et al. Effect of external radiant heat flux on upward fire spread: measurements on plywood and numerical predictions. In IAFSS-Proceedings of the fourth international symposium, pages 421–432, 1994.

[41] C. DiBlasi. Multi-phase moisture transfer in the high temperature drying of wood particles. Chemical Engineering Science, 53:353–366, 1998.

[42] Y. Fei, Z. Lin, Z. Jianjun, and T. T. Chow. Direct numerical simulation on the pyrolysis of materials with volatile residue layer. Applied Mathematical Modelling, 31:770–779, 2007.

[43] Ansys Fluent. Ansys fluent 12.0 tutorial guide. Technical report, Ansys, Inc, April, 2009.

[44] M. Foley and D. D. Drysdale. Heat transfer from flames between vertical parallel walls. Fire Safety Journal, 24:53–73, 1995.

[45] B. Fredlund. Modelling of heat and mass transfer in wood structures during fire. Fire Safety Journal, 20:39–69, 1993.

[46] George Grant and Dougal Drysdale. Numerical modelling of early flame spread in warehouse fires. Fire Safety Journal, 24:247–278, 1995.

[47] FM Global Group. Americal national standard for cleanroom materials flammability test protocol. Technical report, ANSI/FM Approval 4910, FM Global, 2004.

[48] Y. Hasemi. Thermal modelling of upward wall flame spread. In IAFSS-Proceedings of the first international symposium, pages 87–96, 1986.

[49] Y. Hasemi. Concurrent flame spread in fires- state of the art of modeling and future problems for engineering applications. Technical report, Technical Report NISTIR 6030, 1997.

[50] Y. Hasemi, M. Yashida, N. Yasui, and W. J. Parker. Upward flame spread along a vertical solid for transient local heat release rate. In IAFSS-Proceedings of the fourth international symposium, pages 385–396, 1994.

[51] Y. Hasemi, M. Yoshida, S. Takashima, and S. Yokobayashi. Wall flame correlations and upward flame spread in a vertical channel and its relevance to fire safety. Technical report, Technical Report NISTIR 6030, 1997.

[52] International Standard Organisation ISO 5560. Fire tests - reaction to fire - rate of heat release from building products. Technical report, International Standard Organisation (ISO), 1991.

[53] M. Janssens. Fundamental thermophysical characteristics of wood and their role in enclosure fire growth. Ph.D Thesis, Ghent University-UGent, 1991.

[54] F. Jia, E. R. Galea, and M. K. Patel. Numerical simulation of the mass loss process in pyrolysing char materials. Fire and Materials, 23:71–78, 1999.

[55] A. I. Karprov and V. K. Bulgakov. Prediction of the steady rate of flame spread over combustible materials. In IAFSS-Proceedings of the fourth international symposium, pages 373–384, 1994.

[56] T. Kashiwagi. A radiative ignition model of a solid fuel. Comb. Sci. and Tech., 8:225–236, 1974.

[57] T. Kashiwagi. Effects of sample orientation on radiative ignition. Combustion and Flame, 44:223–245, 1982.

[58] T. Kashiwagi. Polymer combustion and flammability-role of the condensed phase. In 25th Symposium (International) on Combustion/The Combustion Institute, pages 1423–1437, 1994.

[59] T. Kashiwagi and T. J. Ohlemiller. A study of oxygen effects on nonflaming transient gasification of pmma and pe during thermal irradiation. In Nineteenth Symposium (International) on Combustion/The Combustion Institute, pages 815–823, 1982.

[60] T. Kashiwagi, T. J. Ohlemiller, and K. Werner. Effect of external radiant flux and ambient oxygen concentration on non-flaming gasification rates and evolved products of white pine. Combustion and Flame, 69:331–345, 1987.

[61] I. M. Kennedy. Models of soot formation and oxidation. Progress in Energy and Combustion, 23:95–132, 1997.

[62] M. M. Khan, R. G. Bill, and R. L. Alpert. Screening of plenum cables using a small-scale fire test protocol. Fire and Materials, 30:65–76, 2006.

[63] M. Kokkala, D. Baroudi, and W. J. Parker. Upward flame spread on wooden surface products: Experiments and numerical modelling. In IAFSS-Proceedings of the fifth international symposium, pages 309–320, 1997.

[64] K. K. Kuo. Principles of Combustion. John Wiley & Sons, 1986.

[65] C. Lautenberger and C. Fernandez-Pello. Generalized pyrolysis model for combustible solid. Fire Safety Journal, doi:10.1016/j.firesaf.2009.03.011, 2009.

[66] C. Lautenberger and C. Fernandez-Pello. A model for the oxidative pyrolysis of wood. Combustion and Flame, doi:10.1016/j.combustflame.2009.04.001, 2009.

[67] C. K. Law. Combustion Physics. Cambridge University Press, 2006.

[68] J. Z. Lin, T. T. Chow, Y. Fei, Z. Jianjun, and Z. Yanghui. A partial differential model for the pyrolysis of materials with movable residual layer. Mechanics of Advanced Materials and Structures, 12:77–83, 2005.

[69] R. E. Lyon. Heat release kinetics. Fire and Materials, 24:179–186, 2000.

[70] K. McGrattan, S. Hostikka, J. Floyd, H. Baum, R. Rehm, W. Mell, and R. McDermott. Fire dynamics simulator (version 5), technical reference guide. Technical report, National Institute of Standards and Technology, US, 2009.

[71] M. C. Melaaen. Numerical analysis of heat and mass transfer in drying and myrolysis of porous media. Numerical Heat Transfer, Part A: Applications, 29:331–355, 1996.

[72] E. Mikkola. Charring of wood based materials. In IAFSS-Proceedings of the third international symposium, pages 547–556, 1991.

[73] M. F. Modest. Radative Heat Transfer. Academic Press, 2003.

[74] B. Moghtaderi. The state of the art in pyrolysis modelling of lignocellullosic solid fuels. Fire and Materials, 30:1–34, 2006.

[75] B. Moghtaderi, V. Novozhilov, D. Fletcher, and Kent J. H. An integral model for the transient pyrolysis of solid materials. Fire and Materials, 21:7–16, 1997.

[76] J. B. Moss and P. A. Rubinin. Coupled soot and radiation calculations in a compartment fire. In Second International Conference on Fire Research and Engineering, NIST, Gaithersburg, Maryland, USA, 1997.

[77] T. J. Ohlemiller, T. Kashiwagi, and K. Werner. Wood gasification at fire level heat fluxes. Combustion and Flame, 69:155–170, 1987.

[78] Won Chan Park, A. Atreya, and H. R. Baum. Determination of pyrolysis temperature for charring materials. Technical report, Technical Report NIST GCR 07-913, 2007.

[79] B. Peters and C. Bruch. Drying and pyrolysis of wood particles: experiments and simulation. J. of Analytical and Applied Pyrolysis, 70:233–250, 2003.

[80] T. Poinsot and D. Veynante. Theoretical and Numerical Combustion. Edwards, 2005.

[81] S. B. Pope. Turbulent Flows. Cambridge University Press, 2006.

[82] J. Quintiere, M. Harkleroad, and Y. Hasemi. Wall flames and implications for upward flame spread. Combust. Sci. and Tech., 48:191–222, 1986.

[83] J. Quintiere and N. Iqbal. An approximate integral mdel for the burning rate of a thermoplastic-like material. Fire and Materials, 18:89–98, 1994.

[84] J. G. Quintiere. The application of flame spread theory to predict material performance. J. of Research of the National Bureau of Standards, 93:61–70, 1987.

[85] J. G. Quintiere. A semi-quantitative model for the burning rate of solid materials. Technical report, Technical Report NISTIR 4840, 1992.

[86] J. G. Quintiere. Fundamentals of fire phenomena. John Wiley & Sons, 2006.

[87] J. G. Quintiere. A theoretical basis for flammability properties. Fire and Materials, 30:175–214, 2006.

[88] J. G. Quintiere and T. G. Cleary. Heat flux from flames to vertical surfaces. Fire Technology, 30:209–231, 1994.

[89] A. S. Rangwala, S. G. Buckley, and J. L. Torero. Analysis of the constant b-number assumption while modeling flame spread. Combustion and Flame, 152:401–414, 2008.

[90] J. Rath, M. G. Wolfinger, G. Steiner, G. Krammer, F. Barontini, and V. Cozzani. Heat of wood pyrolysis. Fuel, 82:81–91, 2003.

[91] G. Rein, N. Cleaver, C. ashton, P. Pironi, and J. L. Torero. The severity of somldering peat fires and damage to the forest soil. Catena, 74:304–309, 2008.

[92] S. J. Ritchie, K. D. Steckler, A. Hamins, T. G. Cleary, J. C. Yang, and T. Kashiwagi. The effects of sample size on the heat release rate of charring. In Fire Safety Science-Proceedings of the 5th international symposium, pages 177–188, 1997.

[93] A. F. Roberts and G. Clough. Thermal decompostion of wood in an inert atmosphere. In 9th Symposium (International) on Combustion, Academic, New York, pages 158–166, 1963.

[94] K. Saito, J. G. Quintiere, and F. A. Williams. Upward turbulent flame spread. In IAFSS-Proceedings of the first international symposium, pages 75–86, 1986.

[95] U. Sand, J. Sandberg, J. Larfeldt, and R. Bel Fdhila. Numerical prediction of the transport and pyrolysis in the interior and sourrounding of dry and wet log. Applied Energy, 85:1208–1224, 2008.

[96] B. Schartel, M. Bartholmai, and U. Knoll. Some comments on the use of cone calorimeter data. Polymer Degradation and Stability, 88:540–547, 2005.

[97] D. K. Shen, M. X. Fang, Z. Y. Luo, and K. F. Cen. Mathematical modelling of melting and freezing processes. Fire Safety Journal, 42:210–217, 2007.

[98] M. Sibulkin. Heat of gasification for pyrolysis of charring materials. In IAFSS-Proceedings of the first international symposium, pages 391–400, 1986.

[99] M. Sibulkin and J. Kim. The dependence of flame propagation on surface heat transfer ii. upward burning. Combustion Science and Technology, 17:39–49, 1977.

[100] D. L. Simms and Margaret Law. The ignition of wet and dry wood. Combustion and Flame, 11:377–388, 1967.

[101] Y. Sohn, S. W. Baek, and T. Kashiwagi. Transient modeling of thermal degradation in non-charring solids. Combust. Sci. and Tech., 145:83–108, 1999.

[102] M. J. Spearpoint and J. G. Quintiere. Predicting the burning of wood using an integral model. Combustion and Flame, 123:308–324, 2000.

[103] M. J. Spearpoint and J. G. Quintiere. Predicting the piloted ignition of wood in the cone calorimeter using an integral model - effect of species, grain orientation and heat flux. Fire Safety Journal, 36:391–415, 2001.

[104] J. E. J. Staggs. A simple model of polymer pyrolysis including transport of volatiles. Fire Safety Journal, 34:69–80, 2000.

[105] J. E. J. Staggs. Heat and mass transport in developing chars. Polymer Degradation and Stability, 82:297–307, 2003.

[106] J. E. J. Staggs. The heat of gasification of polymers. Fire Safety Journal, 39:711–720, 2004.

[107] International Standard. Reaction-to-fire tests-heat release, smoke production and mass loss rate - part i: Heat release rate (cone calorimeter method). Technical report, ISO 5660-1, Second Edition, ISO copyright office, Geneva.

[108] A. Tewarson and S. D. Ogden. Fire behavior of polymethylmethscrylate. Combustion and Flame, 89:237–259, 1992.

[109] E. Theuns. Numerical modelling of flame spread. Ph.D Thesis, Ghent University-UGent, 2003.

[110] E. Theuns, B. Merci, J. Vierendeels, and P. Vandevelde. Critical evaluation of an integral model for the pyrolysis of charring materials. Fire Safety Journal, 40:121–140, 2005.

[111] E. Theuns, B. Merci, J. Vierendeels, and P. Vandevelde. Extension and evaluation of the integral model for transient pyrolysis of charring materials. Fire and Materials, 29:195–212, 2005.

[112] E. Theuns, J. Vierendeels, and P. Vandevelde. A moving grid model for the pyrolysis of charring materials. Intl. J. Num. Methods for Heat and Fluid Flow, 12:541–559, 2002.

[113] E. Theuns, J. Vierendeels, and P. Vandevelde. Validation of the integral model for the pyrolysis of charring materials with a moving grid. Journal of Computational and Applied Mathematics, 168:471–479, 2004.

[114] H. C. Tran. Heat release in fires. New York: Elsevier Applied Science, 1992.

[115] J. Urbas and W. J. Parker. Surface temperature measurements on burning wood specimens in the cone calorimeter and the effect of grain orientation. Fire and Materials, 17:205–208, 1993.

[116] H. K. Veersteeg and W. Malalasekera. An Introduction to Computational Fluid Dynamics. Longman Scientific & Technical, 1995.

[117] C. Vovelle, R. Akrich, and J. L. Delfau. Mass loss rate measurements on solid materials under radiative heating. Combust. Sci. and Tech., 36:1–18, 1984.

[118] C. Vovelle, R. Akrich, and Delfau J. Thermal degradation of solid materials under a variable radiant heat flux. In 20th Symposium (International) on Combustion/The Combustion Institute, pages 1647–1654, 1984.

[119] S. R. Wasan, P. Rauwoens, J. Vierendeels, and B. Merci. Application of a simple enthalpy-based pyrolysis model in numerical simulations of pyrolysis of charring materials. Fire and Materials, 34:39–54, 2010.

[120] S. R. Wasan, P. Rauwoens, J. Vierendeels, and B. Merci. An enthalpy-based pyrolysis model for charring and non-charring materials in case of fire. Combustion and Flame, 157:715–734, 2010.

[121] S. R. Wasan, P. Van Hees, and B. Merci. Study of vertical upward flame spread on charring materials - part i: Experimental study. Fire and Materials, (submitted), 2009.

[122] S. R. Wasan, P. Van Hees, and B. Merci. Study of vertical upward flame spread on charring materials - part ii: Numerical simulations. Fire and Materials, (submitted), 2009.

[123] W. D. Weatherford and Jr. D. M. Sheppard. Basic studies of te mechanism of ignition of cellulosic materials. In 10th Symposium (International) on Combustion, pages 897–910, 1965.

[124] J. R. Welty, C. E. Wicks, R. E. Wilson, and G. Rorrer. Fundamentals of Momentum, Heat and Mass Transfer. John wily & Sons, 2001.

[125] W. G. Weng and W. C. Fan. A pyrolysis model of charring materials considering the effect if ambient oxygen concentration. Fire and Materials, 31:463–475, 2007.

[126] W. G. Weng and Y. Hasemi. A numerical model for flame spread along combustible flat solid with charring material with experimental validation of ceiling flame spread and upward flame spread. Fire and Materials, 32:87–102, 2008.

[127] H. R. Wesson, J. R. Welker, and C. M. Sliepcevich. The pilot ignition of wood by thermal radiation. Combustion and Flame, 16:303–310, 1971.

[128] Indrek S. Wichmann and Arvind Atreya. A simplified model for the pyrolysis of charring materials. Combustion and Flame, 68:231–247, 1987.

[129] F. A. Williams. Mechanisms of fire spread. In Sixteenth Symposium (International) on Combustion - The Combustion Institute, pages 1281–1294, 1976.

[130] Z. Yan and G. Holmstedt. Cfd and experimental studies of room fire growth on wall lining materials. Fire Safety Journal, 27:201–238, 1996.

[131] L. Yang, X. Chen, X. Zhou, and W. Fan. The pyrolysis and ignition of charring materials under an external heat flux. Combustion and Flame, 133:407–413, 2003.

[132] L. Yang, Z. Guo, Y. Zhou, and W. Fan. The influence of different external heating ways on pyrolysis and spontaneous ignition of some woods. J. Anal. Appl. Pyrolysis, 78:40–45, 2007.

[133] L. Yang, Y. Zhou, W. Yafei, and Z. Guo. Predicting charring rate of woods exposed to time-increasing and constant heat fluxes. J. Anal. Appl. Pyrolysis, 81:1–6, 2008.

[134] G. H. Yeoh, R. K. K. Yuen, S. C. P. Chueng, and W. K. Kwok. On modelling combustion, radiation and soot processes in compartment fires. Building and Environment, 38:771–785, 2003.

[135] Y. Yoshizawa and H. Kubota. Experimental study on gas-phase ignition of cellulose under thermal radiation. In 19th Symposium (International) on Combustion/The Combustion Institute, pages 787–795, 1982.

[136] R. Yuen, D. de Vahl Davis, E. Leonardi, and G. H. Yeoh. The influence of moisture on the combustion of wood. Numerical Heat Transfer, Part A: Applications, 8:257–280, 2000.